Report prepared by:
Julio Saire Yañez
Nelly S. Orozco Martínez
Gray Mullins
Christopher L. Alexander

FINAL REPORT (Project BDV25-977-56)

QUANTIFYING THE DURATION OF THE CORROSION PROPAGATION STAGE IN STAINLESS STEEL REINFORCEMENT

Final Report to Florida Department of Transportation

Christopher L. Alexander (PI)

Gray Mullins (Co – PI)

Ronald Simmons (FDOT Project Manager)

UNIVERSITY OF SOUTH FLORIDA

Tampa, FL 33620

December 2020

Disclaimer page

The opinions, findings, and conclusions expressed in this publication are those of the authors and not necessarily those of the Florida Department of Transportation.

Universal conversion table

SI* (MODERN METRIC) CONVERSION FACTORS

APPROXIMATE CONVERSIONS TO SI UNITS

Symbol	When You Know	Multiply By	To Find	Symbol
		LENGTH		
in	inches	25.4	millimeters	mm
ft	feet	0.305	meters	m
yd	yards	0.914	meters	m
mi	miles	1.61	kilometers	km
		AREA		
in^2	square inches	645.2	square millimeters	mm^2
ft^2	square feet	0.093	square meters	m^2
yd^2	square yard	0.836	square meters	m^2
ac	acres	0.405	hectares	ha
mi^2	square miles	2.59	square kilometers	km^2
		VOLUME		
fl oz	fluid ounces	29.57	milliliters	mL
gal	gallons	3.785	liters	L
ft^3	cubic feet	0.028	cubic meters	m^3
yd^3	cubic yards	0.765	cubic meters	m^3
		NOTE: volumes greater than 1000 L shall be shown in m^3		
		MASS		
oz	ounces	28.35	grams	g
lb	pounds	0.454	kilograms	kg
T	short tons (2000 lb)	0.907	megagrams (or "metric ton")	Mg (or "t")
		TEMPERATURE (exact degrees)		
°F	Fahrenheit	5 (F-32)/9 or (F-32)/1.8	Celsius	°C
		ILLUMINATION		
fc	foot-candles	10.76	lux	lx
fl	foot-Lamberts	3.426	candela/m^2	cd/m^2
		FORCE and PRESSURE or STRESS		
lbf	poundforce	4.45	newtons	N
lbf/in^2	poundforce per square inch	6.89	kilopascals	kPa

APPROXIMATE CONVERSIONS FROM SI UNITS

Symbol	When You Know	Multiply By	To Find	Symbol
		LENGTH		
mm	millimeters	0.039	inches	in
m	meters	3.28	feet	ft
m	meters	1.09	yards	yd
km	kilometers	0.621	miles	mi
		AREA		
mm^2	square millimeters	0.0016	square inches	in^2
m^2	square meters	10.764	square feet	ft^2
m^2	square meters	1.195	square yards	yd^2
ha	hectares	2.47	acres	ac
km^2	square kilometers	0.386	square miles	mi^2
		VOLUME		
mL	milliliters	0.034	fluid ounces	fl oz
L	liters	0.264	gallons	gal
m^3	cubic meters	35.314	cubic feet	ft^3
m^3	cubic meters	1.307	cubic yards	yd^3
		MASS		
g	grams	0.035	ounces	oz
kg	kilograms	2.202	pounds	lb
Mg (or "t")	megagrams (or "metric ton")	1.103	short tons (2000 lb)	T
		TEMPERATURE (exact degrees)		
°C	Celsius	1.8C+32	Fahrenheit	°F
		ILLUMINATION		
lx	lux	0.0929	foot-candles	fc
cd/m^2	candela/m^2	0.2919	foot-Lamberts	fl
		FORCE and PRESSURE or STRESS		
N	newtons	0.225	poundforce	lbf
kPa	kilopascals	0.145	poundforce per square inch	lbf/in^2

*SI is the symbol for the International System of Units. Appropriate rounding should be made to comply with Section 4 of ASTM E380.

Technical Report Documentation Page

1. Report No.	2. Government Accession No.	3. Recipient's Catalog No.
4. Title and Subtitle Quantifying the Duration of the Corrosion Propagation Stage in Stainless Steel Reinforcement		5. Report Date November 25, 2020
		6. Performing Organization Code
7. Author(s) N. S. Orozco, Julio Saire Yañez, C. L. Alexander, G. Mullins		8. Performing Organization Report No.
9. Performing Organization Name and Address Department of Civil and Environmental Engineering University of South Florida (USF) Tampa, FL 33620		10. Work Unit No. (TRAIS)
		11. Contract or Grant No. BDV25-977-56
12. Sponsoring Agency Name and Address		13. Type of Report and Period Covered Final Report 2/5/18 – 12/30/20
		14. Sponsoring Agency Code
15. Supplementary Notes		

16. Abstract

Present durability projections for concrete reinforced with stainless steel (SS) are limited in that, while accounting for a substantial increase in the corrosion initiation stage (CIS) duration, credit tends not to be given for any added corrosion propagation stage (CPS) duration over that of carbon steel (CS). The objectives of this work were to: (1) develop a rational quantitative estimate of the duration of the corrosion propagation stage of concrete reinforced with SS in current and anticipated FDOT practice, establishing alternative corrosion monitoring methods if needed; (2) apply the findings as inputs to damage function models to determine how any resulting added durability credit can be used to optimize materials and design options. Experiments were performed to obtain estimates of corrosion rates, corrosion morphology, and the critical corrosion penetration. The results were then used to suggest a service limit state that accounted for the mechanical properties of the steel. The results were incorporated into durability projections to provide recommendations of concrete cover to be used based on service conditions.

17. Key Words: Durability, Corrosion rate, corrosion morphology, critical corrosion penetration, limit state	18. Distribution Statement		
19. Security Classif. (of this report)	20. Security Classif. (of this page)	21. No. of Pages 163	22. Price

Form DOT F 1700.7 (8-72)   Reproduction of completed page authorized

Acknowledgements

Executive summary

Durability of Florida Department of Transportation (FDOT) reinforced concrete structures is greatly limited by corrosion of the steel reinforcement. This issue becomes even more critical in structures exposed to aggressive environments such as marine structures. The FDOT has instituted corrosion prevention strategies such as increased concrete cover thickness, higher concrete quality, and corrosion-resistant alloys such as stainless steel (SS) for some applications. Over the past couple of decades, SS reinforcement has garnered attention due to its increased durability. Several investigations have found that the cumulative cost of structures reinforced with SS may be considerably lower than that of plain carbon steel (CS). The service life of steel reinforcement is typically divided into two stages: the corrosion initiation stage (CIS) and corrosion propagation stage (CPS). The durability of SS reinforcement has been commonly approached using the model proposed by Tuutti[1] where the service life of a structure, which is the time required for corrosion loss in the steel to reach a serviceability limit state, is determined by the added duration of the CIS and the CPS .

The increased durability of SS reinforcement has been mostly attributed to a greater corrosion initiation threshold (C_T) which could be up to one order of magnitude greater when compared to that of CS. Nevertheless, no significant benefit has been associated to extents attributed to the subsequent CPS. Hence, existing durability projections of concrete reinforced with SS are limited by the scarce information available regarding the CPS yielding to highly conservative approaches based on investigations performed on concrete reinforced with CS.

This investigation compiles relevant information from literature focusing on the few cases where SS reinforcement had reached, and preferably finalized, the corrosion propagation stage. The information garnered was compared to laboratory experimental results obtained at the Infrastructural Corrosion Laboratory of the University of South Florida. The reliability of the most commonly used corrosion detection and monitoring methods were examined in SS reinforcement and alternatives were stablished if necessary. In addition, different failure mechanisms were examined as a first approach to determine the expected limit state of SS reinforced concrete considering aspects such as corrosion morphology, corrosion products, and corrosion rates. In addition, the effect of the concrete condition was also taken into consideration to predict potential limit states for SS reinforced concrete. Results from this and previous investigations were used to update existing durability estimates of the duration of the corrosion propagation stage of concrete reinforced with SS in current FDOT practices. These updated estimates were in the form of cumulative quantitative damage functions that could be translated into future cost estimates that could be used to avoid over-specification for certain alloys of SS reinforcement. Any propagation stage added credit identified by this research – as well as any limitations that were uncovered – can then be used for rational decisions on rational design and material selection decisions. Up to now, it has not been possible to implement such decisions because the information was lacking.

Table of contents

List of figures

List of tables

1 Introduction

1.1 Background statement

One of the main factors affecting the durability of Florida Department of Transportation (FDOT) reinforced concrete structures is corrosion of the steel reinforcement. This issue is even more challenging when structures exposed to aggressive environments are considered. In an attempt to increase the durability of reinforced concrete structures, corrosion-resistant alloys, such as stainless steel (SS), have garnered attention over the past two decades.[2-12] Different investigations have suggested that the higher material cost may be recovered throughout the service life of structures as the chloride threshold can be as much as an order of magnitude greater than that of carbon steel (CS) reinforcement.[13-17] SS durability has been commonly approached using the model proposed by Tuutti[1] where the service life of a structure, which is the time required for corrosion loss in the steel to reach a serviceability limit state, is determined by the summation of the duration of the corrosion initiation stage (CIS) and the corrosion propagation stage (CPS).[18] The enhanced durability of structures reinforced with SS reinforcement has been mostly attributed to the increased duration of CIS, based on research-based evidence that suggests a greater corrosion initiation chloride threshold of SS compared to that of plain carbon steel. Nevertheless, no significant benefit has been attributed to the subsequent CPS. [19, 20]

The duration of the CPS may be estimated as the quotient between the critical corrosion penetration and the corrosion rate of the steel reinforcement where cracking of the concrete is considered as the limit state. Current durability projections of concrete reinforced with SS are also limited due to the lack of information regarding the governing limit state. In plain steel-reinforced concrete structures, the limit state has been defined as cracking or spalling of the concrete cover caused by the expansive action of the corrosion products. However, there are only a few documented cases of cracking or delamination of concrete due to corrosion in SS reinforcement.[21] Furthermore, differences in the corrosion morphology and corrosion mechanisms in SS reinforcement could yield alternative limit states such as mechanical failure of the steel due to sufficient cross-sectional loss, or loss of bond between steel and concrete.

Experimental and field-exposure studies from documented investigations are often limited when using natural chloride exposure conditions in which the inherent corrosion resistance attributes of SS combined with the short execution period of existing studies do not allow SS to reach the CPS. In most occasions, investigations are terminated before distress or mechanical failure is observed in the sample. Thus, the limit state criteria for SS has been mostly based on experimental data and empirical models of plain CS reinforcement.

The same challenge is faced when considering existing studies addressing the reliability of corrosion techniques. While investigations have thoroughly addressed the reliability of corrosion detection techniques of CS reinforcement, very little work has addressed the variations in the applicability of these techniques to stainless steel reinforcement. Thus, the uncertainty in the service life projections of structures reinforced with SS is often exacerbated by the lack of information regarding the sensitivity of traditional corrosion detection and monitoring techniques wherein the increased degree of localized corrosion expected in SS reinforcement may limit the feasibility of traditional NDT methods to detect corrosion.

The duration of the CPS of SS reinforcement could potentially be evidently longer than that of CS due to its intrinsic corrosion resistance characteristics. Hence, the duration that is considered to be only a few years for CS, could be greatly extended in case of SS. The expected delay in the CPS would require further analysis since it could be limited by the action of highly aggressive environments and the degree of localized corrosion in SS reinforcement. Since the concentration of chlorides required to initiate corrosion is much greater in SS when compared to CS reinforcement, the relation between corrosion resistance and medium aggressiveness may be comparable between SS and CS reinforcement. This would indicate that the corrosion resistance of SS reinforcement may be balanced by the aggressiveness of the environment leading to comparable corrosion rate values. Similarly, highly localized corrosion in SS reinforcement could possibly cause mechanical failure of the steel. This is not the case of CS reinforcement given that corrosion is expected to attack the surface uniformly, causing the expansive corrosion products to crack the concrete surface cover before mechanical failure of the steel occurs. Both factors cast doubt in the expected delay in the CPS of SS, nevertheless, the present lack of quantification results in potentially overly conservative estimates of the duration of the CPS basing the corrosion behavior of SS reinforcement on information abstracted from CS reinforcement investigations.

If the assumptions negating the extended CPS in SS reinforcement turned out to be unjustified, this high conservatism level could cause considerable service life underestimations of SS reinforced structures, as well as, costly additional corrosion control strategies such as added clear concrete cover or higher concrete classes. Alternatively, if these assumptions were turned out be justified and no significant durability benefit was found in SS, quantifiable and solid arguments would be obtained for decision making in terms of appropriate design for durability. In either case, more reliable estimates of the duration of the propagation stage for SS reinforcement would allow for realistic durability projections, to credit full value of the use of the material at the design stage and allow for redirecting limited resources to best advantage elsewhere. The investigation proposed here seeks to obtain a more accurate estimate of the extent of the propagation stage benefit that may be derived from the use of SS, toward optimizing the use of this newly implemented material in FDOT concrete construction. The work will also examine the reliability of means of monitoring SS rebar corrosion as part of a forecasting process and establish alternatives if necessary. Literature data, experiments and computer models will be used to obtain the updated estimates.

The information developed in this project will be used to update current estimates of the cost/performance benefit from using SSs, by accounting for any adjustment derived from improved knowledge of the propagation stage duration. The updated estimates will be in the form of quantitative damage functions (amount of repair needed as function of structure age) translatable into projected future cost estimates. Any propagation stage added credit identified by this research -as well as any limitations that may be uncovered- can then be used for rational decisions on cost saving changes in design of concrete cover thickness or concrete quality. Such decisions cannot be implemented at present as the necessary information is lacking.

1.2 Project objectives

The objectives of this investigation are to:

1. Develop a rational quantitative estimate of the duration of the corrosion propagation stage of concrete reinforced with SS in current and anticipated FDOT practice.
2. Apply the findings as inputs to damage function models, to determine how any resulting added durability credit can be used to optimize materials and design options.
3. Establish alternative corrosion monitoring methods if needed.

2 Literature review

Scarce information regarding the potential increase in durability due to the extension in the CPS of SS reinforcement has allowed highly conservative service life estimations for SS reinforcement to be adopted. In this chapter, the literature available was gleaned for the few cases where SS reinforcement had reached, and preferably finalized, the corrosion propagation stage. Special attention was given to:

- Actual structural service experience
- Outdoor/service environment tests of SS reinforced concrete
- Laboratory test in concrete or simulated pore solutions

Solely one case of actual service in a structure was found for which t_p could be estimated, albeit indirectly. The result suggests a t_p of several decades for the case of austenitic Cr-Ni rebar in marine service. Outdoor tests without unnatural acceleration showed a few cases where t_p was reached, but only for straight Cr ferritic alloys which showed some limited improvement over t_p for CS. Preliminary findings from laboratory tests from the literature suggest that SS reinforcement made with high pitting resistant grades, and thoroughly descaled, presented a promising outlook for CPS durations that could considerably exceed that of CS reinforcement.

This literature review seeks to highlight the most notable findings from different investigations on the CPS. Further testing is presented in subsequent chapters wherein that improvement is preliminary quantified as a damage function in terms of the expected limit state, corrosion morphology, microstructure, corrosion rates and corrosion products microstructure.

2.1 Review of propagation stage literature for actual structural service

2.1.1 SS performance in structures in service

The listing in Appendix A shows that more than 100 bridges and related structures or sizable parts of structures have been built with SS reinforcement during the last 80 years. As shown in Figure 2.1, the pace of utilization of SS has increased during the last two decades without sign of abatement. This fast-growing tendency of the SS usage in structures emerged as designers become more persuaded of the potential economic benefits of corrosion-resistant rebar, and the greater commercial availability of SS rebar. Current implementation of SS rebar in the field is evolving with various levels of quality assurance and control of rebar condition. [22, 23] Economic considerations are often a determining factor in the selection of rebar materials.[24]

"A graphical representation of the cumulative worldwide tally of bridges with stainless steel rebar as a function of year (increments of 20). Line begins at year 1940 and stays steadily low (below about 10) until the 1980s where in just 20 years, about 20 structures existed and approaching year 2020 over 100 structures exist with stainless steel rebar."

Appendix A classified SS-reinforced structures by country of origin. As shown in the Figure 2.2, the U.S. leads with Europe and Canada filling much of the rest. Per Appendix A, the oldest major structure with SS reinforcing is located in Mexico (Progreso pier), having been the subject of several notable investigations. That work is detailed next, followed with a sampling of experience from other structures. It is noted that while there is abundant literature on the use of SS rebar in new structures, there are relatively few reports on actual performance evaluation after the structures were in service for an appreciably long period. The selection of cases discussed, accordingly limited, is presented in the following subsections. A summary of the main literature review findings is presented next. For a detailed account of the literature please refer to Appendix C.
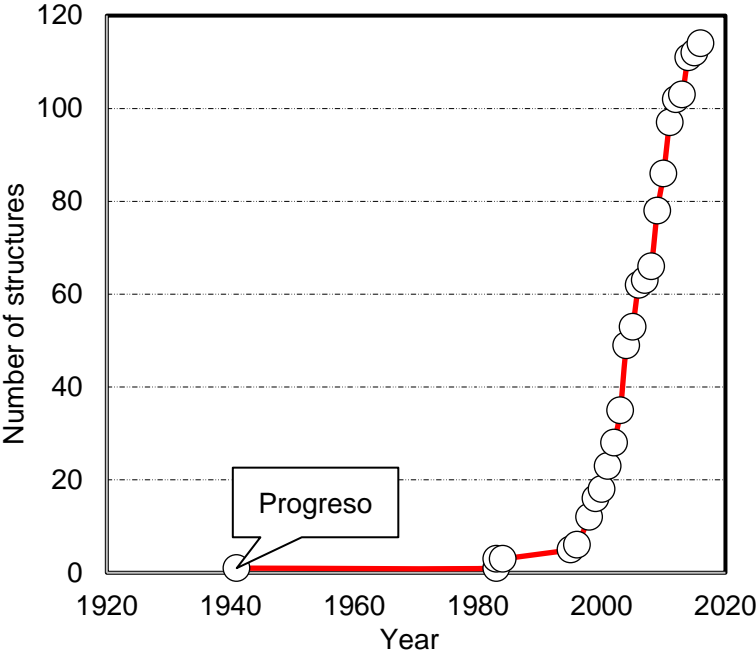
Figure 2.1: Cumulative worldwide tally of bridges with SS rebar.
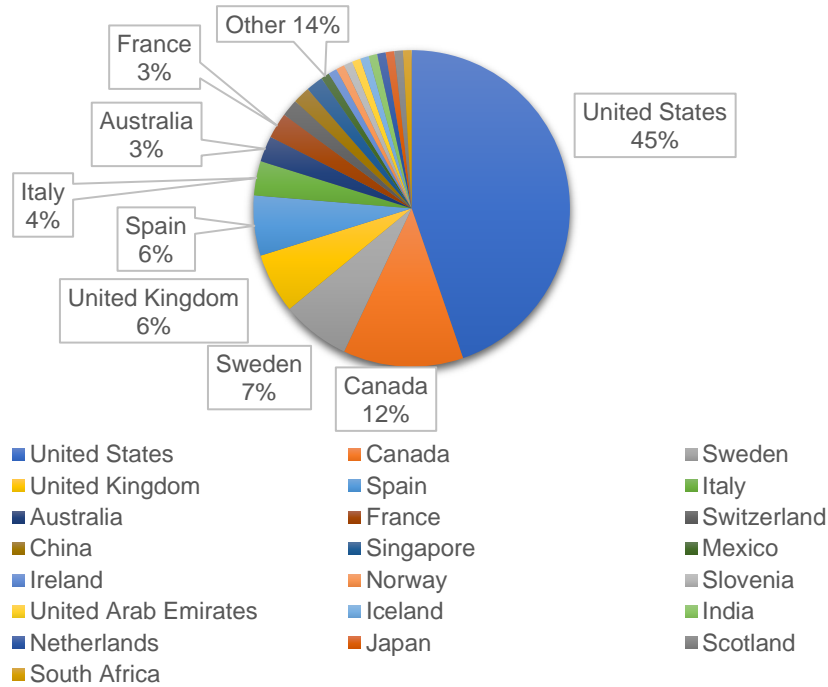
Figure 2.2: The use of SS reinforcement in bridges categorized by country.

2.1.2 Summary of findings on SLS mode and duration of the propagation stage

The overall evidence on the most likely SLS mode for SS reinforcement remains scant, but it is generally indicative of corrosion-induced concrete cover cracking. That is supported by the (albeit indirect) identification of that mode at the Progreso pier for an austenitic steel, the various direct observations of cracking for straight Cr or low alloy SSs in outdoor exposures, and direct evidence of concrete cracking for higher performance alloys in accelerated laboratory tests. The corrosion morphology in the concrete cracking cases for the low alloy steels was found to be in the form of pronounced localized pitting of the bars. That strong localization of the corrosion was clearly as able to form through-cover concrete cracks as the often moderately localized corrosion seen on CS rebar. Because of the paucity of data, the corrosion morphology on the higher SS alloys is less known for actual service or outdoor exposures. The overall indications, supported by results from the accelerated laboratory tests, are also of rebar corrosion localization, in the form of perhaps even more isolated pits than in the case of the lower SS alloys. That increased corrosion localization would suggest the possibility of an alternative SLS mode via rebar failure by plastic/partially brittle overload of a locally reduced cross-section, perhaps especially in cases of corrosion at preexisting structural cracks. However, no reported instance of such event was found. Thus, for now it can only be considered theoretically in predictive models. An EAC-related alternative SLS mode for SS rebar has not been reported either and it remains largely hypothetical. However, because of its potential for high risk events (as witnessed by the non-rebar structural service swimming full failures), and the apparent signs of EAC in one Progreso pier case, this mode merits careful future consideration as well. Notwithstanding those alternatives, pending new evidence to the contrary a concrete-cover cracking SLS mode seems to be for now the most reasonable working assumption for durability estimates.

With that SLS choice, the survey revealed glimpses of the duration of the propagation stage carried to full completion for a few of the more realistic experiences and test conditions. In particular, the survey provided the basis for an educated indirect estimate of t_p in the actual service conditions at the Progreso pier. The result was a t_p value of several decades for a rebar material (austenitic type 304 SS), design (permeable concrete but thick cover, roughly comparable to a thinner cover of less permeable concrete) and service (marine exposure) not too far removed from those where SS rebar would be specified today. That estimate represents an encouraging several-fold improvement over the t_p of only a few years which would be normally expected for CS rebar in similar conditions. The other full completion t_p observations in outdoor/service environment tests, but not in actual structure placement, were limited to straight Cr SSs tests in BRE tests and a Florida test, showing modest improvement over CS. The picture for outdoor/service exposure cases became more complete when considering cases where SLS was not reached, but where active corrosion rate estimates could still be obtained. Those cases (the other BRE tests, Treat Island, Durban Bluff, Swiss Highway Tunnel, Florida) confirmed the natural exposure experience-based expectation of strong t_p increase over that of CS for high PREN austenitic and Duplex SS, and of modest increase for use of low PREN ferritic or no-Ni austenitic SSs. Mechanistic insight from the laboratory tests suggested that the concept of an X_{CRIT} value (averaged on an intermediate space scale) to produce concrete cover cracking can be reasonably extended to the case of SS rebar, with t_p estimated by the ratio of X_{CRIT} to the (properly averaged) corrosion rate. While the information is still scant, the values of X_{CRIT} for SS rebar for a given concrete and spatial geometry do not appear to be radically different from those encountered for CS rebar.

Overall, the information available at present suggests that propagation stage corrosion forecasting methodology already in place for CS rebar may be translatable to SS rebar, with nominal corrosion rates during the propagation stage severalfold lower than for CS rebar for the higher PREN SSs. Because of the present paucity of data, this review stops short of recommending particular t_p multiplier factor values relative to CS. It recommended instead that further research be conducted to resolve uncertainty and to guide parameter selection choices in tentative modeling updates.[25, 26] Caveats apply in the conservative direction by noting for example that performance of SS rebar can be seriously degraded by insufficient descaling, and that unexpected failure modes (e.g., EAC) may have not been revealed yet in the limited service experience to date. Excessive conservativeness may take place too, by not taking sufficient credit for the repassivation potential for SSs being higher than for CS, and for the higher cathodic polarizability of SS rebar.[27] Thus, beneficial cathodic prevention of the rest of the rebar assembly by galvanic coupling with an earlier corroding region[28] could be more important for SS than for CS rebar. Continuing investigation of these issues as well as careful monitoring of existing structures should assist in achieving the full benefit of increasing use of SS rebar.

2.1.3 Summary of findings on methods of detection and measurement of corrosion of SS reinforcement

Many of the investigations discussed in the previous subsection used half-cell potential mapping (per ASTM C876 or modifications thereof) as a method of detection of the corrosion condition of SS reinforcement. In principle any passive material that experiences local stable passivity breakdown, with the formation of a local anode, is expected to experience a drop on open circuit potential as the result. That should be the case as much of the surface responsible for the cathodic reaction remains more or less the same as before, and the only way to transact the greater number of electrons released by the anode is through a drop of potential. The effect is strong for plain steel rebar, given the high rates of corrosion at play in that case. Stainless steel, at least in the pickled condition anticipated for successful rebar service, is a poorer anode than plain steel[27, 29] so for a given local anode the potential drop could be even greater than for plain steel. However, as was discussed in Section 2.1.2, at least in the more corrosion-resistant SSs the anodes tend to be much localized and involve sometimes much smaller currents than for plain steel. The overall balance of those opposite factors, especially for the best performing steels, is not apparent beforehand and should be examined carefully.

A more reliable electrochemical way of assessing corrosion condition is by means of transient electrochemical techniques such as LPR, but those tests are more laborious and time consuming than potential mapping, so they are used less frequently. In some of the work reviewed here both mapping and LPR were used permitting some examination of the former. Other considerations were reported elsewhere as well, with mixed results. In the Progreso pier investigations[30-33] (see appendix C) relatively good correlation was reported between half-cell mapping and LPR. Half-cell data were used for the A6059 bridge surveys (Item 2.1.6) but confidence on the results was limited. Good correlation between low corrosion rates and less negative potentials was reported for the Treat Island field exposure[34] (See appendix C). The laboratory investigations tended to report reasonable correlations between half-cell potentials and passivity condition, with some reservations. Notable among those is the cracked concrete investigation[35] (see appendix C), where the authors expressly questioned the direct application of ASTM C876 to SS rebar in concrete. In summary, this matter should be reviewed more thoroughly in the remainder of this investigation. A strategy being considered is the establishment of various classes of applicability of potential mapping, depending on the type of SS being considered. It is anticipated that for given alloy types, for example straight Cr, low alloy ferritic steels, the applicability of ASTM C876 may be similar to that for plain steel bars. Variations for the higher SS grades are expected to require additional consideration and evaluation of probability of detection. These findings are further contrasted to laboratory evaluations and computations simulations described in Chapter 5.

Supplemental spot assessment by polarization methods may serve for verification of half-cell corrosion indications. Moreover, the recent advent of impedance measurement methods that do not require contact with the rebar assembly,[36] perhaps may enable more rapid surveys with less uncertainty on the interpretation of the results. Similar to the HCP, the applicability of the EIS technique in SS reinforcement is evaluated using experimental and computational simulation results, further detailed in Chapter 5.

3 Experimental methods

In this chapter, four interconnected laboratory experiments used to obtain information on the CPS of stainless steel reinforcement are described. The objective was to obtain typical corrosion rates of SS in concrete, its corrosion morphology, and the appropriate limit states that may be used to bound the end of the propagation stage for both sound and locally deficient concrete.

3.1 Reinforced concrete beams with chloride-contaminated section

Concrete specimens reinforced with UNS S41000 SS and AISI1018 CS were prepared to determine whether corrosion of stainless steel in concrete can be detected by methods traditionally used for carbon steel reinforcement, and to what extent localization of corrosion of stainless steel compares with that of carbon steel in concrete. Macrocell corrosion was promoted by creating a central chloride-contaminated concrete section surrounded by chloride-free concrete. In this way the macrocell activity of carbon steel corrosion in concrete may be compared to that of SS corrosion in concrete. Half-cell potential and electrochemical impedance measurements were performed regularly to monitor the corrosion performance of the steel reinforcement bars at designated points along the beams. The details of the specimen design and measurement methods are described.

3.1.1 Materials

3.1.1.1 Reinforcing steel

The specimens were reinforced using UNS S41000 SS and AISI1018 CS, detailed in Table 3.1. Both types of steel were supplied by Metal Supermarkets Corporate based in Tampa, FL. Chemical compositions for the steel reinforcements are described Table 3.2 and Table 3.3. Both types of steel reinforcement were smooth No. 4 round bars with a diameter of 1.27 cm (0.5-inch). The SS and CS bars were ~180 cm (5'11") long and 183 cm long (6'), respectively. The surface condition of the reinforcement was annealed in the case of SS and cold rolled for CS. In addition, the surface of the reinforcement bars was cleaned with acetone before being placed in the concrete to remove any residual mill-scale and create a uniform surface.

Table 3.1: Types of steel used in the investigation.

Designation	Surface condition	Microstructure	PREN
UNS S41000	Annealed / Cold draw	Martensitic	12.13
AISI 1018	Cold Rolled	Ferritic	-

Table 3.2: Chemical composition of stainless steel (weight percent).

Designation	Al	C	Co	Cr	Cu	Mn	Mo
UNS S41000	0.003	0.126	0.01	11.66	0.07	0.44	0.011
	N	Ni	P	S	Si	Sn	
	0.031	0.11	0.019	0.0013	0.38	0.5	

Table 3.3: Chemical composition of carbon steel (weight percent).

Designation	C	Mn	P	S	Si	Cu	Ni
AISI 1018	0.17	0.65	0.014	0.020	0.2	0.30	0.008
	Cr	Mo	Sn	Al	N		
	0.11	0.03	0.008	0.004	0.0094		

3.1.1.2 Concrete

Two mix designs were required to cast chloride-contaminated and chloride-free concrete regions in the specimens. The chloride-free concrete was prepared approximating the technical requirements provided by the FDOT for Class IV concrete, choosing not to use Pozzolanic admixtures.[37] The summary of technical requirements and mix design proportions are shown in Table 3.4 and Table 3.5, respectively. In total, a nominal volume of concrete of 20.2 liters was used. The coarse aggregate was Florida limestone with nominal maximum size (3/8 in), 2.28-bulk specific gravity under a saturated surface dry (SSD) condition and 7.42% absorption capacity following the ASTM C127. In addition, the fine aggregate was standard silica sand per FDOT grading requirements.

Table 3.4: Concrete Class IV – FDOT. [37]

Criteria	Minimum Requirement
Cement content	658 pcy
Water to cement ratio	0.41

Table 3.5: Chloride-free concrete - mix proportions.

Material	Weight/vol pcy	Weight/vol kg/m^3	Batch kg
Cement	658	390	7.88
Water	270	160	3.23
Fine aggregate (SSD)	1428	847	17.09
3/8 Coarse Aggregate (SSD)	1486	881	17.79
Total Weight	3841	2279	45.99

Similarly, the chloride-contaminated concrete was prepared approximating the specifications provided by the FDOT for class IV concrete.[37] A 5.84 % of chloride ions by weight of cement was included to the concrete to accelerate the onset of corrosion and allow the study the CPS of SS in concrete. Certified Sodium Chloride (NaCl) from Fisher Scientific CO LLC was used to reach the anticipated chloride content. The chloride content chosen exceeded by more than one order of magnitude the chloride threshold value usually estimated for CS reinforcement. Per observations in the literature review this chloride ion content was deemed to have a high probability of inducing corrosion in SS reinforcement.

3.1.2 Specimen preparation

Six reinforced concrete specimens were prepared at the corrosion laboratory at the University of South Florida following the concrete mix procedure given by ASTM C192. UNS S41000 SS and AISI1018 CS specimens were investigated. The dimensions of the beams were 2 inches (~5 cm) wide, 2.5 inches (~6.4 cm) high and 70 inches (~180 cm) long as shown in Figure 3.1.
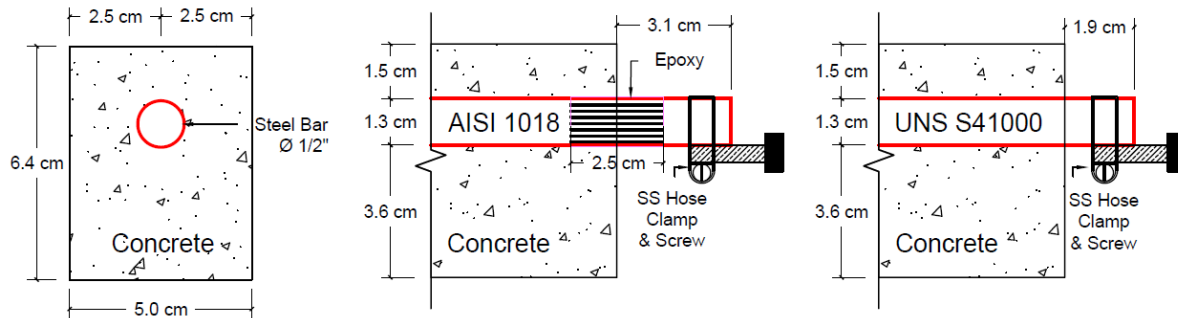
Figure 3.1: SS and CS reinforced concrete cross-sections.
Specimens were casted upside down and flipped for use afterwards.

As shown in Figure 3.1, SS and CS reinforcement bars are projected out approximately 1.2 inches (3.1 cm) and 0.75 inches (~1.9 cm) respectively from the concrete block at one of the ends of the beams. The CS-reinforced specimen cross-section, that the steel bar was epoxy-coated at both ends, at the outside and inside of the concrete contact area approximately 0.5 inches (~1.2 cm).

Specimens were cast upside down and flipped for use afterward. Initially, the reinforcement was located closer to the bottom surface of the specimen with a concrete rebar cover of 0.6 inches (~1.5 cm). Mold release agent was applied to the wood form before concrete placement. The six specimens were cast in the wood mold displayed in Figure 3.2.

Chloride-free and chloride-contaminated concrete were cast in two batches. The first batch cast was the chloride-free concrete and the second was the chloride-contaminated concrete as displayed in Figure 3.3. The chloride-free concrete batch was cast (at day zero) at the ends of all specimens as shown Figure 3.4 following the preparation procedure given by ASTM C192[38]. Before the second batch was cast, the polystyrene foam and 3D spacers were removed from the wood mold, as shown in Figure 3.5.

Figure 3.2: Wood mold coated with a mold release agent. Temporary polystyrene foam and 3D printed spacers were in place to implement the casting sequence to keep the concrete cover uniform.
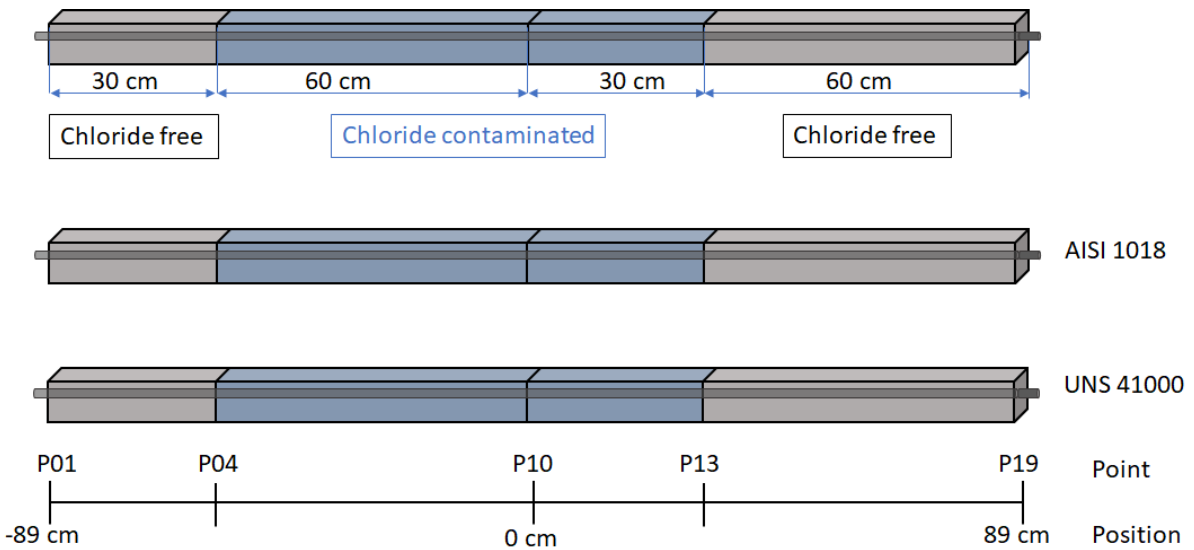
Figure 3.3: Longitudinal profile for UNSS41000SS/ AISI1018CS specimens in concrete. "0 cm" represents the central point of the specimens, representing he longitudinal midpoint position. Spatial distribution of two types of concrete is shown as well.

Figure 3.4: Chloride-free concrete batch covered with a plastic film. Polystyrene foam and 3d printed spacers were in place for the chloride-free concrete batch, removed before chloride-contaminated concrete placement.

Figure 3.5: First concrete batch – left end of all specimens.

At Day 3 and also per ASTM C192[38], the second concrete batch (chloride-contaminated concrete) was cast in the central section of the specimens (between the chloride-free concrete ends. Three 2 in x 4 in concrete cylindrical samples were also collected from the concrete batch, to measure concrete resistivity evolution with curing time.

Eight days after the concrete placement, the specimens were released from the mold, and flipped over to match the orientation in Figure 3.8 so that the lower cover side was facing up, where the reference electrode and EIS electrodes were placed from then on.

Wood molds were removed approximately 14 days after casting the chloride-contaminated concrete. After demolding, a plastic film covered the specimens all the time to avoid moisture evaporation, as shown in Figure 3.6. In addition, a ½ in stainless steel hose clamp was affixed to one end of the reinforcing bars to guarantee electrical connection for the half-cell potential and EIS measurements as shown in Figure 3.1 and Figure 3.8. Lastly, specimens were labeled according to the designations displayed in Figure 3.8.

The average laboratory temperature was~23°C during the first exposure stage this investigation. Moisture conditions were also supervised to assure a proper curing for each of the specimens until an age of approximately 67 days was reached. During this first exposure stage, dry-moist cycles were used. The specimens were kept moist by spraying them periodically with deionized water during the moist part of the cycle and let air-dry during the dry part of the cycle.

Against expectations, the admixed 5.84% Cl/cement chloride content was found not to be sufficient to induce, by itself, corrosion of the SS bars within the time frame of the test. Thus, a second exposure stage was initiated, in which a combination of mild corrosion acceleration means was employed to speed up the onset of corrosion. Accordingly, ponding and heat cycles were implemented to both the chloride-contaminated and chloride-free regions of the SS specimens. When the specimens reached an age of ~245 days, acrylic reservoirs were placed on the top surface of SS specimens to perform cyclic ponding with a saturated sodium chloride solution, as detailed in Section 3.2.3. Subsequently, low-high heat cycles were initiated at Day ~300, with temperature cycling between periods of ~22 °C and ~38 °C, to further promote corrosion initiation. Detailed information regarding exposure cycles and durations is summarized in Section 3.2.3.

a)   b)
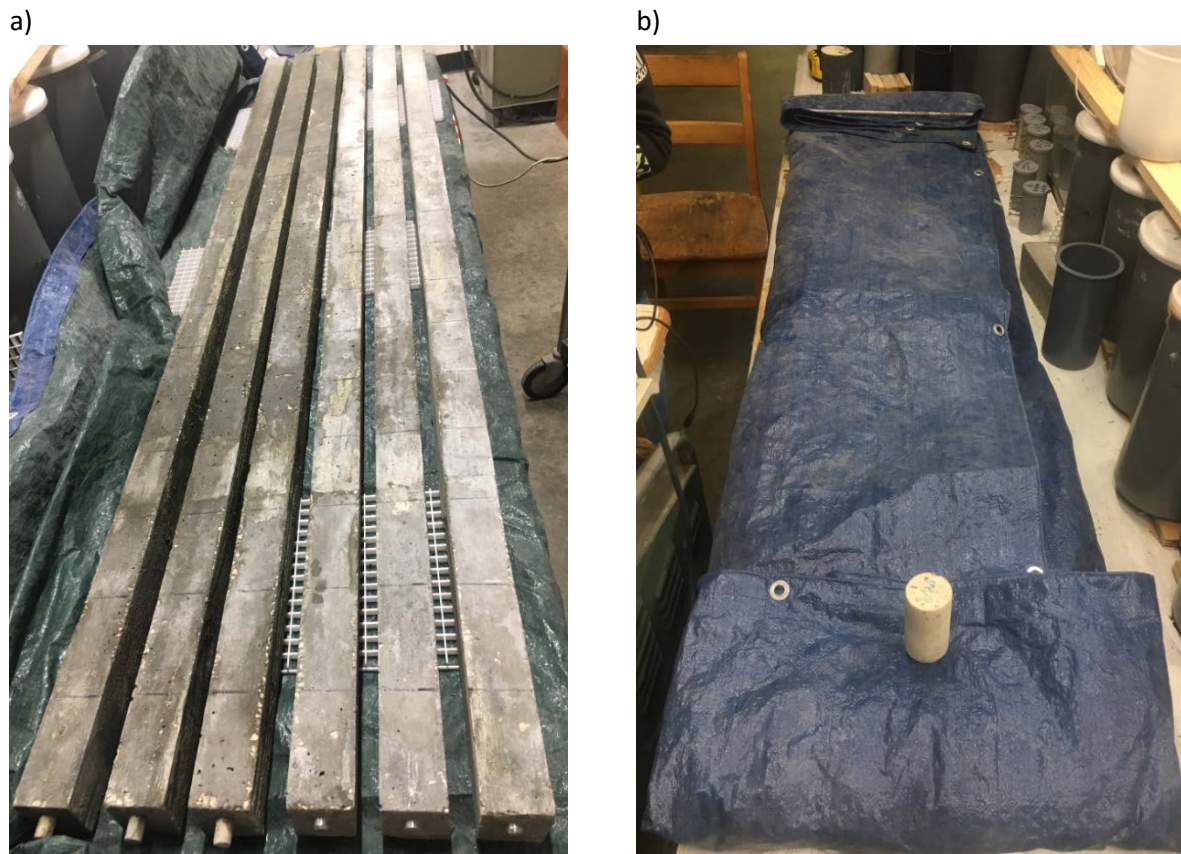
Figure 3.6: Concrete specimens with and without a tarp. Tarp usually covering the specimens was normally in place to avoid moisture evaporation and removed temporarily to take measurements.

3.1.3   Data acquisition

A series of methods, including resistivity of concrete cylinders, half-cell potential, and electrochemical impedance were used to monitor the corrosion performance of the steel reinforcements. Furthermore, visual inspections were performed periodically to detect potential signs indicating that the specimens reached their limit state.

Measurements were initiated at an age of 60 days (denominated as "cycle 0"). At an early stage, data were acquired with a higher frequency since faster relative changes were expected then. After the first cycle of measurements, the length of each cycle was set to approximately four weeks until the eight cycle (~35 weeks after specimens were cast) when ponds were installed in the SS specimens. Each one of the first seven cycles had a duration of about 4 weeks, in which measurements were taken two weeks after the exposure condition was changed. After that, measurements were acquired for a two-week period and a new cycle would initiate. Further information about exposure conditions for the specimens until the seventh cycle is detailed in Table 3.6.

Beginning on cycle 8, cyclic ponding in SS specimens was initiated. A ponding solution of saturated sodium chloride was used as a mild technique to accelerate chloride transport. The increase of temperature was initiated around cycle 12. After this cycle, the SS have been continuously heated for a 2-3-week period. The specimens are kept at room temperature before and while taking measurements and are later placed at the high temperature chamber.

Table 3.6: Exposure conditions per measurement cycle and duration.

Cycle No.	Exposure conditions (duration in weeks)
0	Moist (1 week)
1	Dry (4 weeks)
2	Moist (4 weeks)
3	Dry (2 weeks) – Moist (1 week)
4	Dry (2 weeks) – Moist (2 week)
5	Moist (4 weeks)
6	Dry (1 week) – Moist (3 weeks)
7	Dry (1 week) – Moist (3 weeks)

Cycle No.	*Exposure conditions (~duration in weeks)
8	Wet (3 weeks) – dry (1 week)
9	Wet (3 weeks) – dry (3 week)
10	Wet (2 weeks) – dry (3 week)
11	Wet (2 weeks) – dry (3 week)
12	Wet (4 weeks) – dry (1 week)
13	Wet (2 weeks) – dry (3 week) + heat
14	Wet (2 weeks) – dry (2 week) + heat
15	Wet (2 weeks) – dry (2 week) + heat
16	Wet (2 weeks) – dry (2 week) + heat
17	Wet (2 weeks) – dry (3 week) + heat
18	Wet (2 weeks) – dry (2 week) + heat

*The second section of the table (week 8-18) consisted of cyclic ponding.

3.1.3.1 Half-cell potential

Prior to performing potential maps, all specimens were marked from the center of the specimen to the sides indicating the points of measurement. The spacing was 10 cm and the distance from the last mark at both ends to the ends of the beam was ~8.9 cm resulting in 19 total measuring points per specimen including the positions of the very ends of the beams. Potentials were measured with a multimeter (Fluke 289) with an input resistance of 10 MΩ and a reference SCE fitted with a sponge at the tip as shown in Figure 3.7.
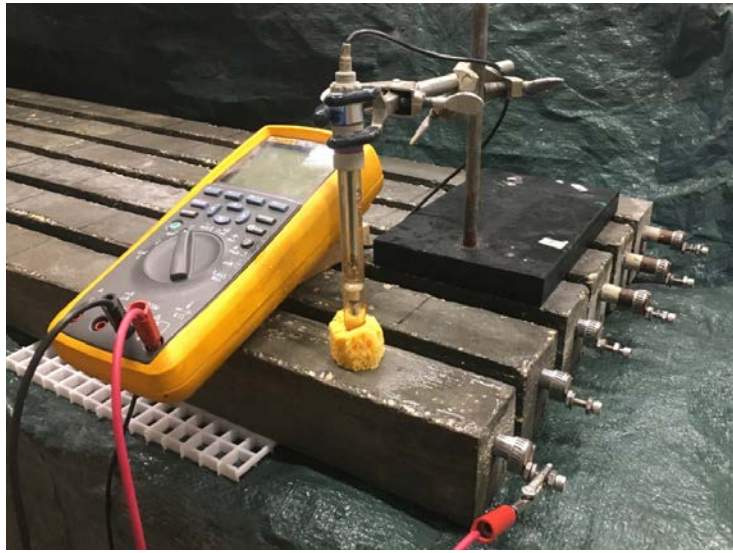
Figure 3.7: Half-cell potential measurement on specimen SS01. Reference electrode (SCE), electrical junction device (yellow sponge).

Starting three days after the chloride-contaminated concrete placement, potential measurements as a function of position were conducted regularly on all specimens.

Figure 3.8: Electrical connections at the right end of all specimens. The left end of AISI 1018 CS specimens was epoxy-coated and UNS S41000 SS specimens were not.

The HCP technique has been standardized in ASTM C876[39] and it is limited to estimating the probability of corrosion and does not provide any indication of corrosion rate. The descriptions of probability of corrosion are provided in Table 3.7.

Table 3.7: Criteria to evaluate the corrosion potential results - ASTM C876.[39]

Probability of Corrosion	CSE	SCE
	mV	mV
High	V < -350	V < -276
Uncertain	-200<V< -350	-124< V <-276
Low	-200<V	-124<V
where "V" is electrical potential		

Potential results were analyzed over time in SS and CS reinforcement at a given location. It is important to note that, when ponding solution was present, a similar arrangement as the one shown in Figure 3.7 was used but without the sponge; in those cases the tip of the SCE was immersed until it was in direct contact with the concrete surface.

3.1.3.2 Electrochemical Impedance Spectroscopy (EIS)

EIS measurements are used to obtain the corrosion rates of a system through the estimation of the value of the polarization resistance.[40] This technique consists in the application of a sinusoidal disturbance of the electrical potential produced by a given alternating current to a circuit. Meanwhile, the potential response of the system (amplitude and phase angle) is measured and the impedance is computed at each frequency of the established range (typically 1 mHz to 1Khz).[41] The impedance "Z" is established by the ratio of the frequency-dependent potential and the frequency-dependent current. A schematic diagram for the EIS measurements performed in this investigation is shown Figure 3.9.
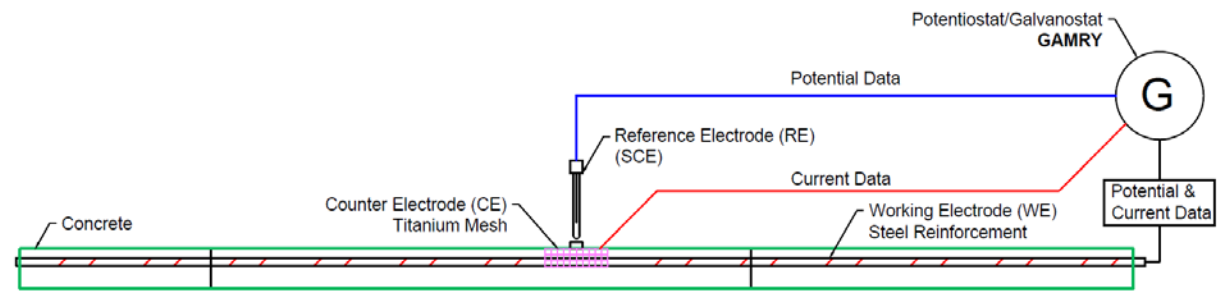
Figure 3.9: Schematic illustration of EIS measurement experimental setup.

The EIS measurements were obtained using a Gamry Reference 600+ potentiostat/galvanostat with a potential perturbation of 10 mV. A three-electrode array, shown in Figure 3.9, in which the steel reinforcement served as the working electrode, a ~10 cm long hollow rectangular titanium mesh on top of a moist sponge was used as the counter-electrode, and a SCE electrode with a small moist sponge on its tip placed in the middle served as the reference electrode. An initial range of frequencies between 10 mHz to 100 kHz with 10 points per decade was selected. The lower bound was later adjusted to 1 mHz at the end locations of the SS specimens to determine behavior in the low frequency portion of the impedance response. EIS measurements were conducted regularly to estimate the values of corrosion rates as a function of position.

Figure 3.10: EIS measurement on specimen CS01. Counter-electrode (titanium mesh), reference electrode (SCE), and electrical junction device (yellow sponge).

An estimate of the polarization resistance (R_p) was acquired from the EIS response using a measurement model software[42] in which a series of Voigt elements is fitted to the data and an extrapolation is made to the high and low frequency limits of the impedance. Subsequently, the Stern-Geary equation was employed to estimate the values of corrosion current density as a function of position. The corrosion current was calculated assuming a value of the Stern-Geary constant (B) for iron (Fe) equal to 26 mV and was later used to obtain corrosion rate estimates according to the procedure described in Section 3.1.3.4. The polarized area of the steel reinforcement at each measurement point was conducted as shown next.

3.1.3.3   Area polarized

One of the requirements for reliable estimation of the corrosion rate of steel in concrete from impedance measurements is the polarized area of steel that results from a perturbation that is applied between the entire steel bar and a much smaller counter electrodes placed on the concrete surface. The polarized area depends on the specimen geometry, thickness of the concrete cover, concrete resistivity, size and location of the counter-electrode, and the steel-concrete interfacial impedance.

The nominal polarizing net area (A_{pol}) was estimated using a finite element simulation. This method provides a more realistic approach to the actual polarized area since conservative assumptions typically used may result in higher corrosion rate results. It was cautiously used because although it provides a reasonable estimate of the polarized area, it did not consider changes in steel corrosion rates. The model reflected the geometry of the beam specimens to simulate the impedance measurements obtained at different locations along the beam.

A three-dimensional, ~5 ft 10 in (178 cm) long beam section, shown in Figure 3.11, was modeled with one steel reinforcement bar representing the geometry of the beam detailed in Section 3.1. A three-section model was assembled to reflect the chloride-contaminated and the chloride-free sections. The steel rebar located along the longitudinal axis of the section was 0.5 in (1.27 cm) in diameter. A counter-electrode, modeled as a rectangular region placed on the top surface, was set as the ground electrode. A circular region cutout at the center of the counter-electrode represented the reference electrode. The steel reinforcement is expressed as a cylinder placed along the longitudinal axis of the beam. All these elements including the location of the chloride-free and contaminated regions mimic the specimens that were tested in Section 3.1.
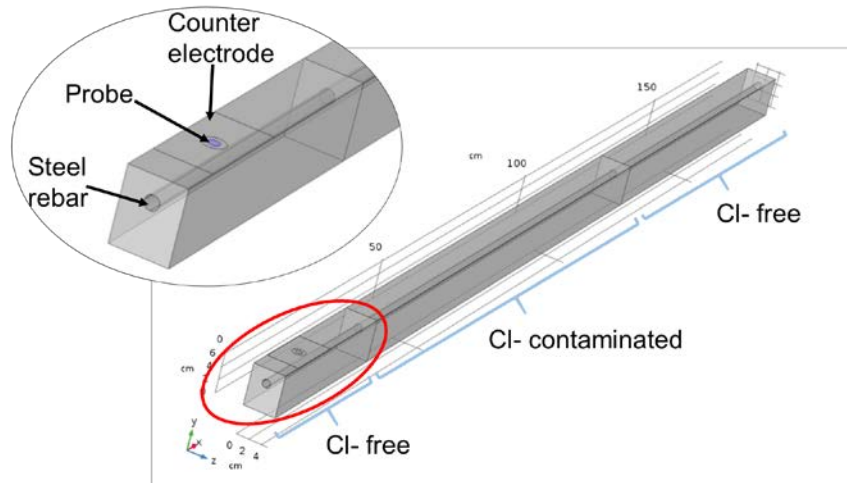
Figure 3.11: 3D model of specimens including chloride-contaminated and chloride-free regions; simulation of EIS test.

The overall mesh of the model and of that near the counter-electrode is shown in Figure 3.12. The mesh used in the model is comprised of free tetrahedral elements that diminish in size at the electrode boundaries. This was done to account for the large variation in potential in this region (i.e., near the counter-electrode).
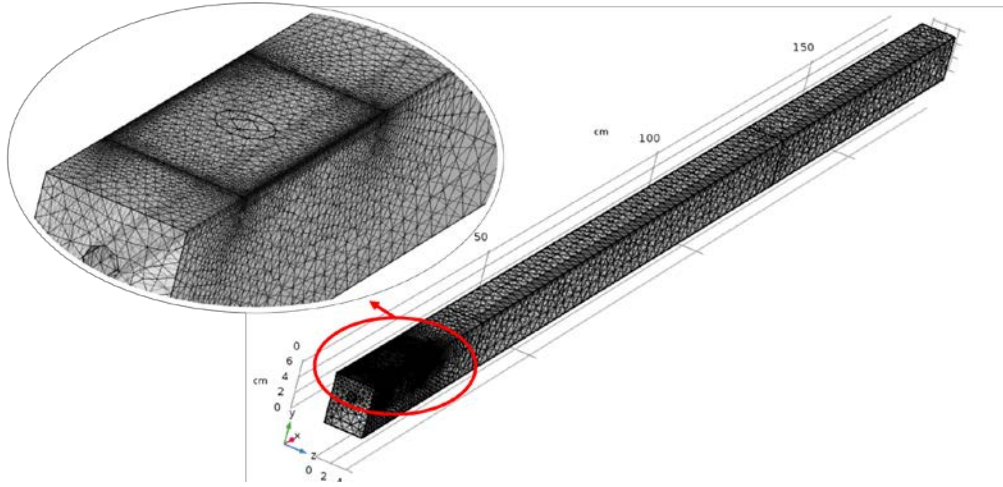
Figure 3.12: Finite-element mesh of the 3D model. Close-ups show the variation on the size in zone of high potential variation.

The potential distribution throughout the electrolyte was governed by Laplace's equation,

$$\nabla^2 \phi = 0 \,,$$

(1)

assuming that the conductivity was uniform. The potential was separated into steady-state and oscillating elements, i.e.,

$$\phi = \overline{\phi} + Re\left\{\tilde{\phi} exp(j\omega t)\right\},$$

(2)

where $\overline{\phi}$ represents the steady-state part and $\tilde{\phi}$ represents a complex phasor, which is dependent on the frequency and position but independent of time. A similar relationship expressed as

$$\phi_m = \overline{\phi_m} + Re\left\{\tilde{\phi}_m exp(j\omega t)\right\},$$

(3)

may be applied to the potential applied to the electrode. $\overline{\phi_m}$ represents the steady state (dc) part of the potential applied and $\tilde{\phi}_m$ is the perturbation amplitude of the oscillating portion.

For indirect impedance simulations, the working electrode boundary conditions were set as an alternating current expressed as

$$\tilde{i} = j\omega C(V_t - V) + \frac{1}{R_p}(V_t - V)$$

<div align="right">(4)</div>

where $\tilde{i}$ is the current density per unit area ($\frac{A}{cm^2}$), j represents the imaginary portion of the equation, ω is the angular frequency (s^{-1}), R_P is the polarization impedance (Ω), V_t is amplitude of the potential perturbation (mV) and V is potential distribution throughout the concrete (mV).

Laplace's equation was solved using a three-dimensional finite element simulation software, COMSOL Multiphysics 5.3. The impedance was simulated as the potential V_t of 10 mV divided by the current between and the counter-electrodes for frequencies ranging from 100 kHz to 10 mHz taking the potential at the counter-electrode as zero. The input quantity of the polarization resistance (R_P) was estimated from equivalent circuit regression of the EIS experimental results described in Section 3.1.3.2. It was assumed that the polarization area of the steel was the product of the perimeter and length of the counter-electrode which is the minimum length as well as the most critical scenario.

One parameter considered in the simulations was the location of the counter and reference probes. By enabling a parametric sweep function in the model, the probe could be moved along the specimen. Nine simulations were performed for each steel material starting at 80 cm to the left of the center of the specimen and finishing 80 cm to the right. The way in which the points in the simulation were taken replicated the experimental setup further described in item 3.1.3.2. In addition, three frequencies (100 kHz, 1 Hz and 10 mHz) were used in the simulation to reduce the computational time.

Considering the cross section of the grout as well as the resistivity, which was obtained experimentally, the ohmic or solution resistance R_s was calculated. The equation to calculate R_s can be expressed as

$$R_s = \frac{\rho}{A_{xs}}$$

<div align="right">(5)</div>

From the 3-D model, a polarization resistance parameter from the simulation ($R_{Psimulation}$) was obtained by calculating the distance between the high and low frequency points.[43] Figure 3.13 shows the Nyquist plot computed by the model for different locations of one specimen including an illustration of how $R_{Psimulation}$ was obtained at the middle of the specimen (0 cm).
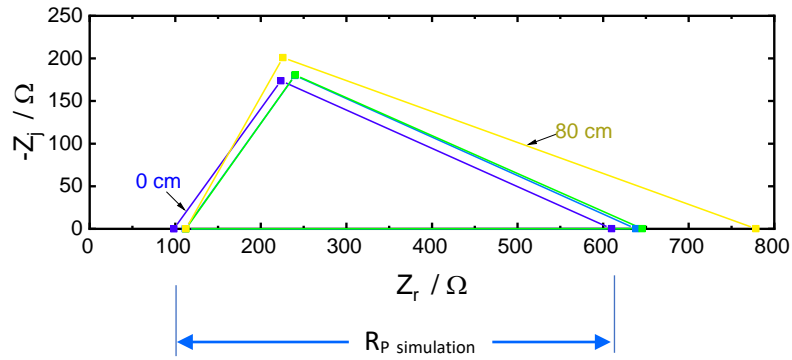
Figure 3.13: Nyquist plot from finite element model.

Finally, the nominal polarizing area (A_{pol}) was calculated as

$$A_{pol} = \frac{R_{p,input}}{R_{p,simulation}},$$ (6)

the quotient between the polarizing resistance obtained from the fittings per unit area and the simulation. The parameter R_{Pinput} was assumed to be the product of the average value of the polarization resistance estimated in the fitting process and the minimum polarized area.

3.1.3.4   Corrosion rate

The penetration rate is one of the widely used corrosion expressions to represent the loss of thickness due to the corrosion of reinforcement in concrete. This research will use micrometers per year (µmyr^{-1}) as the unit of material loss. To calculate this value, the mass loss formula was derived based on Faradays Law and is given as

$$W = \frac{\dfrac{I_{corr}}{A} t M}{nF}$$ (7)

where W is the mass loss (g), I_{corr} is the corrosion current associated with the rate of the anodic reaction (A), A is the estimated anodic area on the reinforcing steel in concrete (cm^2), t is the time and it is given per one year (s), M is the molar mass (g/mol), n is the valence of the metal and it is assumed n=2 for Iron (Fe), F is the Faraday constant ($F = 96500 \dfrac{c}{mol}$).

The corrosion rate was then obtained by computing the quotient between the mass loss (W) and the density of iron. The corrosion rate was multiplied by a conversion factor, so the resulting value was given in units of microns per year. The previously described operation can be expressed as

$$CR = \frac{W*10^4}{\rho},$$

(8)

where CR is the corrosion rate (µmyr^{-1}) and ρ is the density of the metal which is assumed to be $d = 55.85 \frac{gr}{cm_3}$ for iron.

EIS measurements were used to obtain estimates of the polarization resistance. The Stern-Geary equation uses polarization resistance values and Stern-Geary constant to calculate corrosion rates.

$$I_{corr} = \frac{\beta}{R_p},$$

(9)

where I_{corr} is the corrosion current (A), B is the Stern-Geary constant for steel (V) and R$_p$ is the polarization resistance (Ω).

The value of $\dot{i}_{corr}$ current density per unit area (A/cm²) can be determined by using the expression

$$\dot{i}_{corr} = \frac{I_{corr}}{A_{pol}},$$

(10)

where I_{corr} is the corrosion current (A), and A_{pol} is the nominal polarizing area (cm²).

3.2   Cylinders

The presence of macrocell currents introduces uncertainty in the estimation of corrosion rate from EIS data measured on the concrete beams. Consequently, small reinforced mortar cylinders with embedded electrodes were prepared to obtain a corrosion condition that does not include substantial macrocell action, simplifying the interpretation of EIS results for those cases and providing insight on how to evaluate the information from the beam tests. Additionally, potential measurements were used to obtain the current density-potential relationship which reveals whether the corrosion rate is limited by the rate of the cathodic reaction.

3.2.1 Materials

3.2.1.1 Reinforcing steel

Three different types of steel reinforcement bars were used in this investigation, detailed in Table 3.8. All reinforcement bars used were supplied by McMaster-Carr. The types of steel employed in this investigation were UNS S31603, UNS S41000 and AISI 1018 reinforcement bars. Originally, the specimens were received as one foot long rounded No. 4 bars with a diameter of 0.5 in (12.7 mm). Detailed information about the chemical composition of each rebar is contained in Table 3.9, Table 3.10 and Table 3.11.

Table 3.8: Types of steel used in the investigation.

Designation	Surface condition	Microstructure	PREN
UNS S31603	Annealed / Cold draw	Austenitic	24.25
UNS S41000	Annealed / Cold draw	Martensitic	12.38
AISI 1018	As received / Cold draw	Ferritic	-

Table 3.9: List of chemical composition for the UNS S31603 reinforcement.

Designation	C	P	Si	Ni	Cu	N	Mn
UNS S31603	0.018	0.028	0.580	10.090	0.480	0.048	1.480
	S	Cr	Co	Mo			
	0.027	16.750	0.304	2.04			

Table 3.10: List of chemical composition for the UNS S410000 reinforcement.

Designation	Al	C	Co	Cr	Cu	Mn	Mo
UNS S41000	0.002	0.131	0.020	11.760	0.120	0.410	0.013
	N	Ni	P	S	Si	Sn	
	0.036	0.170	0.024	0.0019	0.310	0.004	

Table 3.11: List of chemical composition for the AISI 1018 reinforcement.

Designation	C	Mn	P	S	Si	Cu	Cr
AISI 1018	0.19	0.8	0.004	0.019	0.21	0.12	0.08
	Ni	Mo	Sn	V	Cb	Al	Pb
	0.07	0.018	0.014	0.005	0.005	0.002	0.003

3.2.1.2 Mortar

The mix design used was comparable to the chloride-contaminated concrete further detailed in Section 3.1. Given the small dimensions of the specimens, mortar was used instead of concrete. The nominal volume of mortar used was 4.08 liters. The fine aggregate was silica sand with a specific gravity of 2.47.

Certified ACS ≥99% reagent grade Sodium Chloride (NaCl) was used to reach the anticipated chloride content. The chloride-contaminated mortar included 5.84 % of chloride ions by weight of cement which is the same content used in the beams (see section 3.1).

Table 3.12: Mortar with admixed chlorides – Mix proportions

Material	pcy	kg/m^3	Batch (kg)
Cement	658	390	1.59
Water	270	160	0.65
FA ssd	1428	847	3.45
Total weight	2356	1397	5.70

3.2.2 Specimen preparation

Nine reinforced mortar cylindrical specimens were prepared at the corrosion laboratory at the University of South Florida following the procedure specified by ASTM C192[38]. UNS S41000 SS, UNS S31603 and AISI1018 CS specimens were investigated. Mortar was prepared using Portland cement without mineral admixture with 0.41 water/cement ratio in accordance to ASTM C109[44]. Given the dimensions of these specimens, mortar was selected instead of concrete to meet the maximum aggregate size requirements contained in ASTM C192[38]. The mortar mixture was designed to simulate the specimens described in item 3.1. In addition, a 5.84% of admixed chlorides per weight of cement in this mix design tried to ensure that corrosion would naturally occur in the samples during a reasonable time of exposure.

Cylindrical plastic molds were prepared so the steel reinforcement would be carefully placed in the center. In addition, an activated titanium wire was placed as close as the steel as possible to act as a reference electrode, and an activated titanium mesh surrounding the steel reinforcement as well as the wire would act as the counter-electrode. Mortar was then poured into each 4-in by 2-in plastic mold until a 2 in mark was reached. For each type of steel, three replicates were prepared.
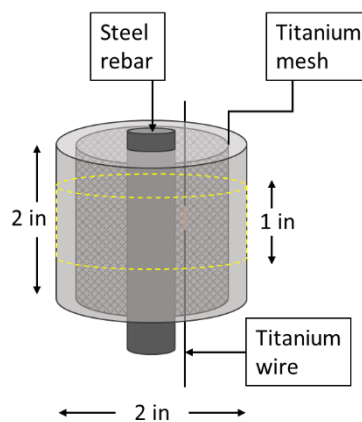
Figure 3.14: Schematic of cylindrical specimen showing the electrode configuration and a region shaded in yellow representing an opening where air flow was allowed (bounded by dashed yellow lines).

All samples were cured in their sealed molds for a 28-day period. After the curing period was completed, a one-inch opening was cut into the plastic mold to allow oxygen ingress into the mortar such that cathodic limitations to the corrosion rate would not be induced. The remainder of the plastic mold was kept in place to ensure the reference and counter electrode wires were securely fixed. The specimens were then stored in the humidity chamber previously mentioned until they reached an age of about 40 days. Following the curing period, specimens reinforced with stainless steel were heated intermittently inside an enclosed glass tank with controlled humidity (~85% RH) and a heat lamp set to 38°C (~100°F) to promote corrosion initiation. Hence, stainless steel specimens were heated for a period of about 50 days where the heat lamps would be turned off to take measurements and to ensure controlled humidity (~85% RH). After this period, the specimens remained at room temperature for about 90 days. The specimens were then heated three times a week to minimize further repassivation of the stainless steel reinforcement. The data was acquired in different cycles of measurements, starting about one month after casting. HCP and EIS data were collected on a monthly basis. 14 cycles of measurements were collected throughout the duration of the investigation.

3.2.3   Data acquisition

Non-destructive corrosion detection and monitoring technique including EIS and half-cell potential were used in this experiment. HCP and EIS were performed periodically. These procedures were conducted in a similar manner as for the first set of specimens while differing in reference and counter-electrode arrangement. The potential of the activated Ti wire reference electrode was periodically calibrated with respect to an SCE.

3.2.3.1   Half-cell potential

Half-cell potential measurements were performed with a SCE on the reinforced concrete specimens, as shown in Figure 3.15. Potentials were measured as described in Section 3.1.3.1 for the beam tests. The measurements acquired from the cylindrical SS specimens coupled with estimated corrosion rates from EIS measurements were used to provide a relationship between expected corrosion activity and potential without substantial influence of macrocell activity. Furthermore, plain steel half-cell potential measurements were also recorded. A potential conversion between the titanium reference and SCE reference electrode was implemented to correlate the OCP values from the EIS measurements to HCP vs. SCE values. The potential conversion procedure is shown in Figure 3.15. HCP results were analyzed using the ASTM C876 criteria (see Section 3.1.3.1), shown in Table 3.7. HCP values were analyzed over time in the different types of SS and CS reinforcement.
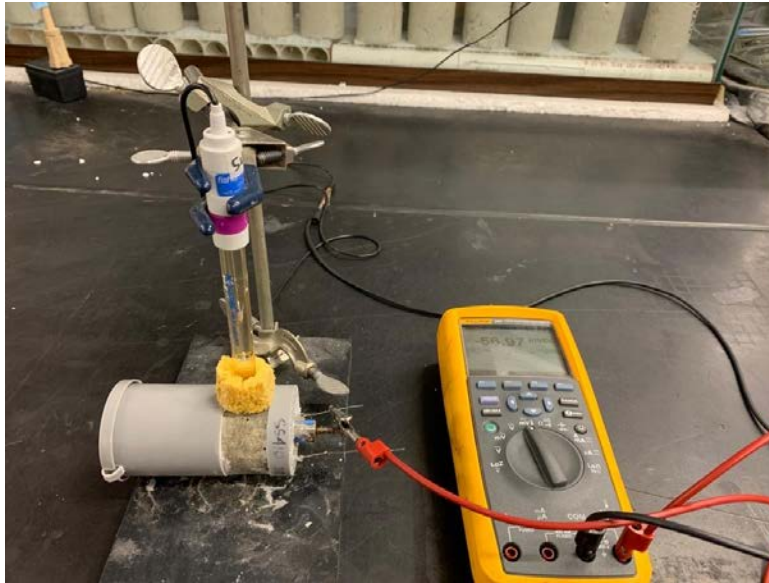
Figure 3.15: Half-cell potential titanium vs. SCE reference electrode measurement on specimen SS410-III. Multimeter, titanium electrode, reference electrode (SCE), and electrical junction device (yellow sponge).

3.2.3.2   Electrochemical impedance spectroscopy (EIS)

EIS measurements were applied regularly in each of the specimens in a similar manner as the procedure described in Section 3.1.3.2 differing in that a titanium mesh and a titanium wire embedded in the concrete served as the counter electrode and reference electrode, respectively. The steel reinforcement acted as the working electrode. The experimental setup is shown in Figure 3.16 and Figure 3.17. The frequency range used in this investigation was 10 mHz to 100 kHz and 10 frequencies per decade. A potential perturbation of 10 mV generated by an alternating current applied to the open circuit potential.
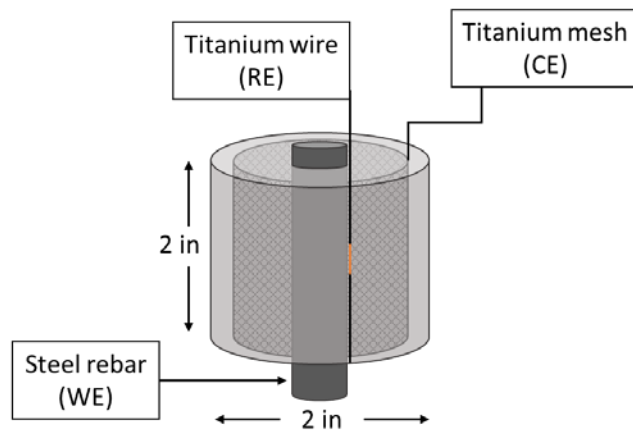
Figure 3.16: Schematic illustration of EIS measurement experimental setup of cylindrical specimen.

Figure 3.17: EIS measurement on UNS S41000 specimen labeled as B-I. Counter-electrode (embedded titanium mesh), reference electrode (embedded titanium wire), and working electrode (steel reinforcement bar).

EIS results were used to obtain estimates of the polarization resistance and ultimately, corrosion rates using a similar procedure as the one described for the beams in Section 3.1.3.2 and 3.1.3.4. Contrarily to the first set of specimens, these were designed to promote a uniform polarization of the steel over a known surface area. Hence, the computation of the corrosion rates did not require the implementation of a finite element model but rather a value for A_{pol} ~20 cm^2 per the bar and specimen dimensions.

3.3   Legacy specimen

A replicate specimen based on the experiments presented in report BDK79-977-02 was obtained from Florida Atlantic University-FAU, one of the few investigations wherein the SS reinforced concrete specimens were suggested to have reached the end of their service life.[45] This legacy specimen was analyzed to glean additional evidence of the factors governing the duration of the CPS in SS compared to those of CS reinforced concrete. The specimen was a simulated portion of a deck slab (SDS) 30 cm wide, 30 cm long and 15 cm high. A schematic diagram of the specimen is shown in Figure 3.18. The concrete section was reinforced with six No. 5 (diameter~16.5 mm) duplex stainless steel UNS S32101 reinforcement bars, placed as 2 layers of three bars. For the top bars, the concrete cover was 25 mm. The reinforcing bars were in the as-received condition (pickled).
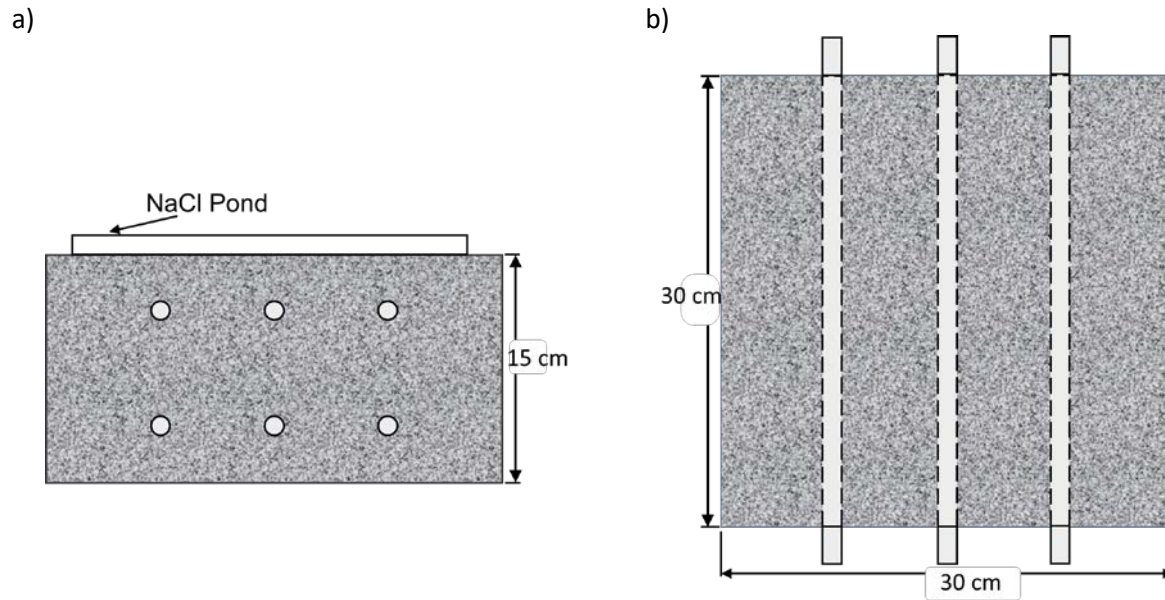
Figure 3.18: Schematic illustration of stainless steel-reinforced concrete specimen obtained from FAU: a) side view, b) top view.

3.3.1 Data acquisition

This legacy specimen was previously exposed to a two-stage procedure at FAU to accelerate the onset of corrosion wherein techniques such as dry-wet cycles and an electric field were used to accelerate chloride ingress during the first and second stage, respectively.

The first stage started right after the passive layer had likely formed (60 days of age). In this stage, the specimen was exposed to relatively elevated temperatures (~37ºC), and were then exposed to dry-wet cycles in which a ponding solution consisting of 20% sodium chloride (NaCl) solution was used for four-day period. The ponding solution was later removed to place the specimen in an elevated temperature environment for a three-day period. This procedure was repeated for about 60 days.

The second stage initiated at an age of 120 days. In this stage, the specimen was placed in a high humidity chamber at room temperature (22ºC) and sprayed frequently to ensure adequate moisture conditions. Subsequently, an electric field was applied between two titanium meshes that were placed embedded in the concrete and within the solution reservoir. The same ponding solution from the first stage was used to fill the reservoir. A potential of 15 mV was then applied between the titanium meshes during the first two measurement periods and was later increased to 20 mV to further accelerate the transport of chlorides throughout the rest of the experiment. Each measurement period had a duration ranging between three and four weeks.

A visual examination was performed of the specimen in the condition it was received to assess the location and width of any surface cracks. The following methods were used to assess the corrosion state of the rebar and determine the parameters that may be used in service life prediction.

3.3.1.1   Potential mapping

Half-cell potential measurements were recorded for each point labelled (N1-N6) in Figure 3.19. Data collected at each of these locations could be useful in determining the corrosion behavior of the reinforcing bars.

3.3.1.2   Electrochemical Impedance Spectroscopy (EIS)

Electrochemical Impedance Spectroscopy (EIS) was conducted by using a potentiostat/galvanostat device suitable for applications in corrosion (Gamry Reference 600+), an electrical junction device (sponge), a set of wires, a SCE reference electrode, and a titanium mesh. The titanium mesh on top of a moist sponge was used as the counter-electrode. Also, each of the stainless steel reinforcement bars were used as the working electrode for each point and a SCE as the reference electrode. Impedance measurements of the top reinforcing bars were obtained using a 10-mV perturbation amplitude over a frequency range of 10 mHz – 100 kHz with 10 measurement points per decade. The experimental setup for one of the six EIS measurements is illustrated in Figure 3.19. The red "x" mark represents the location of the reference electrode.
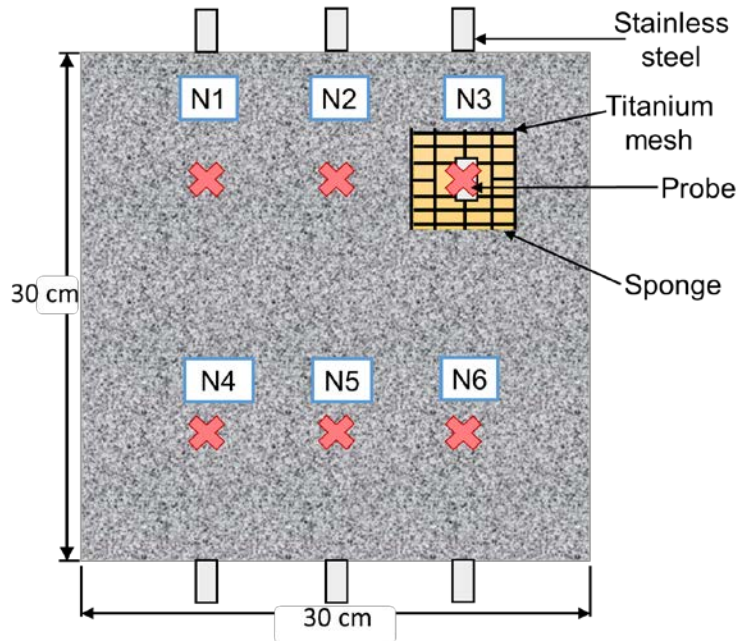
Figure 3.19: Schematic illustration of EIS experimental set-up of legacy specimen.

3.3.2 Autopsy

After the previously described visual examination and electrochemical impedance analysis was performed, the specimen was opened and evaluated in accordance to the following procedure:

1. The acrylic reservoir was removed.
2. A wet saw was used to cut the specimen into 6 sections, each containing one reinforcing bar, according to the cut lines shown in Figure 3.20. In the perpendicular direction of the top surface, two saw cuts were made. These cuts were performed in between and parallel to the rebar of each layer. Additional saw cuts were made to each one of the sections to isolate the reinforcing bars for individual analysis.
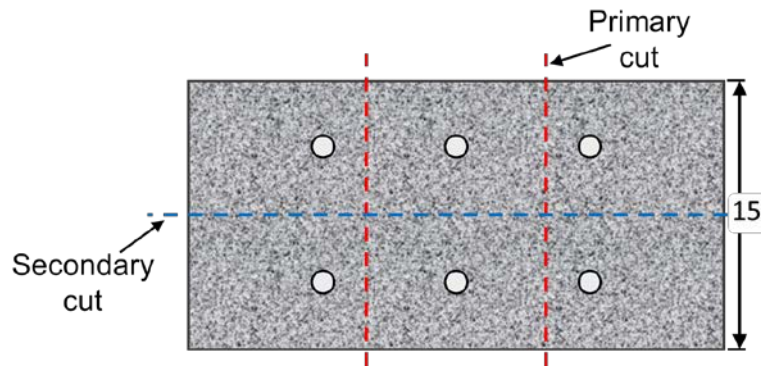
Figure 3.20: Schematic illustration of saw cuts performed in step 2 (red) and step 3 (blue).

3. For each of the six resultant specimen sections which can be observed in Figure 3, a hydraulic press was used to break the sample longitudinally along the axis of the reinforcement bar. The resultant sections consisted of a bottom piece containing the rebar and a top section containing the rebar trace as shown in Figure 3.21.

Figure 3.21: Resultant legacy specimen sections.

4. Immediately after exposing the steel surface and trace, the specimen was examined and photographed. In cases where corrosion was visible on any of the steel reinforcement, these additional steps were followed:

   a. The condition of the surface of the rebar, including corrosion products if already corroding was recorded in pictures.

   b. The rebar was carefully removed by using a hydraulic press. As a result, both the steel and the concrete would be in good conditions for any further tests.

   c. After extracting the rebar from the specimen, any corrosion products present were cleaned following ASTM G01 C.3.511 procedures. Before the application of any chemicals, a light brush was used to remove any remaining concrete from the specimen and to ease the removal of corrosion products. A chemical process was then used in which the remaining corrosion products were removed. This process involved immersion of the stainless steel sample in a mild acid solution comprised of 250 mL of hydrochloric acid, 1.75 gr of hexamethylene tetramine and 500 mL of type IV reagent water for a period of ten minutes. The weight of the specimen was recorded before and after each immersion. Additionally, photographs were taken for the duration of the process to keep record of the evolution of the rebar. The process was repeated until the mass loss of the specimen was negligible. Finally, the sample was rinsed, dried and cleaned carefully with acetone to remove any undesired material (i.e., Epoxy).

Figure 3.22: Steel reinforcement and concrete section after extraction.

   d. A cross-sectional cut of the concrete was performed where the most corrosion products were observed. To preserve the presence of the corrosion products, a cut using a rotary tool was performed up until the middle of the depth of the sample. Three-point bending was then used to break the sample. A schematic illustration of the procedure described is shown in Figure 3.23(a). This process results in a cross like the one illustrated in Figure 3.23(b), it can be noted that the bottom half of the cross section was relatively flat when compared to the upper half. Additionally, highly magnified photos of the cross-section were used to determine the penetration depth of the corrosion products.

a)   b)
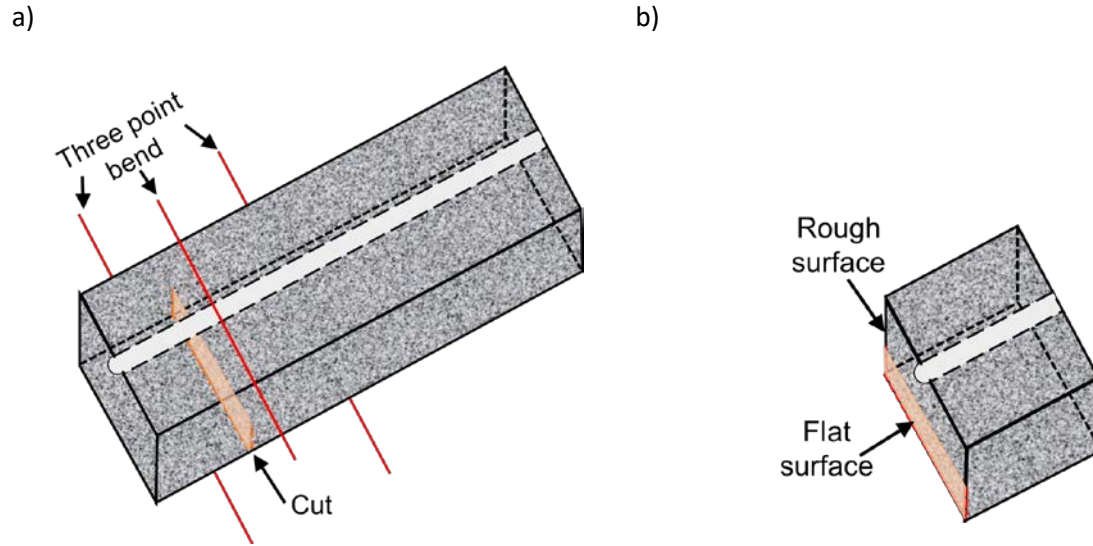
Figure 3.23: Schematic illustration of a) cross-sectional cut and b) three point bend-cross section.

3.3.2.1   Reduction in the steel reinforcement radius

The reduction in the steel reinforcement radius was obtained using a preliminary optical procedure using a three-dimensional wide area system. The results obtained were later compared with existing models developed for CS reinforcement. The detailed analysis procedure to obtain this parameter using the methodologies mentioned is further described in Section 3.1.3.

3.3.2.2   pH

The pH of each concrete section was assessed using phenolphthalein. The face of the concrete facing the rebar was uniformly sprayed with phenolphthalein immediately after breaking open the concrete specimen. Subsequently, the face sprayed would change colors indicating the level of alkalinity of the concrete. If the sample turned a bright purple/pink color, it would be indicative of an alkaline pH (greater than approximately nine). Otherwise, substantial carbonation would be indicated.

3.3.2.3   Chloride analysis

For each one of the anodes, concrete was milled at the depth of the rebar to determine the chloride content at this location by following a moderately modified FDOT method.[46] This was performed on the rebar trace closest to the pond

3.3.3 Critical corrosion penetration (X$_{CRIT}$)

3.3.3.1 Preliminary optical procedure

An autopsy was performed to obtain information regarding the critical reduction in the reinforcement bar radius (X$_{CRIT}$). The condition of the steel reinforcement after cleaning was evaluated using a wide area 3D-system (VR 5000) manufactured by Keyence Corporation. Plane, profilometric, area and volumetric measurements were performed to obtain parameters including the length of the anode, maximum penetration and X$_{CRIT}$. A section that did not show any signs of corrosion was treated as a reference surface. Subsequently, volume measurements were then taken of both the corroded and the reference section.

Reduction in the steel reinforcement radius was calculated for two cases, described as follows:

I. Steel reinforcement bar assumed corroding uniformly across the length of the anode in which corrosion only occurred in the portion facing the top surface of the concrete cover. Hence, only half of the circumference will be considered in the surface area estimations. The surface area (A_{surface}) was calculated as

$$A_{\text{surface}} / \text{mm}^2 \approx \frac{\pi \phi \text{L}}{2} \tag{11}$$

II. No corrosion morphology was assumed. The surface area of the steel reinforcement subjected to corrosion (A_{surface}) was estimated by using the wide area 3D-system. The X$_{CRIT}$ could be calculated as the quotient between the volume loss of steel reinforcement (Vol_{loss}) and the surface area (A_{surface}) of each one of the cases previously described, expressed as

$$X_{crit} = \frac{Vol_{loss}}{A_{surface}} \tag{12}$$

3.3.3.2 Empirical models for X$_{CRIT}$

Additionally, and for comparison to the measured values obtained with the 3D surface analysis procedure, the reduction in the steel reinforcement radius was calculated using existing predictive models developed from empirical data of carbon steel and epoxy-coated carbon steel, respectively.

Torres-Acosta and Sagues[26] developed a model which consisted of an empirical relationship between X$_{CRIT}$, the length of the corroding segment (L$_a$), the concrete cover depth (C) and diameter of the reinforcement bar (ϕ). The equation describing this relationship can be expressed as

$$X_{crit}/mm \approx 0.011 \left(\frac{C}{\phi} \right) \left(\frac{C}{L_a} + 1 \right)^2 \quad . \tag{13}$$

While this investigation was limited in that it did not include cases of sufficiently localized corrosion, it served as a starting formulation for a subsequent investigation performed by Busba.[25] A modified version of this relationship was proposed in which the exponent of the second term in the equation was replaced by a variable "n" that would be calculated through regression techniques. The equation describing this relationship can be expressed as

$$X_{crit}/mm \approx 0.011 \left(\frac{C}{\phi} \right) \left(\frac{C}{L_a} + 1 \right)^n \quad . \tag{14}$$

Where the value selected for n was 1.48 in localized corrosion scenarios.

The relationship proposed by Busba[25] provided an improved model, however, it assumed that the steel was corroding uniformly over a defined length or segment. This may not be applicable to cases of highly localized corrosion where distinctive pits are found in the steel reinforcement surface, such as in the case of stainless steel.

In 2011, an investigation by Darwin et al.[47] suggested another relationship to estimate X_{CRIT}. It included additional variables such as fractional length of the bar corroding (L_f) expressed as

$$L_f = \frac{L}{L_{bar}} \, , \tag{15}$$

and the fractional area of bar corroding (A_f) that can be calculated as

$$A_f = \frac{A_{corr}}{A_{bar}} \, . \tag{16}$$

Ultimately, the equation describing this relationship can be expressed as

$$X_{crit} = 45 \left[\frac{\left(\frac{c}{25.4} \right)^{2-A_f}}{D^{0.38} L_f^{0.1} A_f^{0.6}} + 0.2 \right] * 3^{A_f - 1} \, . \tag{17}$$

An investigation performed by Presuel et. Al.[45] analyzed six replicate specimens like the one shown in Figure 3.18, at FAU. This study compared X_{CRIT} values obtained by approximating the mass loss and parameters of bars that were thought to cause cracking of the concrete. This could be expressed as

$$X_{crit} = \Delta W * \frac{10^3}{\pi \varphi L_a \rho_{Fe}} \tag{18}$$

where ΔW is the mass loss, φ is the diameter of the rebar, L is the anode length and ρ_{Fe} is the density of iron.

In the present investigation, the models proposed by Torres-Acosta[26], Busba[25] and Darwin et al.[47] expressed by Equation (15), (16), and (19), respectively, were used to calculate X$_{CRIT}$ and compare to the measured values. Parameters such as the length of the anode, concrete cover, fractional length and area, and bar diameter were obtained experimentally from the autopsy performed to the legacy specimen.

3.4   Locally-deficient concrete specimens

Prismatic concrete specimens reinforced with UNS S31653, UNS S32304 and ASTM A615 were prepared to determine the effect of the condition of the concrete on the service limit state. Specifically, it will be determined whether corrosion of SS at locally deficient regions of concrete will lead to mechanical failure of the reinforcement prior to any subsequent damage to the concrete.

a)   b)
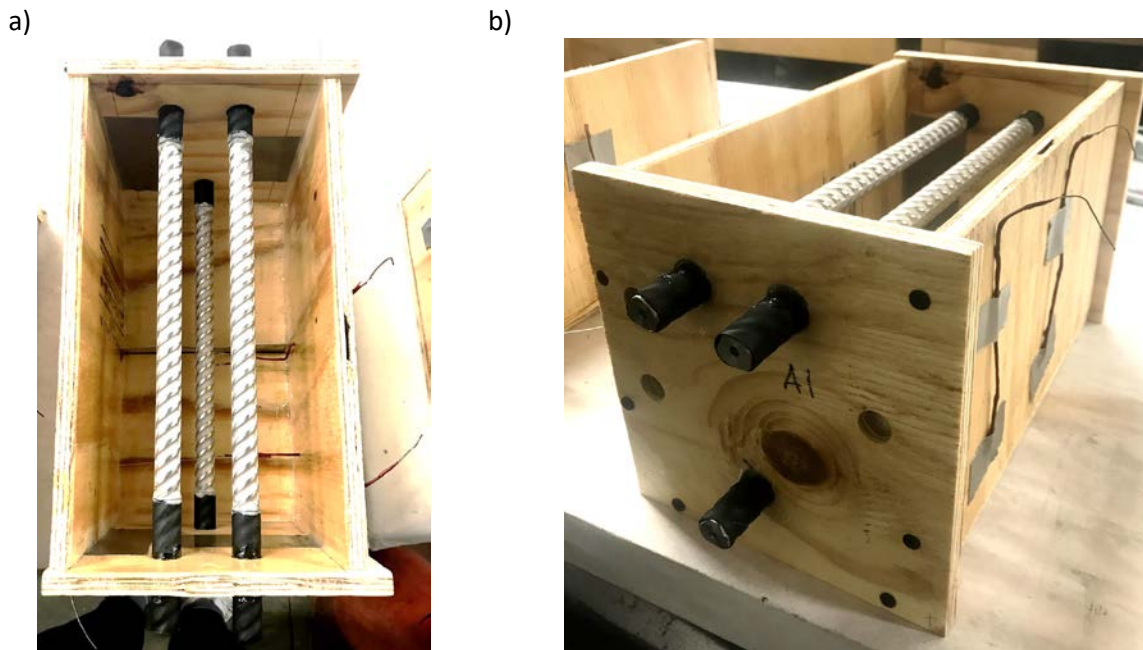
Figure 3.24: Final setup of specimens before casting. Wood mold was coated with a mold release agent, titanium reference electrodes and steel rebars were in place. (a) Top view, and (b) side view.

3.4.1 Materials

3.4.1.1 Reinforcing steel

Table 3.13 lists the three types of steel used in this section. Contractors Materials Co. based in Cincinnati, OH supplied all types of steel. Chemical compositions for the steel reinforcement bars are described in Table 3.14 and Table 3.15. All types of steel reinforcement were corrugated No. 5 reinforcement bars with a nominal diameter of ~15.9 mm (0.625 in). According to the mill scale provided by the manufacturer, the stainless steel bars were grade 75 while the plain steel bars were ASTM A615[48] grade 60. Additionally, the surface condition was pickled in the case of stainless steel reinforcement bars and as-received for plain steel bars. The surface of the reinforcement bars was cleaned with acetone before being placed in the concrete to remove any residual mill-scale and create a uniform surface.

Table 3.13: Types of steel used in cracked specimens.

Designation	Surface condition	Microstructure
UNS S31653	Pickled & passivated / Hot rolled	Austenitic
UNS S32304	Pickled & passivated / Hot rolled	Ferritic
ASTM A615	As-received	--

Table 3.14: Chemical composition of stainless steel reinforcing bars (weight percent).

Designation	C	Co	Cr	Cu	Mn	Mo	N	Ni	P	S	Si
UNS S31653	0.018	--	17.75	--	1.030	2.065	0.129	10.010	0.029	0.001	0.250
UNS S32304	0.016	0.220	22.540	0.290	1.630	0.260	0.149	4.530	0.030	0.001	--

Table 3.15: Chemical composition of plain steel ASTM A615 reinforcing bars (weight percent).

Designation	C	Mn	P	S	Si	Cu	Ni
ASTM A615	0.270	1.270	0.020	0.022	0.240	0.370	0.010
	Cr	Mo	Al	V	B	Cb	Sn
	0.150	0.035	-	0.041	-	-	-

3.4.1.2 Concrete

Concrete with a water to cementitious material ratio of 0.45 was prepared in accordance to the technical requirement provided by the ASTM A955-A3[49] guidelines, summarized in Table 3.16. The coarse aggregate met ASTM C33[50] specifications with 2.60-bulk specific gravity under a saturated surface dry (SSD) condition and 3.14% absorption capacity following the ASTM C127. The fine aggregate with 2.47-bulk specific gravity under a saturated surface dry (SSD) condition was graded and washed. Test results for both types of aggregate are detailed in Table 3.17.

Mixture proportions of the concrete are summarized in Table 3.18. The total nominal volume of concrete was approximately 85 liters (3 ft^3), equally divided into three batches. Type I Portland cement was used. In addition, two concrete admixtures were used consisting of a high range water reducer and a workability-enhancing admixture, ADVA and WRDA, respectively. These admixtures were used following the guidelines provided by the manufacturer to ensure the suggested air content in the concrete.

Table 3.16: Concrete per ASTM A955-A3 guidelines.

Criteria	Requirement
Cement content	598 pcy
Water content	270 pcy
Water to cement ratio	0.45
Fine aggregate volumetric fraction	32.5 %
Coarse Aggregate volumetric fraction	34 %
Air content	6 ± 1 %

Table 3.17: Test results for specific gravity and absorption for water calculations (ASTM C127).

	Specific gravity	Absorption %	Max. size in
Fine aggregate	2.47	-	
Coarse aggregate	2.60	3.14	3/8

Table 3.18: Concrete mixture proportions.

Material	Weight/vol pcy	Weight/vol kg/m^3	Batch kg
Cement	598	355	30.35
Water	270	160	13.68
Fine aggregate	1355	804	68.74
Coarse aggregate (SSD)	1492	885	75.67
Total weight	3715	2204	188.43

3.4.2   Specimen preparation

Nine prismatic reinforced concrete specimens were prepared at the corrosion laboratory at the University of South Florida following the concrete mix procedure given by ASTM A955-A3[49]. The steel reinforcement was set in two layers for each specimen. The top layer consists of a single No. 5 bar while the bottom layer consists of two No. 5 reinforcement bars. The dimensions of the beams were 6 inches (~15 cm) wide, 7 inches (~17.75 cm) high and 12 inches (~30 cm) long, as shown in Figure 3.25. The reinforcement bars projected out approximately 2 in (~5 cm) from the concrete block at each of the ends of the specimen. The concrete rebar cover was ~2.5 cm (1 in) for both the top and bottom layers of reinforcement bars.

Prior to casting the specimens, the steel reinforcement bars were drilled and tapped at one end of each one. A stainless steel screw would be later attached to assure an electrical connection during the testing period, shown in Figure 3.25 (a). Subsequently, they were cleaned using acetone to remove any contamination such oil, and heat shrink wrap was placed at both ends of the reinforcement bar one inch into the concrete. A 12 mil (0.30 mm) thick, 6 inch (~15 cm) long stainless steel shim was fixed on the bottom part of the form of the specimens, located in the middle of the specimen and perpendicular to the reinforcement bars, as shown in Figure 3.25(b). This shim was removed after casting during early curing leaving behind an artificial crack perpendicular to the direction of the steel reinforcement. This would allow direct infiltration of chlorides to the steel reinforcement.

(a)   (b)
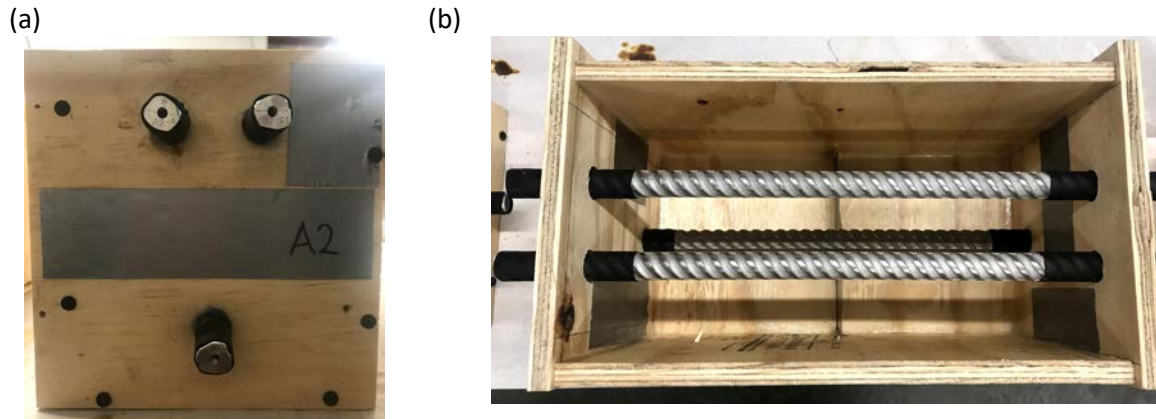
Figure 3.25: Steel placement in wood form prior to casting (a) front view of mold. Stainless steel reinforcement was tapped and drilled, and (b) top view of mold. Stainless-steel shim was placed parallel to the rebar.

Two reference electrodes were carefully placed as close to the steel reinforcement as possible. Rare earth-oxide activated titanium wire was selected as the material. They were uniformly coated using two layers of epoxy leaving only the tip close to the steel reinforcement bar exposed. Two locations were chosen to set the electrodes; one of them was placed in a sound concrete region leaving a one-inch cover while the other was placed in a defective concrete region located in the longitudinal mid-point of the specimen, shown in Figure 3.24. A more detailed view of the setup of the reference electrodes is shown in Figure 3.26.

Figure 3.26: Experimental setup of reference electrodes.

Mold release agent was applied to the wood form before concrete placement. All nine specimens were cast in the wood mold displayed in Figure 3.24(a). Each specimen was cast in the position shown in Figure 3.25, and vibrated for a 30-second period on a vibrating table (see Figure 3.27). The surface of the specimen was finished using a wooden float after the second layer was vibrated.

The specimens were cast in sets of three, therefore, three replicate concrete batches were mixed. The concrete was mixed in accordance to practice ASTM C192[38]. Three concrete cylindrical samples of 2 in x 4 in were also cast from each concrete batch to measure concrete resistivity, resulting in nine concrete cylindrical samples in total. In addition, Table 3.19 details which concrete batch was used for each of the steel reinforcement type.

Table 3.19: Batch labelling and number of specimens.

Batch	Reinforcement type	Replicates
A	UNS S316	3
B	UNS S2304	3
C	ASTM A615	3
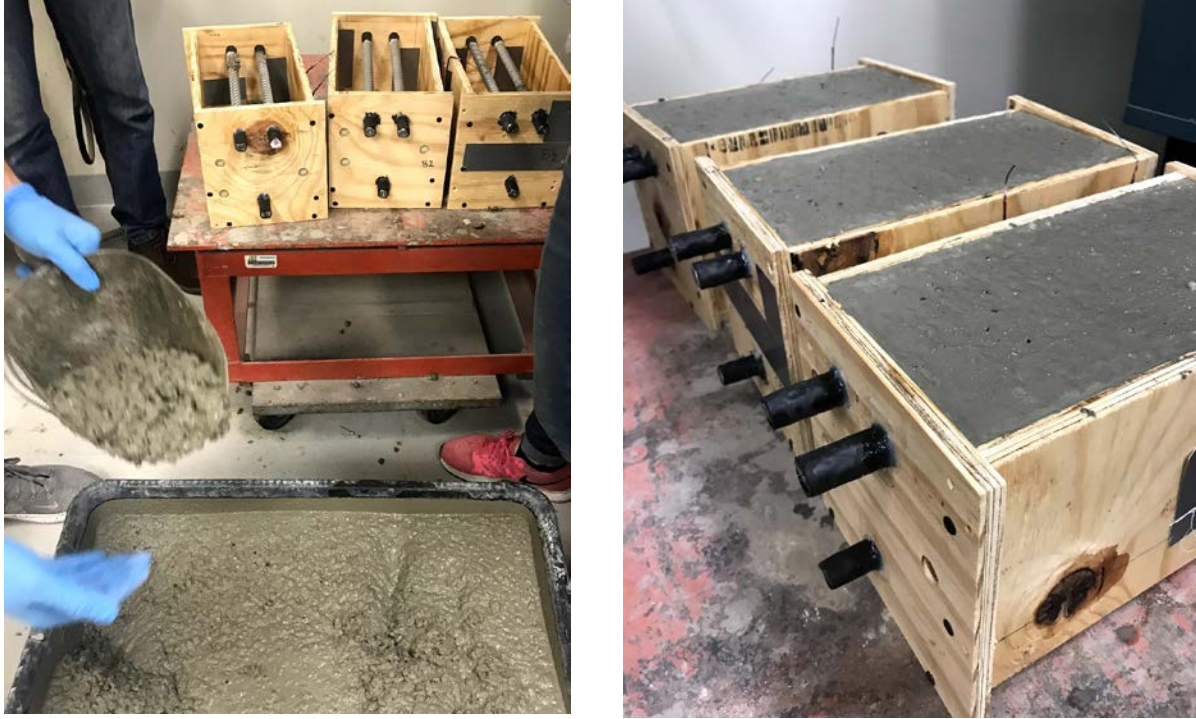
Figure 3.27: Concrete mixing and casting of samples.

Initially, specimens were cured in the wood forms for approximately 6 hours. After this initial curing period, the specimens were removed from the wood molds and plastic bags were used to cover them preventing moisture to evaporate. The stainless steel shims were supposed to be removed immediately after removing the wood molds. However, that removal was not feasible without damaging the specimen. Instead, a modification to this procedure was performed to adequately remove the stainless steel shims without compromising the concrete and still create a controlled zone of concrete deficiency to achieve the objective of the experiments.

The concrete surrounding the stainless steel shim was removed using a concrete saw approximately 24 hours after casting. The section removed was then replaced about 48 hours after the initial casting with a higher porosity concrete that also included a simulated crack. The simulated crack was formed with a stainless steel shim like it was previously done, however, it had a greater lever arm that would ease the removal after the initial curing period of the newly casted concrete. The specimens were clamped on each side of the shim with steel plates, and the stainless steel shim was pulled out. Figure 3.29 illustrates the latter described stainless steel shim and the setup used to remove it.
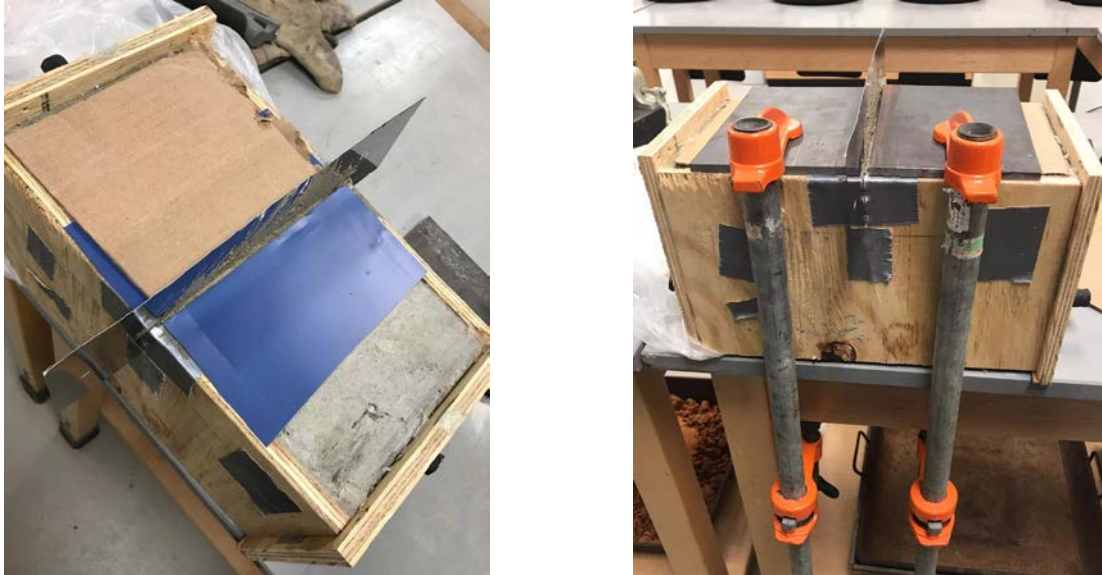
Figure 3.28: Shim removal process to generate local deficiency in concrete specimens.

The specimens were then flipped so the bottom layer of reinforcement consisted of two cathodes while the top layer of steel reinforcement consisted of an anode. The SS shim was then removed, and the locally-deficient concrete specimens were placed in plastic bags to maintain moist conditions and were stored in a high humidity chamber (~85%) at room temperature (22 ºC) for 25 days. A preliminary visual inspection was performed to assess quality of the concrete at each one the specimens.

The top of the specimen was lightly sanded using 150-grit sandpaper. 6-inch wide, 6 inch-long and 2-inch high, acrylic reservoirs were then placed on top of the specimens using marine adhesive sealant as shown in Figure 3.30(a). In addition, a one-inch mark was drawn in the acrylic reservoirs to keep a constant ponding solution level during the cyclic ponding state.

Electrical insulated wire of 16 gauge (1.5 mm^2) was attached to the steel reinforcement bars in the specimens using 10-24 threaded stainless steel bolts. The electrical connections on the sides of the specimen were covered with epoxy sealer (Sikadur 32) to prevent crevice or galvanic corrosion from occurring. In addition, two layers of the same epoxy sealer were used to cover the vertical sides of the specimen to prevent flow towards those surfaces. An electrical connection was provided between the top and bottom layer of steel reinforcement 36 days the initial casting; a 10-ohm resistor was placed to connect the top with the bottom layer of steel based on the guidelines provided in the cracked beam test described in ASTM A955. The final setup prior to data collection is shown in Figure 3.30(b).

Figure 3.29: Specimens with concrete deficiencies. (a) Top view after acrylic reservoirs were installed; (b) preparation procedure prior to testing finished, two layers of epoxy were used to coat specimens and electrical connections. Circuit with 10-ohm resistor between anode and cathodes.

The specimens were placed in a large enclosed glass container, as shown in Figure 3.31. The flow of air under specimens was ensured by lifting the samples about four inches and recirculating using two fans placed in the bottom of the container. The specimens were placed on two pieces of wood of 2-in thick which were also supported on two other pieces of wood of about the same thickness. Subsequently, for heated exposure test portions two heat lamps were placed on top of the glass container and a reflective wrap was used to reduce heat loss, shown in Figure 3.32 (a). The final placement of the specimens inside the enclosed contained is illustrated in Figure 3.32 (a) and Figure 3.32 (b).

Figure 3.30: Specimens with concrete deficiencies in enclosed glass container.

a)

b)
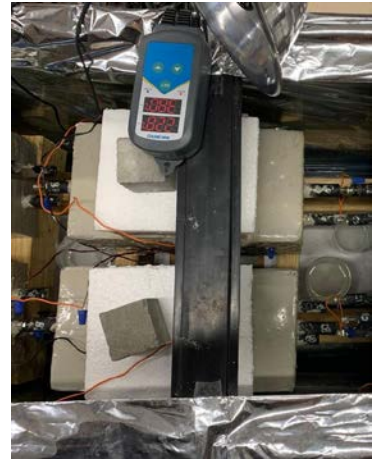
Figure 3.31: Experimental set-up of locally-deficient specimens in enclosed glass container covered in reflective wrap and heat lamps on top, (a) front view and (b) top view.

3.4.3   Data acquisition

A series of methods including resistivity of concrete cylinders, half-cell potential, and electrochemical impedance were used to monitor the corrosion performance of the steel reinforcements. A first set of measurements were taken at an age of 37 days after casting. Subsequently, exposure conditions were alternated following a modified procedure based on ASTM A955-A3[49] guidelines. These were divided into two stages. Eight specimens consisting of three replicates of each type of stainless steel and two replicates of plain steel were subjected to both stages. The procedures for each stage are described below.

The <u>cyclic ponding</u> stage consisted of wet-dry cycles. In this stage, a seven-day procedure was performed in which the reservoirs of the specimens were filled on the first day with a 15% sodium chloride solution at room temperature and covered to prevent changes in the concentration of the solution. On the fourth day of a cycle, data were collected, and the reservoirs were emptied. Subsequently, heat lamps were used to increase the temperature of the specimens to 100 +/-3 ºF (~38 +/-2 ºC) for a three day period. The heat would be then disconnected, and the specimens were again ponded to repeat the cycle. The wet-dry cycle was repeated for 12 weeks during the first stage.

Subsequently<u>, continuous ponding</u> with 15% sodium chloride solution at room temperature was initiated. Ponding solution was constantly checked and refilled if necessary, to maintain the desired solution depth on the specimens. During this stage, specimens were subjected to 6 weeks of continuous ponding in which data would be continued to be acquired weekly. The ponding solution remained on the specimens for this period at room temperature. Given that no significant variations were observed, the cyclic ponding stage was repeated to account for the most aggressive exposure condition. A second <u>cyclic ponding</u> stage was repeated for a 24-week period after the completing the continuous ponding stage. The same procedure described for the initial cyclic ponding stage was used.

3.4.3.1   Control specimens

The exposure conditions of the remaining plain steel replicate specimen were slightly modified. This specimen was treated as a control sample to compare experimental results between stainless steel and plain carbon steel subjected to aggressive conditions versus carbon steel subjected to mild environments. During the wet-dry control cycle, this specimen was first ponded using 15% sodium chloride solution. The ponding solution was then removed, and the specimen was allowed to dry in laboratory air at room temperature for three days. The wet-dry control cycle was then repeated for 12 weeks; however, deionized water was used instead of 15% sodium chloride solution after the second week of the cycle. The specimen was then subjected to a six-week continuous ponding period using deionized water. The solution depth was constantly checked, and deionized water was added to maintain the desired solution level. Subsequently, the wet-dry control cycle procedure was repeated throughout the remaining duration of the experiment for this specimen.

3.4.3.2   Potential difference between locally-deficient and sound concrete region

Half-cell potential measurements were performed using a multimeter. These measurements recorded the potential difference between the reference electrode within the locally-deficient and sound concrete region of each specimen. The reference electrode in the locally-deficient region and the sound concrete region was connected to the positive and negative terminal, respectively. The difference in potential between the two electrodes sought to provide a better indication of local corrosion activity in the vicinity of the crack that may not be obvious in the total macrocell current.
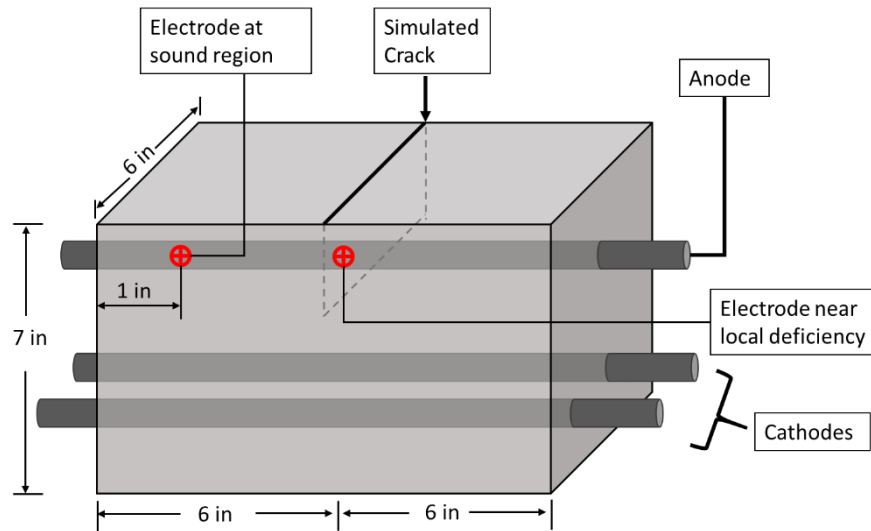
Figure 3.32: Experimental set-up of potential drop between reference electrodes placed near the local deficiency and the sound concrete region of the anode.

3.4.3.3   Macrocell current

The drop in potential across the resistor was recorded as shown in Figure 3.34. The macrocell current was then calculated using Ohm's law. The macrocell current density was later estimated as the quotient between the macrocell current and the polarized area which was assumed to be the total embedded surface area of one anode bar.
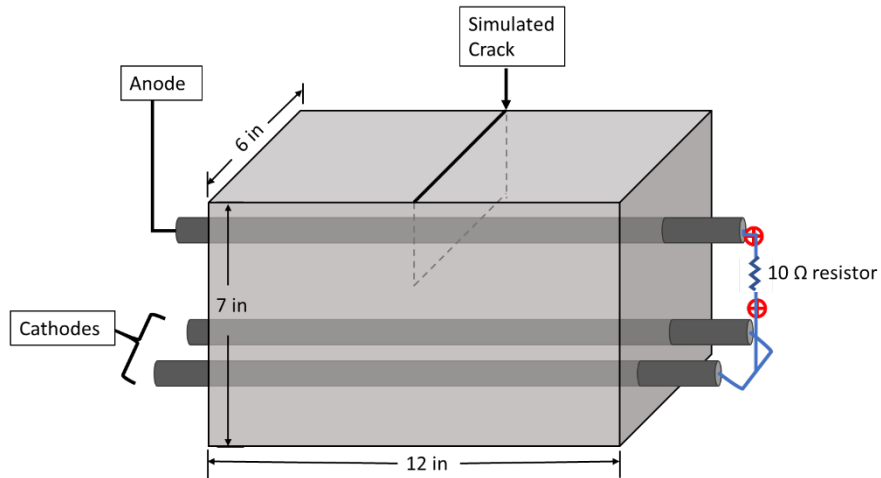
Figure 3.33: Experimental set-up of macrocell current density measurement. Measured across 10-ohm resistor.

3.4.3.4   EIS

EIS measurements were conducted to the locally-deficient concrete specimens with the highest macrocell current density or potential difference variation. In addition, EIS measurements were taken periodically to monitor these specimens. Prior to data acquisition, the macrocell was disconnected and a 30-minute period was ensured before initiating the EIS measurement. The apparatus for this experiment was a Gamry Reference 600+, also, a titanium wire served as the reference electrode and a rectangular titanium mesh on top of a moist sponge was used as the counter-electrode. The anode (steel reinforcement at the top layer) acted as the working electrode. The frequency range used in this investigation was 10 mHz to 100 kHz and 10 frequencies per decade. A potential perturbation of 10 mV generated by an alternating current applied to the open circuit potential.

4   Corrosion propagation stage parameters

In this section, the parameters required to estimate the duration of the corrosion propagation stage are presented based on experimental and simulation results, and literature evidence. Results are presented for corrosion rates, corrosion morphology, and X_{CRIT}. The results are used to propose a serviceability limit state based on structural design parameters such as concrete cover thickness and rebar diameter. Two possible limit states including cracking of the concrete cover and mechanical failure are considered. The critical loss in radius to cause cracking of the concrete cover considers corrosion morphology and is estimated according to existing empirical models based on carbon steel corrosion. In contrast, the critical loss in radius to cause mechanical failure of the steel reinforcement takes into consideration the reduction of the yield strength and the ductility. Subsequent to the comparison of the proposed limit states, preliminary predictions were performed to suggest the expected limit state based on design metrics such as concrete cover, rebar diameter, rebar type, and exposure condition.

4.1   Sound concrete

4.1.1   Corrosion morphology

The corrosion morphology of steel reinforcement in concrete has a significant effect on damage propagation. Although steel reinforcement is generally protected by an oxide film that is formed on its surface, carbonation of the concrete and high amounts of chloride ions may alter the stability of the oxide film leading to localized breakdown of the passive layer.[51]

Prediction models proposed by different investigators[25, 26, 47] for carbon steel agree on the fact that the amount of critical penetration required to cause cracking of the concrete depends on the length of the anode. According to these models, highly localized corrosion would be expected to require higher penetration depths to cause cracking of the concrete. This is the case for stainless steel reinforcement; however, few investigations have obtained experimental results for this parameter.

A study by Presuel et. Al[45] investigated corrosion-resistant reinforcement alternatives to plain carbon steel. The geometry selected for this study was a simulated deck slab reinforced with two layers of duplex stainless steel bars. Two types of steel reinforcement were used, UNS S32101 and UNS S32304. The specimens were subjected to a migration cell approach in which the rate of chloride transport was increased. After these showed signs of cracking, three specimens of each type of steel reinforcement were autopsied. As expected, small pitting corrosion spots were observed in some of the steel reinforcement bars on the top layer. The length of the corroding segments was measured for each of the rebars on the side where the crack was observed. For the matter of the present investigation, no-overlapped corrosion spots were considered when measuring the length of anode given that this represents the most critical penetration scenario. It was found that the specimens reinforced with 2101 SS reinforcement presented corroding lengths between 19 and 43 mm (~32 mm average). Furthermore, the corroding length for specimens reinforced with UNS S32304 reinforcement ranged between 16 and 27 mm (~20 mm average). Considering that the entire length of each rebar is about 360 mm (36 cm), the percentage of the length corroding compared to the total length is no more than 9%.

A legacy specimen reinforced with UNS S32101 from the same investigation performed by Presuel[45] was analyzed at the corrosion laboratory at the University of South Florida. Plane measurements were performed using a wide area 3D-system (see Section 3.3.5) to estimate the corroding length at the corrosion spot suspected to have caused cracking of the concrete. The length of the anode was estimated to be ~39 mm. This result is shown in Figure 4.1 and Figure 4.2, and was found to be comparable to length of the anode values described in the investigation performed by Presuel et. al[45] for the same type of reinforcement which ranged between 19 and 43 mm. It is worth highlighting that there was approximately a six-year gap between the original investigation and this report, in which the sample was stored indoors after the initial exposure was terminated.
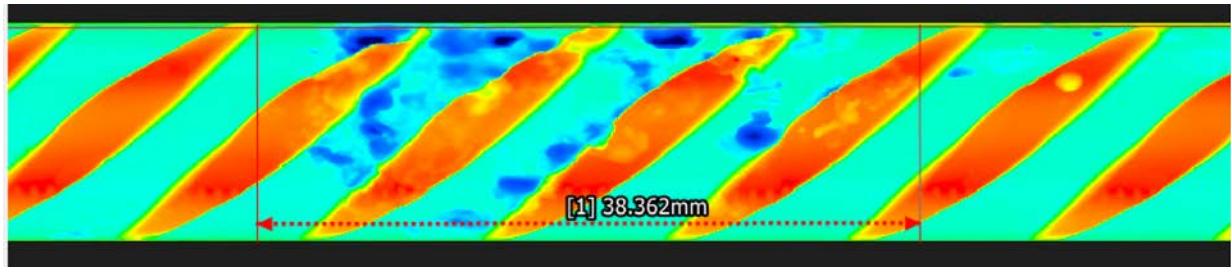
Figure 4.1: Height image of plane measurement of the length of the anode in steel reinforcement.

Figure 4.2: Optical image of plane measurement of the length of the anode in steel reinforcement.

One of the main findings was that corrosion was only found on the side of the SS steel reinforcement facing the concrete cover; thus, corrosion was limited to only a portion of the circumference. This observation agrees with the visual inspection results presented by Presuel et al.[45] that indicated that only an area limited to half of the circumference of the bar was corroding.

A similar observation was found by a subsequent investigation performed by Niejenhuis[35] to sound, transversely-cracked and longitudinally-cracked SS reinforced concrete specimens. This investigation, performed for six different grades of SS (UNS S30453, UNS S31653, UNS S32101, UNS S32205, UNS S32304 and UNS S24100), found that corrosion was generally limited over an area of about one-third of the circumference.[35] According to the author, this was found to be the case for both longitudinally and transversely cracked SS reinforced concrete specimens. It is important to note that due to the corrosion resistance of SS reinforcement, this project implemented corrosion acceleration techniques such as extremely aggressive exposure environments such as continuous exposure to chloride as well as variation in temperatures ranging between ~-10ºC and 25ºC. It is important to note that the investigations performed by both Presuel[45] and Niejenhuis[35] were significantly accelerated compared to field conditions and the concrete cover used (~25mm) was less than the minimum concrete cover typically provided for reinforced concrete structures subjected to aggressive environments.

The corrosion propagation behavior will have a direct impact on the limit state of a reinforced concrete structure. After corrosion initiates in SS, pits could potentially grow in three dimensions. Due to the complexity of this mechanism, different authors have tried to study this mechanism by developing simplified models[52] in which only lateral and radial corrosion damage propagation is considered. These models were often limited by either one or a combination of these factors: ohmic resistance, mass transport of the reactive species at the location of the pit, charge transfer during the anodic reaction and cathodic reaction rate.[52]

An investigation performed by Hurley[19] attempted to find the influencing factors that control radial and lateral corrosion propagation in plain steel and austenitic SS reinforcement. All samples were evaluated in Ca(OH)$_2$ solution. The results were then extrapolated to concrete. The results from their radial corrosion propagation experiment suggest that the pit growth mechanism is ohmically controlled in Ca(OH)$_2$ solution.

Lateral corrosion propagation was also evaluated using a micro-electrode array. As expected, it was concluded that while corrosion of carbon steel rapidly spread across the surface, austenitic SS exhibited major resistance with little to no corrosion in surrounding areas. Hence, SS316 presented a higher lateral corrosion propagation resistance when compared to that of plain steel.[52]

4.1.2   Corrosion products

The type of corrosion products formed on metals in concrete has a significant effect on damage propagation. Although steel reinforcement is generally protected by an oxide film that is formed on its surface, carbonation of the concrete and high amounts of chloride ions may alter the stability of the oxide film leading to localized breakdown of the passive layer.[51]

Even though information regarding the morphology and composition of the passive layer is important, very little research material has been performed to characterize the corrosion products generated by stainless steels. An investigation by Serdar et al.[53] aimed to solve these questions by studying the type, morphology and in-situ spatial distribution of the crystalline phases of corrosion products formed under natural conditions. Reinforced mortar samples exposed to aggressive chloride solution for a period of 2 years were monitored by using EIS and open circuit potential measurements. Later, micro-X-Ray diffraction (XRD), micro X-Ray Fluorescence (XRF) and Scanning Electron Microscopy (SEM) Energy Dispersive Spectrometry (EDS) techniques were employed to determine the chemical composition of corrosion products present in 10% and 16% weight chromium steels. As the phases are usually hard to distinguish, Backscattered SEM (BSE) images were recorded.

Results obtained by Serdar[53] suggested that the crystalline phases present in plain steel and stainless steel were comparable. The main crystalline phases found for both types of reinforcement were, goethite (α-FeOOH) and akaganeite ($Fe^{3+}O(OH,Cl)$ aka β-FeOOH). In the case of akaganeite, it was suggested by different authors that it is usually present in corrosion occurring in marine environments.[54-57] Although corrosion products with Cr were identified, these were not as predominant as the iron phases. This observation is not unusual as Cr and Ni have a lower contribution in comparison to Fe to the chemical composition of stainless steel.

Elemental maps were also created to analyze the distribution of these two main products plotted as two-dimensional phase distribution maps. From the results, Serdar et al. found a layer of goethite close to the steel surface followed by layers of akaganeite. It was also suggested that there could be a favorable environment in the steel/cement mortar interface for akageneite formation due to an increased amount of dissolved iron and chloride ions.[53]

A different investigation performed by Marcotte[58] studied the specific volume of corrosion products whereby iron was the parent metal. Crystallographic data was used to compute these values using pure iron as the reference volume (Relative volume Fe=1). This investigation revealed that akaganeite occupies approximately three and a half times the volume of iron while goethite occupies about three times the volume of the original volume of iron.

The same findings were concluded from an investigation performed by Scully.[59] Based on the composition of the alloys, the density for possible oxides and hydroxides that could be formed due to corrosion was found. The author concluded that corrosion products from UNS S316 and UNS S32101 could present similar densities to the oxides of plain steel. Furthermore, the specific volume of corrosion products formed during active corrosion suggested that CrO_3 would be the only compound higher than iron oxides and hydroxides. Experimental results were also obtained after performing XRD-powder diffraction suggesting that the corrosion products formed mostly were comprised of iron oxides and hydroxides.

4.1.3   Corrosion rates

The beam specimens presented in Section 3.1 were used to provide corrosion rate values based on impedance data measured at each designated position along the beam. To facilitate interpretation of the results, a finite element model was developed to simulate the impedance measurements in an effort to consider the polarized area of steel. Model information such as governing equations, mesh sizing and functions used are explained in Section 3.3.3. The average corrosion rate at certain locations (representing each region of the specimen) as a function of time were plotted in a semi-log diagram in Figure 4.3(a) and (b) for SS and CS, respectively. The values pointing to each series correspond to the position along the beam according to the number line provided in Figure 3.3. The included error bars represent the standard deviation of the results of the three samples.

Figure 4.3(a) shows the evolution of the calculated corrosion rates in the specimens reinforced with stainless steel over time. Prior to adjusting the low frequency limit of the impedance measurements from 10 mHz to 1 mHz for the measurement obtained at the end of the beams (-80 cm and 80 cm), locations in the chloride-free and the chloride-contaminated regions seemed to have similar values. However, after the final frequency at the end locations was modified, the calculated corrosion rates at these locations dropped significantly. Adjusting the low frequency limit of the measurement taken within the chloride-contaminated region did not result in significant changes to the estimated corrosion rate. The calculated corrosion rates in the chloride-contaminated locations increased noticeably in the first 180 day and later stabilized with slight fluctuations until an age of ~330 days was reached. The maximum corrosion rate values have maintained values ranging between 0.3 and 0.6 $\mu m.yr^{-1}$ assuming uniform corrosion over a large length of the reinforcement. However, it is expected that the measured corrosion rates are underestimated in the case that localized corrosion occurs.

Figure 4.3(b) shows the evolution of the calculated corrosion rates in the specimens reinforced with carbon steel over time. According to the results, it can be suggested that these specimens have been corroding for over 200 days since the average calculated corrosion rates were consistently ranging between 2.5 and 6.7 μm.yr^{-1} for this period. The appearance of a crack was observed in two out of 3 of the specimens around 310 days after these were cast, thus exposures of those CSA and CSB were terminated. The remaining specimen CSC presented different corrosion rates than the other two. As a result, the corrosion rates appear to be decreasing in Figure 4.3(b) following the termination of the cracked specimens.
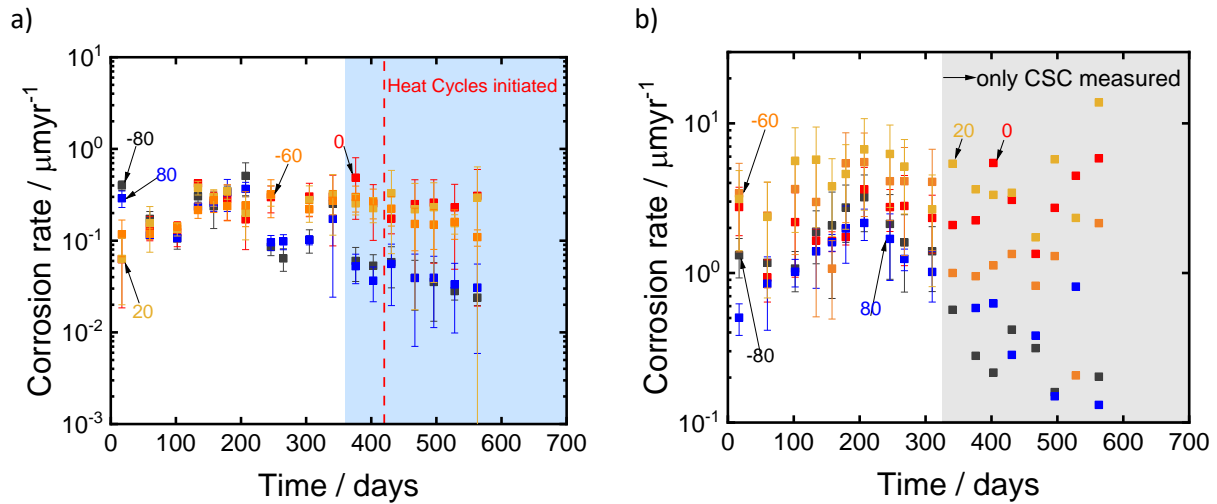
Figure 4.3: Behavior of the corrosion rate over time in (a) stainless steel (SS01, SS02, and SS03), and (b) carbon steel (CSA, CSB and CSC) specimens. Each data point represents the average value for the three specimens and the error bars the standard deviation. Black, orange, red, yellow and blue represented data points at locations -80 cm, -60 cm, 0 cm, 20 cm and 80 cm, respectively. Dashed line indicates initiation of elevated temperature exposure. Blue-shaded region designates the point at which low frequency limit of the impedance was extended to 1 mHz for points -80 cm and 80 cm. The number pointing to each series represents the position along the beam as described by number line shown in Figure 3.3.

The average corrosion in the chloride-contaminated specimen is about 10 times higher than in the chloride-free regions. This observation was found to be applicable to both types of reinforcement and became more evident in the SS specimens after modifying the frequency threshold. Moreover, corrosion rates in CS specimens are about one order of magnitude higher than the SS specimens.

From these results it is still not clear whether corrosion of the stainless steel has initiated. Detection limitations inherent to the EIS technique described later in Chapter 5 of this report are such that if highly localized corrosion was occurring, it would not be clearly detected by these measurements. To address this, results from the cylinders described in Section 3.2 are compared to those obtained for the beams in Section 3.1. The cylinders are expected to provide a lower level of uncertainty given that the corrosion rates are based on what was assumed to be a known polarized area.

Corrosion rates of both, beams and cylinders, are presented in Figure 4.4 as a function of time. Figure 4.4(a) and Figure 4.4(b) show corrosion rates in chloride-contaminated and chloride-free regions compared to those of cylinders reinforced with carbon steel and stainless steel, respectively. The RILEM criteria[60] was included by colored regions designated as high corrosion activity (shaded in gray), and negligible corrosion activity (shaded in blue).

For the CS reinforced specimens, the corrosion rate values of the cylinders were initially greater than those of the beams as shown in Figure 4.4(a). At an approximate age of 100 days, the corrosion rates of the beams and the cylinders converged to similar values ranging between 1 μm.yr^{-1} and 3 μm.yr^{-1}. The values for the chloride-contaminated region remained within the same order of magnitude of those in the chloride-free region until an age of ~300 days was reached. This could be indicative of the actual steel condition or the existence of error in the polarized area assessment. After ~300 days, corrosion rates of the CS beams showed a significant decrease in the chloride-free region while remaining within the same order of magnitude in the chloride-contaminated region. In the case of the CS cylinders, initial corrosion rate values were fairly high during the first ~100 days and decreased until stabilizing at values ranging between ~2 μm.yr^{-1} and ~5 μm.yr^{-1}. A slight increase was observed after the specimens reached an age of ~235 days, reaching a mean value of ~7 μm.yr^{-1} in the most recent results. Similar corrosion rates of the small cylinders and those estimated from EIS performed within the chloride-contaminated region of the beams suggests some level of accuracy of the EIS method in assessing corrosion rates of CS reinforcement.

For the SS beams, corrosion rates within the chloride-contaminated and chloride regions present corrosion rates ranging between 0.06 μm.yr^{-1} and 0.4 μm.yr^{-1}, shown in Figure 4.4 (b). After decreasing the final frequency of the experimental setup by one order of magnitude at the ends of the SS specimens, corrosion rates dropped to ~0.01 μm.yr^{-1} at the chloride-free location (80 cm). Simultaneously, corrosion rates in the chloride-contaminated region reached maximum values of 0.4 μm.yr^{-1}-0.5 μm.yr^{-1}. Corrosion rates have not exceeded values within the negligible corrosion range at any of the locations measured in the SS reinforced beams. In the case of SS cylinders, initial corrosion rates presented values lesser than those of the SS beams (~0.1 μm.yr^{-1}). Nevertheless, at an age of ~100 days a sharp increase was observed wherein the corrosion rate reached a value of ~0.7 μm.yr^{-1}. Subsequent to that, corrosion rate estimates of the SS cylinders continued to increase reaching values as high as ~10 μm.yr^{-1}. This value is about one order of magnitude greater than those of the beams and indicative of active corrosion according the corrosion rates criteria proposed by RILEM.[60]
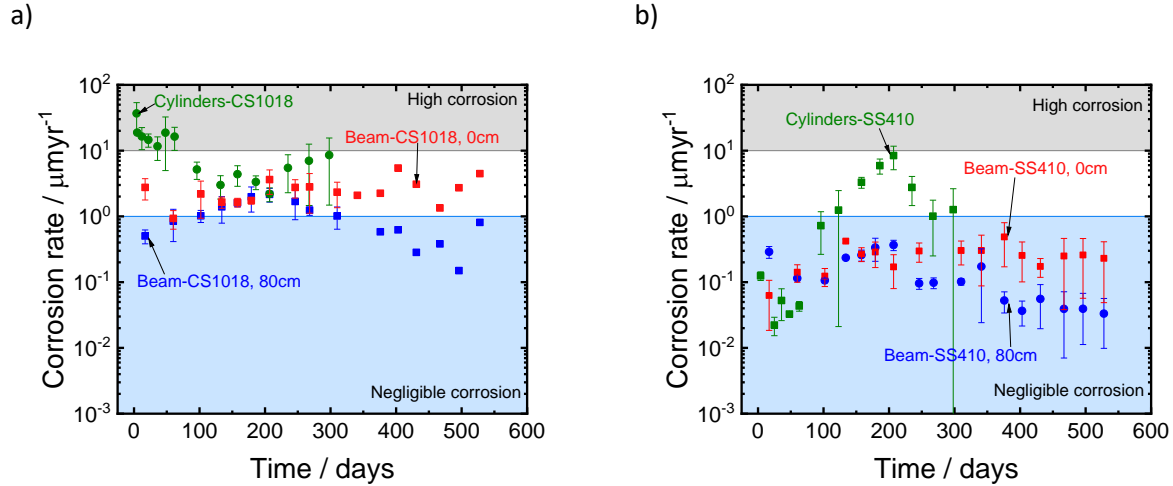
Figure 4.4: Corrosion rate as a function of time at different locations (i.e. end and center) of beams compared to cylindrical specimens reinforced with (a) SS and (b) CS.

Due to the findings regarding the corrosion morphology of stainless steel reinforcement and the experimental results presented here, it is likely that the analysis of the impedance response would result in underestimations of corrosion rates, as suggested by the larger corrosion rates obtained from the cylindrical specimens.

4.1.4   Estimates of X_{CRIT}

Preliminary results for the reduction in the steel reinforcement radius are described in this section for a legacy specimen obtained from FAU as described in Section 3.3. The obtained values are compared to those obtained from established empirical models described in Section 3.3.3.2 developed for carbon steel and epoxy coated rebar.

4.1.4.1   Legacy specimen autopsy

Autopsy results from the legacy specimen described in Section 3.3 following the procedure in Section 3.3.3.1 were used to estimate X_{CRIT}. The surface area and volume loss (only case II) of corrosion were computed and summarized in Table 4.1. In the first case, X_{CRIT} was found to be approximately 48 μm using Equation (12). In contrast, a value of 157 μm was determined when the corroded area was estimated using the proposed optical procedure which corresponds to the second case. When the latter is used, the X_{CRIT} value is about three times larger than when assuming uniform corrosion across one side of the rebar along the length of the anode.

Table 4.1: Surface area and volume loss estimates.

Case	$A_{surface}$ mm^2	Volume mm^3	X_{CRIT} (12) μm	X_{CRIT} (13) μm	X_{CRIT} (14) μm	X_{CRIT} (17) μm
I	994	-	48	39	32	67
II	303	47.4	157			

X_{CRIT} was also estimated using the existing models described by Equation (13), (14) and (17) considering a concrete cover of 23 mm, a reinforcement bar diameter of 16.5 mm and an anode length of 38.4 mm. The area corroding was estimated using the optical procedure. Furthermore, the fractional length (L_f) and fractional area (A_f) estimated using Equation (15) and (16), were 0.107 and 0.016, respectively.

4.1.4.2   Previously reported values

Additional values based on autopsy results of similar specimens were presented by Presuel et al[45]. The experimental results of mass loss were used to estimate X_{CRIT} according to Equation (18). The values obtained were compared to existing models including the one proposed by Torres-Acosta[26] and Busba[25] per Equation (13) and (14), respectively. The estimated values of X_{CRIT} are summarized in Table 4.3. The results obtained using the model proposed by Torres-Acosta ranged between 36 and 76 µm for SS2101; and 50 and 93 µm for SS2304. Furthermore, results using the model proposed by Busba[25] estimated values ranging between 29 and 50 µm for SS2101; and 38 and 98 µm for SS2304. While the results obtained by these models did not exceed 76 µm for SS2101 and 93 µm for SS2304, the experimental results were up to 169 µm and 93 µm, respectively.

Table 4.2: Critical penetration depth estimates from simulated deck slab specimens reported by FAU.[45]

Rebar	ID	X_{CRIT} (13)	X_{CRIT} (14)	X_{CRIT} (18)
		µm	µm	µm
2101	1-1C	36.5	29.17	108.2
2101	1-2B	43.5	33.24	107.6
2101	1-5B	75.6	50.02	168.7
2304	2-1B	50.4	38.51	98.1
2304	2-2B	92.9	58.29	58.7
2304	2-4B	91.9	57.842	303.6

Another investigation performed by Hurley[52] performed theoretical calculations of X_{CRIT} for SS316, SS2101 and plain steel. In the case of SS316 it was assumed that localized attack would be expected. The ratio between the corroding length and the critical penetration (L/X_{CRIT}) was assumed to be approximately four.[55] Since duplex SS reinforcement is expected to have a less localized form of corrosion attack when compared to SS316, the L/X_{CRIT} value was assumed to be 8. In contrast, a more uniform corrosion attack would be expected for CS. The L/X_{CRIT} values of CS was assumed to be 40. Thus, the author suggested that the X_{CRIT} values for SS316, SS2101 and CS were approximately 234 µm, 152 µm, and 56 µm, respectively. For analysis purposes, the concrete cover and bar diameter values were adjusted to match ones used in the specimens from the investigation performed by Presuel et al.[45] (~1-in cover and No. 5 bar) and the present report. The X_{CRIT} values found for SS316, SS2101 and plain were approximately 185, 129 and 64 µm.

The X_{CRIT} value obtained by Hurley[52] for SS2101 (129 µm) is comparable to the one obtained for the same type of SS in this investigation accounting for only the area corroding using the optical procedure (157 µm). In contrast, the X_{CRIT} results obtained using the models developed for CS reinforcement seem to be slightly more conservative since these are based on the assumption that corrosion occurs uniformly along the length of the anode around the entire circumference.

The comparisons made in this investigation between the true X_{CRIT} values, based upon either mass loss or surface damage measurements, suggest that the models developed for carbon steel reinforcement may provide overly conservative estimates of X_{CRIT} for stainless steel reinforcement. Further work is required to develop a suitable model of X_{CRIT} that accounts for the extremely localized nature of the corrosion morphology of stainless steel in concrete.

4.1.5   Preliminary laboratory evaluation of corrosion localization influence on limit state

This experiment described was initially developed to indicate a ratio of the length of corroding region to concrete cover that does not result in tensile cracking. Preliminary results describing the feasibility of the method is described here. Future experiments are then suggested based on the results. The volumetric expansion of corrosion products in reinforced concrete was mimicked by using a lead plug inside of a cored 4x8-inch cylinder, shown in Figure 4.5.

a)

b)
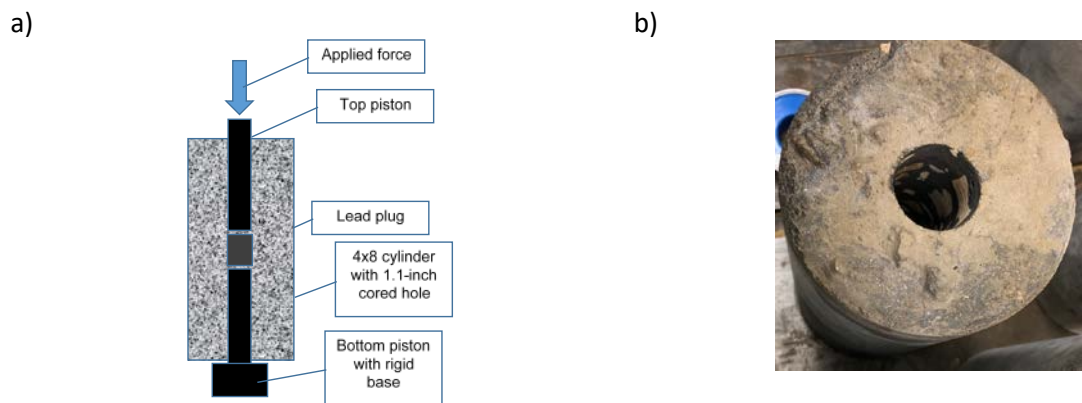
Figure 4.5: 4 x 8-inch concrete cylinder with 1.1-inch core hole.

The lead sample was then compressed inside the cylinder, allowing it to expand radially and create lateral pressure in the concrete cylinder. The axial load applied to the lead sample, the strain on the outside of the concrete cylinder and the lead deformation were recorded for each test. At the end of the test, the final height of the lead piece was measured at 0.402-inch, a 0.098-inch difference from the original 0.5-inch height. Figure 4.6(a) and (b) show that even with highly localized deformation, concrete cracking, provided a substantial enough amount of corrosion, is still feasible.
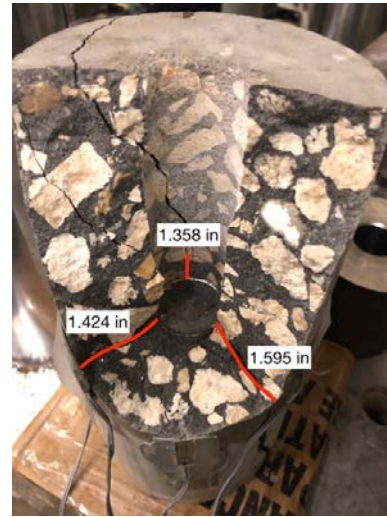
Figure 4.6: Extreme localized corrosion experimental results showing (a) concrete cracks, and (b) failure locations at the concrete cover. The red lines around the lead plug represent the concrete cover thickness at different locations ranging between 1.358 in and 1.595 in.

From the horizontal strain data, an increase in tensile strain was observed after 0.028 inches of vertical lead displacement. This signals that it took 0.028 inches of lead displacement and about 2.8 kips of load for the outside of the concrete cylinder to start experiencing horizontal tensile strains. In the case of vertical strain, a significant increase in tensile strain was observed after 0.020 inches of displacement and 1.7 kips of load. Data from the strain gages is presented in Figure 4.7 and Figure 4.8.
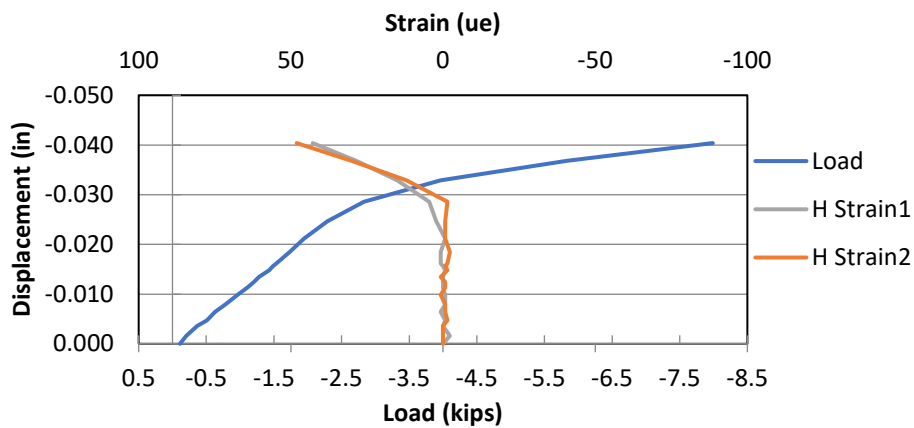
Figure 4.7: Horizontal strain.
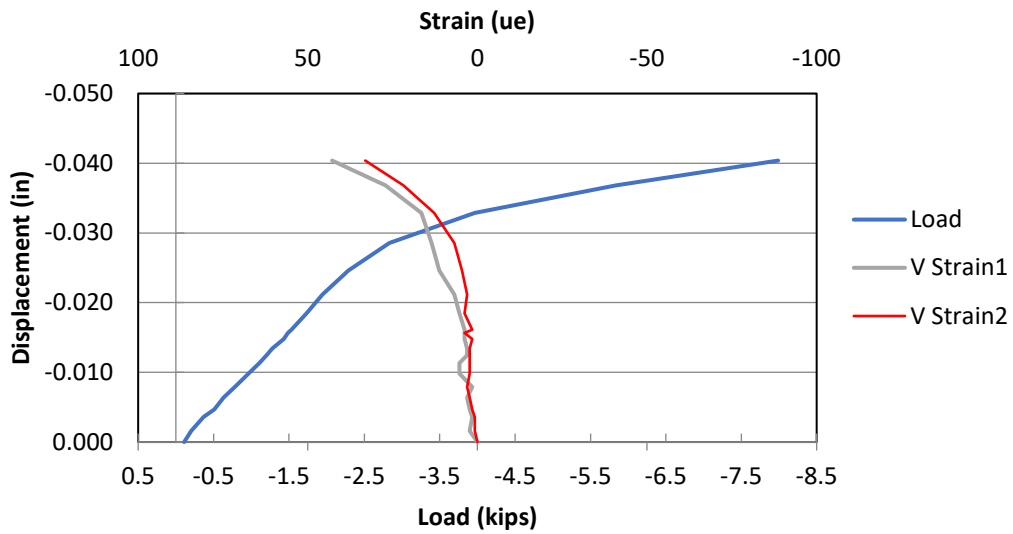
Figure 4.8: Vertical strain.

In order to calibrate the axial force experienced by the concrete, another lead sample, also of 1.09-inch diameter and 0.5-inch height, was compressed. This time, the piece of lead was not confined and was allowed to deform, as shown in Figure 4.9(a). The final deformation of the sample is shown in Figure 4.9(b).

Figure 4.9: (a) Initial lead sample and (b) deflected shape of lead calibration.

74

The axial force was then corrected by subtracting the force obtained from the lead calibration curve from the force obtained from test, as shown in Figure 4.10. The difference between test data and the calibration curve is the axial force that resulted from the concrete confinement around the lead.
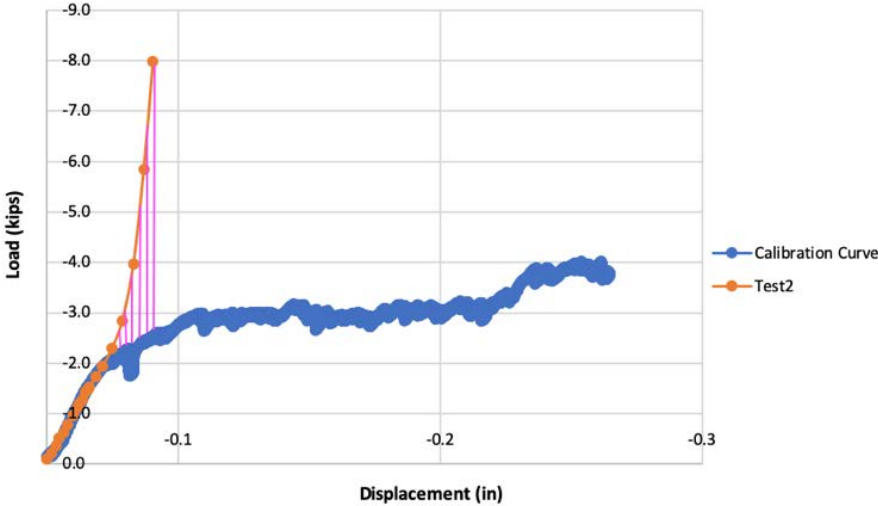
Figure 4.10: Load calibration.

Figure 4.11 shows the resulting axial load experienced by the concrete during the test versus the displacement or deflection of the lead sample. Note at a lead deformation of approximately 0.020-inch the corrected load increases which also corresponds to the onset of strain in Figure 4.7 and Figure 4.8.
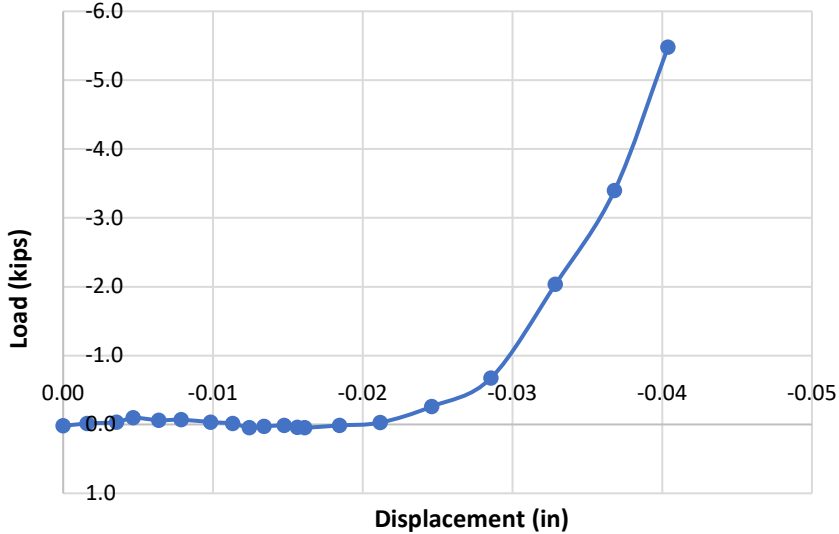
Figure 4.11: Concrete load vs. displacement.

Future tests will focus on refining the length of corrosion product to concrete cover ratio necessary to cause concrete tensile failure. The change in diameter of the lead sample throughout the test is also important since the rebar/concrete interface tensile strain can be directly computed from the distortion of the lead and the increase in diameter and perimeter.

4.1.6   Critical radius loss for mechanical failure

Given that corrosion in plain carbon steel reinforcement spreads along the rebar, as well as around its perimeter, enough volumetric expansion can occur to cause cracking or spalling of the concrete. However, when corrosion is highly localized, a given loss of local rebar cross section could threaten the steel's mechanical durability before showing any signs of cracking or spalling.

Corrosion degrades the mechanical properties of materials as determined in standardized tests.[61-64] [[65-67] .For steel reinforcement, the two most significant mechanical properties for design are yield strength and ductility. The yield strength is governed by the grade of the reinforcement bar (usually grade 60 or 75). For stainless steel rebars, the minimum yield strength requirements as well as ductility in terms of elongation and bending are contained in ASTM A955.[49].

In this section, two limit state scenarios are proposed to assess the influence of corrosion on the mechanical properties of steel reinforcement. The first one presents the case in which the steel reinforcement may fail due to the loss in load-capacity, whereby the yield strength requirement would not be fulfilled. The second case consists of the onset of brittle steel behavior. That condition, which would be detrimental to the structure in the event loads became excessive, could be present even if the other limit state had not yet been reached. It is recognized that other mechanical degradation scenarios may be present instead of or concurrent with the above.

4.1.6.1   *Mechanical failure limit states - Insufficient strength*

A mathematical model was developed by Ting and Nowak[68] to estimate the effect of the loss of metal due to corrosion (evaluated in terms of area) of plain carbon steel reinforcement on flexural behavior of reinforced concrete beams. The authors suggested that the relationship between the decrease of strength and the loss of cross-sectional area caused by corrosion of the steel reinforcement was linear.

Various investigations have adopted a linear model to relate the degree of corrosion and degradation of parameters such as the yield strength (f_y), ultimate tensile strength (f_u) and elongation to fracture (ε_u). The degree of corrosion (Q_{corr}) was defined as the average cross-section area expressed as a percentage of the original area. In some cases, this was measured experimentally as the ratio of the mass loss to corrosion of a representative portion of the bar, to the initial mass of that portion. The model relations are expressed as

$$f_y = (1 - \alpha_y Q_{corr}) f_{yo} ; \tag{19}$$

$$f_u = (1 - \alpha_u Q_{corr}) f_{uo}; \tag{20}$$

$$\varepsilon_u = (1 - \alpha_1 Q_{corr}) \varepsilon_{yo} \tag{21}$$

where the "0" subscript indicates the initial values in the un-corroded condition, and the empirical coefficient α quantifies the rate of degradation and has values influenced by the experimental setup and exposure conditions. Cairns [66] summarized the coefficient values proposed by various authors, listed in Table 4.4.

Almusallam[65] studied the effect that the corrosion degree may have on the properties of reinforcing plain steel bars. Concrete specimens reinforced with grade 60 of ASTM A615 were immersed in 5% sodium chloride solution while an anodic current of 2 mA/cm^2 was impressed to accelerate corrosion. The findings showed that bars with a 6-mm and 12-mm diameter would not meet the tensile stress requirements when the degree of corrosion exceeded values of 11 and 24%, respectively.

A subsequent investigation performed by Cairns et al.[66] aimed to evaluate the effect of corrosion attack on the mechanical properties of steel reinforcement. Several tests were performed wherein the loss of cross-sectional area was simulated by performing mechanical cuts or accelerating the corrosion of the metal.

Table 4.3: Empirical coefficients for strength and ductility based on literature review.[66]

Author(s)	Specimen	Exposure	Q_{corr}, %	α_y	α_u	α_1
Palsson and Mirza[69]	Concrete	Service, chlorides	0 to 80*	0	0	NS
Castel, François and Airliguie[70]	Concrete	Chlorides, 0.0 mA/cm^2	0 to 20	0	NS	0.035
Du[71]	Bare	Accelerated, 0.5 to 2.0 mA/ cm^2	0 to 25	0.014	0.014	0.029
	Concrete	Accelerated, 1.0 mA/ cm^2	0 to 18	0.015	0.015	0.039
Maslehuddin et al.[72]	Bare	Service, marine	0 to 1	0	0	0
Allam et al.[73]	Bare	Service, Arabian coast	0 to 1	0	0	0
Morinaga [74]	Concrete	Service, chlorides	0 to 25	0.017	0.018	0.06
Zhang, Lu, and Li [75]	Concrete	Service, carbonation	0 to 67	0.01	0.01	0
Andrade et al.[76]	Bare	Accelerated, 1 mA/cm^2	0 to 11	0.015	0.013	0.017
Saifullah and Clark [77]	Concrete	Accelerated, 0.5 mA/ cm^2	0 to 28	0.013, 0.012	0.017, 0.014	NS
Lee, Tomosawa, and Noguchi [78]	Concrete	Accelerated, 13 mA/ cm^2	0 to 25	0.012	NS	NS
Cairns[66]	Concrete	Accelerated, 0.01 to 0.05 mA/cm^2	0 to 3	0.012	0.011	0.03

The loss of cross-sectional area was considered as non-uniform or pitting corrosion, shown in Figure 4.12, which should be applicable to the corrosion morphology of stainless steel. A non-linear numerical method based on the stress-strain behavior of an uncorroded bar was proposed to evaluate the impact of different parameters on the strength of corroded steel samples.
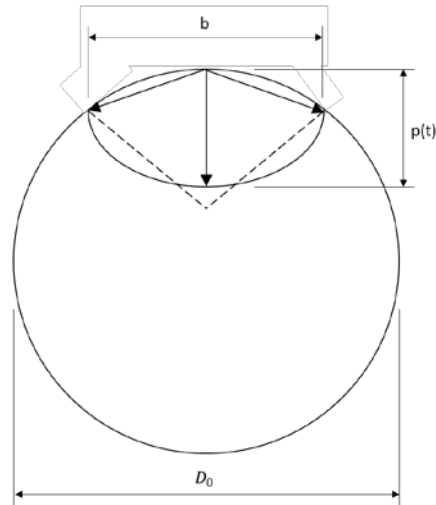
Figure 4.12: Schematic illustration of cross-sectional loss of rebar subjected to pitting corrosion.[66]

Cairns et al.[66] compared yield and ultimate strength between corrosion-free and 10%-corrosion plain steel samples. Although no evident change was observed in the yield strength between the samples, the ultimate tensile strength dropped approximately 10% when a corrosion degree of 10% was present. It is important to note the latter is not as significant for construction application since the yield strength is the one specified in the codes.

The specimens were classified as lightly (less than 7%) or heavily corroded. The lightly corroded specimens presented an approximately linear relation with the reduction of the area of cross-section. In contrast, heavily corroded specimens presented a milder relationship since the reduction in yield strength was less than the maximum reduction in the area of the cross section.[66]

Fernandez[79] analyzed the mechanical response of corroded specimens after being subjected to two phases consisting of monotonic and cyclic load tests. Plain carbon steel with 10-mm and 12-mm diameters were used for the experiment. The first phase of tests allowed the author to obtain stress-strain parameters of corroded specimens with corrosion degrees ranging from 8 to 22%. Results from this first phase suggested that the corrosion degree strongly influenced the yield and ultimate stresses of the steel. It was also concluded that assuming uniform corrosion around the cross-section provided good insight of the evolution of mechanical properties of the steel reinforcement based on actual corrosion penetration. A parabolic function was observed to provide a good fit for yield and ultimate tensile strength data when assuming uniform corrosion around the cross section, also referred as idealized corrosion.

Fernandez[79] noted that the experimental results obtained for the tensile capacity of bars subjected to corrosion underestimated the theoretical capacity when using Equation (19). In all cases studied, the author found that the mechanical properties were not proportional to the degree of corrosion. Moreover, other factors such as stress concentrations, displacement of the center of gravity and non-homogeneity of the material should be considered.[79]

Stewart[67] studied the effect of corrosion on flexural and shear reinforcement in structural reliability in plain steel-reinforced concrete beams. It was found that even relatively low loss of the cross-sectional area could cause reductions on the yield strength. When high corrosion degrees were observed, the effect on the ductility would become more predominant than the reduction in the yield strength. This is further described in 4.1.6.2. This investigation also revealed that the pit morphology played an important role in the spatial capacity of the steel reinforcement, shown in Figure 4.13.
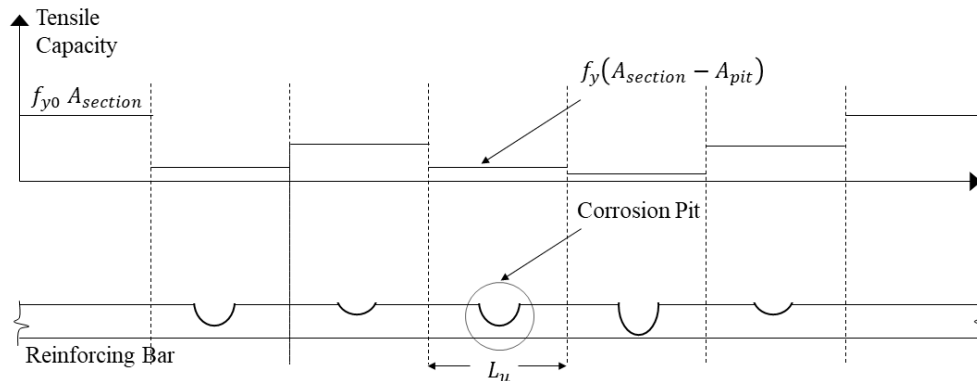
Figure 4.13: Spatial tensile capacity of non-uniformly corroding reinforcement bar.

A subsequent investigation by Tang et al.[80] developed a statistical method to assess the effect of non-uniform corrosion attack on the mechanical properties of plain carbon steel (ASTM A615[48]) reinforcement. This investigation aimed to provide more accurate cross-sectional area loss measurements by using a 3D laser scanner. This method provided an improvement for types of steel with localized corrosion attack, such as stainless steel.

Tensile tests and a statistical analysis were then performed to obtain the relation between corrosion loss and yield strength. Various average corrosion degrees were evaluated, ranging from 0% to 29%. The results obtained by Tang indicated that the yield and ultimate strength presented a linear relationship with the loss of the cross-sectional area. The improved loss of cross-sectional area 3D measurements seemed to correlate better to the results than the average loss of cross section. However, none of the results showed drastic decreases in the yield strength that would cause the steel to violate ASTM A615[48] requirements.

Only one author was found to study the effect of corrosion degree on the yield strength of stainless steel reinforcement. Wu et al.[81] studied the influence that different strain levels could have on corrosion of stainless steel reinforcement. The selection of the material was based on cost savings; thus, ferrite stainless steel bars were used. The specimens were subjected to an accelerated corrosion test and a uniaxial tensile test of corroded specimens to evaluate the effect on mechanical properties of the material. Results from the uniaxial test suggested that the corrosion degree had a direct influence on the mechanical performance of stainless steel. Hence, higher corrosion degrees would cause a decrease in the yield and ultimate tensile strength. This conclusion agrees with the findings from similar investigations performed in plain carbon steel rebar. It is important to note that only the final area of the cross-section is used to make yield strength estimations.

Given that the composition of stainless steel is different than plain steel, the effect of the different alloying elements in the microstructure and surface appearance should also be considered. Different investigations have suggested that stainless steel may be subjected to higher (compared to those for CS) deterioration rates in the mechanical properties.[82-85]Nevertheless, for specimens with corrosion degrees lower than 25%, the yield strength was still higher than that of most plain steel bars. In most cases, the yield strength reported by stainless steel manufacturers significantly exceeds the minimum requirements.

- For illustrative purposes to estimate the required corrosion degree to cause a ductile mechanical failure, two types of stainless steel were chosen, duplex UNS S32304 and austenitic UNS S31653. Those corresponded to the bars in the experiments in Section 3.4.11. Manufacturer reported strength, ductility and specified grade are listed in Table 4.5.

Table 4.4: Mechanical properties of steel reinforcement bars.

Type of steel	0.2% Yield Strength		Elongation/8"	Grade	
	ksi	MPa	%	ksi	MPa
UNS S32304	91.29	629.42	20.13	75	517.11
UNS S31653	97.21	670.24	21.15	75	517.11
ASTM A615	72.98	503.18	15	60	413.69

Two limit state value scenarios were selected for IS declaration for each alloy. One was conservatively equivalent to a reduction of strength from the manufacturer-reported value to the Grade value of the alloy (i.e. from ~95 ksi to 75 ksi, or a ~21% reduction in strength). The other, less conservative, was a reduction from ~95ksi to 32 ksi (~66%), where the end value is representative of the lower bound specification for some structural steels.[86] As shown next, the projected result does not depend on the specific values chosen but rather on their ratio (percentage), which were selected to bracket a likely range of interest between high or low conservative approaches. It is emphasized that these choices presented only as an example for the following illustrations of the methodology, and that alternative values may be readily substituted for specific case analyses.

The corrosion penetration amount corresponding to the conditions indicated above was estimated as follows. Approximating the corrosion effect as a simple, effectively uniform loss of cross sectional area, then the area of the corroded rebar (A_{corr}), and the nominal cross-sectional area of the uncorroded bar (A_{xs}) are related by

$$A_{corr} = Q_{corr}A_{xs} \tag{22}$$

From Equation (19) the Q_{corr} value for each condition is:

$$Q_{corr} = \frac{1}{\alpha_y}\left(1 - \frac{f_y}{f_0}\right) \tag{23}$$

where f_{y0} as the initial yield strength per Table 4.5 and f_y as the corroded bar yield strength at the failure condition (either the Grade value or 32 ksi). The chosen value of α_y was 0.017, which is representative of those reported earlier on.

With that value of Q_{corr} and for a given bar size and corresponding value of A_{xs}, then A_{corr} is obtained per Equation (22). Given the uniform loss assumption, the diameter of the corroded section (d_{red}) at the limit condition is then given by:

$$d_{red} = \sqrt{\frac{4A_{corr}}{\pi}} \tag{24}$$

Finally, the value of the critical corrosion penetration $Xmech_{IS}$ can be estimated by subtracting the reduced diameter (d_{red}) from the initial diameter (d):

$$Xmech_{los} = \frac{d - d_{red}}{2} \tag{25}$$

Results are presented in Table 4.7 for the case of a No. 5 bar, with significance discussed subsequently.

Table 4.5: $Xmech_{IS}$ estimation for the more conservative alternative (~21% strength loss)

Type of steel	Q_{corr} % per Grade fy value	$Xmech_{IS}$ mm
UNS S32304	10.50	0.43
UNS S31653	13.44	0.55

Table 4.6: $Xmech_{IS}$ estimation for the less conservative alternative (~66% strength loss)

Type of steel	Q_{corr} % per 32 ksi value	$Xmech_{IS}$ mm
UNS S32304	38.26	1.70
UNS S31653	39.52	1.76

4.1.6.2   Onset of brittle behavior

The second mechanical limit state type considered that at some level the loss of cross section resulted in marked loss of ductility of a stainless steel-reinforced element. This behavior, promoted in part by the development of multiaxial stress regimes in a constricted cross section, has been observed by various researchers.[62, 65, 87-93]

Almusallam[65] attempted to find the effect of corrosion on the mode of failure of the reinforcement bars. The author found that as the degree of corrosion increased, ductility measured as the elongation to fracture would decrease. The investigation indicated that after the corrosion degree exceeded 12%, the minimum elongation required by the ASTM A615[48] would not be fulfilled and a brittle behavior of the steel reinforcement would be expected.

Another investigation performed by Cairn et al. also considered the influence of corrosion on ductility of steel reinforcement. It was concluded that ductility was the most sensitive mechanical property to corrosion degree. The author suggested that heavily corroded steel reinforcement (degree of corrosion of ~8%) could present a ductility decrease of about 20%.[66]

The investigations performed by Almusallam[65] and Cairn et al.[66] concerned the effect of corrosion on the mechanical properties of plain steel reinforcement. Although they serve as a first approach to examining the influence of corrosion on the ductility of steel reinforcement, these do not consider the corrosion morphology characteristics of stainless steel. Moreover, even for similar corrosion morphology changes the ductility of austenitic stainless steel reinforcement could be quite different from those encountered in predominantly ferritic plain steel material.

The second phase of an investigation performed by Fernandez et al.[79] subjected specimens to cyclic loads using three stress ranges representative of common service loads (150 MPa, 200 MPa and 300 MPa). Thus, fatigue life reductions due to corrosion could be estimated. The specimens presented a similar range of corrosion degree between 8 and 28%. This study considered other factors associated with localized corrosion morphology that may cause stress concentration at the pit location, such as the influence of pit geometry. Although no strong correlations were found between the degree of corrosion and pit length or depth, it was suggested that the pit depth has a higher influence on fatigue life behavior than pit length. Furthermore, the effect of low degrees of corrosion in fatigue life are not very significant. Nevertheless, when high degrees of corrosion ($Q_{corr} > 8\%$) were observed, the fatigue life was severely decreased. Fernandez et al.[79] also concluded that premature failure was observed due to critical loss of ductility of the steel.

A similar conclusion was drawn from an investigation performed by Stewart.[67] This author concluded that although low corrosion degrees might still allow ductile yielding, higher corrosion degrees could result in brittle fracture.[67] This author estimated that the likelihood of failure of reinforced concrete assuming brittle reinforcement behavior was up to 450% higher than that of reinforced concrete assuming ductile behavior.[67] This suggests that failing to meet the required ductility criteria would significantly threaten the reliability of a structure. Stewart proposed two scenarios to study the effect of each phenomena in structural reliability, expressed as

    I.   Perfectly ductile parallel system, and
    II.   Perfectly brittle parallel system.

Additionally, pitting morphology was also considering by assuming a Gumbel distribution of the pits following a stochastic model. These scenarios served as reference to assess the transition from ductile to brittle behavior of the steel reinforcement. Stewart suggested that this transition was both spatial and time dependent.[67] Similar investigations[65, 66, 69] found corrosion degree values where ductility was reduced, detailed in Table 4.8.

Table 4.7: Experimental results on the influence of corrosion degree on ductility.

Author(s)	Q_{corr} %	Obs
Almusallam[65]	12.60	Brittle behavior
	20.00	complete loss of ductility
Palsson and Mirza[69]	15.00	33% reduction in ductility
	50.00	Highly brittle behavior
Cairn[66]	20.10	Brittle behavior

Based on Table 4.8, Stewart[67] proposed a corrosion degree limit (Q_{corr}) of 20% to characterize the failure behavior of the steel. Hence, when the corrosion degree was lower than 20%, a ductile behavior would be assumed. Otherwise, a brittle behavior would be expected.

The results of tests on plain steel specimens subjected to non-uniform corrosion obtained by Tang et al.[80] showed a stronger influence. They reported for plain steel that ductility values dropped exponentially when the loss of the cross-sectional area increased, an effect more critical than that of the loss of yield strength.

A similar conclusion was drawn by Wu Xun et al.[81] The degradation of elongation produced by corrosion seemed more prominent than the yield and ultimate strength. It was observed that the necking phenomenon progressively weakened suggesting that the ductility of the specimen decreased as the corrosion degree increased. Furthermore, when the corrosion degree reached a value of 8.6%, the elongation failed to meet the minimum criterion of 15%, specified by YB/T 4362-2014 (China). In the United States, ASTM A955 requires a minimum elongation/8-in of 20% for of stainless steel reinforcement grades 60 and 75.

The above information was used here for a tentative estimate of the degree of corrosion penetration required to reach an onset of brittle behavior ($Xmech_{OB}$). The treatment used earlier with Equation (22), (23), and (25) was applied to the case of a No. 5 bar, using as input the findings of the investigations listed in Table 4.8 as well as those form Wu Xun et al. The results are summarized in Table 4.9. While the results show a significantly lower corrosion amount to reach brittle behavior for SSs than for carbon steel, they are merely based on literature evidence for only one case of SS reinforcement. Thus, future experimental evidence will be needed to establish trends adequately.

It is noted that this limit state does not mean that mechanical failure of the rebar necessarily takes place as the limit state is reached. Rather, the state means that if mechanical load were to become excessive the fracture of the rebar could take place in a brittle manner. The resulting reduction in the amount of energy needed to propagate structural damage is the adverse consequence associated with this limit state.

Table 4.8: Tentative $Xmech_{OB}$ estimates from experimental findings from various sources.

Author(s)	Type of rebar	Q_{corr} %	$Xmech_{OB}$ mm
Almusallam[65]	Plain steel	12.60	0.52
		20.00	0.84
Palsson and Mirza[69]	Plain steel	15.00	0.62
		50.00	2.32
Cairn[66]	Plain steel	20.10	0.84
Wu Xun[81]	Stainless steel	8.60	0.35

It is furthermore noted that much of the embrittlement addressed above is related to geometric stress multiaxiality and intensity enhancement in the irregular geometry of corroded cross sections. Reductions in critical stress intensity from phenomena such as chloride-induced EAC can exist. For example, an investigation by Martin et al.[94] suggests that a 4 wt% addition of chloride could have a detrimental effect to the mechanical properties of austenitic stainless steel reinforcement, including a transition from ductile to brittle behavior. The literature review in Appendix C comments on this issue as well. Such mechanisms should merit careful consideration in follow up investigation.

4.1.6.3   Discussion on mechanical failure mechanism

In summary, the information available in the literature and the above analysis indicate that corrosion induced reduction in the cross-sectional area degrades the mechanical properties of the steel reinforcement in both plain carbon and stainless steel. Two mechanical properties, yield strength and ductility, were selected as the governing properties of loss of strength and brittle behavior, respectively. It was assumed for simplicity that corrosion was occurring uniformly around the circumference of the steel reinforcement. Corrosion penetration values that would compromise the structural reliability (Xmech) were then estimated and compared. In the ductile failure case, two relative yield strength loss criteria were selected representing high and low conservative alternatives.

The corrosion degree and $Xmech_{IS}$ results are plotted in Figure 4.9 and Figure 4.10. Results suggest that a value of 430 μm would be required to fail to meet the more conservative criterion. It is evident that about 3 times larger amounts of corrosion would be required to reach the less conservative service criterion compared with the more conservative alternative.
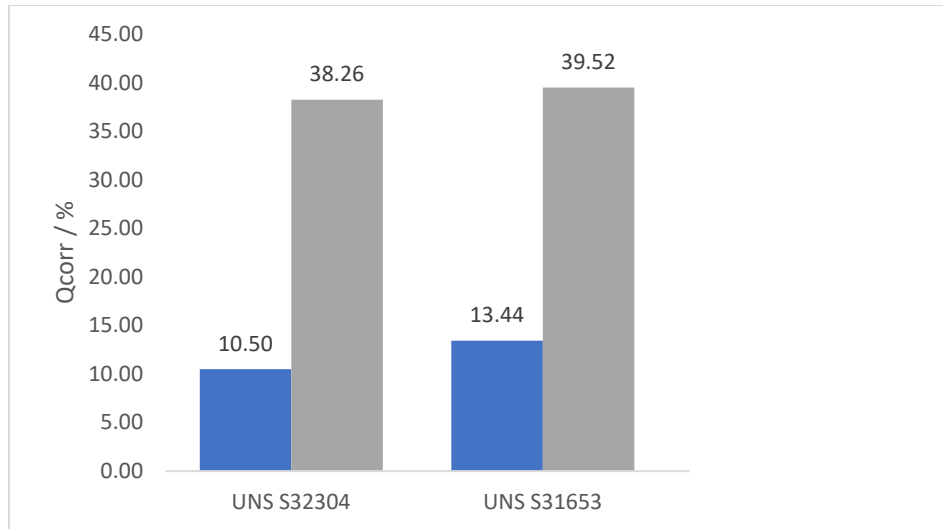
Figure 4.14: Comparison of corrosion degree to reach the IS limit state for the indicated percentage strength loss criteria. Each color illustrates a case of insufficient strength, in which blue represents ~21% strength loss and gray represents ~66% strength loss.
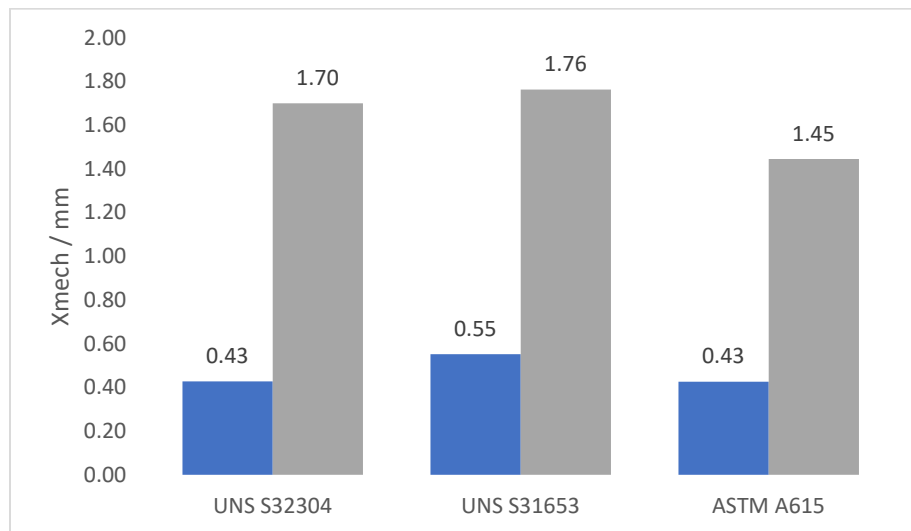
Figure 4.15: Comparison of corrosion penetration $Xmech_{IS}$ required to reach the IS limit state for the indicated percentage strength loss criteria. In the onset of brittleness case, a threshold corrosion degree value 8.6%[81] was selected given that it was the most critical and the only experimental value obtained for stainless steel. In this scenario, $Xmech_{OB}$ was estimated to be 350 μm. The $Xmech_{IS}$ and $Xmech_{OB}$ values are summarized in Table 4.10. Each color illustrates a case of insufficient strength, in which blue represents ~21% strength loss and gray represents ~66% strength loss.

Table 4.9: Summary of Xmech estimated in ductile and brittle behavior scenarios for No. 5 bars.

Xmech		Onset of brittle behavior cases
Insufficient strength cases		
μm ~21% reduction	μm ~66% reduction	μm
430	1700	350

Notably, the degree of corrosion projected in Table 4.10 to result in brittle behavior onset was reached earlier in the corrosion process than even the most conservative insufficient strength condition. While based on highly preliminary and limited information, this finding merits attention for possible implications in practice, given that building and structural codes specify minimum reinforcement ductility requirements. From a practical standpoint, the most conservative IS condition appears to be too moderate, so attention is directed to the least conservative value of X_{mechIS}. Consequently, in the following section the onset of brittle behavior will be assumed as the first mechanical manifestation of corrosion damage, with the less conservative insufficient strength condition being adopted and becoming the prevalent choice when the corrosion penetration reaches the IS condition.

Discussion on preliminary sound concrete limit state

The critical radius loss responsible for causing cracking of the concrete and/or mechanical failure are analyzed in this section. The models to estimate X_{CRIT} described in Section 3.3.5.2 are used to create preliminary predictions based on the corrosion morphology. The X_{CRIT} estimations were compared with the $Xmech_{IS}$ and $Xmech_{OB}$ to preliminarily forecast the expected limit state of a structural member. This indicates that for X_{CRIT} larger than the X_{mech} estimations, deterioration of mechanical properties of the steel reinforcement would occur prior to showing signs of cracking or spalling of the concrete. This can be expressed as

$(i)\ Xcrit < Xlim\ \longrightarrow Cracking\ or\ spalling\ of\ the\ concrete$

$(ii)\ Xcrit \geq Xmech_{OB}\ \longrightarrow Onset\ of\ steel\ reinforcement\ brittle\ behavior$

$(iii)\ Xcrit \geq Xmech_{IS} \longrightarrow Insufficient\ strength\ per\ the\ least\ conservative\ case.$

cases (i), (ii) and (iii) are shaded in green, yellow, and orange, respectively. The limit values in Table 4.10 will be used for the attributions here.

Various anode lengths and concrete cover values were used to simulate different scenarios representative of stainless steel in the practice. The models proposed by Torres-Acosta and Busba are expressed in Equation (15) and (16). These two models assume uniform corrosion across the length of the anode. A third model proposed by Darwin was used in which a more localized type of corrosion was considered through the inclusion of the terms A_f and L_f. It is described by Equation (19). Based on the findings by Niejenhuis et al.[35], Presuel et al.[45] and the present investigation, it was assumed that only half of the circumference was corroding.

1-inch, 2-inch and 3-inch cover was used to estimate X_{CRIT} as a function of the length of the anode shown in Table 4.11, Table 4.12 and Table 4.13, respectively. These tables present three shaded regions. The green shaded region represents the anode lengths where cracking of the concrete would be expected as the limit state (i). The yellow region represents the anode lengths where mechanical degradation due to onset of brittle behavior would be expected (ii) whereas the orange shaded region represents the anode lengths where mechanical failure of the bar due to insufficient strength would be expected (iii). Typical anode lengths for stainless steel were detailed in Section 4.1.1 and ranged between ~20 mm and ~50 mm.

Table 4.10: X_{CRIT} estimations with varying anode lengths for 1-inch cover based on empirical models.

Lanode	X_{CRIT} (15)	X_{CRIT} (16)	Lf	Af	X_{CRIT} (19)
mm	μm	μm	-	-	μm
50	40	33	0.139	0.069	37
40	47	37	0.111	0.056	43
30	61	44	0.083	0.042	51
20	92	60	0.056	0.028	65
10	223	115	0.028	0.014	102
7.5	342	158	0.021	0.010	124
5	657	257	0.014	0.007	163
2.5	2212	631	0.007	0.003	262
2	3333	855	0.006	0.003	305
1.5	5712	1273	0.004	0.002	372

*1-in cover, ~14-in long No. 5 bar.

It is emphasized that all values listed are nominal abstractions and that numeric precision of listings is given for consistency, but does not represent accuracy. Moreover, it is recognized that the depths of penetration in the more extreme cases correspond to degrees of corrosion projected beyond the limits of validity of the correlations used to develop the empirical equations cited. Indeed, in Tables 4.12 and 4.13 some projections exceed the radius of the rebar (as indicated by the entry > radius). Thus, instances where the projected value x_{CRIT} exceeds e.g ~1000 μm should be considered only as semi quantitative indications subject to refinement in future treatments.

Table 4.11 indicates that for structural members with 1-in cover or less, cracking of the concrete would be the predominant expected limit state. X_{CRIT} values for typical lengths of the anode do not exceed Xmech$_{OB}$ in any of the models. Results suggest that corrosion as localized as an anode length of only 7.5 mm of corrosion would steel result in concrete cracking before mechanical rebar degradation would dominate.

The increase of the concrete cover from 1 to 2 inches increased noticeably, as expected, the projected X_{CRIT} values in all models. Table 4.12 shows that for lengths of the anode greater than 30 mm, cracking of the concrete would be the expected limit state. Although this range includes some of the typical corroding lengths for stainless steel, the limit state would be uncertain for anode lengths ranging between 20 and 30 mm. The likelihood of mechanical failure occurring prior to cracking of the concrete is projected to increase when the anode length decreases to ~10 mm.

Table 4.11: X$_{CRIT}$ estimations with varying anode lengths for 2-inch cover, based on empirical models.

L$_{anode}$	X$_{CRIT}$ (15)	X$_{CRIT}$ (16)	L$_f$	A$_f$	X$_{CRIT}$ (19)
mm	μm	μm	-	-	μm
50	144	100	0.139	0.069	134
40	183	120	0.111	0.056	155
30	258	154	0.083	0.042	187
20	445	231	0.056	0.028	246
10	1313	514	0.028	0.014	396
7.5	2146	739	0.021	0.010	483
5	4424	1262	0.014	0.007	640
2.5	>radius	3289	0.007	0.003	1036

*2-in cover, ~14-in long No. 5 bar.

Similarly, Table 4.13 shows that cracking of the concrete would be the anticipated limit state for corroding lengths that exceed 50 mm. Although onset of brittleness would be expected as the dominant mode for corroding lengths ranging between 50 and 20 mm, it is unknown whether concrete cracking or mechanical failure would be the governing limit state. Results indicate that the range of corroding length values wherein the limit state is uncertain increased. This is also expected for larger concrete cover values.

It is worth restating that the limit states proposed in this section for all scenarios are based on simplified models to estimate critical loss of radius to cause either cracking of the concrete or mechanical failure. The models mentioned in Section 3.3.5.2 had been proposed based on information relevant for plain carbon steel reinforcement. Thus, further investigation is necessary to validate the applicability of the models in SS.

Table 4.12: X$_{CRIT}$ estimations with varying anode lengths for 3-inch cover, based on empirical models.

L$_{anode}$	X$_{CRIT}$ (15)	X$_{CRIT}$ (16)	L$_f$	A$_f$	X$_{CRIT}$ (19)
mm	μm	μm	-	-	μm
50	339	210	0.139	0.069	288
40	450	258	0.111	0.056	336
30	668	346	0.083	0.042	411
20	1233	545	0.056	0.028	544
10	3959	1292	0.028	0.014	882
7.5	6636	1893	0.021	0.010	1078
5	>radius	3298	0.014	0.007	1431
2.5	>radius	>radius	0.007	0.003	2323

*3-in cover, ~14-in long No. 5 bar.

The preliminary values proposed for the expected limit states are subject to change based on additional experimental evidence. In addition, the validity of the assumption of uniform corrosion around the steel circumference should be examined carefully given that experimental results suggest that this simplification may be inadequate for SS. Furthermore, the relationship between the decrease in yield strength and corrosion degree should be evaluated due to the scarcity of experimental data available for SS specimens.

4.2 Locally-deficient concrete

Corrosion in locally-deficient concrete whether it be a structural crack, or completely exposed rebar, or poor patch repair resulting in a locally porous region can influence the service life. Studies of corrosion of carbon steel in cracked concrete have provided information on the controlling variables regarding corrosion propagation. Corrosion is known to usually initiate at the base of a transverse crack that intersects the reinforcing steel and propagate laterally along the surface of the steel until a suitable macrocell forms limiting further lateral propagation. In predicting the corrosion damage evolution at locally deficient concrete regions, the parameters of interests are the length and perimeter length of the rebar that acts as the anode, the macrocell corrosion rates, and the fate of the corrosion products.

Prismatic concrete specimens reinforced with UNS S31653, UNS S32304 and ASTM A615 were prepared to determine the effect of the condition of the concrete in limit state formulations. Nine reinforced concrete specimens were prepared at the corrosion laboratory at the University of South Florida following the concrete mix procedure given by ASTM A955-A3.28. The specimens are further described in Section 3.3.

Deficiencies in the concrete were simulated by following a modified version of the ASTM A955 -A3 guidelines for the cracked beam test.[49]. Two embedded reference electrodes were placed near the steel surface, one close to the position of the concrete deficiency and the other near the end of the exposed portion of the rebar, shown in Figure 3.32. The difference in potential between the two electrodes sought to provide a better indication of local corrosion activity in the vicinity of the crack that may not be obvious in the total macrocell current. The exposure condition of the specimens followed a modified procedure of ASTM A955[49], further detailed in Section 3.4.3. Preliminary half-cell potential measurements and macrocell current density were performed on the concrete specimens as a function of time and steel reinforcing material, shown in Figure 4.16 (a) and (b), respectively. Moreover, preliminary EIS measurements were performed. The results show that corrosion in the carbon steel specimens initiated after approximately 60 days while the stainless steel specimens likely have remained passive.
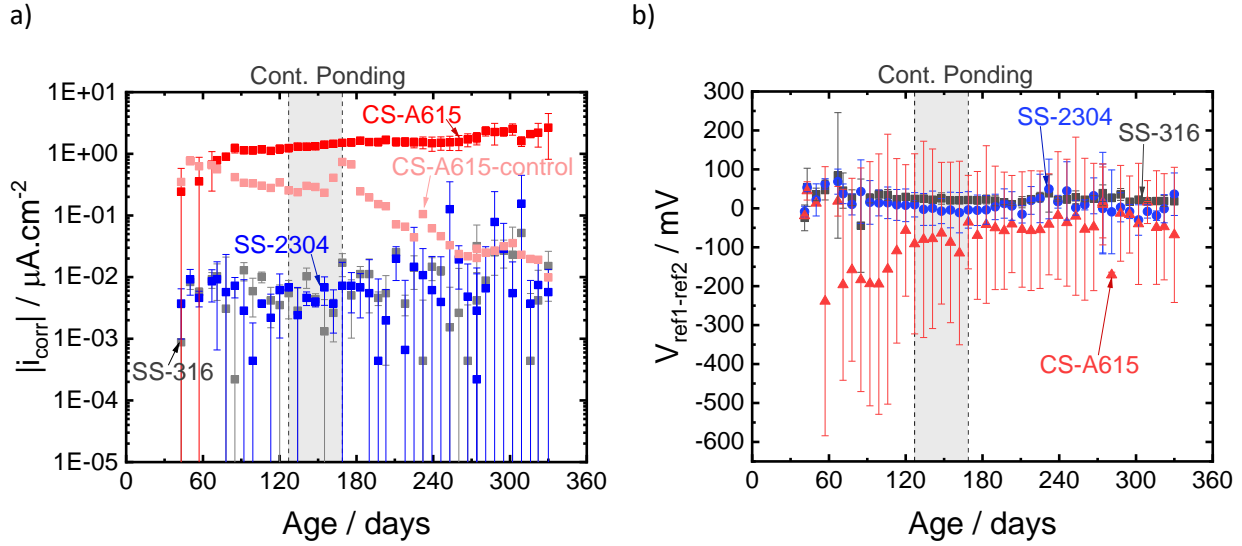
Figure 4.16: Preliminary results of specimens with concrete deficiencies (a) macrocell current density and (b) potential difference between defective and sound concrete region.

While the results to date suggest that corrosion of the stainless steel has not yet initiated, the expected limit state for locally deficient concrete may be deduced from literature evidence of the corrosion damage morphology in cracked concrete, and expected corrosion rates based on macrocell current simulations.

4.2.1   Corrosion morphology

In flexural cracks that are transverse to the steel, the stress distribution around the reinforcement results in slight bond failure and secondary cracks between the steel and the concrete in the vicinity of the crack. Wu Xun et al.[81] suggested that this region is what determines the size of the corroding region and is proportional to the width of the crack. The damage length as a function of crack width is shown in Figure 4.17 where a linear relationship is provided based on a fit to experimental data. This provides a means to estimate the anode length at locally deficient concrete. However, the experiment only included plain carbon steel and verification is required on its applicability to stainless steel reinforcement.

$$L_{\text{anode}} = 340 \times w_{\text{crack}} \qquad (26)$$

The existing literature on corrosion of stainless steel in cracked concrete is minimal but there are some results that describe the size of the corroding anode. Presuel[45] showed an anode length of ~8cm on 3Cr12 steel under a 1.5-mm crack. Hansson et al. reported extensively on the corrosion morphology within cracked concrete and their results are appended to the empirical model used to calculate the length of the anode for carbon steel shown in Figure 4.17. While the results have substantial scatter, generally the anode length is similar or less than those expected for carbon steel. However, and more interestingly, while the corrosion of carbon steel usually occupies the entire circumference of the reinforcement, stainless steel has been reported to only result in corrosion of a portion of the circumference of the reinforcement. According to Niejenhuis[35], only one third of the circumference corrodes while similar results were reported by Presuel.[45] This difference in corrosion morphology may have a substantial influence on the limit state.
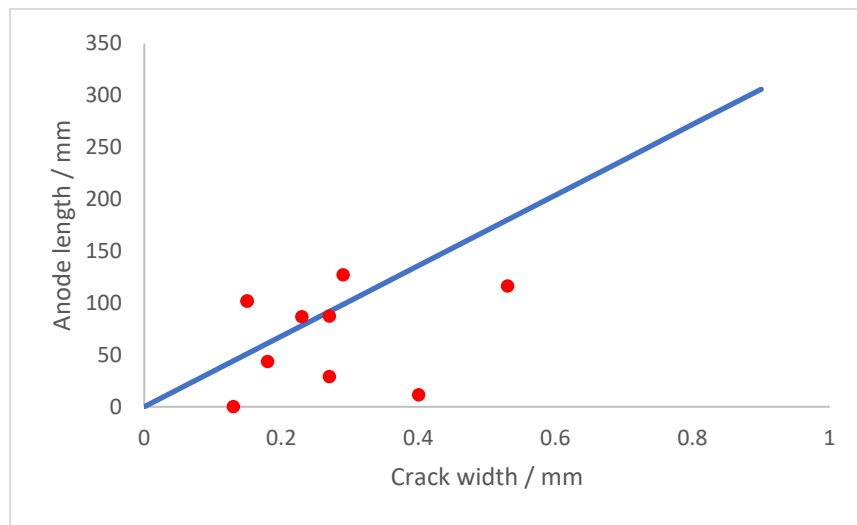
Figure 4.17: Anode length as a function of crack width. The line represents the empirical Equation (28) developed for CS. The points represent experimental results of SS taken from Niejenhuis.[35]

4.2.2 Corrosion rates

The corrosion rate of steel in concrete is often dependent on the rate of the cathodic reaction occurring on the steel surface surrounding corroding regions. The cathodic reaction is most often oxygen reduction and therefore the rate depends on the concentration of oxygen in the concrete and its diffusivity. The cathodic kinetics of stainless steel in solution simulating the concrete pore water have been studied by Cui and Sagues[27] for both pickled and sandblasted surfaces. Values of the Tafel constant and cathodic exchange current density were reported as 110 mV/dec and 5.8×10^{-7} $\mu A/cm^2$ respectively. Comparing this to typical values of CS reinforcement (190 mV/dec, 6.4×10^{-4} $\mu A/cm^2$), it is clear that oxygen reduction is much slower on passive stainless steel than it is on CS.

A finite element model was developed to calculate the expected macrocell current in cracked concrete considering the differences in corrosion morphology and cathodic kinetics between carbon steel and stainless steel. A reinforced concrete beam with one longitudinal steel bar with one surface exposed to the atmosphere with a ~three-inch concrete cover was considered. The length of the anode was set to 68 mm corresponding with a crack width of 0.2 mm. For the carbon steel calculation, the entire circumference of the steel was set as the anode while only half of it was set as the anode for stainless steel. It was assumed that anodic kinetics were the same for carbon and stainless steel.
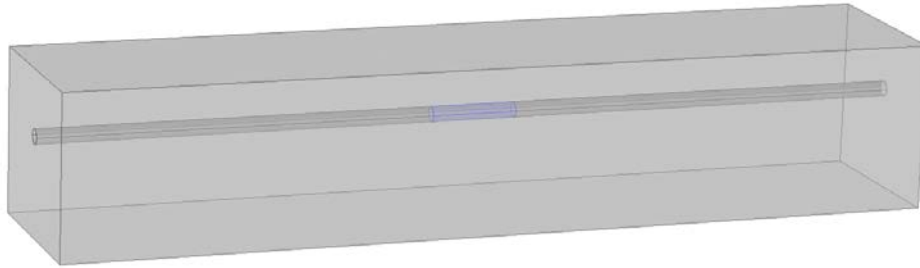
Figure 4.18: Finite element model geometry showing locally corroding anode of length 688 mm corresponding to a crack width of 0.2 mm.
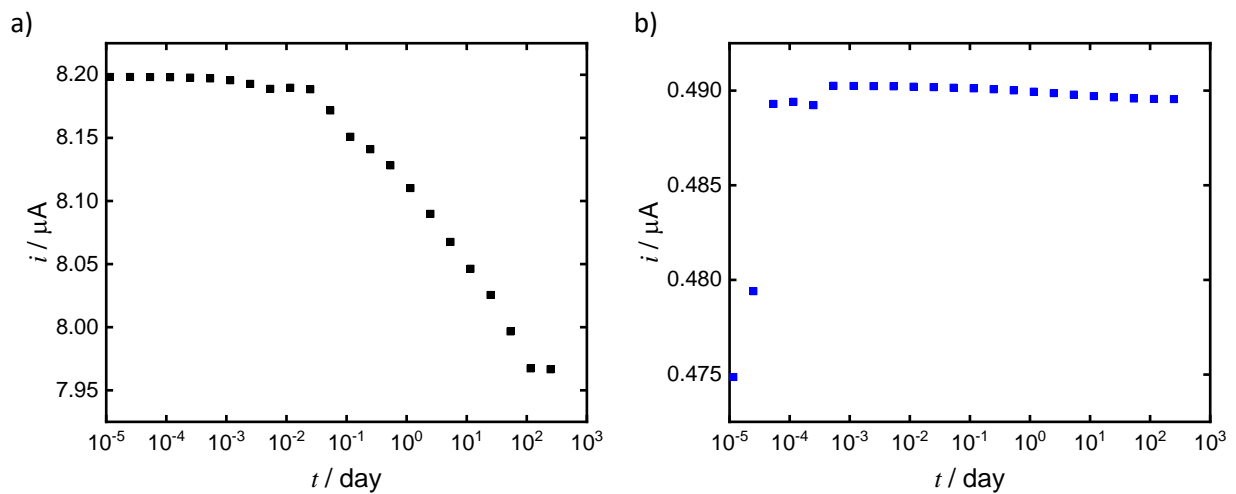
Figure 4.19. Macrocell corrosion rates as a function of time in cracked concrete: (a) CS and (b) SS.

The macrocell corrosion rates for CS and SS are shown in Figure 4.19. As expected, and likely due to the greater cathodic efficiency of CS, the macrocell corrosion rates for SS are much lower. The significance of this is that the corrosion products potentially have much more time to diffuse away from the concrete and steel interface and therefore alleviate the stresses that may buildup and cause further concrete cover damage.

4.2.3 Discussion on preliminary locally-deficient concrete limit state

Similar to the methodology presented for sound concrete, the limit state for locally-deficient concrete will depend on the criteria presented in section 4.1.6. The same limits will be used for mechanical failure modes, but an estimate of the corrosion required for additional concrete damage is required. Currently, there does not seem to be a model that can be used to assess this value for locally damaged or cracked concrete. For that reason, a simple model has been developed to try to formulate reasonable estimates based on the corrosion morphology, and the degree of pre-existing concrete damage.

The model takes in as an input a preexisting damage volume which describes the space available for corrosion products to occupy prior to inducing stress to the concrete cover. It has been shown that corrosion induced stresses may develop prior to filing up the adjacent pore space. However, since the model does not account for corrosion product washout, a critical fill fraction is not used. It is assumed that once the damage volume has been filled, the amount of corrosion required to cause further damage is the value for sound concrete. Therefore, the critical damage amount for a concrete damage limit state in cracked concrete may be expressed as

$$X_{crit,crack} = \frac{V_{PD}}{F_{ex}A_{corr}} + X_{crit,sound} \qquad (27)$$

where V_{PD} represents the preexisting damage volume, F_{ex} represents the volume expansion factor of the corrosion products, and A_{corr} represents the surface area of steel corrosion.

As an example, the corrosion required for further concrete damage was calculated for a pre-existing damage volume of 0.5 cm^3 corresponding to 0.2 mm gradient thick space surrounding the rebar in concrete with a 0.2 mm wide crack. The volume expansion factor was assumed to be 3 for both CS and SS. The corroding area for CS was 25.6 cm^3 and 12.8 cm^3 for SS. The X_{CRIT} for sound concrete was calculated as 317 μm. According to Equation (27) and the values presented here, the corrosion required to cause further concrete damage is 1.2 $X_{CRIT,sound}$ for CS and 1.4 $X_{CRIT,sound}$ for SS. Based on these results and those of the macrocell corrosion rate model, it is more likely that corrosion of SS in locally deficient concrete will result in mechanical failure than it is for CS. The current analysis would not be able to provide a confident conclusion as to the appropriate limit state of SS in locally deficient concrete without more experimental evidence. However, the formulation presented may be used as an initial model to describe the corrosion required for additional corrosion induced concrete damage in locally deficient concrete. The model may be modified to account for corrosion product washout and the rate of corrosion product diffusion.

5 Feasibility of corrosion detection

In theory, with the formation of an anode due to the local breakdown of the passive film results in a drop of the open circuit potential at that location, as discussed in Section 2.1.3. Although this has been proven for the case for plain steel, differences in corrosion behavior in the more corrosion-resistant alloys may limit the applicability of the half-cell potential technique to stainless steel reinforcement. Recent investigations suggest that corrosion of stainless steel reinforcement in sound concrete is not only longitudinally limited by the length of the anode but also circumferentially limited around the steel bar (see Section 4.1.1). Experimental results from this investigation and abstracted from the literature suggests that the portion of the circumference subjected to corrosion may be ~1/2 and ~1/3 by investigations performed by Presuel[45] and Niejenhuis[35], respectively (see Section 4.1.1).[35, 45] Furthermore, Presuel[45] suggested that corrosion occurs preferentially in the portion of the steel facing the concrete cover surface.

A traditional NDT that has been widely used to detect the corrosion condition in steel reinforcement is half-cell potential (HCP) mapping. The half-cell potential method (per ASTM C876[39] guidelines) provides potential ranges associated with different probabilities of corrosion serving as a reference to identify areas of high corrosion risk. Table 3.7 presents the HCP ranges, in reference to a Copper-copper Sulfate Electrode (CSE) and a Saturated Calomel Electrode (SCE), suggested by ASTM C876.[39] A similar specification was proposed by RILEM[95], technical committee on Electrochemical techniques for Measuring Corrosion of steel in concrete, 154 EMC. The RILEM technical recommendation on HCP, applicable to structures with ordinary or stainless steel reinforcement, provides typical active corrosion potential ranges of normal steel reinforcement. According to the authors, stainless steel and carbon steel exhibit similar passive potentials.[95]

It is important to note that HCP values are strongly influenced by the resistivity of the concrete, as an indication of the saturation condition, and the concrete cover (X_c).[95] The macrocell current that is formed due to action of the anode polarizing the passive regions yields a drop in potential that is easily detected in concretes with a low resistivity. Nevertheless, as the resistivity of the concrete increases, the electrical conductivity and macrocell current decrease, making it more difficult to detect corroding regions. Similarly, the HCP drops are more evident at the steel surface. Therefore, as greater concrete cover values are considered, the more challenging it is to detect corrosion locations. The effect of these parameters on the reliability of the HCP technique is further exacerbated when highly localized corrosion is analyzed.

Several investigations have found that HCP results may provide reasonable correlations for passive and active corrosion regions of stainless steel reinforcement in concrete. A previous investigation studied the corrosion performance at Progreso Pier, the oldest major structure reinforced with SS.[30] Field measurements showed highly negative (as much as ~-550 mV CSE) suggesting active corrosion at particular regions. In addition, a recent investigation compared half-cell potential and LPR results for different types of stainless steel reinforcement. This recent study included 2-year field-exposure experiments of ~11 mm diameter SS rebars embedded in mortar with very low cover (~7mm) as well as bare bars, to a high-tide marine environment. After the two-year exposure period, the SS specimens exhibited potential values ranging between -100 mV and -200 mV which correlated to low corrosion current densities estimated with the LPR technique.[34] Although these HCP values have not been correlated directly to corrosion severity, they provide some indication of the range of potentials that may be expected for SS reinforced concrete in field service.

Another investigation by Gonzalez et. al.[96] found that although the HCP should not be rejected, its results should be treated with high reservation. The authors found that the ASTM C876 criteria was in theory correct to detect actively corroding regions, nevertheless, it ignores the possible presence of short-circuited passive and active areas.[96] The latter could lead to severe misinterpretation when identifying active and passive regions in steel reinforcement. This issue could become more challenging when considering highly localized corrosion. A similar conclusion was drawn by a subsequent investigation performed in cracked concrete by Niejenhuis8 which questioned the applicability of the ASTM C876 in stainless steel reinforcement. The disagreement between authors and scarce available literature on SS reinforcement suggest that further investigation would be required to determine the correlation between the recommended half-cell potential ranges for each corrosion probability category per ASTM and similar guidelines.[39, 97]

Other NTDs, such as electrochemical impedance spectroscopy (EIS), have been proposed to assess corrosion conditions in SS. The literature review indicated that the reliability of EIS is expected to be higher when compared to the HCP technique (see Section 2.1.3). While the HCP technique is limited to identifying the risk of corrosion at a certain location, EIS measurements may also be used to obtain information regarding the electrochemical state of steel in reinforced concrete. Wenger[98] developed a model that allowed estimating the charge transfer resistance from the EIS data which could be later used to obtain corrosion rate estimations. A subsequent investigation by Wenger[99] (1990) validated the model conclusion with experimental results from large reinforced concrete specimens and a small counter-electrode. A spatial distribution of the electrochemical impedance was obtained. When local corrosion was considered, it was found that the EIS enabled the detection and location of corrosion, as well as quantitative data from ongoing corrosion mechanisms in the area of interest.[99] Corrosion currents densities were estimated to range between 3 μA.cm^{-2} and 7 μA.cm^{-2} along an area of 25 cm^2. These values were correlated to the electrical conductivity of the concrete and the inverse of the charge transfer resistance.[99] One limitation that is important to note is that the method is based on a predetermined corroding area, however, this parameter is rarely known. Thus, the difficulty of obtaining accurate local corrosion current estimates should be considered. In addition, the detection of localized corrosion with the EIS technique could be limited by small values of the concrete resistivity, as well as, increased distance between the probe and the corroding region.

A finite difference model was successfully developed to analyze the d-c polarization phenomenon of reinforcing bars with a high localized corrosion degree.[100] It was suggested that the increased anode to cathode ratio resulted in smaller excitation currents than those of uniform electrodes. The a-c signal distribution was also considered. The authors concluded that methods used for uniform corrosion should be carefully considered in localized corrosion scenarios. It was also concluded that the electrochemical response was limited by the position of the reference electrode.[100]

The RILEM technical committee 154 EMC developed a set of specifications to obtain on-site corrosion rate measurements of steel reinforcement in concrete by means of the polarization resistance method. Although the EIS technique is not in the scope of the specification, it is suggested that the polarization resistance can be also obtained with this technique.[60] Similar criteria were developed to evaluate corrosion rates in which values higher than 10 µm.yr^{-1} could be associated with high corrosion levels. Likewise, corrosion for values smaller than 1 µm. yr^{-1} were suggested as negligible.[60] When the corrosion is limited to a small area, the authors suggested that the error could be minimized by either restricting the polarized area or identifying the corroding area.[60] While the first solution could be implemented by using a guard ring to confine the current, the second one is often challenging since there is no accurate way to predict that parameter in real-size structures.

The present chapter includes a set of experiments and computational simulations to assess the reliability of traditional NDTs used to detect corrosion in stainless steel. Two sets of specimens, simulated concrete beams and mortar cylinders, reinforced with stainless and plain carbon steel are used to monitor and compare traditional corrosion detection methods. Given the increased chloride threshold of stainless steel,[45] chlorides were admixed to the concrete in the mid-region of the simulated beams and the mortar of the cylindrical specimens. A finite element model (FEM) is developed to analyze the detection limits of HCP and EIS technique considering different scenarios including several lengths of the anode and concrete cover, in addition to different corrosion morphology conditions. This analysis is expected to provide valuable information regarding existing NDTs specifications as well as recommendations to improve the reliability of these techniques to monitor the onset and intensity of corrosion in stainless steel reinforcement.

5.1   Laboratory exposure

Two sets of concrete specimens reinforced with UNS S41000 SS and AISI1018 CS were prepared to study the corrosion behavior of stainless steel compared to that of CS, and to determine whether corrosion of stainless steel in concrete could be detected by methods traditionally used for carbon steel reinforcement. The plain-chromium SS alloy has only moderate pitting resistance. This type of SS reinforcement was selected to be able to induce in the experiments an actively corroding regime without resorting to impressed potential polarization Concrete specimens were made in triplicate per type of reinforcing steel for each set. The experimental setup of each set of specimens is further described in Section 3.1 and 3.2.

Figure 5.1(a) shows HCP values as a function of location for three CS specimens at an age of ~200 days. A significant drop in the HCP is evidenced in the region with admixed chlorides (lower bound values of ~-600 mV vs SCE). Figure 5.1(b) shows the potential results of the three beams reinforced with SS at an age of 500 days. While SS01 and SS03 show similar potential values, SS02 shows a significant drop (reaching values of ~-450 mV vs SCE) when compared to the other SS specimens. All three SS specimens show a similar pattern throughout the length of the specimen with a very small variation in the HCP results where the macrocell action is barely evidenced. The half-cell potential distribution throughout the length of the plain steel specimens exhibits a very different behavior suggesting that the macrocell activity may be greater when compared to that of SS reinforcement.
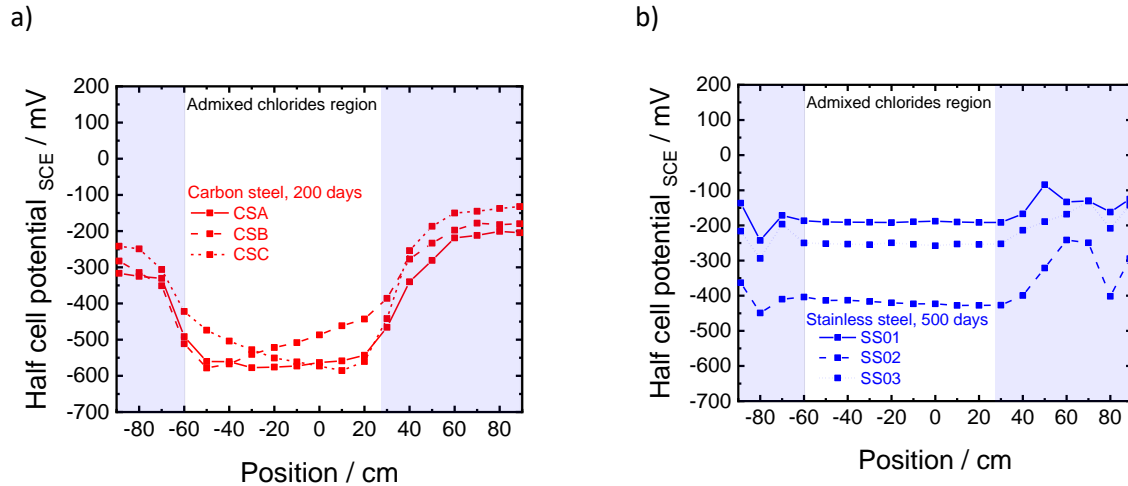
Figure 5.1: HCP results of specimens as a function of location in simulated beam specimens reinforced with (a) carbon steel at 200 days, and (b) stainless steel at 500 days (after ~250 days of aggressive ponding and ~120 days of heating).

The potential variation in the chloride-contaminated and chloride-free regions are shown in Figure 5.2(a) and Figure 5.2(b) over time for carbon steel and stainless steel reinforcement, respectively. These results are compared with the values obtained for the cylinders with the same type of steel reinforcement. In the case of carbon steel, all specimens presented potentials within the range of high corrosion risk as shown in Figure 5.2(a). HCP results were presented as the mean and standard deviation of the three CS replicate specimens for ~300 days. At this time, cracking of the concrete was observed in two of the specimens and were terminated. Beyond this time, measurements were obtained for only one CS specimen. A significant difference between the potential values between the chloride-contaminated and chloride-free region was initially observed, however, this difference seemed to decrease over time. The HCP results at the end location of the beam (without admixed chlorides) increased until stabilizing at a more positive potential within the low risk of corrosion and uncertain region. Contrarily, the mid-point of the CS beams has shown potentials within the high risk of corrosion region for most of the exposure period. The cylinders were found to exhibit less negative potential values than those of the beams, shown in Figure 5.2(a). This could be attributed to the minimization of macrocell action in the cylinders.

In the case of stainless steel, the potential difference between the chloride-contaminated and chloride-free region was considerably small during the first 50 days, after which the magnitude of the potential difference then increased to ~200 mV as shown in Figure 5.2(b). This difference started to decrease at an age of ~400 days after which values from both regions decreased, showing lower bounds of ~-425 mV. This value is still more positive than the lower bound of active CS beams. The cylindrical specimens exhibited a potential drop at an approximate age of 100 days wherein the lower bound of potential values was about 550 mV while approaching a steady state of ~-450 mV. In contrast, Figure 5.2(b) reveals that only one of the SS beams has shown a significant drop in HCP in which values more negative than -400 mV (high risk of corrosion per ASTM C876[39] specifications) were reached at an age of ~500 days. This could suggest that the potential values of the SS beams are more so indicative of microcell action.
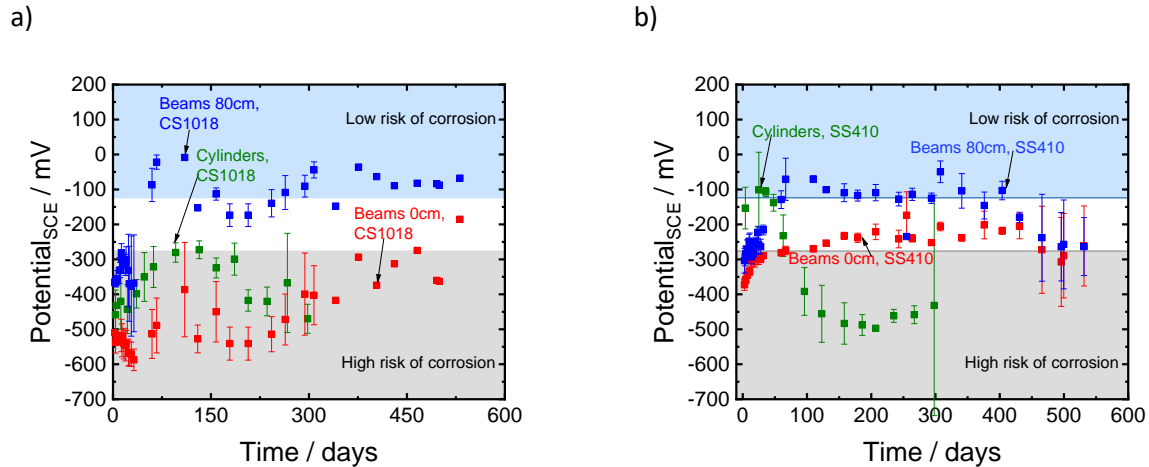
Figure 5.2: HCP results of specimens as a function of time considering different locations (i.e. end and center) in simulated beams compared to those of the cylindrical specimens reinforced with (a) carbon steel and (b) stainless steel.

Estimates of the corresponding corrosion rates were previously reported in Section 4.1.3. As stated earlier, EIS measurements may yield significantly underestimated values of corrosion rates when measured on large specimens without a current confinement method.

The relationship between the corrosion current density and potential measurements is shown in Figure 5.3. Figure 5.3(a) illustrates this relationship for cylindrical specimens reinforced with CS and SS. It can be observed that CS specimens have presented HCP values less than ~-300 mV throughout the duration of the experiment. Moreover, higher corrosion current densities have been observed in CS specimens. On the other hand, SS specimens have presented a wider range of potentials over time. The data acquired for SS cylinders present a clear trend in which the potential shows a logarithmic relation to the current density. Thus, as the potentials become more negative, the corrosion rates seem to increase exponentially likely indicative of cathodic control. This trend is not observed for the cylinders reinforced with CS probably due to the lack of data at more positive potentials. It is also important to note that highly negative potentials observed in the cylinders reinforced with SS may reflect less severe corrosion than those reinforced with CS. Hence, modification of HCP standards such as the ASTM C876[39] may be required to account for less corrosion activity at similar potentials to that of CS. These results require further confirmation from future autopsy of the specimens, as well as model simulations.

Figure 5.3(b) shows the corrosion current density and potential measurements of the beams. The results are shown until the CS and SS beams reached an age of ~200 days and ~560 days, respectively. Results of the CS beams show a similar trend to that of the CS cylinders shown HCP results ranging between ~-200 mV and ~-600mV. In comparison, it took about 465 days for one of the SS beams to reach a steady value at the high corrosion risk region as shown in Figure 5.1(b). The potential drop in the SS specimen could be indicative of localized corrosion; nonetheless, it may not be shown due to the sensitivity of the method.

Figure 5.3(b) shows that the relationship between the potential and current density is not as evident when compared to the cylinders. Thus, it is not clear whether this specimen is under cathodic control or not. In theory, the corrosion current density of the beams should be greater than that of the cylinders due to the possible influence of macrocell action; thus, the corrosion rates of the beams should present greater values as well. Nevertheless, there is uncertainty in the calculation of the corrosion rates associated with the analysis of the EIS response, which could be causing unusual results. Figure 5.3(a) and Figure 5.3(b) present an indication of the possibly lesser uncertainty the measurements obtained on the cylinders when compared to that of the beams. It is expected that the added action of the macrocell and microcell of the beams should be more than the microcell corrosion occurring in the cylinders. In practice, however, the corrosion current densities estimated for beam SS02 are still considerably lesser than those of the cylinders reinforced with SS, which may be due to the lack of current confinement in the measurement resulting in a surface averaged impedance that may include a significant portion of passive regions.

a)   b)
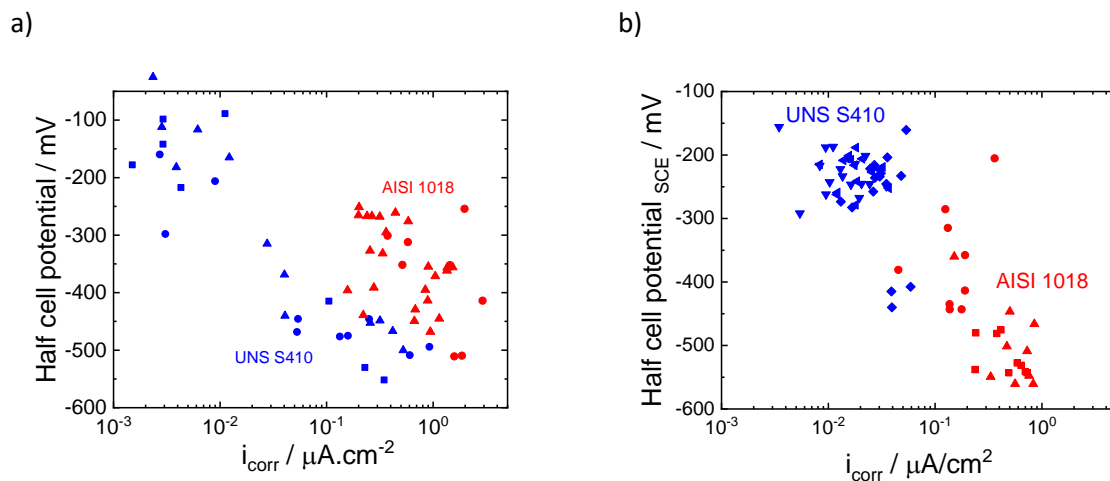
Figure 5.3: Potential as a function of corrosion current density for (a) cylindrical specimens and (b) midpoint of simulated beam with the highest potential drop.

Overall, the experimental results suggest that there may be added uncertainty in corrosion detection using HCP and EIS when SS reinforcement is used. The HCP values obtained for the CS beam specimens within the chloride-contaminated region were slightly more negative to the values of the chloride-contaminated cylinders, likely indicative of the added macrocell action in the beams. The corresponding corrosion rates estimated by EIS measurements suggested active corrosion as determined by the RILEM[97] designations and therefore agree with the ASTM C876 HCP[39] designations of high corrosion risk. Conversely, when the HCP values for the SS beams dropped to values assumed to be indicative of a high risk of corrosion, the associated corrosion rates estimated from the EIS measurements were within the negligible corrosion range. However, when the HCP of the SS reinforced cylinders indicated a high risk of corrosion, the associated corrosion rates indicated active corrosion. While the results presented here cannot be used to suggest quantifiable changes to the existing standards without further testing and specimen autopsy, they do indicate that a change is required. The next section present finite element model simulation of HCP and EIS to uncover the influence of cathodic kinetics and corrosion morphology on corrosion detection.

5.2   Computational simulations

Two sets of finite element models were developed to simulate the HCP and impedance measurements in an attempt to assess the sensitivity of each method when considering highly localized corrosion detection, and to develop a more reliable estimation of the corrosion rate. A location in the midpoint on the top surface of the specimen was selected to take HCP and EIS measurements in the FEM simulations.

The mesh used in the model is comprised of free tetrahedral elements that diminish in size at the electrode boundaries. This was done to account for the large variation in potential in this region (i.e., near the intersections between active and passive regions of the steel reinforcement). An illustration of the model geometry for the HCP and EIS model are shown in Figure 5.4(a) and Figure 5.4(b), respectively. Laplace's equation was solved using a three-dimensional finite element simulation software, COMSOL Multiphysics 5.3. The parameters used in the HCP and EIS simulations are presented in Table 5.1. The values used in these models were abstracted from previous investigations in which stainless steel and plain carbon steel were compared.[27, 101]

Table 5.1: Finite element model parameters - HCP and EIS.

Model Parameters							
HCP					EIS		
Stainless steel		Plain steel					
β_a	60	mV/dec	60	mV/dec	R_p	3012.2	$\Omega.cm^2$
β_c	-110	mV/dec	-160	mV/dec	R_{pc}	6.0244	$\Omega.cm^2$
E_{0a}	780	mV	780	mV	C	0.1	$F.m^{-2}$
E_{0c}	-160	mV	-160	mV	$\tilde{v}$	10	mV
i_{0a}	1.80×10^{-04}	$A.cm^{-2}$	1.80×10^{-04}	$A.cm^{-2}$	freq	100 kHz - 1 mHz	
i_{0c}	5.80×10^{-09}	$A.cm^{-2}$	6.00×10^{-06}	$A.cm^{-2}$			
i_L	1.16×10^{-04}	$A.cm^{-2}$	1.16×10^{-04}	$A.cm^{-2}$			
D_{O2}	1.00×10^{-09}	$m^2.s^{-1}$	1.00×10^{-09}	$m^2.s^{-1}$			
C_0	0.3	$mol.m^{-3}$	0.3	$mol.m^{-3}$			
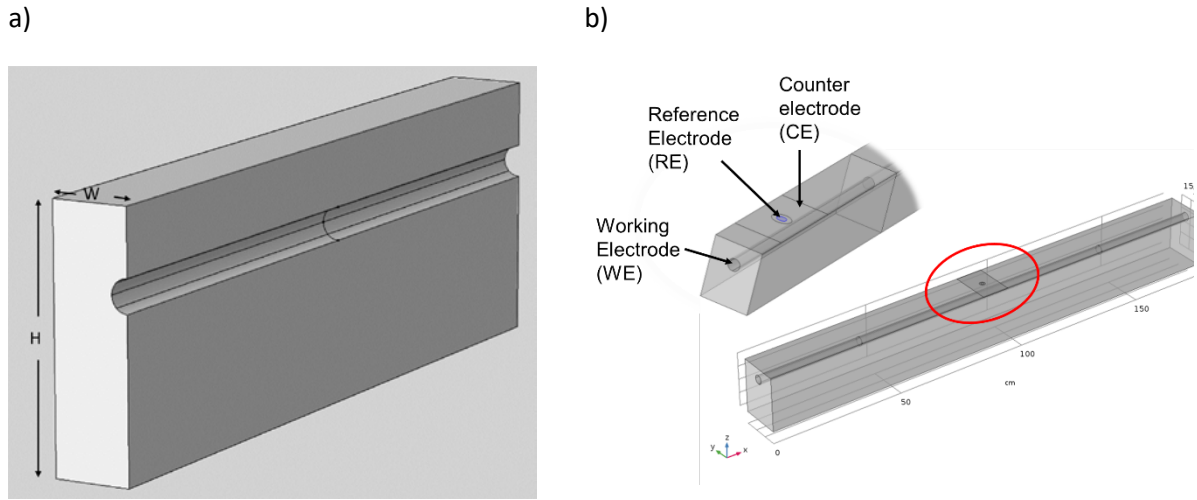
Figure 5.4: Schematic illustration of (a) HCP and (b) EIS Finite Element Model simulations.

5.2.1 HCP

A three-dimensional beam section was modeled with one steel reinforcement bar. The steel rebar located along the longitudinal axis of the section with a cover of 5.08 cm and a 1.27 cm (0.5 in) diameter. The length, width and height of the beam model was 120 cm, 12 cm, and 20 cm, respectively. Given the symmetry of the specimen, the finite element model considered a quarter of the element (H=20 cm, W=6 cm and L=60 cm), shown in Figure 5.4(a). The concrete was modeled as a homogeneous material with an electrical conductivity of 0.008 S.m^{-1}. Active and passive regions were designated by including a variable for the length of the anode. The influence of the corrosion morphology was also considered by limiting the actively corroding region of the steel to half and a quarter of the circumference throughout a given length of the anode.

The computational model was set to solve for two main equations for the potential throughout the electrolyte and the concentration distribution of oxygen, provided a set of boundary conditions. The potential distribution throughout the electrolyte was governed by Laplace's equation,

$$\nabla^2 V = 0,$$ (28)

Two current densities were designated for the anodic and cathodic regions of the steel, i_a and i_c, expressed as

$$i_a = i_{oa} \exp\left(2.303 \frac{E_{0a} - V}{\beta_a} \right)$$ (29)

where i$_{oa}$ is the anodic exchange current density (A/m^2), E$_{0a}$ is the anodic equilibrium potential (V) and β$_a$ is the anodic Tafel slope (V).

101

$$i_c = -i_{oc} \frac{C_{O2}}{C_O} \exp\left(2.303 \frac{E_{0c} - V}{\beta_c} \right)$$ (30)

where i_{oc} is the cathodic exchange current density (A/m^2), C_{O2} is the concentration at the rebar surface, C_O is the concentration of oxygen at the concrete surface (i.e. in direct contact with air), E_{0c} is the cathodic equilibrium potential and β_c is the cathodic Tafel slope (V/dec).

The values of the parameters in this equation for stainless steel and plain carbon steel were based on a previous investigation performed by Cui and Sagüés, and Xu et. al., respectively.[27, 101] The parameters are summarized in Table 5.1.

Equation (28) was solved by considering the boundary conditions expressed in Equation (31) and (34) wherein the current density at the corroding region due to the macrocell action may be expressed as

$$i_a + i_c$$ (31)

and the current density at the passive region was set according to Equation (30). In this way, the macrocell current and the microcell corrosion current may be evaluated.

The concentration distribution of oxygen was governed by

$$\nabla^2 C_{O2} = 0.$$ (32)

At the metal surface, the flux of oxygen was estimated as

$$N_{O2} = -\frac{i_c}{4F}.$$ (33)

Assuming aerated conditions, the oxygen concentration was given a value of $C_{O2}=0.3$ mol.m^{-3} at the exposed surface above the reinforcement. This parameter was expressed as an effective value, equivalent to that of water in local equilibrium with concrete.

5.2.2 EIS

A three-dimensional, 178 cm (~5 ft 10 in) long beam section was modeled with one steel reinforcement bar simulating the geometry of the experimental beams. The width and height of the section was 15 cm (~6 in) and 20 cm (~8 in), respectively. An electrical conductivity value of ~0.016 S.m^{-1} was assigned based on experimental results obtained from region without admixed chlorides of the beams. The steel rebar located along the longitudinal axis of the section was 3.22 cm (1.27 in) diameter. Active and passive regions were designated by including a variable for the length of the anode ranging between 1 cm and 100 cm with a logarithmic variation of three steps per decade. The influence of the corrosion morphology was also considered by limiting the actively corroding region of the steel to half and a quarter of the circumference throughout a given length of the anode. In addition, to account for the effect of the concrete cover, simulations were performed for a range of concrete cover values ranging between 2.5 cm (1 in) and 12.5 cm (5 in).

The potential distribution throughout the electrolyte was governed by Laplace's equation for the oscillating potential,

$$\nabla^2 \tilde{\phi} = 0,$$ (34)

For EIS simulations, the steel surface boundary conditions were set as an alternating current expressed as

$$\tilde{i} = j\omega C(\tilde{V} - \tilde{\phi}_0) + \frac{1}{R_p}(\tilde{V} - \tilde{\phi}_0)$$ (35)

where $\tilde{i}$ is the oscillating current density per unit area (A.cm^{-2}), j represents the imaginary portion of the equation, ω is the angular frequency (s^{-1}), R_p is the polarization impedance (Ω), $\tilde{V}$ is amplitude of the potential perturbation and $\tilde{\phi}_0$ within the simulated concrete adjacent to the surface of the boundary. A counter-electrode, modeled as a rectangular region placed on the top surface, was set as the ground electrode. A circular region cutout at the center of the counter-electrode represented the reference electrode.

Two normal current densities were used to represent the passive and the corroding regions of steel, thus, two variations of Equation (35) were proposed (i.e. one for each region). Based on experimental results of the cylindrical specimens, the passive and active regions were expected to present corrosion rates of 5 µm.yr^{-1} and 0.01 µm.yr^{-1}, respectively. The corrosion rates were used to estimate the R_p value of each region assuming that the interfacial capacitance was the same. The impedance was calculated as the potential $\tilde{V}$ divided by the current at the counter-electrode boundary for frequencies ranging from 100 kHz to 10 mHz taking the potential at the CE as zero. The steel reinforcement is expressed as a cylinder placed along the longitudinal axis of the beam. The impedance data obtained from this simulation was analyzed in the same manner as the experimental results obtained for the beams and cylindrical specimens allowing the comparison between corrosion rates from experimental data and computational simulations.

5.2.3   Simulations Results

The effect of corrosion morphology of SS on the reliability of the HCP and EIS was evaluated. Three values of the length of the anode were selected to represent different degrees of localized corrosion (anode to cathode ratios ranging from ~0.01 to ~1). In addition, three different scenarios of corrosion extent around the circumference were considered in which the steel would corrode uniformly or partially throughout the length of the anode. To account for this, a parameter Θanode was introduced to represent the portion of the circumference in the anodic region subjected to corrosion. Three scenarios in which corrosion around the full, half or a quarter of the circumference (i.e. Θanode=2π, Θanode=π and Θanode=π/2), was considered. The corroding region was preferentially placed facing the exposed concrete surface which is in agreement with the characteristic corrosion morphology of SS abstracted from the literature.[35, 102]

To further comprehend the HCP experimental results and assess the detection limits of the technique for SS reinforcement, a model simulation was developed using the dimensions shown in Figure 3.3. The HCP simulation results and sensitivity of the technique were plotted as functions of the anode to cathode ratio in Figure 5.5(a) and Figure 5.5(b), respectively. Figure 5.5(a) illustrates the expected HCP values for varying anode to cathode ratios for different fractions of the circumference corrosion. In the case of SS, the highest expected degree of localized corrosion was selected for this analysis with a corroding surface of a quarter of the perimeter of the circumference (i.e. Θanode=π/2) while the full circumference was assumed to be corroding in the case of CS (i.e. Θanode=2π). Both types of steel show an increase in the HCP for smaller anode to cathode ratios. Nevertheless, the difference between the HCP of SS and CS becomes more marked as the anode to cathode ratio increases.

The sensitivity of the HCP method for SS and CS reinforcement was evaluated for different anode diameters and fraction of the circumference values as shown in Figure 5.5(b). The sensitivity was calculated as the percent difference between the potential calculated directly above the center of the anode and the potential at the end of beam above the cathodic region of the steel surface. Differentiated patterns between SS and CS are observed which could be attributed to the difference in the cathodic kinetics between the two types of steel reinforcement wherein the cathodic exchange current density is expected to be smaller than that of CS.[103] The sensitivity of the HCP technique in CS shows an approximately linear relationship in which it decreases as the anode to cathode ratio increases. Nevertheless, the sensitivity of SS for very small anode to cathode ratios is about a half of that of CS. An increase is later observed until an anode to cathode ratio of 0.1 is reached and then decreases as the anode to cathode ratio continues to increase. Only as this ratio approaches a value of 0.5, the SS and CS sensitivities seem to be comparable where small sensitivity values are observed. It is also important to note that the sensitivity of SS is lesser than that of CS for all anode to cathode ratios.
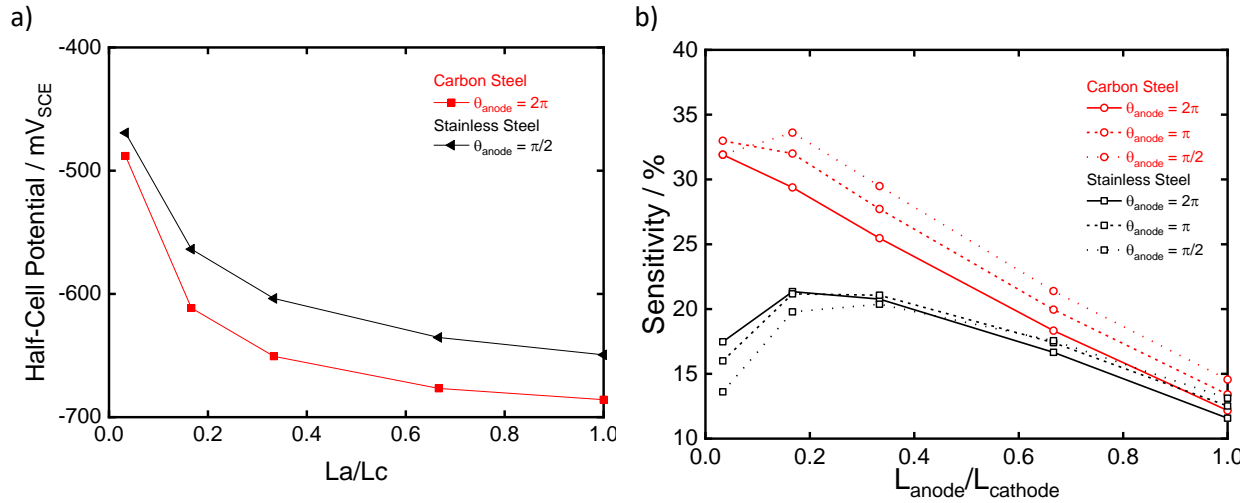
Figure 5.5: Finite Element Model results for SS and CS with varying corrosion morphologies showing (a) sensitivity and (b) HCP as a function of the anode to cathode ratio.

Subsequently, several iterations were performed using the EIS finite element model for the selected anode lengths and surface area ratios previously mentioned. The sensitivity of the EIS technique was evaluated based on the input corrosion rate at the anode (5 μm.yr^{-1}) of the Finite Element Model. Figure 5.6 illustrates the ratio of the simulation and the actual corrosion rates as a function of different anode to cathode ratios for $\Theta_{anode}=2\pi$, $\Theta_{anode}=\pi$ and $\Theta_{anode}=\pi/2$. The points below the region gray-shaded indicate that the estimated corrosion rate for a given anode to cathode ratio is lesser than the real value (i.e. underestimation of corrosion rates). Similarly, the points above the region shaded in gray are indicative of greater corrosion rate estimates than the real value (i.e. overestimation of corrosion rates). It is important to note that Figure 5.6 shows the corrosion rate values estimated from the simulations considering the polarization resistance associated with the entire EIS spectra and not the one associated with the time constant shown at the high frequency portion of the graph. Hence, these results suggest that EIS results should be carefully analyzed since the underestimation of corrosion rates is highly critical, not only because it casts doubt on the reliability of the technique at identifying localized corrosion spots but also due to the great variation of about one order of magnitude when compared to the input value. Similarly, overestimation of corrosion rates often leads to overly conservative service life estimations and inefficient allocation of resources in the design and construction of structures.
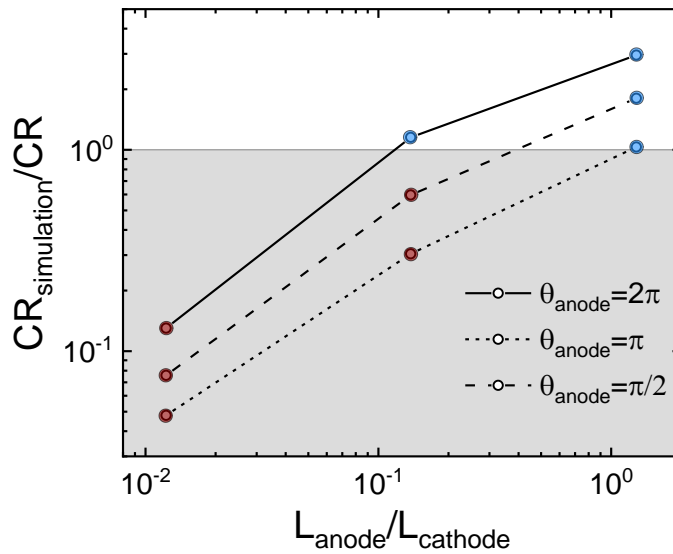
Figure 5.6: The ratio of the corrosion rate obtained from analysis of the simulated impedance and the input corrosion rate as a function of anode to cathode length ratio with anode circumference as a parameter.

5.3   Summary

Based on the experimental results of traditional NDTs, HCP and EIS, finite element models were proposed to assess the sensitivity for each. Furthermore, the applicability of existing technical standards on stainless steel reinforcement was also analyzed. In this study, the effect of parameters such as corrosion morphology, cathodic kinetics and geometric properties of the structural element was considered. From the experimental and computational results obtained in this study, the following conclusions can be drawn:

1. Half-cell potential measurements and simulations indicate that the corrosion morphology and cathodic kinetics of stainless steel reinforcement may cause a reduction in sensitivity.
2. Existing standards should be updated to provide half-cell potential ranges that could correlate more appropriately to the probability of corrosion of stainless steel reinforcement.
3. Electrochemical impedance spectroscopy measurements on reinforced concrete without a current confinement method may greatly under-predict corrosion rates if the corrosion is highly localized.

6   Durability Forecasting Modeling

A forecasting model of SS service life deterioration for FDOT structures of interest, suitable for cost benefit analysis and optimization of SS was proposed. The model, in response to the project objectives outlined in Section 1.2, was developed in the form of a damage function calculation of representative structural elements of FDOT infrastructure. The fraction of elements projected to reach a specified limit state was estimated as a function of bridge age.

The results obtained using this model are expected to provide valuable insight for criteria to evaluate repair or rehabilitation costs as a function of the design cost variables of interest. Those variables of interest included type of steel, concrete cover thickness (X_C), concrete class, structural element type, geometric parameters, and exposure conditions. The statistical formulations and other features were based on prior FDOT sponsored work at the University of South Florida (USF).[15] Reference to the final report for that modeling project is made subsequently in this chapter under the abbreviation FRM.[104]

The model assumes the two-stage corrosion deterioration model as introduced in earlier sections.[13] In the first period, the CIS, the concentration of chloride ions at the steel surface is lesser than the critical concentration of chloride ions for depassivation of the steel, also known as C_T.[60] The CIS concludes when the surface chloride concentration reaches the C_T. Subsequently, an active corrosion period begins, the CPS. Corrosion products accumulate until a limit state is reached, designating the end of the service life. The duration of the CIS (t_i) is calculated assuming simple Fickian diffusion. Experimental results have suggested that this provides a good approximation for structural elements without preexisting cracks.[105]

In earlier efforts, the duration of the CPS (t_p) was assumed to be a fixed value given that for elements reinforced with plain steel this stage is considered to be relatively short. As discussed in length in this report, the inherent corrosion resistance of SS reinforced concrete indicates that the t_p for SS might be substantially greater than that of plain CS. Therefore, t_p was allowed to vary here considering the expected limit state and corrosion rates for each type of steel. The methodology used to obtain the limit state is further described in Section 4.1.6 of the present investigation. Furthermore, expected corrosion rates were provisionally estimated from ongoing laboratory experiments and available literature described elsewhere in this report.

6.1   Model parameters

The input parameters evaluated in this investigation are chosen to approximate the specifications contained in the FDOT Structure Design Guidelines (SDG).[106] Only the substructure of the bridge was evaluated since it is the region of greatest corrosion risk in marine environments. Furthermore, commonly encountered structural elements, structural configuration, construction materials and exposure conditions were considered. A damage function was then obtained for a 200-year period for the overall structure, as well as, each type of structural element. Each set of parameters are described as follows:

6.1.1 Structural properties

The present investigation considered structural properties such as the type of component, dimensions, type, and size of rebar, as well as steel clear cover. Three types of structural components were considered: square piles, rectangular footings, and round columns. Additionally, the clear cover was first selected in accordance to FDOT SDG[106] environmental classification of service environment and then compared to user-selected values to evaluate the effect of variation from suggested values for every type of steel reinforcement.

Concrete cover variability was assumed to follow a truncated normal distribution, with a coefficient of variation of 0.125, which was conservatively deemed to be representative of as-built construction.

It is important to note that depending on the type and size of component, a portion of its surface could be subjected to a designated chloride penetration regime: flat wall, 2-way corner, 3-way corner and round.[104] The overall characteristics and surface fraction subjected to each regime per type of element are further described in the FRM.[104]

6.1.1.1 Exposure conditions

Two possible exposure conditions were proposed for every type of structural component: in water (IW) and in soil (IS). Furthermore, four subcategories were proposed for the elements subjected to the first condition and two subcategories for the second one. The possible categories and subcategories for each type of element are summarized in Table 6.1.

Table 6.1: Exposure condition categories and sub-categories for structural components.

Category	Water	Soil
Subcategory	Atmospheric (A)	Atmospheric (A)
	Splash-Evaporation (SE)	Buried (B)
	Tidal (T)	
	Submerged (S)	

The elevation range of each component type was selected to approximate those on typical FDOT marine bridges. The portion of each element at corrosion risk was then estimated by considering the exposure conditions categories and subcategories listed above. Following For IW elements, the sub-exposure portions of the total elevation range were assigned, in the manner of the FRM[104], as 1/8, 1/8, 3/8 and 3/8 for S, T, SE and A, respectively. Additionally, the cross-section of the piles and columns was assumed to be uniform and exposed laterally throughout their full length. Footings were assumed to be exposed to three out of the four sub-exposure conditions (S, T and SE) laterally and only to one (SE) on the top surface. For elements IS, the sub-exposure portions of the total elevation range were assigned as ½ for each condition.

6.1.1.2 Environmental classifications

Three environmental classifications per FDOT SDG[106] specifications were considered for all structural components: slightly, moderately and extremely aggressive. It is important to note that for marine structures only moderately and extremely aggressive exposure conditions were considered in this chapter.

6.1.1.3 Surface conditions

The exposure and sub-exposure conditions listed in Section 6.1.1.1 were associated with a given value of chloride ion surface concentration C_S as described in Table 6.2. These preliminary C_S values, obtained from FDOT reports and available literature, are provided as a reference to consider the subsiding buildup of chlorides as elevation increases for evaporative regimes as well as concentration of chlorides for submerged conditions.

The C_S parameter was assumed to be represented by a normal distribution per the probabilistic model realizations in the FRM.[104] The mean, coefficient of variance, upper and lower limit are listed in Table 6.2.

6.1.2 Concrete properties

A concrete class ranging from I to VI could be assigned to each structural element type. In this investigation, concrete class IV is selected for moderately aggressive scenarios and class V with pozzolanic replacement was selected for extremely aggressive environments.

For simplicity, the concrete class selected is associated with a time and space invariant value of chloride diffusion coefficient (D) based on reference values presented in the FRM.[104] These baseline values for D are summarized in Table 6.2. For higher concrete class types, such as the one selected for piles under extremely aggressive exposure, D was estimated using the relationship developed under FDOT project BA502[107] in which the percentage of cementitious material replacement, cementitious factor and water to cementitious material ratio are considered.

In the FRM as in here, subsequent to the estimation of a base D values, multiple corrections were performed to account for rebar obstruction and geometric regime effects (2-way corner, 3-way corner and round). First, a correction to account for the obstruction presented by the rebar is performed based on the ratio of rebar diameter to concrete cover. A multiplier ($1/T_f$), abstracted from previous FDOT investigations, is assigned.[30, 34] Subsequently, a multiplying factor was adopted to correct for geometric regime effects. The latter was abstracted from a prior FDOT project.[39] For round columns, this factor was suggested as a function of the ratio C_T/C_S and the ratio of the radius r of the column to concrete cover X_{Cobs} corrected for the rebar obstruction effect. For square piles and footings, the same investigation found that corner geometry was possibly incorporating a strong multi-dimensional magnification of chloride ingress, thus, no obstruction correction was required. It is recommended that these regimes are further evaluated. More detailed information regarding the correction procedure for each type of structural element is contained in the FRM.[104]

The chloride diffusion coefficient distribution was assumed to follow a normal distribution with a mean value adequate to each concrete class. The distribution formulation, coefficient of variation, upper and lower limit are summarized in Table 6.2.

Additionally, a simplified methodology is used to select the value of D for a given structural element. The value representative of the most severe exposure condition is selected for the entire element, thus, resulting in an increased conservativeness of the life-cycle analysis results.

The FRM-base model used in this investigation does not account for the time-variability of D in which a reduction in this value would be likely expected over time.[96] A previous FDOT report suggests that since most chloride diffusion coefficient values were obtained from structures at mature ages, the effective long-term diffusion could be represented.[108] Similarly, the effect of variations in temperature throughout the structural elements is not taken into consideration. It is important to highlight that this approach is rather conservative due to the scarcity of data and should be examined in follow-up investigations as more information becomes available.

6.1.2.1   Chloride threshold

The value of C_T was obtained using the formulation proposed in a prior FDOT investigation in which a reference value was calculated for plain steel. The C_T for CS was assumed to be equal to 0.4% of the nominal cementitious factor (CF) of a given concrete class. Preliminary multipliers were selected for each type of steel which would account for the expected increase of C_T for corrosion-resistant alloys such as SS. The multipliers for each type of steel, CF and C_T values per type of concrete class are listed in Table 6.2. These values have been obtained from existing literature as well as FDOT previous investigations[13, 104, 109], however, these are only included to provide as a reference to perform more realistic estimations and require further investigation.

The value of C_T, treated as constant in the model, is subject to variability with time, random changes in the concrete-steel interface, and the value of the local potential of the steel while still in the passive condition. For the first two categories the C_T variability was subsumed within the assumed variability in C_S, given that the t_i depends on the ratio between C_T/C_S rather than C_T itself. Thus, the variability of C_S is conservatively considered to account for the variability of the C_T/C_S term. For the variability due to the potential dependence, a tentative approach by means of a correcting parameter was used and incorporated in the forecasts as described in the FRM.[104]

Table 6.2: Concrete and steel bar parameters for durability projections.

Chloride Diffusion Coefficient, D

D / in^{2}y^{-1}	1	0.3	0.1	0.02	0.01	0.0075
Concrete class	I	II	III	IV	V	VI

Distribution formulation	mean u	Standard deviation sd	lower limit	upper limit		
	D	25%	3*sd	10*sd		

Chloride Surface Concentration, Cs

Cs / pcy

Cl- concentration in Water / ppm	>6000		Sq. piles	Footings	Columns
		Submerged	15	15	15
		Tidal	40	40	40
		Splash-Evap	40	40	40
		Atmospheric	15		15
Cl- concentration in Water / ppm	≤6000				
		Submerged	7.5	7.5	7.5
		Tidal	20	20	20
		Splash-Evap	40	40	40
		Atmospheric	10		10
Cl- concentration in Soil / ppm	>2000				
		Buried	10	10	10
		Atmospheric	10	10	10
Cl- concentration in Soil / ppm	≤2000				
		Buried	7.5	7.5	7.5
		Atmospheric	7.5	7.5	7.5
Distribution formulation	mean μ	Standard deviation sd	lower limit	upper limit	
	Cs	25%	3*sd	3*sd	

Chloride Threshold, C$_T$

Type of rebar	Plain Steel	Ferritic	E.Duplex	Austenitic	-	-
Multiplier	1	2	4	10	-	-

Concrete class	I	II	III	IV	V	VI
CF / pcy	544	575	600	650	700	752
C$_T$ / pcy	2.18	2.3	2.4	2.6	2.8	1

Notice: The values contained in this table are used to exemplify durability projections of SS and CS. These are subject to further evaluation.

6.1.3 Duration of the propagation stage

As discussed earlier in this report, laboratory results and literature evidence indicate that any corrosion propagation behavior improvement of SS with respect to that of CS may vary significantly. Influential parameters determined earlier such as the corrosion morphology, type and size of rebar, X_C, corrosion penetration and corrosion rate were included in obtaining estimates of t_p for the various material choices considered. The adopted value of t_p for each case was obtained as the ratio of the corrosion radius loss (see Section 6.1.3.2), which is responsible for causing cracking of the concrete or mechanical failure, and the corrosion rate (see Section 6.1.3.1).

6.1.3.1 Corrosion rate

Each type of reinforcement bar was assigned a flat corrosion rate value based on the experimental results obtained in this investigation. A baseline corrosion rate value for plain steel of 20 μm.yr^{-1} was provisionally abstracted from a prior FDOT investigation.[110] This investigation performed by Sagüés et al.[110] suggest that values ranging between 11.68 -116.8 μm.yr^{-1} may be representative of high risk of corrosion damage for humid concrete exposed to chloride-contaminated environments.

For the present investigation the baseline value was calculated assuming that the duration of the corrosion propagation time was 5 years and the X_{CRIT} value was about 100 μm. Subsequent to the selection of the baseline value, a multiplier was assigned to each type of SS reinforcement bar. Three classes of SS were considered: ferritic SS comparable to straight-Cr alloys, economic duplex (E. Duplex) SS selections of moderate PREN, and high-grade austenitic SS with high PREN.

For this investigation, corrosion rates once corrosion initiates are tentatively assumed to be similar for CS and ferritic SS and smaller for the economic duplex and austenitic SS. For the ferritic SS a value of that multiplier =1 (essentially no corrosion rate benefit over CS) was chosen considering the experimental data obtained in this investigation. Furthermore, conservative multipliers for the economic duplex and austenitic SS were provisionally assigned based on experimental data obtained in this investigation from the specimens described in Section 3.1 and 3.2. The values assigned for each type of steel are listed in Table 6.3. It is important to note that the available information regarding the corrosion propagation of SS is still limited. Hence, as more data becomes available, more accurate corrosion rate estimates could be used.

Table 6.3: Tentative corrosion rate for each type of steel reinforcement.

Corrosion Rate, CR					
Type of rebar	Plain Steel	Ferritic	E. Duplex	Austenitic	-	-
Multiplier	1	1	0.50	0.25	-	-
CR / μmyr^{-1}	20	20	10	5		

6.1.3.2 Local limit state

Due to the highly localized corrosion morphology of SS, two service life limit states were considered: cracking of the concrete and mechanical degradation due to the loss of yield strength and/or ductility of the steel, further detailed in Section 4.1.4 and 4.1.6 and elsewhere in Chapter 4.

The critical corrosion penetration to cause cracking of the concrete was first estimated using the model proposed by Busba, expressed in Equation (14).[25] This model considered the clear cover, diameter of the rebar and length of the anode. Several iterations were performed using different combinations of clear cover ranging from 5 in to 2 in. Additionally, the diameter of the rebar was selected based on FDOT marine structures and the length of the anode was assigned considering experimental results from this investigation as well as previous a FDOT report.[45] The length of the anode was assumed as 8 in and 1.5 in for CS and SS, respectively.

X_{CRIT} calculations were compared to corrosion penetration values required to reach the mechanical limit (Xmech) as expressed in Equation (19). The initial yield strength (f_{y0}) was conservatively assumed as 60 ksi (~413 MPa), which is typically the grade used for CS reinforcement. The evaluated yield strength (f_y) was assumed as ~32 ksi (220 MPa), which was selected as the critical serviceability yield strength in this section of the report. Corrosion penetration values are listed in Table 6.4 and Table 6.5.

Table 6.4: Corrosion penetration estimations for SS where cells highlighted in light and dark gray represent cracking of the concrete and mechanical failure, respectively.

Corrosion penetration \ µm											
Clear	Bar size \ No.										
cover \ in	3	4	5	6	7	8	9	10	11	14	18
1	62	47	37	31	27	23	21	19	17	13	10
2	206	154	123	103	88	77	69	62	56	44	34
3	447	335	268	224	192	168	149	134	122	96	75
4	707	602	482	401	344	301	268	241	219	172	134
4.5	707	770	616	514	440	385	342	308	280	220	171
5	707	943	771	642	551	482	428	385	350	275	214

Table 6.5: Corrosion penetration estimations for CS where cells highlighted in light and dark gray represent cracking of the concrete and mechanical failure, respectively.

Corrosion penetration \ µm											
Clear	Bar size \ No.										
cover \ in	3	4	5	6	7	8	9	10	11	14	18
1	37	28	22	19	16	14	12	11	10	8	6
2	92	69	55	46	39	34	31	28	25	20	15
3	166	125	100	83	71	62	55	50	45	36	28
4	264	198	158	132	113	99	88	79	72	57	44
4.5	322	242	193	161	138	121	107	97	88	69	54
5	387	290	232	194	166	145	129	116	106	83	65

6.1.3.3   Preliminary estimates of the duration of the CPS

The estimates of t_p used in this study per the parameter values chosen in the previous subsections are listed in Table 6.6. It is noted that many of the assumptions used are working propositions. For example, the degree of corrosion localization could be even greater than those indicated earlier, resulting in the estimates below being conservative for SS reinforcement. Further data will be required to validate the applicability of the existing models to SS and implement corrections to account for the non-uniformity of corrosion throughout the length of the anode.

Table 6.6: Time of propagation for different types of steel reinforcement, concrete cover and bar size.

X_c	Bar size	t_p / yr			
		Plain Steel	Ferritic	Duplex	Austenitic
in	No.				
5	11	5.3	17.5	35.0	70.1
	10	5.8	19.3	38.5	77.1
4.5	11	4.4	14.0	28.0	56.0
	10	4.8	15.4	30.8	61.6
4	11	3.6	10.9	21.9	43.8
	10	4	12.0	24.1	48.2
3	11	2.3	6.1	12.2	24.4
	10	2.5	6.7	13.4	26.8
2	11	1.3	2.8	5.6	11.2
	10	1.4	3.1	6.2	12.3

6.1.4   Global limit state

A global limit state was assigned to each group of elements, i.e. piles, footings and columns as well as to the integrated structure. In the present investigation, a value of 2.3% representing the permitted surface-apparent damage in the entire structure was selected. This integrated, total damage (not to be confused with the local limit states addressed previously) was estimated considering the fraction of elements that would reach the limit state in the structure. This value was abstracted from the FRM[105] and was comparable to the one adopted by a representative agency of European practice.[111] The global limit state was selected to exemplify the durability of SS in comparison to CS for FDOT structures. It is important to note that this value was provided as a reference since it depends on a number of factors such as type of bridge, and serviceability requirements. In addition, only the substructure portion of a marine bridge or similar entity was analyzed in this investigation, thus, the meaning of this parameter could vary if the entire structure were considered.

6.2 Case study

The substructure of a representative FDOT bridge was used to evaluate the serviceability life of structures reinforced with plain steel and SS in terms of durability. The bridge was composed of 36 substructure bents (piers) for each exposure condition (IW and IS) which were comprised of square piles, rectangular footings, and columns. All elements were assumed to be cast-in place. The square piles were about 40 ft long and presented 30 in sides. One type of pile array was examined for simplicity to all the piers in the substructure which consisted of 12 piles per pier. The footings were ten feet long, eight feet wide and ten feet high. Moreover, the columns of the substructure were assumed to have a round shape with a ten ft diameter and a length of 40 ft. Each pier was assumed to have one footing and one column. The number of elements and dimensions considered for each exposure condition (IW and IS) are contained in Table 6.7.

Table 6.7: Summary of structural components for each exposure condition.

Structural components		Sq. piles	Footings	Columns
No.		432	36	36
Dimensions	A / in	30	120	120
	B / in		96	
Bar size	No.	11	11	10

Each component was divided into discrete elements to evaluate the sub-exposure conditions to which it would be expected to be subjected. This is further explained in Section 6.1.1.1. Similarly, default chloride surface concentrations were assigned to each sub-exposure category as explained in Section 6.1.1.3. The propagation time was estimated for each iteration as described in Section 6.1.3.

A first set of iterations was performed to evaluate the proposed substructure for each type of steel under two scenarios. The concrete cover, concrete class, and rebar diameter for each were abstracted from the FDOT SDG. The main variations between scenarios are listed in Table 6.8. The remaining parameters including D, C_S, C_T, X_C and t_p were the same in the two proposed scenarios.

First scenario: Moderately aggressive environmental exposure

As base values, the minimum requirements from the FDOT SDG[106] were selected to evaluate the durability of plain steel and SS reinforced structure under a moderately aggressive environment. A minimum concrete cover of four inches is required for external surfaces cast against water and/or earth in the substructure per FDOT SDG[106] specifications. Similarly, concrete class IV is specified for cast-in place elements for this environmental classification. The diffusion coefficient was assigned the default value for concrete class IV, contained in Table 6.2.

Second Scenario: Extremely aggressive environmental exposure

As in the previous scenario, the minimum requirements are abstracted from the FDOT SDG[106] and used as inputs for this evaluation. A minimum concrete cover of four and half inches is required for external surfaces cast against water and/or earth in the substructure per FDOT SDG[106] guidelines. Similar to the moderately aggressive requirements, concrete class IV is permitted for cast-in place elements. Nevertheless, concrete class V with pozzolanic cement replacement was used for the piles. The diffusion coefficient was calculated as described in Section 6.1.2 using a cementitious factor of 750 and a water to cementitious material ratio of 0.41.

Subsequently, a second set of iterations was performed to evaluate the effect of the concrete cover on the same environmental classifications. Clear concrete covers ranging from two to five inches were examined for each type of steel.

Table 6.8: Variations between first and second scenarios for the given substructure.

Scenario	I	II
Environmental classification	Moderately aggressive	Extremely aggressive
Concrete type Square piles Footings Columns	IV IV IV	V* IV IV

V* consists of concrete class V with a cement replacement.

6.2.1 General discussion

Service life design for two different scenarios was performed using the parameters described in Section 6.2, and the adopted global limit state of 2.3% surface damage. The minimum requisites specified in the FDOT SDG[106] for each environmental exposure class were met and evaluated for different steel reinforcement types such as CS and three SS alternatives. The results are also contrasted with the 75-year FDOT design life criterion.[106] Cumulative damage functions per the FRM[105] were obtained for every group of structural element as well as the overall substructure (bridge). Results were plotted in one graph per steel reinforcement type for each scenarios as shown in Figure 6.1 and Figure 6.2. The results for both scenarios suggest that footings are usually the most vulnerable structural element under these conditions. This could be explained by the sub-exposure conditions to which footings are subjected. About three quarters of the footings were assumed to be under tidal or splash-evaporation regimes which are associated with higher concentration of chlorides on the concrete surface.

Under moderately aggressive environmental classification it was found that CS reinforcement failed to meet the 75-year design life criterion, shown in Figure 6.1(a). The estimated serviceability limit for plain steel was projected to be about 50 years indicating that additional measures would be required to meet the 75 year criterion. In contrast, all the types of SS reinforcement bar were projected to surpass the 75-year lower limit with a service life of about 80 years, 140 years and over 200 years for ferritic, economic duplex and austenitic, respectively. Figure 6.1(a), (b), (c) and (d) shows the cumulative damage function for the stainless steel rebar alternatives.

(a)

(b)

(c)
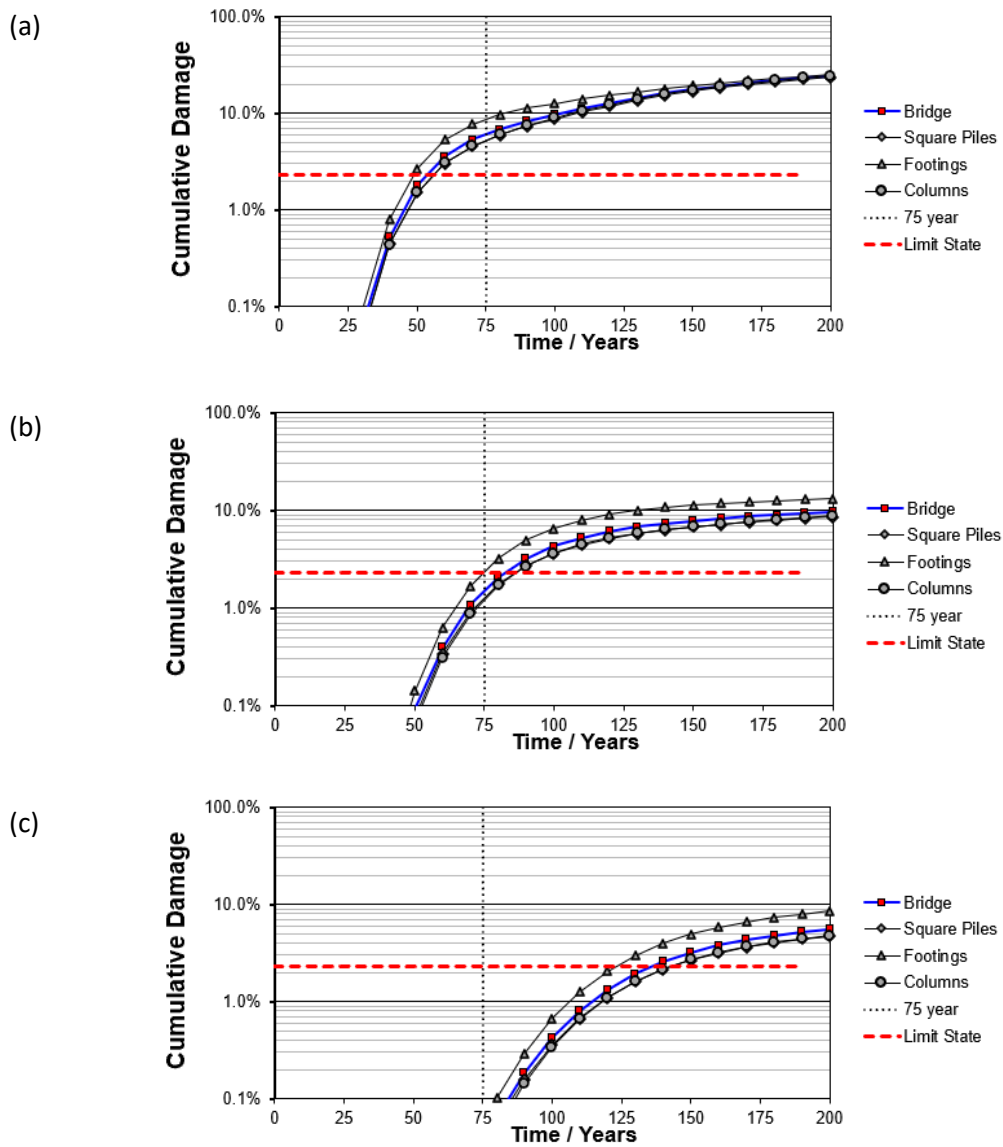
Figure 6.1: First scenario (moderately aggressive): life cycle analysis under moderately aggressive conditions for (a) Plain steel, (b) Ferritic SS, (c) E. Duplex SS and (d) Austenitic SS.

(d)
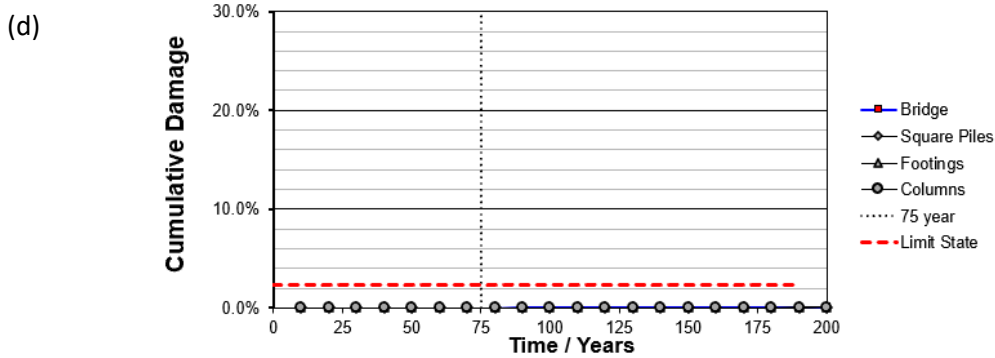
Figure 6.1 (continued): First scenario (moderately aggressive): life cycle analysis under moderately aggressive conditions for (a) Plain steel, (b) Ferritic SS, (c) E. Duplex SS and (d) Austenitic SS.

Similarly, concrete reinforced with plain CS under extremely aggressive conditions is not projected to meet the 75-year service life requirement. Although a higher concrete class was used in the piles to account for the increased concentration of chlorides, the projected 70-year service life is still five years less than the minimum criterion, shown in Figure 6.2(a). Thus, it would need additional improvements to the concrete or corrosion protection methods to satisfy this specification. The concrete class improvement for the piles appeared to have a greater effect on the projected lifetime of elements reinforced with SS. Figure 6.2(b), (c) and (d) shows that all of the cumulative damage function results for SS reinforcement exceeded the 75-year service life specification. The service life of ferritic, duplex and austenitic SS was approximately 110 years, 190 years and over 200 years, respectively. In this scenario, the service life estimation for duplex and austenitic SS is about four times greater than that of CS. In addition, the projected service life of ferritic SS exceeds by a factor of two that of CS.

(a)
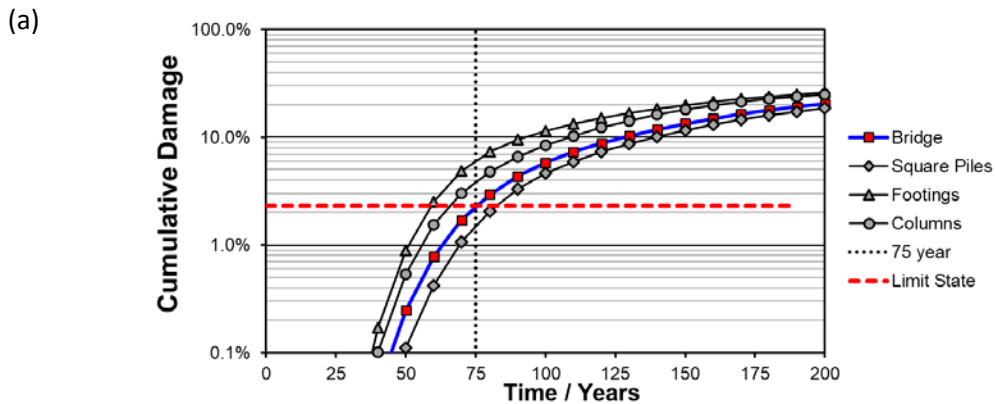
Figure 6.2: Second scenario (extremely aggressive): life cycle analysis under extremely aggressive conditions for (a) Plain steel, (b) Ferritic SS, (c) E. Duplex SS and (d) Austenitic SS.

118

(b)

(c)

(d)
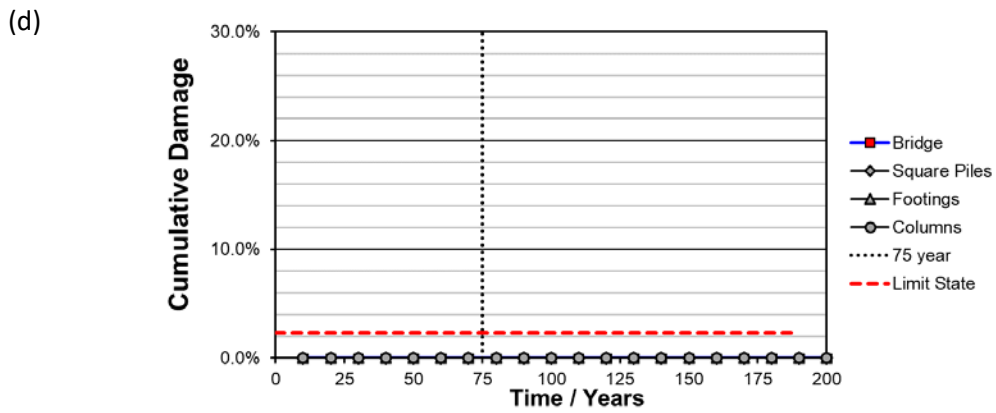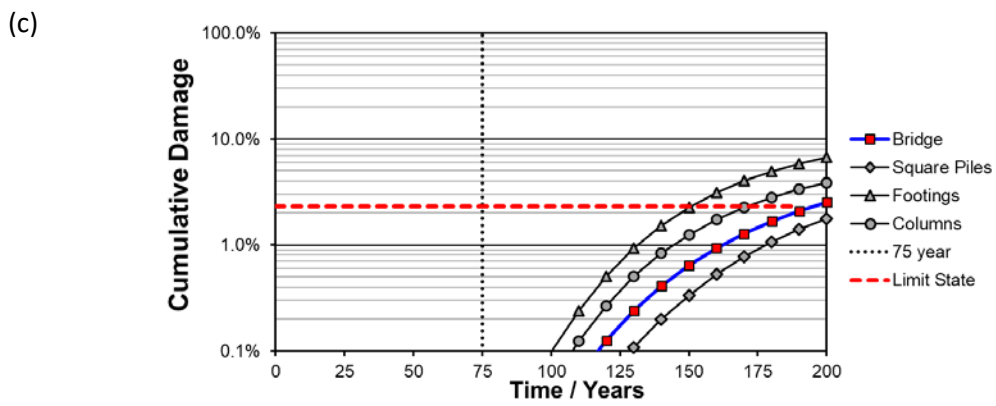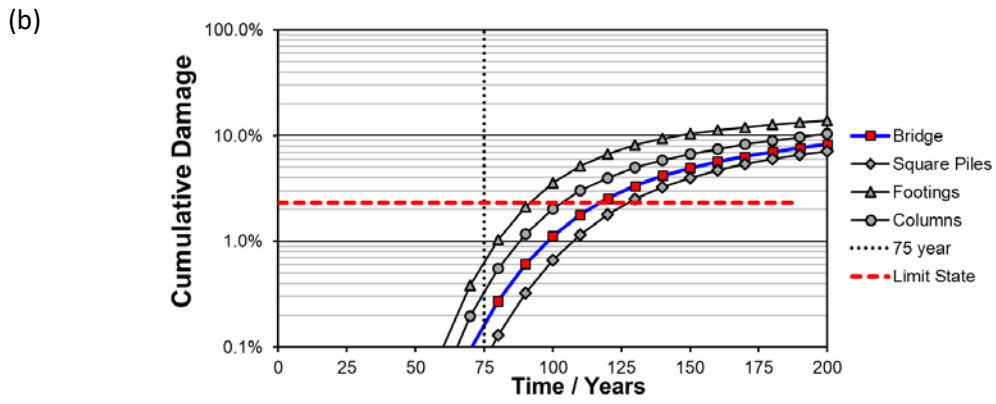
Figure 6.2 (continued): Second scenario (extremely aggressive): life cycle analysis under moderately aggressive conditions for (a) Plain steel, (b) Ferritic SS, (c) E. Duplex SS and (d) Austenitic SS.

119

The same scenarios were selected to examine CS and three types of SS, those being ferritic, economic duplex and austenitic, with variations in the clear concrete cover. The results were plotted in Figure 3 and Figure 4 for the moderately and extremely aggressive environmental exposure, respectively. It can be observed that for both scenarios CS presents the lowest projected performance in terms of durability. As it was previously mentioned, CS was projected to fail to meet the 75-year design criterion in both cases. It can be observed that the durability of SS will highly depend on the alloy. Although ferritic SS presents a larger projected service life when compared to that of CS, the projected added benefit of duplex and austenitic SS is much greater.

Figure 3 shows that for moderately aggressive exposure conditions, the model projected that CS would need a clear cover greater than 4 ½ -in to meet the 75-year service life specification. While the projection indicated that ferritic SS barely passed the minimum service life requirement when considering a 4-in cover, duplex SS considerably exceeded it. Nevertheless, a 3-in cover was not enough for the projected duplex SS behavior to meet this requirement. For austenitic SS, a concrete cover as small as 2-in still was projected to meet the 75-year service life criterion. This was also found to be the case for the second scenario evaluated.

Similar findings were obtained for extremely aggressive conditions, as shown in Figure 6.4. The 75-year service life criterion was projected to be met with a concrete cover of 5-in, 4-in, 3-in and 2-in for plain steel, ferritic, duplex and austenitic SS, respectively. It is important to note that the clear concrete covers displayed in this investigation are only provided to give an estimate of the benefit in terms of durability that SS reinforcement could represent over plain carbon steel.
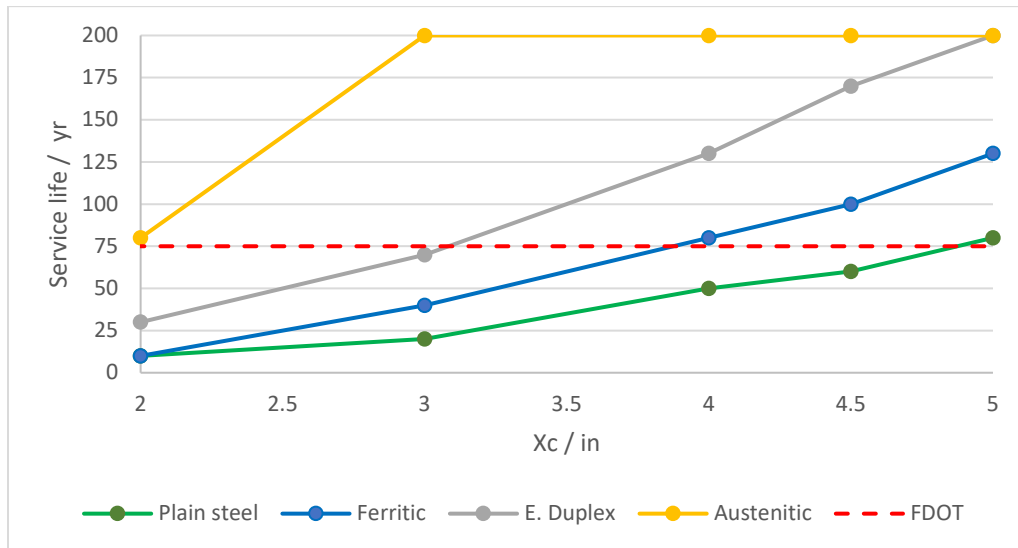
Figure 6.3: First scenario: life cycle analysis under moderately aggressive conditions as a function of concrete cover for each type of steel.
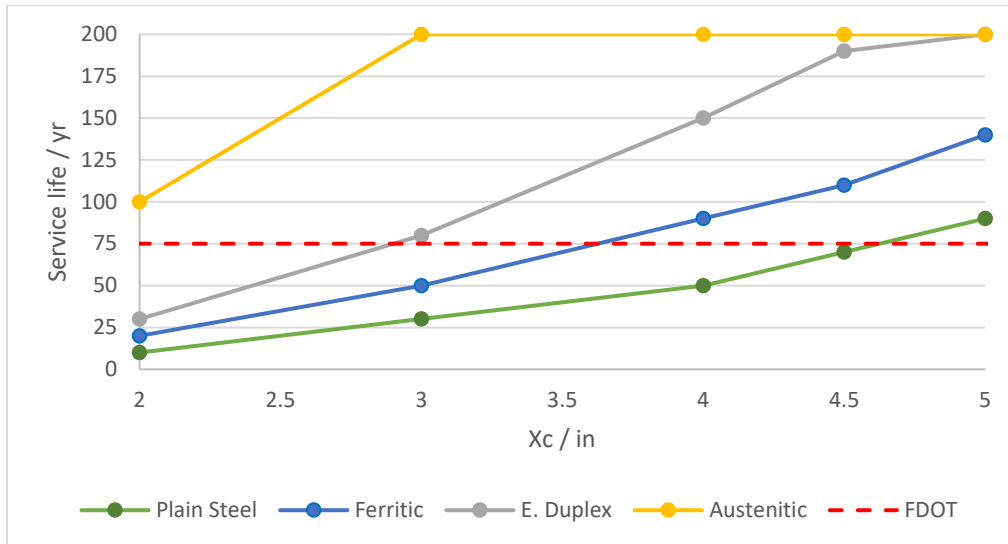
Figure 6.4: Second scenario: life cycle analysis under extremely aggressive conditions as a function of concrete cover for each type of steel.

6.2.1.1 Significance of Model Projections

Recognizing the inherent uncertainty of any modeling approach, the durability projections strongly supported the expectation of improved performance by using stainless steel of any of the types considered, as a replacement for plain steel rebar. For the most corrosion resistant SS alloy and for the global limit state assumed the target design life of 75 years was forecasted to be met even with moderate concrete cover values. While it is known that the extended durability is in part due to much greater times to corrosion initiation, it was previously uncertain how much credit could be provided to the corrosion propagation stage. The model projections suggest that the portion of extended durability that may be attributed to the propagation stage is could be quite substantial. For the two more corrosion resistant SS alloys, the projected corrosion propagation stage duration was over one order of magnitude greater than that for plain steel. This point was enhanced especially when the cover to rebar diameter ratio was greater. Thus, it is recommended that in future evaluations of the relative benefit of using SS rebar instead for plain steel, leading to revised SDG statements, modeling calculations of the type described here be used to update accordingly requirements such as minimum cover or concrete class. An illustration of how such update may be expressed is addressed in Chapter 8.

While based on numerous working assumptions, the modeling approach used here is a promising first step in rational durability forecasting of concrete structures reinforced with stainless steel. Future improvements of this model could also include accounting for the variation of diffusivity over time, the effect of temperature on the diffusivity as well as the surface concentration of chlorides on the structure. Furthermore, more advanced modifications could include the variation of the corrosion rates over time due to fluctuations in environmental parameters.

7 Conclusions

Corrosion propagation stage parameters

- Experimental results suggest that provided an aggressive enough environment, the **corrosion rates** of the least corrosion-resistant stainless steel grades may be comparable to those of carbon steel. However, it is likely that the highest corrosion rate achievable for even ferritic SS in concrete is less than that of CS.
- The **corrosion morphology** for stainless steel in concrete is more localized than the corrosion normally observed for carbon steel reinforcement. In sound concrete the length of the corroding portion of stainless is only a fraction of that of carbon steel. Additionally, while corrosion on carbon steel eventually occurs around the entire circumference of the steel, corrosion of stainless steel may be confined to less than half of the circumference.
- Based on the corrosion morphology of stainless steel and the known relationship between **X_{CRIT}** and corrosion morphology, it can be expected that an X_{CRIT} associated with cover cracking will be greater for SS than for CS. However, alternative limit states such as mechanical failure of the reinforcement must be considered.

Limit state sound concrete

- Due to the highly localized corrosion morphology of SS, corrosion induced mechanical failure of the reinforcement may need to be considered as a limit state. Whether mechanical failure significantly impacts the overall structural durability will need to be assessed.
- Particularly, for larger cover thicknesses (4-5 in), a mechanical failure limit state may be likely. Further work is required to confirm this.

Limit state locally-deficient concrete

- For locally deficient concrete, SS corrosion results in a damage morphology that only covers a portion of the steel circumference and may have an anode length that is less than that of CS.
- Based on a simple model developed to determine the amount of corrosion required to further damage the concrete cover in locally deficient concrete, it seems as though SS corrosion is more likely to result in mechanical damage than CS. However, more work is required to determine the accuracy of the model and whether any modifications are required.

Feasibility of corrosion detection techniques

- Half-cell potential experimental results and simulations indicate that the corrosion morphology and cathodic kinetic limitations of SS reinforcement may cause a reduction in sensitivity.
- The ASTM corrosion probability designations based on HCP values may require modification for application to SS corrosion.
- Electrochemical impedance spectroscopy measurements in reinforced concrete without a current confinement method may greatly underpredict corrosion rates if corrosion is highly localized.

SS reinforced concrete service life forecasts

- The introduction of propagation time values for each type of steel reinforcement and concrete cover provided less-conservative estimates service life. The more corrosion-resistant alloys of SS reinforcement presented propagation stage durations of about one order of magnitude greater than those of plain carbon steel reinforcement.
- Exploratory calculations based on a service life model prototype suggest that previously highly conservative approaches have led to the underestimation of actual service life with the more corrosion-resistant alloys of SS.

8 Illustrative Concrete Cover Recommendations

Durability forecasts incorporating estimates of the propagation stage such as those presented in chapter 6 may be used during the design phase to specify concrete covers that minimize the likelihood of reaching the assumed serviceability limit state during a nominal 75-year service life. Tentative concrete cover recommendations for concrete free of local deficiencies, based on the preliminary durability projections in Chapter 6, are illustrated for a notional bridge configuration. It is emphasized that these values are presented as a starting point for further discussion on possible guideline updates. Further work is required to confirm the assumptions used in the calculations, as well as any numerical model updates necessary to refine the approach or remedy any existing inaccuracies. Moreover, the values presented may require modification if other bridge designs are considered, and be subject to detailed analysis and more conservative formulation to address situations like locally deficient concrete, use of mixed rebar types and any other specialized circumstance.

Bridge Setup

The bridge is a structure exposed near or full marine conditions, o assumed to contain 3 types of structural elements liable to corrosion damage. The listing includes the portion of each element surface exposed to each of the indicated regimes per chapter 6. The two regimes, Moderate and Extreme are also per the discussion in Chapter 6.

Square Piles & Columns.
-
  - 1/8 – Submerged
  - 1/8 – Tidal
  - 3/8 – Splash Evaporation
  - 3/8 – Atmosphere

Footing
-
  - 1/5 – Submerged
  - 1/5 – Tidal
  - 3/5 – Splash Evaporation

Illustrative cover specification summary

The cover values are numeric indications presented regardless of feasibility of implementation. Some of these values may merit removal upon consideration of other constraints. For example, the listed cover value for piles may be disqualified in some cases because of inability to retain integrity during driving. The cover values are computed based on the concrete class selections used in the chapter 6 example.

Table 1

Carbon Steel		
	Moderate	Extreme
Square Piles	5 in	4.5 in
Footings	>5 in	>5 in
Columns	5 in	5 in

Table 2

Ferritic Steel		
	Moderate	Extreme
Square Piles	4 in	4 in
Footings	4.5 in	4.5 in
Columns	4 in	4 in

Table 3

Duplex Steel		
	Moderate	Extreme
Square Piles	3.5 in	3 in
Footings	3.5 in	3.5 in
Columns	3.5 in	3.5 in

Table 4

Austenitic Steel		
	Moderate	Extreme
Square Piles	2 in	2 in
Footings	2.5 in	3 in
Columns	2 in	3 in

** > - *The size of the cover exceeds 5 inches to reach the 75-year design life.*

9 Future Research

The results ad projections presented in this report should be verified with extended experimental studies. Presently, the models that were used in this work to estimate the critical corrosion penetration are empirical models that were based on experiments with carbon steel reinforcement and are likely not directly applicable to stainless steel due the difference in corrosion morphology. Since corrosion of stainless steel reinforcement may be confined to only a portion of the circumference it is likely that the critical corrosion required to crack the concrete will be greater than that of carbon steel potentially making a mechanical failure limit state more probable. Therefore, a thorough understanding of mechanical properties of corroded stainless steel reinforcement is required to identify the most likely limit state. The mechanical relationships used in the work were developed for carbon steel and therefore mechanical testing of corroding stainless steel should be performed to develop a relationship between corrosion morphology and residual strength. Based on the limitations of the present work, the following research is proposed:

1. Develop X_{CRIT} model applicable to SS that considers localized corrosion morphology.

Accelerated corrosion experiments should be performed to establish an X_{CRIT} model suitable to corrosion of SS in concrete. Experiments should be performed with known anode sizes and cover dimensions. The results may be used to determine a mathematical model that would be a function of anode length, circumference, rebar size, and cover thickness. Finite element simulations may be performed in conjunction that consider the fracture toughness of the concrete and the expansion of the corrosion products.

2. Establish relationships between corrosion damage and mechanical properties of SS alloys while considering extreme localization.

The residual strength of the reinforcement will depend significantly on the corrosion morphology. Corroded stainless steel bars may be mechanically tested to develop a mathematical relationship between corrosion penetration and localization and residual tensile strength and ductility.

References

1.   Tuutti, K., *Corrosion of steel in concrete*. Cement-och betonginst.: 1982.

2.   Cox, R.; Oldfield, J., The long-term performance of austenitic stainless steel in chloride contaminated concrete. *Royal society of chemistry* 1996, *183* (1), 662-669.

3.   Bertolini, L.; Gastaldi, M.; Pastore, T.; Pedeferri, M.; Pedeferri, P. In *Effects of galvanic coupling between carbon steel and stainless steel reinforcement in concrete*, International Conference on "Corrosion and Rehabilitation of Reinforced Concrete Structures", Orlando, December; Federal Highway Administration: Orlando, 1998; pp 7-11.

4.   Bertolini, L.; Pedeferri, P.; Pastore, T., Stainless steel in reinforced concrete structures. *Concrete under severe conditions* 1998, *2*, 94-103.

5.   Pedeferri, P., Behavior of Stainless Steel in the Rehabilitation of Corrosion Damaged Infrastructures and Effects of Galvanic Coupling Between Carbon Steel and Stainless Steel "Rehabilitation of Corrosion Damaged Infrastructure. *Chapter I: Case and Laboratory Studies* 1998, 1-7.

6.   Pedeferri, P.; Bertolini, L.; Bolzoni, F.; Pastore, T. In *Behavior of stainless steels in concrete*, 1997 International Seminar on Repair and Rehabilitation of Reinforced Concrete Structures: The State of the Art, American Society of Civil Engineers: 1998; pp 192-206.

7.   Bertolini, L.; Gastaldi, M.; Pastore, T.; Pedeferri, M. In *Effect of chemical composition on corrosion behaviour of stainless steels in chloride contaminated and carbonated concrete*, Proc. of 3rd European Congress" Stainless Steel'99", Associazione Italiana di Metallurgia: 1999; pp 131-140.

8.   Castro-Borges, P.; Troconis-Rincón, O.; Moreno, E. I.; Torres-Acosta, A. A.; Martinez-Madrid, M.; Knudsen, A., Performance of a 60-year-old concrete pier with stainless steel reinforcement. *Materials Performance* 2002, *41* (10), 50-55.

9.   Clemena, G. G.; Virmani, Y. P., Comparing the chloride resistances of reinforcing bars. *Concrete International* 2004, *26* (11), 39-49.

10.   Presuel-Moreno, F.; Scully, J. R.; Sharp, S. R. *Identification of commercially available alloys for corrosion-resistant metallic reinforcement and test methods for evaluating corrosion-resistant reinforcement*; Virginia Transportation Research Council: 2008.

11.   Van Niejenhuis, C. The Case for Stainless Steel Reinforcing Bars. University of Waterloo, 2015.

12.   Meng, X. H.; Zhang, S. Y. In *Application and development of stainless steel reinforced concrete structure*, MATEC Web of Conferences, EDP Sciences: 2016; p 03009.

13.   Hurley, M. F.; Scully, J. R., Threshold chloride concentrations of selected corrosion-resistant rebar materials compared to carbon steel. *Corrosion* 2006, *62* (10), 892-904.

14.   Knudsen, A.; Jensen, F.; Klinghoffer, O.; Skovsgaard, T. In *Cost-effective enhancement of durability of concrete structures B intelligent use of stainless steel reinforcement*, Proceedings of the international conference on corrosion and rehabilitation of reinforced concrete structures held 7-11 December 1998, Orlando, Florida, USA, Orlando, Florida, USA, 1999.

15.   McDonald, D.; Sherman, M.; Pfeifer, D.; Virmani, Y., Stainless steel reinforcing as corrosion protection. *Concrete International* 1995, *17* (5), 65-70.

16.   Society, C., Guidance on the Use of Stainless Steel Reinforcement. The Concrete Society Surrey: 1998.

17.   Val, D. V.; Stewart, M. G., Life-cycle cost analysis of reinforced concrete structures in marine environments. *Structural safety* 2003, *25* (4), 343-362.

18.   Sagues, A., Modeling the effects of corrosion on the lifetime of extended reinforced concrete structures. *Corrosion* 2003, *59* (10), 854-866.

19.   Hurley, M.; Scully, J., Lateral and radial corrosion propagation behavior of 9–21% Cr and 18% Cr+ 2.8% Mo stainless steel reinforcing materials in simulated concrete environments. *Materials and Corrosion* 2013, *64* (9), 752-763.

20.   Schiegg, Y.; Voûtea, C.; Peterb, H.; Haslerb, S.; Urlaub, U. In *Initiation and corrosion propagation of stainless steel reinforcements in concrete structures*, proceedings of EUROCORR, 2004.

21.   Treadaway, K.; Cox, R.; Brown, B. In *Durability of corrosion resisting steels in concrete*, Proceedings of the Institution of Civil Engineers, 1989.

22.   Hartt, W. H.; Powers, R. G.; Leroux, V.; Lysogorski, D. K. *Critical literature review of high-performance corrosion reinforcements in concrete bridge applications*; United States. Federal Highway Administration. Office of Infrastructure …: 2004.

23.   Mameng, S. H.; Tigerstrand, C.; Larsson, T.; Gedge, G.; McCray, J. In *Experience of duplex stainless steels as construction materials in bridges: Results of seven inspections*, IABSE Symposium Report, International Association for Bridge and Structural Engineering: 2017; pp 1679-1686.

24.   Presuel-Moreno, F.; Scully, J. R.; Sharp, S. R., Literature review of commercially available alloys that have potential as low-cost, corrosion-resistant concrete reinforcement. *Corrosion* 2010, *66* (8), 086001-086001-13.

25.   Busba, E.; Sagüés, A. A. In *Critical Localized Corrosion Penetration of Steel Reinforcement for Concrete Cover Cracking*, NACE conference and Expo 2013, NACE International, Houston: 2013.

26.   Torres-Acosta, A. A.; Sagues, A. A., Concrete cracking by localized steel corrosion--Geometric effects. *Materials Journal* 2004, *101* (6), 501-507.

27.   Cui, F.; Sagues, A. A., Cathodic Behavior of Stainless Steel 316LN Reinforcing Bars In Simulated Concrete Pore Solutions, Paper No. 08323. In *Corrosion*, International, N., Ed. Houston, 2008.

28.   Sánchez, A. N.; Sagüés, A. A., Potential-Dependent Chloride Threshold in Reinforced Concrete Damage Prediction–Effect of Activation Zone Size, Paper No. 2704. In *Corrosion*, International, N., Ed. Houston, 2013; p 14.

29.   Bertolini, L.; Bolzoni, F.; Pastore, T.; Pedeferri, P., Behaviour of stainless steel in simulated concrete pore solution. *British corrosion journal* 1996, *31* (3), 218-222.

30.   Moreno, E. I.; Acosta, A. A. T.; Borges, P. C., Construcción del muelle de Progreso. *Ingeniería* 2004, *8* (1), 61-66.

31.   Christensen, A., Pier at Progreso, 50 Years of Civil Engineering. *Christiani & Nielsen, Copenhagen, Denmark* 1954.

32.   Stainless, A., Research and Development, Pier in Progreso, Mexico. *Arminox Stainless, Progreso, Mexico* 1999.

33.   Torres Acosta, A.; Castro Borges, P.; Martinez Madrid, M.; Fabela Gallegos, M.; Del Valle Moreno, A.; Vazquez Vega, D.; Flores Centeno, O.; Hernandez Jimenez, J.; Lomeli Gonzalez, M.; Balancan Zapata, M., Viaducto de Arcos de Progreso, Yucatan: Primera Obra de Concreto Construida con Acero Inoxidable. *Publicacion Tecnica* 2018, (510).

34.   Fahim, A.; Dean, A. E.; Thomas, M. D.; Moffatt, E. G., Corrosion resistance of chromium-steel and stainless steel reinforcement in concrete. *Materials and Corrosion* 2019, *70* (2), 328-344.

35.   Van Niejenhuis, C.; Walbridge, S.; Hansson, C., The performance of austenitic and duplex stainless steels in cracked concrete exposed to concentrated chloride brine. *Journal of materials science* 2016, *51* (1), 362-374.

36.   Scientific, G. New Technique for Rebar Corrosion Rate Measurement in Concrete. https://www.giatecscientific.com/education/a-new-technique-for-rebar-corrosion-rate-measurement-in-concrete/.

37.   (FDOT), Florida Department of Transportation. Standard Specifications for Road and Bridge Construction. Tallahassee, Florida, 2019.

38.   Conshohocken, W., C192-07 In *Standard Practice for Making and Curing Concrete Test Specimens in the Laboratory (ASTM C192-07).* West Conshohocken, PA, 2007.

39.   ASTM, C876-15 In *Standard Test Method for Corrosion Potentials of Uncoated Reinforcing Steel in Concrete*, American Society for Testing and Materials: Philadelphia, Pa, USA, 2015.

40.   Sagüés, A., Notes on Electrochemical Impedance Spectroscopy. In *CGN 6720*, College of Engineering, U. o. S. F., Ed. Tampa, FL, 2018.

41.   Sagüés, A. A. In *Corrosion measurement techniques for steel in concrete*, Corrosion-national association of corrosion engineers (NACE) annual conference, NACE: 1993.

42.   Orazem, M. E.; Tribollet, B., *Electrochemical impedance spectroscopy*. John Wiley & Sons: 2017.

43.   Andrade, C.; Macias, A.; Feliu, S.; Escudero, M. L.; Gonzalez, J. A., Quantitative measurement of the corrosion rate using a small counter electrode in the boundary of passive and corroded zones of a long concrete beam. In *Corrosion Rates of Steel in Concrete*, ASTM International: 1990.

44.   ASTM, C109/C109M. In *Standard Test Method for Compressive Strength of Hydraulic Cement Mortars (Using 2-in. or 50-mm Cube Specimens)*, ASTM International: West Conshohocken PA, 2020.

45.   Presuel-Moreno, F. J.; Gutierrez, F.; Zielske, J.; Casas, V.; Wu, Y.-Y. *Analysis and estimation of service life of corrosion prevention materials using diffusion, resistivity and accelerated curing for new bridge structures: volume 1: corrosion prevention materials (monitoring and forensic examination)*; Florida. Dept. of Transportation. Research Center: 2013.

46.   (FDOT), Florida Department of Transportation. Florida Method of Test For Determining Low-Levels of Chloride in Concrete and Raw Materials. In *FM 5-516*, FDOT: Gainesville, Florida, 2018.

47.   Darwin, D.; Browning, J.; O'Reilly, M.; Locke Jr, C. E.; Virmani, Y. P. *Multiple corrosion protection systems for reinforced concrete bridge components*; University of Kansas Center for Research, Inc.: 2011.

48.   ASTM, A615/A615M-09b. In *Standard specification for deformed and plain carbon-steel bars for concrete reinforcement*, 2009.

49.   ASTM, A955/A955M In *Standard Specification for Deformed and Plain Stainless-Steel Bars for Concrete Reinforcement*, 2017.

50.   ASTM, C33 In *Standard specifications for concrete aggregates*, 2003.

51.   NACE *State of the Art Report on Corrosion-Resistant Reinforcement*; NACE International: 2018.

52.   Hurley, M. F., Corrosion initiation and propagation behavior of corrosion resistant concrete reinforcing materials. *PhDT* 2007.

53.   Serdar, M.; Meral, C.; Kunz, M.; Bjegovic, D.; Wenk, H.-R.; Monteiro, P. J., Spatial distribution of crystalline corrosion products formed during corrosion of stainless steel in concrete. *Cement and Concrete Research* 2015, *71*, 93-105.

54.   Koleva, D.; De Wit, J.; Van Breugel, K.; Veleva, L.; Van Westing, E.; Copuroglu, O.; Fraaij, A., Correlation of microstructure, electrical properties and electrochemical phenomena in reinforced mortar. Breakdown to multi-phase interface structures. Part II: Pore network, electrical properties and electrochemical response. *Materials Characterization* 2008, *59* (6), 801-815.

55.   Pérez, F.; Barrero, C.; Arnache, O.; Sánchez, L.; García, K.; Walker, A. H., Structural properties of iron phases formed on low alloy steels immersed in sodium chloride-rich solutions. *Physica B: Condensed Matter* 2009, *404* (8-11), 1347-1353.

56.   Rodrıguez, J. S.; Hernández, F. S.; González, J. G., XRD and SEM studies of the layer of corrosion products for carbon steel in various different environments in the province of Las Palmas (The Canary Islands, Spain). *Corrosion Science* 2002, *44* (11), 2425-2438.

57.   Koleva, D.; van Breugel, K.; de Wit, J.; van Westing, E.; Copuroglu, O.; Veleva, L.; Fraaij, A., Correlation of microstructure, electrical properties and electrochemical phenomena in reinforced mortar. Breakdown to multi-phase interface structures. Part I: Microstructural observations and electrical properties. *Materials Characterization* 2008, *59* (3), 290-300.

58.   Marcotte, T. D., Characterization of chloride-induced corrosion products that form in steel-reinforced cementitious materials. 2001.

59.   Scully, J. R.; Hurley, M. F.; Sharp, S. R. *Investigation of the corrosion propagation characteristics of new metallic reinforcing bars*; Virginia Transportation Research Council: 2007.

60.   Andrade, C.; Alonso, C., Test methods for on-site corrosion rate measurement of steel reinforcement in concrete by means of the polarization resistance method. *Materials and Structures* 2004, *37* (9), 623-643.

61.   Apostolopoulos, C. A.; Papadakis, V., Consequences of steel corrosion on the ductility properties of reinforcement bar. *Construction and Building Materials* 2008, *22* (12), 2316-2324.

62.   Apostolopoulos, C. A.; Papadopoulos, M., Tensile and low cycle fatigue behavior of corroded reinforcing steel bars S400. *Construction and Building Materials* 2007, *21* (4), 855-864.

63.   Zhang, R.; Castel, A.; François, R., Concrete cracking due to chloride-induced reinforcement corrosion–influence of steel–concrete interface defects due to the 'top-bar effect'. *European journal of environmental and civil engineering* 2012, *16* (3-4), 402-413.

64.   Apostolopoulos, C. A.; Papadopoulos, M.; Pantelakis, S. G., Tensile behavior of corroded reinforcing steel bars BSt 500s. *Construction and building Materials* 2006, *20* (9), 782-789.

65.   Almusallam, A. A., Effect of degree of corrosion on the properties of reinforcing steel bars. *Construction and building materials* 2001, *15* (8), 361-368.

66.   Cairns, J.; Plizzari, G. A.; Du, Y.; Law, D. W.; Franzoni, C., Mechanical properties of corrosion-damaged reinforcement. *ACI Materials Journal* 2005, *102* (4), 256.

67.   Stewart, M. G., Mechanical behaviour of pitting corrosion of flexural and shear reinforcement and its effect on structural reliability of corroding RC beams. *Structural safety* 2009, *31* (1), 19-30.

68.   Ting, S.-C.; Nowak, A. S., Effect of reinforcing steel area loss on flexural behavior of reinforced concrete beams. *Structural Journal* 1991, *88* (3), 309-314.

69.   Palsson, R.; Mirza, M. S., Mechanical response of corroded steel reinforcement of abandoned concrete bridge. *Structural Journal* 2002, *99* (2), 157-162.

70.   Castel, A.; François, R.; Arliguie, G., Mechanical behaviour of corroded reinforced concrete beams—Part 1: Experimental study of corroded beams. *Materials and Structures* 2000, *33* (9), 539-544.

71.   Du, Y. Effect of reinforcement corrosion on structural concrete ductility. University of Birmingham, 2001.

72.   Maslehuddin, M.; Allam, I. A.; Al-Sulaimani, G. J.; Al-Mana, A.; Abduljauwad, S. N., Effect of rusting of reinforcing steel on its mechanical properties and bond with concrete. *Materials Journal* 1990, *87* (5), 496-502.

73.   Allam, I. M.; Maslehuddin, M.; Saricimen, H.; Al-Mana, A. I., Influence of atmospheric corrosion on the mechanical properties of reinforcing steel. *Construction and Building Materials* 1994, *8* (1), 35-41.

74.   Morinaga, S., Remaining life of reinforced concrete structures after corrosion cracking. *Durability of Building Materials & Components* 2018, *1*, 127.

75.   Zhang, P.; Lu, M.; Li, X., The mechanical behaviour of corroded bar. *Journal of Industrial Buildings* 1995, *25* (257), 41-44.

76.   Andrade, C.; Alonso, C.; Garcia, D.; Rodriguez, J., Remaining lifetime of reinforced concrete structures: Effect of corrosion on the mechanical properties of the steel. 1991.

77.   Saifullah, M.; Clark, L., Effect of corrosion rate on the bond strength of corroded reinforcement. *Corrosion and corrosion protection of steel in concrete* 1994, 591-602.

78.   Lee, H.; Tomosawa, F.; Noguchi, T., Effects of rebar corrosion on the structural performance of singly reinforced beams. *Durability of building materials and components* 1996, *7* (1), 571-580.

79.   Fernandez, I.; Bairán, J. M.; Marí, A. R., Corrosion effects on the mechanical properties of reinforcing steel bars. Fatigue and σ–ε behavior. *Construction and Building Materials* 2015, *101*, 772-783.

80.   Tang, F.; Lin, Z.; Chen, G.; Yi, W., Three-dimensional corrosion pit measurement and statistical mechanical degradation analysis of deformed steel bars subjected to accelerated corrosion. *Construction and Building Materials* 2014, *70*, 104-117.

81.   Wu, X.; Li, L.; Li, H.; Li, B.; Ling, Z., Effect of strain level on corrosion of stainless steel bar. *Construction and Building Materials* 2018, *163*, 189-199.

82.   Azzi, M.; Benkahoul, M.; Klemberg-Sapieha, J.; Martinu, L., Corrosion and mechanical properties of duplex-treated 301 stainless steel. *Surface and Coatings Technology* 2010, *205* (5), 1557-1563.

83.   Heng, N.; Jun, X.; Changsheng, G.; Xiangjuan, Z.; Jun, L.; Xueshan, X., Effects of multi-scale microstructure on pitting corrosion and mechanical properties of high-Mn-N low-Ni superduplex stainless steel. *Rare Metal Materials and Engineering* 2012, *41* (4), 575-580.

84.   Serdar, M.; Žulj, L. V.; Bjegović, D., Long-term corrosion behaviour of stainless reinforcing steel in mortar exposed to chloride environment. *Corrosion science* 2013, *69*, 149-157.

85.   Solomon, H.; Devine, T. M., Influence of microstructure on the mechanical properties and localized corrosion of a duplex stainless steel. In *MiCon 78: Optimization of Processing, Properties, and Service Performance Through Microstructural Control*, ASTM International: 1979.

86.   Baddoo, N.; Chinien, V.; Gozzi, J.; Clarin, M.; Conrad, F.; Talja, A.; Ala-Outinen, T.; Viherma, R.; Nilimaa, H.; GARDNE, L., Structural design of cold worked austenitic stainless steel. *EUR* 2006, (21975), 1-121.

87.   Apostolopoulos, A.; Matikas, T.; Apostolopoulos, C.; Diamantogiannis, G. In *Pit corrosion examination of bare and embedded steel bar*, 10th international scientific and technical conference, Advanced Metal Materials and Technologies (AMMT), Saint Petresburg, June; Saint Petresburg, 2013; pp 25-29.

88.   Apostolopoulos, C. A.; Demis, S.; Papadakis, V. G., Chloride-induced corrosion of steel reinforcement–Mechanical performance and pit depth analysis. *Construction and Building Materials* 2013, *38*, 139-146.

89.   Bairán García, J. M.; Marí Bernat, A. R.; Ortega, H.; Rosa, J. C., Efecto del enrollado y enderezado en las propiedades mecánicas de barras de acero de diámetro medio y grande fabricadas en rollo. *Materiales de construcción* 2011, *61* (304), 559-581.

90.   El Maaddawy, T. A.; Soudki, K. A., Effectiveness of impressed current technique to simulate corrosion of steel reinforcement in concrete. *Journal of materials in civil engineering* 2003, *15* (1), 41-47.

91.   Fernández, E. M.; Escamilla, A. C.; Cánovas, M. F., Ductility of reinforcing steel with different degrees of corrosion and the 'equivalent steel'criterion. *Materiales de Construcción* 2007, *57* (286), 5-18.

92.   Garcia Alonso, M.; Alonso Alonso, M.; Andrade Perdrix, M.; Rodriguez Santiago, J., Influencia de la corrosión en las propiedades mecánicas del acero. *Hormigón y Acero* 1998, (210).

93.   Li, S.; Zhang, W.; Gu, X.; Zhu, C., Fatigue of reinforcing steel bars subjected to natural corrosion. *The Open Civil Engineering Journal* 2011, *5* (1).

94.   Martin, U.; Ress, J.; Bosch, J.; Bastidas, D., Stress corrosion cracking mechanism of AISI 316LN stainless steel rebars in chloride contaminated concrete pore solution using the slow strain rate technique. *Electrochimica Acta* 2020, *335*, 135565.

95.   Elsener, B., Half-cell potential mapping to assess repair work on RC structures. *Construction and Building Materials* 2001, *15* (2-3), 133-139.

96.   Gonzalez, J.; Benito, M.; Feliu, S.; Rodriguez, P.; Andrade, C., Suitability of assessment methods for identifying active and passive zones in reinforced concrete. *Corrosion* 1995, *51* (2), 145-152.

97.   Elsener, B.; Andrade, C.; Gulikers, J.; Polder, R.; Raupach, M., Half-cell potential measurements—Potential mapping on reinforced concrete structures. *Materials and Structures* 2003, *36* (7), 461-471.

98.   Wenger, F.; Galland, J. In *Study of corrosion of steel in concrete by electrochemical impedance measurements*, Materials Science Forum, Trans Tech Publ: 1989; pp 375-386.

99.   Wenger, F.; Galland, J., Analysis of local corrosion of large metallic structures or reinforced concrete structures by electrochemical impedance spectroscopy (EIS). *Electrochimica Acta* 1990, *35* (10), 1573-1578.

100.   Kranc, S.; Sagues, A., Computation of corrosion macrocell current distribution and electrochemical impedance of reinforcing steel in concrete. In *Computer Modeling in Corrosion*, ASTM International: 1992.

101.   Xu, F.; Xiao, Y.; Wang, S.; Li, W.; Liu, W.; Du, D., Numerical model for corrosion rate of steel reinforcement in cracked reinforced concrete structure. *Construction and Building Materials* 2018, *180*, 55-67.

102.   Presuel-Moreno, F.; Gutierrez, F. In *Corrosion Initiation and Propagation of Two Duplex Stainless Steels Embedded in Concrete*, Corrosion 2014, San Antonio, TX, NACE International: San Antonio, TX, 2014.

103.   Cao, C., 3D simulation of localized steel corrosion in chloride contaminated reinforced concrete. *Construction and Building Materials* 2014, *72*, 434-443.

104.   Sánchez, A. N.; Sagüés, A. A. *Modeling reinforced concrete durability*; Florida Department of Transportation (FDOT): 2014.

105.   Cady, P. D.; Weyers, R. E., Deterioration rates of concrete bridge decks. *Journal of Transportation Engineering* 1984, *110* (1), 34-44.

106.   (FDOT), Florida Department of Transportation. Structure Manual. In *Structure Design Guidelines*, 2020.

107.   Sagues, A. A.; Kranc, S.; Presuel-Moreno, F.; Rey, D.; Torres-Acosta, A.; Yao, L. *Corrosion forecasting for 75-year durability design of reinforced concrete*; Florida Department of Transportation Research Center: Tallahassee, FL, 2001.

108.   Bamforth, P., The derivation of input data for modelling chloride ingress from eight-year UK coastal exposure trials. *Magazine of Concrete Research* 1999, *51* (2), 87-96.

109.   Pachón-Montaño, A.; Sánchez-Montero, J.; Andrade, C.; Fullea, J.; Moreno, E.; Matres, V., Threshold concentration of chlorides in concrete for stainless steel reinforcement: Classic austenitic and new duplex stainless steel. *Construction and Building Materials* 2018, *186*, 495-502.

110.   Sagues, A. A.; Moreno, E.; Morris, W.; Andrade, C. *Carbonation in concrete and effect on steel corrosion*; 1997.

111.   Marques, P. F.; Costa, A.; Lanata, F., Service life of RC structures: chloride induced corrosion: prescriptive versus performance-based methodologies. *Materials and structures* 2012, *45* (1-2), 277-296.

112.   Kahl, S., Stainless and Stainless-Clad Reinforcement for Highway Bridge Use. Final Report (RC-1560). *Michigan Department of Transportation, Michigan* 2012.

113.   Institute, N. Stainless Steel Reinforcement.
https://www.nickelinstitute.org/~/media/Files/TechnicalLiterature/Ni_StainlessSteel-Rebar-LD.ashx.

114.   International Stainless Steel Forum, I. Stainless Steel Rebar Application.
http://www.stainlesssteelrebar.org/applications/. (accessed 11/17).

115.   Jouannais, E. Stainless Steel in Bridges and Footbridges.
http://www.constructalia.com/repository/Publications/Stainless%20Bridges%20and%20Footbridges/stainlesssteelbridges_EN.pdf.

116.   International Molybdenum Association, I. Stainless Steel Reinforcement.
https://www.imoa.info/download_files/stainless-steel/StainlessSteelReinforcement.pdf. (accessed
12/21/2018).

117.   Smith, F. N.; ENG, P. In *Stainless steel reinforcement for concrete construction*, 12th Middle East
Corrosion Conference and Exhibition, Febrero, Bahrain, 2008.

118.   SASSDA Millennium Bridge thriving after 18 Years. https://sassda.co.za/millennium-bridge-thriving-after-18-years.

119.   Wenzlick, J. D. *Evaluation of Stainless Steel Reinforcement in Bridge Decks*; Missouri. Dept. of
Transportation: 2007.

120.   Baddoo, N.; Kosmac, A., Sustainable duplex stainless steel bridges. *Duplex 2010* 2010.

121.   International Stainless Steel Forum, I. Stainless Steel in Infrastructure.
http://www.worldstainless.org/Files/issf/non-image-files/PDF/ISSF_Stainless_Steel_in_Infrastructure_English.pdf. (accessed 01/14).

122.   Hartt, W. H.; Powers, R. G.; Lysogorski, D. K.; Pardes, M.; Virmani, Y. P.; Virmani, P. *Job site
evaluation of corrosion-resistant alloys for use as reinforcement in concrete*; United States. Federal
Highway Administration. Office of Infrastructure …: 2006.

123.   Cochrane, D., Success for stainless steel. *Concrete Journal, March issue* 2003, 26-28.

124.   Gedge, G., Structural uses of stainless steel—buildings and civil engineering. *Journal of
constructional steel research* 2008, *64* (11), 1194-1198.

125.   Xing, L. Evaluation of Multiple Corrosion Protection Systems and Corrosion Inhibitors for
Reinforced Concrete Bridge Decks. University of Kansas, 2010.

126.   Mullins, G.; Sen, R.; Sagüés, A.; Winters, D.; Morton, C.; Fernandez, J.; Johnson, K.; DePianta,
V.; Vomacka, J.; Mitchell, E. *Design and construction of precast piles with stainless reinforcing steel*;
Florida. Dept. of Transportation: 2014.

127.   Forum, I. S. S. Stainless Steel Rebar Application.
http://www.stainlesssteelrebar.org/applications/. (accessed 11/17).

128.	Association, S. S. S. Cedinox - Stainless Steel. http://www.cedinox.es/en/acero-inoxidable/application/02.-civil-engineering/.

Appendix A: Bridges and related structures reinforced with stainless steel. Representative listing subject to update

#	YEAR BUILT	STRUCTURE	LOCATION	COUNTRY	Tons of SS	Max Span	LENGTH	SS TYPE	REF
1	1941	Progreso Pier	Progreso, Yucatan, Mexico.	Mexico	200	12 m	1752 m	304	8
2	1983	I-295 over Arena Drive (Bridge)	I-295 over Arena Drive in Hamilton Township, Trenton, New Jersey.	United States	22			304 Clad.	15
3	1983	Bridge S03 of 63103	S03 of WB I-696 over Lenox Rd., Ferndale and Royal Oak, Michigan, US	United States	18			304	112
4	1995	Underpass	Newcastle, Tyneside, UK	United Kingdom	265			316	113
5	1995	Schaffhausen N4 Rhine Bridge	Schaffhausen, Schaffhausen, Switzerland	Switzerland				316 L	114
6	1996	Highway 407 (Bridge) PC, Mullet Creek in Ontario, Canada.	Ontario, Canada.	Canada	11	21 m		316 LN	22
7	1998	Bridge	Ajax, Ontario, Canada	Canada	150			316 LN	113
8	1998	Box girder deck (Bridge)	Waldeck-Rousseau Bridge at Saint-Brieuc.	France				316L & 304	115
9	1998	Ramp for Garden State Parkway	New Jersey	United States	165			2205	113
10	1998	Bridge	Smith River, Oregon	United States	122			316 LN.	116
11	1998	Bridge	Hwy 401 Bridge	United States	150			316 LN.	117
12	1998	Bridge	Brush Creek, Oregon	United States	75			316 LN.	117
13	1999	Bridge S09 of 82104	M-8 (Davison Freeway) under Oakland Avenue	United States				304	112
14	1999	Pedestrian bridge	Suransuns Bridge.	Switzerland		40 m		318 LN	114
15	1999	Parking garage.	Brighton, MA	United States	21			316 LN & 304	113
16	1999	Bridge	Millennium Bridge	South Africa				304 & 3CR12	118
17	2000	Bridge S09 of 82104	Oakland over Davidson.	United States	50			316	112
18	2000	Bridge Crossing Medicine Creek	Missouri	United States				316 LN	119
19	2001	Pedestrian bridge	Millennium Bridge, York.	United Kingdom		80 m		318 LN	120
20	2001	Road-Deck Replacement in a River-Crossing tunnel.	Dartford	United Kingdom	474		7.4 m	316	121
21	2001	Bridge R12-4 of 33045	WB I-496 over Holmes Rd. and CSX RR.	United States	70			304 L.	112
22	2001	Bridge on I29.	A6059 in Grundy County (Route 6), Missouri	United States		180 m		316 LN.	122
23	2001	Replaced Bridge (MT-01-01).	U.S. 02	United States				316 LN.	122
24	2002	Pedestrian bridge.	Apate Bridge, Stockholm.	Sweden				318 LN	120
25	2002	Bridge S19 of 82191.	I-75 under London-Moore, Detroit.	United States	28			316 LN.	112
26	2002	BridgeS22 of 82191.	I-75 under Champaign, Detroit.	United States	37			316 LN.	112
27	2002	Bridge S01 of 82194.	I-75 under Cicotte Ave., Detroit.	United States	23			316 LN.	112
28	2002	Bridge crossing the Middle Fork of the Flathead River	Bridge crossing the Middle Fork of the Flathead River on U.S. 2 near Essex, Flathead County, MT.	United States				316 LN & 2205	122
29	2003	Bridge Repair (24 pier) (2 m above Tidal Zone).	Lidingo Bridge Repair Stockholm	Sweden			1100 m	318 LN	123
30	2003	Broadmeadows Bridge.	Dublin	Ireland	186	69 m	313 m	316	113
31	2003	Pedestrian bridge.	Pedro Arrupe Bridge, Bilbao.	Spain			140 m	2304	120
32	2003	Rail bridge, upgrade. (After 8 years)	Kungalv.	Sweden				318 LN	120
33	2003	Haynes Inlet Slough Bridge.	Haynes Inlet Slough Bridge, Oregon	United States	400		230 m	2205	113
34	2003	French Creek Bridge.	French Creek, Chautauqua, New York	United States	17			316 LN.	116
35	2003	Foot Bridge/Cycle Way.	Puerto Arrupe, Bilbao	Spain			45 m	2304	23
36	2004	Bridge	Jamestown	United States	20			2005	117
37	2004	Bridge	Falconer	United States	40			2005	117
38	2004	Thorold Tunnel.	Ontario, Canada	Canada	60			316 LN	113
39	2004	Road Bridge.	Siena Bridge, Ruffolo	Italy			60 m	318 LN	124
40	2004	Pedestrian bridge.	Likholefossen Bridge.	Norway			24 m	2101 LDX	120

Appendix A (Continued): Bridges and related structures reinforced with stainless steel. Representative listing subject to update

#	YEAR BUILT	STRUCTURE	LOCATION	COUNTRY	Tons of SS	Max Span	LENGTH	SS TYPE	REF
41	2004	Road bridge.	Viaduct Črni Kal.	Slovenia	110	140 m	1056 m	2101 LDX	[120]
42	2004	Bridge S27 of 82022.	I-94 over Greenfield Road, Detroit.	United States	79			304	[112]
43	2004	Belt Parkway Bridge.	Brooklyn, NY	United States	200			2205	[113]
44	2004	Bridge on I29.	Sioux Falls, South Dakota	United States	37			2205	[116]
45	2004	Bridge South Work St.	South Work St, New York	United States	40			2205	[116]
46	2004	Replaced Bridge (FL-00-01).	Road SR 679	United States				2205	[122]
47	2004	Bridges on S-54	(Chisholm Road over Tidal Creek), Charlestown County, South Carolina	United States				2205	[122]
48	2004	Bridge No. 7-22-18.21(004)	Doniphan County Bridge, K-7 over the Wolf River, Kansas	United States			75.8 m	2205	[125]
49	2004	Bridge No. 4-89-4.58(281)	Mission Creek Bridge, K-4 over Mission creek in Shawnee, Kansas	United States			27.5 m	2205	[125]
50	2005	Single arch road suspension.	Arco di Malizia, Siena	Italy				2304	[120]
51	2005	Road bridge.	Cala Galdana Bridge, Menorca.	Spain	160		45 m	318 LN	[120]
52	2005	Driscoll Bridge.	New Jersey	United States	1300			2205	[113]
53	2005	Bridge 890145	Bridge crossing the St. Lucie River at Jensen Beach, Florida	United States				2201	[122]
54	2006	Steel footbridge, with 316L.	Simone-de-Beauvoir Footbridge, Paris.	France				316 L	[115]
55	2006	Cable stayed pedestrian bridge.	Siena Bridge, Ruffolo.	Italy		60 m		2101 LDX	[120]
56	2006	Dual arch road suspension.	Piove di Sacco Bridge, Padua.	Italy	110			2304	[120]
57	2006	Arch pedestrian bridge.	Celtic Gateway Bridge, Holyhead, Wales.	United Kingdom	220	70 m	160 m	2304	[120]
58	2006	New Bridge (ND-00-01).	I-94	United States				SS Clad*	[122]
59	2006	Replaced Bridge (MI-01-02).	EBD I-496	United States				Solid SS	[122]
60	2006	Replaced Bridge (SD-01-01).	U.S. 281	United States				2205	[122]
61	2006	Replaced Bridge (SD-02-01).	Russell Avenue	United States				2205	[122]
62	2006	Replaced Bridge (SD-02-01)	Maple Avenue	United States				2205	[122]
63	2007	Woodrow Wilson Bridge.	Maryland	United States	1000			316LN & 2205	[113]
64	2008	Pedestrian bridge	Zumaia Bridge.	Spain	20	5 m Deck	28 m	318 LN	[120]
65	2008	Pearl Harbor Navy Port Facilities Project	Hawaii	United States				XM-29	[126]
66	2008	Bridge B01 of 11015.	I-94 over Galien River, Berrien County, Michigan	United States	36 & 48			304 & 316LN	[112]
67	2009	Sea wall construction.	Arabian Gulf	United Arab Emirates	4000			2205	[113]
68	2009	Cable - stayed road bridge.	Stonecutters Bridge, Hong Kong	China	2000	1 km	1596 m	318 LN	[120]
69	2009	Footbridge pillars.	Reykjavik,	Iceland		170 m		316 L	[127]
70	2009	Tension rods in a footbridge.	New Delhi	India	2.5		30m	318 LN	[127]
71	2009	Tubular pedestrian bridge.	The Helix, Marina Bay.	Singapore	220	3@65 m + 2@45 m	280 m	318 LN	[120]
72	2009	Tubular structure footbridge in 2205.	Marina Bay Pedestrian Bridge.	Singapore				318 LN	[115]
73	2009	Pedestrian arch bridge.	Sant Fruitos Bridge.	Spain				2101 LDX	[120]
74	2009	Road bridge.	Stockfjarden outlet in Flen.	Sweden				2101 LDX	[120]
75	2009	Pedestrian bridge.	Meads Reach, Bristol.	United Kingdom	75		55 m	318 LN	[120]
76	2009	Orrhammarvägen Road Bridge.	Orrehammar, Flen	Sweden	12			2101 LDX	[23]
77	2009	East Montpelier Bridge	Vermont	United States	17			2304	[32]
78	2009	Hennepin Counties Bridge	Minnesota	United States	15			2304	[32]
79	2010	Road bridge over river.	Second Gateway Bridge, Brisbane	Australia		260 m*	1627 m	2101 LDX	[120]
80	2010	Alexander Hamilton Bridge	New York	United States	750			SS	[32]

Appendix A (Continued): Bridges and related structures reinforced with stainless steel. Representative listing subject to update

#	YEAR BUILT	STRUCTURE	LOCATION	COUNTRY	Tons of SS	Max Span	LENGTH	SS TYPE	REF
81	2010	Cameron Heights Dr. Bridge.	Edmonton, Alberta	Canada	190			2304	113
82	2010	Bridge S05 of 13081.	EB and WB I-94 over Riverside Drive, Battle Creek, Michigan	United States	31			2304	112
83	2010	Rabbit Hill Road Bridge	Alberta	Canada	140			2304	32
84	2010	Bridge.	Hastings, Minnesota	United States	365			2304	113
85	2010	Rehabilitation of the Existing Bridge Carrying Sherburne Road Over I-95	City of Portsmouth, New Hampshire	United States				2304	32
86	2010	Cameron Heights Bridge	Alberta	Canada	190			2304	32
87	2011	New Farm Riverwalk.	New Farm Riverwalk	Australia	158			316 L	128
88	2011	S. Saskatchewan River Bridge.	Medicine Hat, AB	Canada	194			2304	113
89	2011	Railway Bridge structure.	Añorga,San Sebastian	Spain	130		20 m	2101 LDX	114
90	2011	Pedestrian bridge.	Harbor Drive Pedestrian Bridge, San Diego, California	United States			162 m	318 LN	120
91	2011	Bridge B01 of 83011.	M-37 over Pine River, Wexford County, Michigan	United States	47			2304	112
92	2011	Road Bridge.	Nynashamn	Sweden				2101 LDX	23
93	2011	Riverwalk	Riverwalk, Brisbane	Australia				2304	128
94	2011	Bridge on HWY 22, 5km E. of Drayton Valley	North Saskatchewan River	Canada	170			SS	32
95	2011	Taconic State Parkway NB Bridge	New York	United States	175			SS	32
96	2011	Reconstruction and 3 New Bridges, 2 Replacements, 3 Rehabilitations, Extend 2 Structures & Rehab Wingwalls at 1 Structure Project,	New York	United States	158			2304	32
97	2011	Athabasca River Bridge	Alberta	Canada			472 m	SS	32
98	2012	Motorway flyover (Cladding).	Kerensheide,	Netherlands			1200 m	316 L	127
99	2012	Pedestrian and cycling bridge.	Sölvesborg,	Sweden	150		756 m @ 3.5 m Wide	2101 LDX	127
100	2012	Road bridge renewal.	Allt Chonoglais, Scotland	United Kingdom	67			2304	127
101	2012	Sakonnet River Bridge	Rhode Island	United States	800			2205	113
102	2012	Road bridge refurbishment.	Nou, Itoigawa, Niigata Prefecture	Japan	60		70 m	410	15
103	2013	Pre-assembled pedestrian bridge.	Malmö	Sweden	12		40 m Length and Width 6.5 m	316 L	15
104	2014	Hurdman Bridge.	Hwy 417, Ottawa	Canada	323			2205	113
105	2014	Kenaston Overpass.	Winnipeg, Manitoba	Canada	200			2304	113
106	2014	Bridge	Ottawa, Ontario,	Canada				2205	114
107	2014	Breakwater repair.	Bayonne Breakwater,	France	130			318 LN	114
108	2014	Mediterranean High way.	Spanish Coast	Spain				SS*	128
109	2014	New deck and barrier walls	Hurdman Bridge, Highway 417, Ontario	Canada	320			2205	127
110	2014	Coastal Protection at Cromer	Coastal Protection at Cromer	United Kingdom	335			2304	127
111	2014	Lafayette Bridge	St. Paul, Minnesota	United States	1950			SS	32
112	2015	Mega project in Canada.	Edmonton, Alberta	Canada	6000 (est.)		47 Bridges	2304	128
113	2016	River delta crossing.	Hong Kong, Macau - China	China		Span 460 m	Bridge Section 29.6 Km	2304	114
114	2016	Queensferry Crossing.	Forth Replacement Crossing	Scotland			2700 m @ 40 m Wide	Duplex*	128

Appendix B: U.S., European, and UNA representative and approximate grade designation

Name	AISI Number / U.S. Common Name	European	UNS Number	Type	PREN (Approx.)
F1	405		S40500	Ferritic	13***
F2	3CR12		S40977	Ferritic	11*
F3	11% Cr	1.4003		Ferritic	11*
F4	3CR12 – TOP12	1.4003	S41003	Ferritic	11*
F5	430	1.4016	S43000	Ferritic	17*
F6	410		S41000	Martensitic	13***

Name	AISI Number / U.S. Common Name	European	UNS Number	Type	PREN (Approx.)
A1	SSC-6MO	AL-6XN	N08367	Austenitic	47##
A2	XM-29 (Nitronic 33)		S24000	Austenitic	23***
A3	18-2Mn / XM-28		S24100	Austenitic	24-28**
A4	302	1.4310	S30200	Austenitic	19***
A5	304	1.4301	S30400	Austenitic	19*
A6	304L - X2CrNi18-9	1.4306/7	S30403	Austenitic	19*
A7	254SMO		S31254	Austenitic	44*
A8	315	1.4541	S32100	Austenitic	19***
A9	316	1.4401	S31600	Austenitic	28*
A10	316L	1.4404	S31603	Austenitic	28*
A11	316LN	1.4429	S31653	Austenitic	28*
A12	317LN	1.4438	S31753	Austenitic	33***
A13	204Cu	1.4597	S20430	Austenitic	19#
A14	304 LN	1.4311	S30453	Austenitic	22*

Name	AISI Number / U.S. Common Name	European	UNS Number	Type	PREN (Approx.)
D1	2101 LDX	1.4162	S32101	Duplex	26*
D2	2205		S32205	Duplex	34*
D3	2304	1.4362	S32304	Duplex	26*
D4	318LN	1.4462	S31803	Duplex	34*

* Source: https://www.bssa.org.uk/topics.php?article=111

** Source: [34]

*** Source: https://www.makeitfrom.com/

Source: http://www.gual.es/

Source: https://www.atimetals.com

Appendix C

The Corrosion Propagation Stage of Stainless Steel Concrete Reinforcement: A Review

Julio Saire Yanez, Christopher L. Alexander, Alberto Sagüés

ABSTRACT:

Stainless steel (SS) reinforcement is increasingly used to control corrosion of reinforced concrete in aggressive marine and deicing salt service. It is well established that the chloride threshold of SS is greater than that of plain steel (PS) rebar, yielding substantially increased duration of the corrosion initiation stage. Much less known, however, is if there is a similar benefit to the duration (t_p) of the corrosion propagation stage. Thus, credit for increased t_p in durability forecasts for SS use tends to be conservatively limited. To reduce that uncertainty the literature was gleaned for the few instances where SS reinforcement had reached, and preferably completed, the corrosion propagation stage. Particular attention was given to actual structural service experience, outdoor tests, and realistic laboratory conditions. Only a single case of actual service in a structure was found for which tp could be estimated, albeit indirectly. The result suggests a t_p of several decades for the case of austenitic Cr-Ni rebar in marine service. Outdoor tests without unnatural acceleration showed a few cases where t_p was reached, but only for straight Cr ferritic alloys which showed some limited improvement over t_p for PS. With the additional insight from laboratory tests, it was concluded that SS rebar made with high pitting resistant grades, and thoroughly descaled, had a positive outlook for propagation stage durations that substantially exceed those of PS rebar. Quantification of that improvement is much in need of further field and laboratory assessment.

INTRODUCTION

Corrosion of reinforcing steel bars (rebar) in concrete is a major limiting factor in the durability of global infrastructure. One of the primary causes is chloride ions present in the environment such as in marine exposure conditions or highway deicing salts. Chloride ions diffuse into the concrete and eventually reach a critical concentration threshold C_T at the rebar depth to initiate corrosion. The corrosion products of the steel can be several times greater in volume than the steel itself, causing tensile stresses within the concrete that lead to concrete cracks and spalls. Progressive steel loss of the cross-section and reduced bond to the concrete further reduce structural strength. Either singly or in combination, these processes gradually decrease the ability of the structure to provide its intended service. Eventually the structure would reach a serviceability limit state (SLS) where extensive repairs or rehabilitation are needed.

The traditional approach used to estimate the service life of reinforced concrete considers two distinct stages. The first is the initiation stage, with a duration t_i for the period from placement in service until C_T is reached. The value of ti is governed by the value of CT and the transport processes of chloride ions into the concrete. The second is the corrosion propagation stage, with a duration tp for the period from the end of the initiation stage until the SLS is reached [1]. The service life duration then is ts = ti+tp. In many chloride exposure service conditions, tp for the widely used uncoated plain steel (PS) reinforcement tends to be only a few years [2] [3] and difficult to extend by simple engineering design. In contrast, in the absence of local deficiencies such as preexisting concrete cracks or poor consolidation ti can be increased considerably (to many decades) by concrete impermeability improvement via mixture proportioning changes, and by thicker rebar cover thickness [4]. Thus, traditional design to improve durability has emphasized manipulating those variables. There are limits however to that approach given the inevitability of local deficiencies in any structure, the cost associated with specialized concrete mixtures, and strength constraints in the use of thick cover which may themselves increase concrete crack incidence. For these reasons, over the last two decades, the use of more corrosion-resistant alternatives, such as stainless steel (SS) reinforcement has received increasing attention, to the extent that now it is included in some state Departments of Transportation specifications [5] [6] .It is well-established that for many SSs, C_T can be an order-of-magnitude greater than that for PS [7] [8], a relative increase amply outside typical uncertainty in C_T values [9].

A greater C_T than that of PS results in a substantial increase in ti estimates for a given concrete permeability and cover value [7] [10]. Additionally, design goals may be achieved without the need for undesirably thick cover or costly mixture proportions, and with greater tolerance for local concrete deficiencies. Therefore, despite the higher cost of SS compared with PS, life cycle cost assessments find that the benefits due to increased corrosion resistance can amply outweigh the initial added costs [11]. The recent trend is in contrast with historic reluctance to use SS as concrete reinforcement, which for many decades was limited to only one major structure, the Progreso pier in Mexico, addressed in detail later in this review.

While the SS benefit from increasing t_i is well-understood and quantifiable to a good extent, little information exists as to whether there is improvement also from increasing tp. Knowledge is scarce of the mechanisms, rates, and morphology of corrosion that may lead up to reaching a service limit state for SS rebar [10] [12]. That scarcity exists because in experimental or field studies with natural chloride exposure the value of C_T was often not reachable within the time frame of the tests - or not ever, if C_T was greater than the chloride content of the concrete at the external surface, CS. Thus, in those cases much of the findings were limited to simply establishing a low bound value for C_T with little if any insight on what happened during the propagation state. Even if corrosion had initiated and some information on corrosion rates was obtained, the investigation might have often ended before a recognizable SLS was reached [13]. Therefore, much of the prior information available on the propagation stage is derived from electrochemically accelerated experiments [2] which rely on hypotheses about their applicability to actual service conditions.

The scarcity of knowledge invites speculation as to what the behavior during the propagation stage may be for SS reinforced concrete. Damage progression could be very slow given the inherent corrosion resistance of SS, resulting in t_p values in the order of decades compared with only a few years for PS rebar. However, that outcome is not assured as there are other factors that could negate at least some of the possible advantages of SS in the propagation stage. For example, corrosion of SS once its high C_T value is reached will proceed at chloride contamination levels that are much greater than those usually experienced by PS at that stage. Thus, the combined effect of corrosion resistance and medium aggressiveness might be comparable in both cases, and lead to similar corrosion rates. Likewise, the degree of corrosion localization in SS could exceed that of PS, potentially promoting earlier mechanical failure in the former, if that SLS modality were the important one instead of concrete cracking/spalling. That possibility merits attention, as Hurley and Scully showed that the corrosion of stainless steel in electrochemically accelerated pore solutions tests tended to propagate radially more so than laterally along the surface [10]. Thus, a deeper pit configuration may be more prevalent for SS than it is for PS rebar with consequent impact on the type of SLS.

Uncertainty in the value of tp for SS rebar can have appreciable impact on the projected service life of new structures. That in turn translates to added cost in the case of overly conservative design for pessimistic tp forecasts, or increased risk for unduly optimistic assumptions. The literature review presented here is intended to be a first step to resolve that uncertainty. The search was focused on finding evidence of the mode and rate of corrosion of SS in concrete during the propagation stage, on the duration of that stage if found to have been completed, and on the observed or likely applicable SLS.

METHODOLOGY

Sources accessed were classified per one or more of the following categories of SS rebar exposure:

- Actual structural service.
- Outdoors/service environment tests of SS reinforced concrete.
- Laboratory tests in concrete or simulated pore solutions.

Those categories reflect a progression from most relevant from an engineering application standpoint but less documented, to greater insight on operating mechanisms while more removed from practice.

The listing also indicates whether the end of the corrosion initiation stage was reached and if so whether the end of the propagation stage had been reached as well. That latter attribute was selected for detailed discussion, in particular if related to a structure in service or natural/test yard exposures.

The review is not intended to be exhaustive but rather highlights examples of notable work. Moreover, given the scope of this work and the availability of prior and recent detailed reviews on the performance of SS reinforcement during the initiation stage [12, 13, 14, 8, 15, 16, 17], conclusions on issues pertaining primarily to that stage and related alloy rankings will not be repeated here. When documented, it was noted whether the SS rebar surface had been thoroughly descaled and freed of surface contamination by pickling and/or so-called passivation procedures [8, 18, 19, 20, 21], as that condition is understood to lead to better performance. Moreover, with few exceptions the review considers only solid SS rebar that is normally commercially available. The reader is referred to other sources [22, 23, 24, 16, 25] for work on the propagation stage of SS-clad rebar, which is not currently in production. The review also focuses on the use of the rebar as reinforcement. SS applications to pre-or post-tensioned applications is an emerging issue that has been considered elsewhere [26] [27].

The findings of the literature review (up to ~2018) are presented next. Relevant alloy designations are presented in Table 1. Frequent reference is made to the Pitting Resistance Equivalence Number (PREN) index, a merit figure of a SS's ability to resist pitting corrosion. The index is usually computed as PREN = wt%Cr + 3.3·wt%Mo + 16·wt%N [8], although there is some variability of multiplier factors among users. Alloys are sometimes referred to as "High" or "Low" depending on whether their PREN exceeds 18 or not. Alloys containing little addition other than Cr are sometimes referred to as "Straight Cr" SSs.

Table 1: U.S., European and UNS representative/approximate grade designations for SS alloys.

AISI Number / U.S. Common Type Name	European	UNS Number	Representative Main Element Content (wt.% - Fe Balance)					Type	PREN (Approx.)
			Cr	Ni	Mo	N	Other		
405	-	S40500	13	--	-	-		Ferritic###	13***
3CR12		S40977	12.5	1	-	0.03			11*
11% Cr	1.4003		10.5	-	-	-			11*
3CR12 – TOP12	1.4003	S41003	10.5	-	-	-			11*
430	1.4016	S43000	16.5	-	-	-			17*
410		S41000	12.5	0.75	-				13***
SSC-6MO	AL-6XN	N08367	21	24.5	6.5	0.2		Austenitic	47##
XM-29 (Nitronic 33)		S24000	18	3.1	-	0.3	Mn: 13		23***
18-2Mn / XM-28		S24100	18	1	-	0.3	Mn:13		24-28**
302	1.4319	S30200	18	9	-	-			19***
304	1.4301	S30400	19	9	-	0.05			19*
304L - X2CrNi18-9	1.4306/7	S30403	19	10	-	0.05			19*
254SMO		S31254	20	18	6	0.2			44*
315	1.4541	S32100?	18	8.25	1.25	-			19***
316	1.4401	S31600	17	12	2.5	0.05			28*
316L	1.4404	S31603	17	12	2.5	0.05	C<0.03		28*
316LN	1.4429	S31653	17	12	2.5	0.2	C<0.03		28*
317LN	1.4438	S31753	18	14	4.2	0.15	C<0.03		33***
204Cu	1.4597	S20430	16.5	2.5	0.2	0.2			19#
304 LN	1.4311	S30453	19	10	-	0.13	C<0.0		22*
2101 LDX	1.4162	S32101	21.5	1.5	0.3	0.22	C<0.0	Duplex	26*
2205	1.4462	S32205?	22	5.7	3.1	0.17			34*
2304	1.4362	S32304	23	4.8	0.3	0.1			26*
318LN (2205)	1.4462	S31803?	22	5.5	3	0.15	C~0.03		34*

* Source: https://www.bssa.org.uk/topics.php?article=111
** Source: [28]
*** Source: https://www.makeitfrom.com/
# Source: http://www.gual.es/
Source: https://www.atimetals.com
Broadly used term; lower Cr content grades may have predominantly Martensitic microstructure.

Frequent comparison is also made of chloride ion content and C_T values of SS and PS. Depending on how those were reported in the cited sources the values are given as mass of Cl-ion as percentage of the cement mass in the concrete (%CmtWt), or as percentage of the total concrete mass (%CcrWt). For rough comparisons and recognizing that considerable variability exists [9], C_T for PS may be thought to be ~0.4%CmtWt, which corresponds to ~0.06 %CcrWt for a generic concrete having 350 kg/m^3 cement and density 2300 kg/m^3. Some of the investigations cited relied on half-cell potential (HCP) surveys [29] as a means to detect corrosion condition of the SS rebar. Implicit in those cases was the assumption that HCP measurements conducted using methodology and criteria established for PS rebar apply to SS rebar as well. That assumption is yet to be adequately demonstrated so interpretation of those measurements should be regarded as tentative for now.

RESULTS

Actual structural service

More than 100 bridges and related structures or sizable parts of structures have been built with SS reinforcement during the last 80 years. As shown in Figure 1, after a long hiatus following the Progreso pier construction, the pace of utilization of SS increased markedly during the last two decades without sign of abatement. This fast-growing tendency of the SS usage in structures emerged as designers become more persuaded of the potential economic benefits of corrosion-resistant rebar, and the greater commercial availability of SS rebar. Current implementation of SS rebar in the field is evolving with various levels of quality assurance and control of rebar condition [15], [30]. Those economic considerations are often a determining factor in the selection of rebar materials [16].
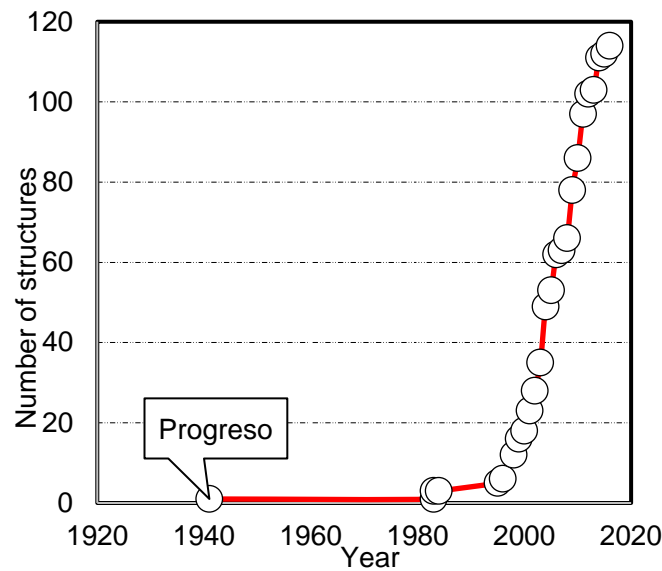
Figure 1: Cumulative worldwide tally of bridges with SS rebar.

The oldest major structure with SS reinforcement, Progreso pier in Mexico has been in service and largely functional for ~80 years since its completion. While functionally superseded by a newly built parallel viaduct, the historic Pier is frequently cited as illustrating the successful application of SS rebar for achieving long term durability. Because of its archival significance and uniqueness, Pier investigations are given detailed attention next, followed with a sampling of experience from other structures. It is noted that while there is abundant literature on the use of SS rebar in new structures, there are relatively few other reports on actual performance evaluation after the structures were in service for an appreciably long period, so the selection is accordingly limited.

Progreso Pier, Mexico, 1941

The Progreso pier is part of the installations of the Port of Progreso in the Yucatan peninsula, located at Progreso, State of Yucatan, Mexico, latitude +21° 20' and longitude 89° 40' on the Gulf of Mexico. The yearly average temperature is 26 °C and water Cl- content is ~20,000 ppm [31]. The initial request for bids by the Mexican government specified a structure with "low corrosion-induced damage" [32]. The Danish company Christiani & Nielsen addressed that requirement by specifying the use of mass concrete and SS rebar and built the pier during the period 1937 – 1941. The original 1941 Pier includes an Embankment, a Viaduct, and a Pier Head. The entire structure is ~2.1 km long, 9.5 m wide in the Viaduct and 50 m wide in the Pier Head. The substructure is arches with horizontal substructure crossbeams beneath the joint of consecutive arches. Those crossbeams are the main SS-reinforced elements, with their lower side about 1 m over seawater, resting on partially immersed columns that connect to underwater footers. A typical crossbeam is 9.5 m long, 3 m high and 2.5 m wide, and contains fourteen #10 (30 mm diameter) rebar made of solid type 304 SS, for a total of ~200,000 kg (200 MT) of SS for the entire Pier. The reinforcement was reported to be smooth with no corrugations. No information however appears to be available on the important issue of whether any mill scale was present on the bars. Rebar concrete cover values per a recent evaluation [33] were 0.2 m on bottom and sides of the beam and 0.08 m at the ends. Based on the as-built report, the cross beams were cast with vibrated mass concrete and the purposed of the reinforcement was to control cracks that may be promoted by shrinkage and temperature fluctuations [32]. Detailed documented evaluations of corrosion performance started in the 1990s.

A 1999 consulting firm report [31] describes findings from evaluation of the SS reinforcement in two arches at spans 8 and 9, a column between spans 9 and 10 [31]] and visual superficial examination of spans 1 to 7. Visual examination revealed a few longitudinal cracks (width <1mm) but without visible signs of corrosion. At two spots in Pier No.9 short segments of rebar (ends of hairpins) were found to be directly exposed to the environment, without any cover, presumably due to previous mechanical damage. At that location, the reinforcement was visibly corroded with a reduced cross-sectional area of about 2/3 of the original size. Exploratory concrete breakage on the hairpins revealed only light corrosion on a fraction of the rebar surface in regions of low cover (~18-28 mm). After concrete removal at two other spots in the same pier, most of the rebar did not show corrosion at a cover depth of 32 mm, and a bar with 105 mm cover showed no corrosion at all. Chloride penetration profiles were essentially flat, with near-saturation levels typically ~1 %CcrWt, with as much as 1.92 %CcrWt up to a depth of ~100 mm. Those values are much greater than the CT normally assumed for PS [9]. The observation of only minor evidence of corrosion on the SS bars under those conditions was thus viewed by the authors as confirming high corrosion resistance of SS in that service.

Follow up work by another team was published in 2002 [34] and 2004 [35], addressing continued examination of pier No. 9. Coring confirmed high chloride levels (1-2.5 %CcrWt) with nearly flat concentration profiles. Concrete carbonation depth was <1.5 mm, typical of moist marine exposure in bridge substructure [36]. On-site concrete resistivity measurements showed values ranging from 0.6 kΩ-cm to 2.5 kΩ-cm in the entire girder surface, consistent with the concrete being highly permeable and the deep chloride penetration noted above. Electrochemical measurements were indicative of some corrosion in progress. The steel showed highly negative half-cell potentials (HCP), down to -553mV CSE (Copper Sulfate Electrode), interpreted as associated with ongoing active corrosion with the qualification noted earlier. Corrosion rates estimated from linear polarization resistance (LPR) measurements with a guard ring counter-electrode ranged from 0.1 µA/cm2 to 0.87 µA/cm2. For CS, such values would be representative of nearly passive and actively corroding behavior at the respective regions being sampled, and the same assignation was assumed here. Inspection of the actual SS bars in normal exposure was not conducted, but a core was extracted containing embedded rebar near a part of the rebar that had been previously directly exposed to the environment. That sample showed "a few rusty spots" identified as pitting corrosion. It was concluded that there was "enough quantitative information to suspect that the SS bars from the girders are exposed to a high chloride concentration that is possibly causing their depassivation", a more cautious message than that of the previous investigation. Of interest to the possibility of presence of modes of failure not commonly encountered in PS rebar, damage to the hook-bent portion of an externally exposed bar was deemed to be in the form of environmentally assisted cracking (EAC), indicating as well that it was not clear whether it took place before or after the bent steel was directly exposed to the external environment.

Evaluation continued in a study conducted by Mexican government agencies, published in 2005, on condition assessment of the Pier Head [37] and load capacity testing of three arches of the Viaduct [38]. Cores were taken from cross beams of piers 9, 12, 13, 30, 34, and 164. As in the previous study, carbonation was found to be negligible. Chloride content in Piers 12, 13, 30, and 34 at the rebar depth was high but below 1 %CcrWt , a value that could be tentatively considered to be in the order of CT for type 304 SS in the present case. Accordingly, the risk of corrosion was interpreted to be nil for those locations. The survey of the Pier Viaduct revealed multiple cracks, which were assumed to be structural cracks and not corrosion-induced. Spalls and concrete damage in the cross girders of the Pier Head zone, where SS bars were found to be exposed, were deemed to be produced by lateral loads and boat impact and thus not due to corrosion. In contrast, cracks observed in the Pier Head at cross beams of arches 161, 163,164, and 165 were deemed to be the result of rebar corrosion. That identification was based on multiple indirect observations: high chloride content (~1.5 %CcrWt) at rebar depth in three cores extracted from No. 164; the cracks being parallel to the SS bar; water used for core drilling having seeped into bottom cracks that were also parallel to the SS bar - an indication of extensive delamination; and evidence of concrete discoloration along the crack albeit not accompanied by outright rust accumulation.

A recent (2018) Mexican transportation agency report [33] compiled work to assess the durability, structural load capacity, and supplemental Carbon fiber reinforced polymer (CFRP) reinforcement of the Pier Viaduct. Yearly visual inspection records from 2002-13 were considered. The surveys showed increasing cracking incidence, to the extent that it was deemed that the structure has reached the end of its service life for heavy loads. A recently built parallel viaduct now serves that function. The still-standing historic structure had been subject to repairs including CFRP strips at arches and pile wrapping reinforcement, but cracks had developed on some of it afterwards. The deterioration however was ascribed primarily to increasing traffic load on account of a pier extension having been built at the end of the 1980s. Corrosion of reinforcement was mentioned, but not identified as the primary cause of the deterioration.

This large structure is the main exponent, and the most potentially informative source, of long-term performance of SS rebar in aggressive, actual service conditions. The investigations noted above found significant structural deterioration of the now 80-year-old Pier, but it was most often ascribed to increased traffic loading and rarely to rebar corrosion. That is illustrated by the notional damage function summary in Figure 2, comparing age-cumulative incidence of damage not attributed to corrosion (manifested by cracks, stains, and structural settlement) in arches [23], with damage in the form of cracks attributed to corrosion in crossbeams. By 2007, the damaged 171-arch tally reached 100%. In contrast only 2.3% or four cross beams (Nos. 161,163,164,165) out of 172 presented corrosion-attributed cracks [33]. It should be noted that even those attributions of corrosion-induced damage were not fully established, as there was no direct evidence that cracking of the concrete cover was caused anywhere by expansive products of the SS bars. In the aforementioned works there was some very limited direct observation of embedded rebar corrosion, in one study [34, 35] apparently limited to only one specimen, and in another [31] referring to discoloration in a few specimens. However, those sources did not indicate that the extent of corrosion was sufficient to cause concrete cracks, or to have resulted in the appearance of corrosion products at the external concrete surface. The two cases of SS rebar that had corroded severely corresponded to two locations where the rebar cover was locally missing for a short distance (several cm) and where the SS had been directly exposed to seawater for a period that may have been decades long [31] [34, 35]. The evidence there was not indicative that the cover missing was from a corrosion spall or other corrosion-induced result, but rather possibly from an external impact such as a ship docking. Much of the other evidence in support of SS corrosion having been enough to produce significant damage, was only indirect. That included the corrosion rates, estimated from LPR tests, that had values that could cause concrete cracking if the rebar were PS [34, 35], and the HCP measurements negative enough to suggest severe corrosion [34, 35] if the rebar were PS. There were also the instances of chloride content values at the rebar depth that would meet or exceed ~1 %CcrWt,, the C_T value considered above for SS. That situation was encountered for one of the cases of concrete cracking and thought to exist at three other comparable locations [34, 35] [37] . However, as no rebars were extracted at the cracked locations, direct confirmation is still lacking that the cracks were actually associated with corrosion product accumulation or other distress of those rebars.

Even if conservatively admitting that some corrosion induced concrete damage existed, the overall performance over an 80-year span is encouraging for the use of SS rebar reinforcement. That is especially so considering that alloy variants commonly specified today (e.g. type 316L SS or duplex type 2205) are anticipated to be more corrosion-resistant than the type 304 SS used in the Pier. A tentative bounding estimate of the duration of the corrosion propagation stage based on the overall findings for this structure is presented in the Discussion section.
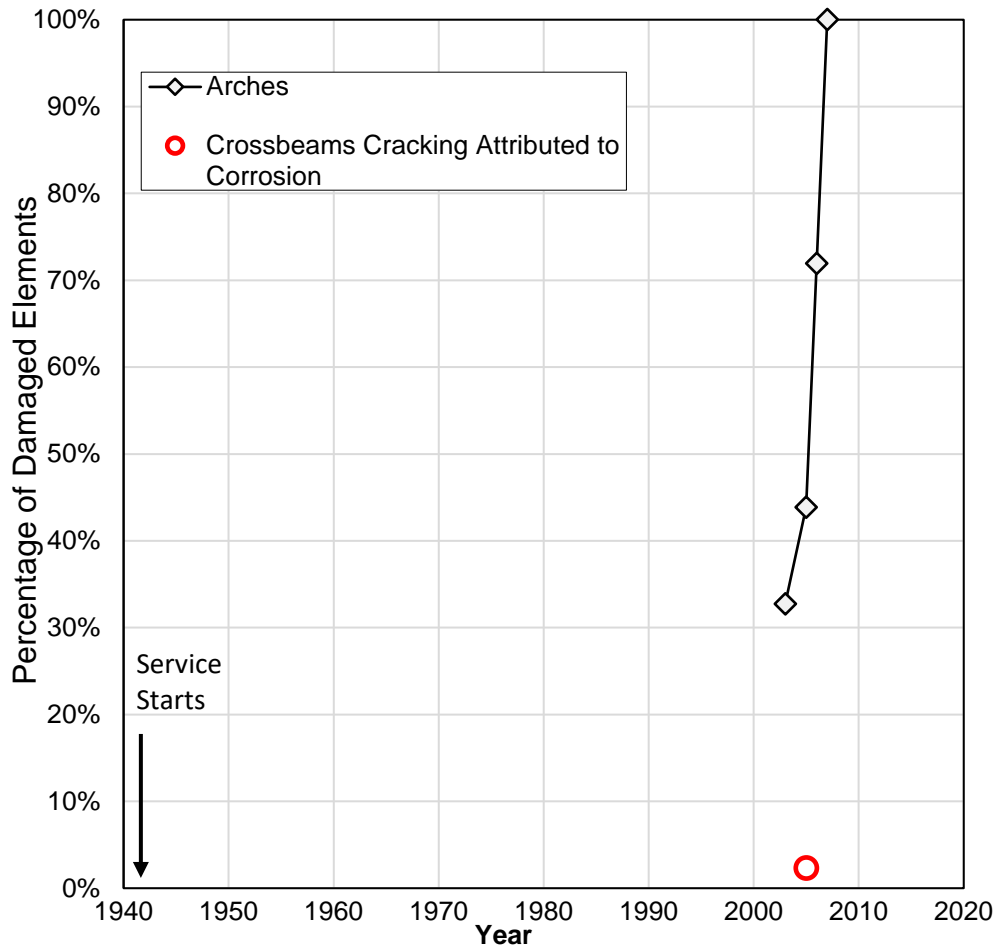
Figure 2: Notional damage function showing the time evolution of ratio of Progreso Pier arches showing distress from all sources (◊), and of crossbeams with cracking attributed to corrosion damage (O).

Other structures

This selection, listed by building date, includes structures with sizable amounts of SS and for which some record of corrosion performance from follow-up examinations is available. Significance to propagation stage behavior is largely indirect, but these entries still merit inclusion given the engineering importance of actual service experience.

Bridge S03 of WB I-696, over Lenox Rd. Michigan, U.S., was built ca. 1983 and placed on deicing salt exposure service. The deck contains ~27 MT of solid type 304 SS rebar [17]. This structure was inspected at age 10 years visually and by coring into the rebar at on- and off-crack locations, as thermal and shrinkage deck cracks were observed. With concrete covers ranging from 72 to 165 mm, chloride content at rebar depth was 0.54 %CmtWt, already in the order of C_T values for PS rebar. Only some minor corrosion stains were reported for the SS rebar surface and no corrosion induced damage was identified at either sound or cracked concrete locations. A second inspection took place after 26 years of service; no cracks of deterioration resulting from corrosion of SS reinforcement were reported at that age either [39]. In summary, SS rebar performance was found to be adequate after 26 years of service, among the longest actual performance periods documented other than for the Progreso pier.

The I-295 Bridge over Arena Drive (Southbound), Trenton, New Jersey, U.S., was built ca 1983 and experiences deicing salt exposure. The deck contains ~20 MT of type 304 SS - Clad rebar [17] [18]. Crack and delamination surveys including 4 cores and chloride profiling were performed at age 10 years. The chloride content at rebar depth was low, <0.013 %CcrWt, below CT values for PS. Not unexpectedly nine rebar segments extracted were found to be in excellent condition with no corrosion of the SS cladding observed. It is noted however that despite the low chloride content corrosion was detected under a plastic end cap where the carbon steel core of the clad bar was exposed. Overall, performance after 10 years met design and service expectations.

Mullet Creek Bridge over Highway 407, Ontario, was built ca. 1996 for service under deicing salt exposure. The bridge deck and barrier walls contain ~11 MT of solid type 316 LN SS rebar, size #4, with specified concrete cover of 80 ± 20 mm [40]. Two early age condition evaluations (<1 year) were made. In the first, three months of concrete placement deck cracks were noted, and minor cracking elsewhere was ascribed to normal shrinkage. The HCPs were -0.41 V (CSE) on average suggesting that the SS surface had not yet achieved a fully passive condition, also supported by LPR results. By the second evaluation (age 1 year) the HCPs had reached -0.14 to -0.26 V (CSE), suggestive of having achieved a passive condition. Overall, the findings are simply indicative of absence of unexpected issues, but included here given the dearth of actual service performance evaluations on the record.

Bridge A6059 in Grundy County, Missouri., U.S., was built ca. 2001 and serves under deicing salt exposure. The deck contains type 316 LN ss rebar [41]. A condition survey was performed 5 years after concrete placement. A nearby conventional comparison bridge deck (Bridge A6060) was built with epoxy-coated rebar and evaluated simultaneously. There was no delamination or spalling found on the surface of either bridge deck, and very little cracking damage on either the SS or the conventional deck. Chloride profile data showed one location well above the CT value for PS at the level of the SS bars. HCP mapping results were uncertain, but overall observations suggested no SS rebar corrosion in progress despite the instance of high local chloride content.

The Doniphan County and Mission Creek Bridges, Kansas, U.S., were built ca. 2004 and are exposed to deicing salt. Both decks both contain type 2205 SS, with pickled surface condition and 65 mm clear cover [42]. Conditions were monitored by HCP mapping over a 4-year period following construction. In addition, test slabs simulating the bridge rebar layout and curing conditions were exposed for the same period to chloride ponding on an outdoor test yard. For both bridges HCPs measured shortly after casting were in the range from -0.050 V to -200 V (CSE), interpreted as being indicative of a passive condition. Four years after casting potential measurements in the central regions of the decks were still more positive that -0.2 V. However, HCPs near the soil-buried abutments tended to be more negative (as much as -0.5 V). That drop was attributed not necessarily to corrosion but rather to restricted access of oxygen in locations where the concrete deck is in contact with soil, combined with contact with mild steel forms leftover from construction in that region. While over a short period, the reported positive performance is of interest since it documents service of a duplex stainless steel, a category for which extended experience has been less reported than for austenitic stainless steel.

Experience in a class of structures (swimming pools) with austenitic SS bars not embedded in concrete is nevertheless noted here, as it concerns notorious catastrophic fracture of load bearing SS [43], leading to loss of human life in two instances. In one case (Uster, Switzerland in 1985 [44]) SS hangers in the roof failed with resulting ceiling collapse and 12 fatalities. In another instance SS threaded bars broke up and enabled a swimming pool's ceiling and air channels collapse in Steenwijk, The Netherlands, in 2001 [44]. In a third case SS bolts failed and dropped heavy components into a heated swimming pool in Tilburg, The Netherlands, in 2011, with one fatality [44]. Here and for the other two failures it was concluded that EAC of SS load bearing components was the cause of this accidents. The likely corrosion agent for this and the other failures was identified as volatile chlorine compounds (originating from the heated pool water) that condensate on the SS surface, leading to high, evaporation concentrated chloride ion levels and some extent of acidification. Notably, the failures occurred at a moderate temperature range previously considered to be of relatively low risk for EAC of SS [45] [46] [47]. The EAC modes of failure cited for these incidents are more likely to affect steel of higher strength than that normally used for regular rebar service, and possibly only very high chloride concentrations. However, it is recalled that damage attribution to some form of EAC was reported for directly exposed steel at the Progreso pier [34] and the possible relevance of this mechanism is discussed later on.

Outdoors/service environment tests of SS reinforced concrete.

This selection highlights some of the few cases where propagation stage progress, and even its completion, has been documented for SS-reinforced concrete exposed to the environment without electrochemical acceleration or other marked laboratory constraints. Conditions and findings are accordingly described in some detail, and further summarized in Table 2.

Building Research Establishment (BRE) tests (ca 1970s - 90s)

Starting in the 1970's the British BRE conducted three series of extensive tests that yielded otherwise rare information of damage taking place during the corrosion propagation stage under non-accelerated exposure in external environments.

A first series of tests took place over a period of 12.5 years in Langstone Harbour near Portsmouth, U.K. on the south coast of England [48]. Reinforcement was round bars (# 4) of PS and type 316 SS, the latter surface condition not reported but in photographs surface appeared to have been machined, with no mill scale. The bars were embedded in concrete blocks exposed to two immersion settings: full immersion (depth 0.6 m) in the harbor, and intermittent or subject to tidal immersion exposure on a bank in the harbor. The blocks were 0.1x0.1x0.2m, with a 3 mm central gap to stimulate localized corrosion and concrete covers of 12, 18, and 40 mm. Concrete was Ordinary Portland cement (OPC, 420 kg/m3, w/c=0.42) and Sulfate–resistant Portland cement (SRPC, 355 kg/m3, w/c=0.45). There were 20 blocks, each with 3 bars of the same material

After just 1 year, the PS already experienced active corrosion, more so in longer specimens under the intermittent exposure regime than for shorter bars in full immersion. The SS specimens were corrosion-free. At 3.5 years, patches of dull appearance were seen on the SS specimens at both immersion settings; mechanical tests revealed that there was no effect on strength or elongation properties. By 7 years, distinct corrosion was observed on SS specimens, more in the tidal exposure than in full immersion, and more in SRPC than in OPC concrete. However, after removal of the rust, corrosion attack was found to be only superficial. By the end of exposure (12.5 years) all SS specimens in OPC and SRPC concrete developed rust staining on the surface. The most severe attack on SS was on a single SRPC concrete block at full immersion. However, corrosion took place preferentially where steel emerged from the concrete with some propagation inwards possibly as a secondary event. No corrosion-induced cracks or damage on the concrete surface were noted, suggesting that distress due to corrosion where the bars were fully embedded seems was quite limited. The results clearly illustrated the onset of the propagation stage for type 316 SS but without reaching a recognizable limit state. Crevice corrosion, which was initially thought to be a concern, developed on only one specimen at the end of the exposure.

A second series of experiments took place over a period of 10 years in Beckton, East London, U.K. [13]. Specimens were placed outdoors in an urban/industrial non-marine site. SSs evaluated were plain Cr ferritic SS types 405 and 430, basic Cr-Ni austenitic SS type 302 and increasing Mo content austenitic types 315 and 316. Al SS surfaces were descaled. High yield strength PS served as a control. Other materials tested included galvanized rebar, discussed only in passing here. Rebar were embedded in 550 concrete prisms, with 10 mm and 20 mm cover. Two considerably permeable concrete mixes were used (220 and 290 kg/m3 OPC, with 0.75 and 0.6 w/c respectively) containing admixed calcium chloride to obtain Cl- content of 0% (controls), 0.32%, 0.96 % 1.92%, and 3.2 %CmtWt. During the exposure, some concrete carbonation took place, to depths ranging from ~2 mm to near the 10-mm concrete cover, but not fully to the design bar depth. Thus, direct carbonation exposure took place only randomly in a few bars that were displaced from their design cover; corrosion could have initiated however from bound chloride release upon carbonation in admixed chloride specimens.

Table 2: Summary of conditions and findings of selected outdoor/service environment tests of SS reinforced concrete.

Region/Program	UK/BRE-1	UK/BRE-2		UK/BRE-3			US	South Africa			Switzerland		US	
Site	Langstone	Beckton		Beckton		Hurst	Treat Is.	Durban Bluff-1	Durban Bluff-2		Hwy. A-13		Florida	
Regime	Marine	Inland Admixed Cl^-		Inland Admixed Cl^-		Marine (Mild)	Marine Tidal	Artificial Salt Fog + Inland Outdoors Weathering	Some Marine Coastal, others as in Durban Bluff-1.		Highway Tunnel, Deicing Salt.		Salt Ponding with Marine Coastal	
Concrete/Mortar	Sound	Sound		Sound	Pre-Crack	Pre-Crack	Sound	Sound			Sound		Pre Crack	
Cover (mm)	12-40	10-20		10-20		15-30	7	12-40			10		25	
Duration(y)	12.5	10		22			2	4.5			3		3.6 to 10	10
SS type	316	302 315 316	405 430	316	302 315 316	302 315 316	304 316LN XM-28 2205	3CR12	304 316	3CR12	1.4462	TOP12	304 316 2304	3CR12
Mill Scale	No	No	No	No	No	No	No	No	Yes		NR	Yes	No	
Rebar Corrosion	Minor Pitting, Staining	Minor Pitting on 302	Strong Pitting	None	None	Minor Bare Bar Pitting	Minor Pitting on XM28	None	Pitting after 2 y.	Strong after 1 y.	None	Strong after 2 y.	NR	Strong
Corrosion Rate Compared with PS	Minor	Minor	Less	None	Non	Minor	Minor	None	Less	Less	None	Less-Similar	NR	Less
Corrosion Induced Cracking	No	No	Start at 3 y	No	No	No	No	NR	NR	NR	No	No	No	Start at 5.2 y

The austenitic SSs showed very high corrosion initiation resistance in all the chloride concentration levels tested. No corrosion was recorded for any of the austenitic test bars examined by year 10 with the exception of isolated pitting on a type 302 steel bar for the 3.2% Cl- regime, next to a plastic insulating sleeve. Thus, the austenitic SSs appeared in large part to remain in the corrosion initiation stage, without completing it for the entire 10-year test period. In contrast and of special interest to this survey, the plain Cr ferritic SSs showed instances of evolving through completion of both the corrosion initiation and propagation stages. While there were no cases of concrete cracking for the specimens with no added chloride, one instance of cracking after 3 years of exposure was observed for 0.32 %CmtWt for a type 405 SS bar placed with 20 mm cover. Increasing amounts of cover cracking by both ferritic steels took place at the higher Cl- contents, culminating with extensive cracking at 10y exposure in the 3.2% %CmtWt specimens. At that severe regime ferritic SSs provided only modest improvement over the performance of PS, and marginal or no improvement over that for galvanized steel. In summary, the plain-Cr ferritic SSs showed better performance than the unalloyed or galvanized steel at the lower Cl- regimes, but progressively less differentiation at the more aggressive conditions. Relatively little difference in corrosion extent and morphology was seen at low Cl- exposure regimes between the two plain Cr alloys. At the higher Cl- regimes somewhat less overall corrosion was noted for the higher Cr content type 430 SS. Examination of extracted bars for 3.2 % %CmtWt exposure showed for both types 405 and 430 SS instances of severe pitting with about 25% local loss of cross-sectional area (deemed to render the rebar unserviceable), with no reported pattern of pitting clustering along the bar. The loss was somewhat greater for the 10 mm cover than for the 20 mm cover cases. For exposure to the less severe 0.96 %CmtWt regime the rebars of these alloys showed only small to near invisible pitting.

This series of experiments produced some limited information on X_{CRIT} values, from evaluation of the ~4% of the exposed specimens that exhibited cracking. The summary did not distinguish between SS and the other lesser alloys tested (which would be expected to be the majority of the sample). However, there was no mention of the data from the SS specimens differentiating markedly from the other materials. Results indicated mean metal thickness loss (not considering corrosion localization) values for incipient concrete cracking ranging from 4.35 µm to 13.21 µm. Considering the clear concrete covers and rebar diameters used, these values are not inconsistent with those expected from empirical relationships developed elsewhere for cracking induced by PS corrosion [49]. However, further work is required to determine the direct applicability of these relationships to highly localized corrosion.

The third series of experiments [50] included analysis of extended exposure (to 22 years) of 12 of the type 316 SS reinforced prism specimens initially exposed at Beckton per the program described above. Newly reported also were results of 22-year exposure of 23 other specimens that had been prepared in the form of stressed concrete beams reinforced with types 302, 315 and 316 SS bars, 15 or 30 mm clear cover. The beams were divided into two parts mutually bent to create a permanent bending moment and crack the concrete. Chloride contents of 0%, 0.32%, and 0.96 %CmtWt were admixed in the beams. Twenty of these beams had been exposed at the Beckton site alongside the other specimens, and 3 (initially with 0% chloride) were exposed at the splash zone on a marine site at Hurst Castle, on the southern cost of England. The 22-year exposure at Beckton with as much as 3.2 %CmtWt admixed chloride resulted in no observed corrosion for types 302, 315 and 316 SS in either the prisms or the cracked beam samples. At the equally long exposure at the marine site, the only sign of corrosion was minor pitting attack (only ~20 μm deep) in one bar each of the three alloys at the point where the bars emerged from the concrete. It is noted that the chloride content at the bar depths at the marine site at the end of the exposure was reported to be quite low, typically < ~1 %CmtWt. Potential and LPR measurement results were suggestive of typically passive behavior in the rebars examined, consistent with the direct examination observations. Carbonation in all specimens in either site had not reached the bar surfaces, so exposure severity was not aggravated in that way. Overall, the third series of tests confirmed the substantial resistance to corrosion initiation of concrete-embedded austenitic SSs - even for low PREN type 302 SS, but was not quite informative of the corrosion propagation regime. Corrosion in the few specimens where it was noted was at locations (emergence points) not representative of most conditions of interest. Given the absence of cover there the corrosion is likely to have started early during exposure. Thus, the low pitting depth over a decades-long period suggests that corrosion rates during propagation for the austenitic SSs under these conditions were also very low.

Marine exposure: Treat Island (ca 2000s -10s)

Two-year field exposures took place in a high-tide marine environment at Treat Island, Maine, U.S., near the Bay of Fundy [28]. This aggressive site also features ~100 freeze-thaw cycles per year. SS rebars of ~11 mm in diameter were embedded in mortar with very low cover (~7mm). Bare bars were also exposed. The metal surface condition was sandblasted. Four SS grades were evaluated: Austenitic SSs 304, 316LN, XM-28 (a Mn-austenitized SS), and Duplex 2205. For control, low alloy steels (PS rebar as well as ASTM A1035 (MMFX, ~9% Cr)) were evaluated as well.

Autopsy of the specimens with the two low alloy steels showed cracking and extensive bar corrosion. Mortar specimens of the other alloys had no external sign of rust stains or spalling. Autopsied bars of XM-28 showed indications of minor pitting, but no distress was reported for the other SS alloys. By the end of the exposure embedded SS types 2205, 316 LN and 304 exhibited HCPs between -100 mV and -200 mV (SSC - Ag/AgCl/Saturated KCl). Moreover, the corrosion rate measured by LPR for these three SS grades were less than 0.1 μA/cm^2 after two years of exposure. Those indirect assessment results suggested a predominantly passive condition, consistent with the absence of corrosion observation on the bars upon autopsy. Exposed bare bars of the low alloy steels showed clear signs of extensive corrosion damage. Bare type XM-28 SS showed clear signs of pitting over the general specimen area, but it was the only SS material that received a degraded visual rating. Type 304 SS showed a few pits over a very limited area. Types 316LN and 2205 SSs showed no signs of corrosion.

Based on the field tests and concurrent lab tests, the authors concluded that SS types 316LN and 2205 "provide true immunity to corrosion over long service-lives required for critical projects (100+ years), even in cracked concrete conditions". In summary, only the Mn-austenitized SS XM-28 showed clear signs of approaching the start of the corrosion propagation stage when in the embedded condition during the test period.

Marine/weathering exposure: Durban Bluff (ca 1980s – 90s)

This work evaluated behavior in two different exposure programs, both 4.5 years long [51]. Rebars 15 mm in diameter and made of Ferritic SS type 3CR12 (low cost straight Cr SS, 10.5-12.5% Cr content, akin to type 409 SS) were embedded in concrete prisms 100 x 100 x 500 mm, with cover of 12, 25, or 40 mm. The concrete was highly permeable (w/c 0.64 to 0.82).

In the first program (80 prisms) the bars were smooth and the SS surface was pickled and passivated. PS pickled control bars were evaluated as well. The prisms were exposed to a simulated marine exposure with alternating salt fog and external subtropical inland weather for drying. In the second program (924 prisms) the rebar was corrugated, and used in the hot rolled condition with mill scale. Mill-scaled corrugated bars of types 304 and 316 SS and PS controls were evaluated as well among other materials not concerned here. Part of the prisms were subjected to the same exposure as in the first program, and the rest were placed 50 m inland from the high marine water mark of the Durban Bluff Coastal Site, a subtropical location on the East coast of South Africa.

The pickled and passivated type 3CR12 SS did not result in any visible concrete distress over the 4.5-year first program exposure. On autopsy the bars showed no visible corrosion except for superficial stains at the cut ends that might have been due to contamination by cutting tool steel. The concrete prisms with PS rebars began to show some cracking after only 6 months of exposure, and severe cracking failure after 4.5 years.

In the second program, the presence of mill scale was associated with strongly degraded performance of the type 3CR12 SS bars, with signs of corrosion detected already after one year of exposure. The mill-scale-bearing higher alloys, types 304 and 316 SS, performed poorly as well, with observation of pitting corrosion initiation after only 2 years of exposure. Unfortunately, it was not reported whether concrete cracking was present as well. On microscopic examination the poor performance of the mill-scale bearing SSs was attributed to rolling laps and embedded scale before and after-fabrication deformation. The prisms with PS bars showed corrosion induced cracking within just one year of exposure. Both the actual and simulated marine exposures provided comparable results.

Given the good performance despite harsh exposure conditions, low cover and permeable concrete, the authors concluded that in the pickled and passivated condition the moderate alloy content type 3CR12 SS would be a viable reinforcing material for concrete. These findings are in contrast with the less favorable performance of the straight CR SSs in the BRE tests. It is noted that the latter study might have included SS with residual mill scale that combined with a high content of admixed chlorides could have increased test severity accordingly.

Highway tunnel deicing salt exposure (ca 2000s)

Reinforced concrete samples were exposed for 3 years to the deicing-salt splash zone between two columns of a Swiss tunnel (Galerie Cianca Presella, Highway A13) [12]. Rebar samples 10 and 16 mm in diameter of Ferritic TOP12 SS (akin to 3CR12) in a mill-rolled condition and Duplex 1.4462 SS (akin to 318-LN or 2205) with an unspecified surface condition, and PS controls (Alloy S500) were embedded in highly permeable (w/c =0.6) OPC concrete prisms 100 x 30 x 20 cm, with 10 mm cover. Half-cell potential and macrocell current measurements were conducted periodically and bars were examined on final autopsy.

Corrosion induced concrete cracking was not reported for any of the specimens. On autopsy, the Cl-content after 3 years at the cover depth exceeded 1.5 %CmWt. The duplex SS showed no electrochemical indications of corrosion initiation over the entire test period, consistent with the elevated C_T value expected for that alloy. However, HCP and macrocell current of the type TOP12 SS specimens indicated sustained active corrosion. Based on the data, the corrosion propagation stage started after ~2 years of exposure, and was preceded by initial fluctuations in HCP thought to reflect the presence of the milling skin. The PS steel showed electrochemical signs of undergoing sustained active corrosion after 1 year. Those results suggest that in these test conditions the value of C_T for the type TOP12 SS, while < 1.5 %CmtWt in the as-rolled condition evaluated, was perhaps 2 to 3 times greater than the typically expected value of C_T~0.4 %CmtWt for PS.

Autopsy and corrosion product removal revealed that the attack on the two alloys that experienced active corrosion (Table 3) was in the form of pits broader but shallower for PS than for the TOP12 SS. The mass loss on TOP12 SS was about 1/3 that of the PS which was partly ascribed to a lower macrocell driving potential difference for TOP12 SS than for PS. However, given the relative areas involved, the estimated pit growth rates were about the same for both, in the order of 1.2 mm/y. Lateral growth of the pitted zones was interpreted to result from anodic acidification at the pit edges: as the passive film on PS is less resistant to an acid environment than the film on Cr steel, broader and shallower corroding zones should be more prevalent in the PS case.

Table 3: Mean and standard deviation of the anodic areas and the maximum attack depths of S500 and TOP12 steel samples and the total time of corrosion (TOC).

	Anodic area / cm2	% of total areas	Max. attack / mm	TOC / month
S500	3.7 +/- 1.2	30 +/- 10	0.7 +/- 0.4	27 +/- 1
TOP12	1.2 +/- 1.1	10 +/- 9	0.5 +/- 0.3	12 +/- 3

This investigation included parallel experiments with exposure to simulated pore solution (pH 13.5) that confirmed the above ratio of ~3 between C_T of (as rolled) TOP12 SS to that of PS. Notably, removing the rolling scale on the TOP12 SS improved the ratio to near 10. Lowering the test solution pH to 10.5 did not result in a difference in relative corrosion behavior of both alloys.

Marine shore exposure: Florida (ca 2003-2013)

These tests are the outdoors component of a recent investigation by Presuel-Moreno et al. [52] [53] that has provided further rare evidence of concrete cracking induced by SS rebar corrosion. Two other components are described in the laboratory tests section.

The outdoors test yard was near the seashore at the subtropical locality of Boca Raton, FL, U.S. The weathering exposure was intensified by simultaneous ponding with a 15 wt% NaCl solution, thus several times more concentrated than if it were seawater splash. The specimens were reinforced concrete prisms containing two rebar mats. The upper mat was positioned beneath the pond with a 25 mm concrete cover. A 1.6 mm wide opening in the concrete cover was used to simulate a transversal crack. Two concrete types were used with respectively 300 kg/m3 and 213 kg/m3 of cement, and w/c= 0.41 and 0.5. Six specimens for each condition were tested. Solid bars of types 304, 316, 2304 and 3CR12 SS were evaluated, apparently in a descaled condition. The first 3 alloys were exposed for periods of 3.6, 10 and 8 years respectively (exposures being an extension of prior work [19]) without any signs of concrete cover cracking in any type of concrete. The last, 3CR12, showed cover cracking that had developed to the side of the initial simulated crack in two w/c=0.5 specimens after 5.2 years. Corrosion staining was observed on the surface of the concrete adjacent to the simulated crack and therefore it was assumed that extensive accumulation of corrosion products on the rebar surface resulted in additional cover cracking. Crevice corrosion was present as well at the ends of the bars which were not masked where they emerged from the block.

Laboratory evaluations

There have been numerous laboratory investigations on the performance of SS rebar in concrete. Many focused on the corrosion initiation stage and were previously reviewed [18, 16, 8, 54] [55] so will not be discussed here. The following selections are cited inasmuch as they exemplify factors relevant to the propagation stage, while recognizing many other contributions elsewhere [56] [57] [58] [59] [60]. Each selection concerns one or more publications from a group researching the issue.

Pit growth on SS rebar in simulated pore water and propagation stage modeling

These works by Hurley and Scully [10] [25] [61] specifically attempted to obtain information on the rate of corrosion and anticipated duration of the propagation stage. First C_T values for solid 316LN SS, 316L SS clad, 2101 LDX duplex SS, MMFX-2 (Fe-9%Cr), and PS control (ASTM A615) rebars were determined through laboratory tests in saturated Ca(OH)2 + NaCl solutions. In its basic form, the method used acceleration by anodically polarizing the samples above the normal HCP, to +200 mV SCE, and increasing Cl concentration until a sharp increase in anodic current, indicative of passivity breakdown was detected. A nominal value of C_T, expressed as a [Cl]/[OH] ratio was thus obtained, with the qualification that it would represent an extreme oxidizing condition seldom encountered in concrete. Bounding C_T values for carbon steel were ~0.3, consistent with typical literature values. C_T values for alloys in the clean, pickled conditions increased with PREN number, to values of ~4 for MMFX-2 (again consistent with other sources), ~10 for 2101, and ~50 for 316LN. The presence of mill scale strongly reduced the C_T values for the high chromium alloys, an observation noted earlier and consistent with other literature [8].

Importantly, the C_T potentiostatic experiments served also as a base to obtain insight on the propagation stage behavior. The anodic current evolution on passivity breakdown was monitored for 2000 seconds, upon which the potentiostatic setting was lowered (e.g., by 100 mV) and the resulting current monitored for 2000s as well. The process was repeated until the current demand vanished, indicative of having reached a repassivation potential. The characteristic current value at each of the potentials evaluated was found to be approximately linearly dependent on the potential value, indicating dominant ohmic control of the anodic process in agreement with expectations on the prevalent pit geometry and electrolyte composition. Examination of the time evolution of the polarizing current on reaching the breakdown potential showed a fractional power time dependence ($\sim t^{1/3}$) of the current. Combining the above observations with an assumption of hemispherical pit shape yielded an expression for the corrosion penetration (as pit radius) as function of time and potential of the form

$$r(E.t) = k(E) t^{1/3} \qquad\qquad\qquad Eq.(1)$$

where E is the applied potential and k is a function of the applied potential characteristic of each rebar material and its service environment. The function k(E) was determined experimentally for each material in the saturated $Ca(OH)_2$ + NaCl solution used, with a concentration of NaCl equal to the C_T value determined earlier.

To translate the liquid solution results into those that may apply to concrete, the observation that pit growth was mainly ohmic-controlled was used to convert the k(E) function measured in solution into a function kC(E) that would rule behavior in concrete, via the anticipated difference between media resistivities. The conversion took into account the resistivity of each liquid solution (depending on their NaCl content) and the anticipated resistivity formation factor (from literature data) between each liquid solution and concrete with pore water of the same composition as the liquid solution.

The kC(E) functions were then used to calculate r(t, 0V) projections, where an applied potential of 0V (SCE) was assumed as a nominal likely operating mixed potential of SS rebar with pits active and the rest of the assembly in the passive condition. A concrete cover cracking limit state criterion was proposed, reached after pit depth was equal to a critical value X_{CRIT}. The value of X_{CRIT} was estimated for each material based on plausible assumed pit size/concrete cover ratios using a literature empirical relationship [49], where the SS rebars were assumed to result in more localized pitting than the low alloy materials. Thus, a duration of the propagation stage t_p was projected for each material, yielding 1.1y, 1.82y, 8.9y and 24.4y respectively for carbon steel, MMFX, 2101 and 316 LN respectively. While based on numerous working assumptions, this approach is a promising first step in rational forecasting of the duration of the propagation stage of SS rebar in concrete, and it appears to be the most advanced model available to date.

Initiation/Propagation stages of SS-reinforced concrete.

While also focused on C_T determination methodology, this work by Pachón-Montaño et al. [62] included an approach to quantify the length of the corrosion propagation stage. Alloys examined were austenitic types 304L, 316L, and duplex 2001, 2304 and 2205. These were placed in concrete with ~30 mm cover, ponded with a 1 M Cl solution at the top. Cl ingress was accelerated by creating a top-to bottom electric field with direction to drive Cl- downwards, using an electrode at the pond and another at the bottom of the concrete specimen, leaving the bar at open circuit conditions. Epoxy resin masking of the parts of the rebar surface not directly facing the pond was used to minimize obscuring stray current effects. The authors proposed that this procedure avoids artifacts, leading to a more precise determination of C_T and of corrosion rates by LPR measurements. Those were performed after C_T was reached and the steel was allowed to corrode undisturbed at the prevalent Cl level at the bar surface, measured by subsequent autopsy. Tests were conducted with six specimens of each alloy; not all specimens achieved stable depassivation so C_T was interpreted in statistical terms. C_T values were found to increase with PREN value. The C_T values (for 50% probability of depassivation) ranged from ~2.5% cement wt for PREN=~19 (type 2201) to ~4.5 % for PREN =~37 (type 2205). Corrosion rates (as i_{corr}) were correlated with prevalent chloride content for each specimen that achieved depassivation, fitting to an empirical functional relationship that had been proposed earlier for PS rebar corrosion in concrete [63]:

$$\ln (i_{corr}) = A + B \ln(C_{Cl^-}) \hspace{4cm} \text{Eq.(2)}$$

where A and B are constants for each alloy and CCl- is the chloride content in % CmWt at the rebar surface measured for each specimen of the group. Combining Eq. (2) with an estimate of the amount of chloride at the bar surface as function of time (choosing a simple diffusional chloride penetration scenario) yields a forecast of corrosion rate as a function of time. That forecasting approach is interesting as it mathematically integrates both the initiation and propagation stages. Using probabilistic estimates from the regression used to evaluate the data from multiple specimens, and assuming a pitting factor of 10, thought to be representative of corrosion of SS in concrete, the authors developed for each alloy forecasts of the amount of corrosion penetration as function of service time in a typical marine application. Results, exemplified for a 2 mm corrosion limit state penetration at 10% probability, projected service life of 10 years for PS, >25 years for 304L, > 30 years for 2001, 45 years for 2304, 85 years for 316-L and ≫ 100 years for 2005. This type of analysis however needs careful examination to separate the effects from increased C_T from those of decreased propagation rate when forecasting durability. Preliminary examination of results from graphically described trends in [62] suggested propagation stage damage rates that are smaller than those of PS by factors of 2-3 times for types 304L and 2001 SSs, ~4-10 times for types 316L and 2304 SSs, and ≫10 times for type 2205 SS.

Propagation stage completion in ponded SS-reinforced concrete

These experiments are laboratory components of an investigation [52] [53]   that included the Florida marine shore exposure class described in the outdoors/service environment tests section

The first component involved prisms resembling those in the outdoors exposure, with 25 mm cover but without simulated pre-existing cracks. The concrete had 390 kg/m^3 cementitious content, with a 10% Fly Ash replacement and 0.42 water/cementitious (w/cm) ratio (see also [64]). The exposure consisted of 20 wt% NaCl-ponding with chloride ion penetration accelerated by means of imposing an electric field between the pond, with a negatively polarized activated Ti mesh electrode in the pond water, and a positively polarized similar mesh embedded in the concrete beneath the lower rebar mat. The upper mat rebars were not connected to the other electrodes. Thus, the applied electric field effect on those bars was only due to secondary, zero-net-current stray currents. It is noted that those were not minimized here by insulating masking, as had been done in the previous study discussed [42]. The tests were conducted with 350 mm-long, 16 mm diameter bars of duplex types 2101 and 2304 SS, both in the pickled condition, 5 prisms for each. These specimens showed multiple instances of cover cracking for each type of steel, as summarized in Table 4.

Table 4: Accelerated chloride ingress test.

Type 2101 SS			Type 2304 SS		
C_T %CmtWt	Duration /days	Crack	C_T %CmtWt	Duration /days	Crack
2.6	T-177	Y-B-1-1	1.84	T-162	Y-B-2-1
-	162	Y-B-1-3	1.22	T-152	Y-B-2-2
1.24	T-158	Y-B-1-2	-	185	N-B-2-3
-	162	Y-B-1-4	2.59	T-162	Y-B-2-4
1.74	T-162	Y-B-1-5	-	185	Y-B-2-5

Y: cracking observed at indicated duration
N: no crack observed at indicated duration
T: terminated specimen for autopsy
C_T: chloride content at bar depth as percentage of cementitious content mass

The chloride content observed on autopsy (shortly after crack appearance) was higher by a factor of ~3 to 6 than that expected for PS in concrete, but not quite as much as the order-of-magnitude factor usually expected for SS in concrete. This observation suggests that the residual stray currents from the procedure used to transport chlorides into the concrete, not minimized here by masking, may have been a major driver of the corrosion damage in these experiments.

There was significant rust development in the bars from autopsied specimens. Mass loss as little as 0.65 gr was associated with a surface crack on specimens with type 2304 SS. The smallest mass loss observed on type 2101 SS was ~1.4 gr, but it is likely that a crack appeared when corrosion mass loss had not been as pronounced. It is noted that for the specimen dimensions used, a 1 gr mass loss would nominally correspond to an average radius loss of ~8 μm. However, if all the corrosion would be concentrated in only a small part of the rebar (e.g a 2.5 cm length of the bar, uniformly around the perimeter), the average radius loss for 1 gr mass loss there would be ~100 μm. That value would be in the order of the values of X_{CRIT} estimated for that level of corrosion localization per the empirical relationship by Torres [49] developed from PS rebar data. The results would then suggest that the X_{CRIT} value for SS is comparable to that of PS. However, that interpretation may be too simplistic and the authors cautioned that effective values of X_{CRIT} for SS could be significantly greater than for PS if the corrosion were limited to only one side of the rebar surface and further localized by pitting.

The second component involved evaluating 13 mm bars of type 304 SS and 16mm bars of duplex types 2304SS and 2101SS under strong natural acceleration: very low cover (~1 cm), mortar with high w/c (0.5), and high chloride solution (15% NaCl, ~2M Cl) ponding, initially continuous wet then alternating wet/dry. The bars were evaluated in three conditions: C: as-received pickled, H: with lab-induced mill scale by air oven heating at 1000 C for 1 hr, and S: lab mill-scaling followed by sandblasting. HCPs and LPR were monitored as function of time for 700 days.

"C" specimens of type 304 SS and 2304 tended to retain potentials around -200 mV SCE over much of the test period, while the 2101 SS experienced a significant potential drop by day 200. LPR results tended to yield relatively high values indicative of low corrosion rates and thus consistent with the HCP data, and supporting the use of the latter as corrosion monitoring method. The H and S conditions tended to show, starting early in the exposure and for all 3 alloys, OCP values that were more negative, and LPR values smaller, thus indicating higher corrosion rates than for the C condition. Several specimens were terminated by about day 300, and visual examination of the rebar surface trace showed an appearance consistent with the indications of the electrochemical data. The results supported the greater corrosion resistance of types 304 and 2304 SS compared to that of the type 2101 SS, and clearly confirmed the detrimental effect of mill scale presence, also favoring the interpretation that abrasive blasting does not provide sufficient mitigation of that effect. Importantly, after 300 days exposure one each of the H and S type 2101 SS specimens had visible pond surface cracking. None of the other conditions of either alloy was associated with concrete cracking at that time. Chloride content analysis of rebar traces in the terminated specimens suggested that a lower bound for C_T (general observations for all surface conditions) was > ~5.9 %CmtWt for type 304SS. The authors warned that those figures might be overestimates in the case of type 2101 SS because of the late preferential chloride ingress at the cracks noted above.

Performance of austenitic and duplex SS in cracked concrete

This recent investigation [65] represents effort addressing an important SS application class, where users specify SS to control corrosion in structural elements prone to structural cracking and in aggressive service, as for example large footers in marine bridges.

Three austenitic types (304 SS, 316SS and S24100 (a Mn-austenitized grade with samples from 2 suppliers)) and 3 duplex (2101, 2205, 2304) SSs were evaluated, alongside PS bar controls. The rebars were 16 and 19 mm in diameter, presumably in pickled condition, placed in ponded concrete prisms with 25 mm cover, made with cement + slag (297 + 98 kg/m^3 respectively, 0.4 water-to-cementitious content ratio). Cracks in transversal and longitudinal directions to the bar length were created, together with control specimens with no cracks. Aggressive brine with near-saturated chloride content was continuously placed in the pond. HCP and galvanostatic pulse tests were regularly conducted. Specimens were autopsied after 400-550 days exposure.

Results for sound concrete showed no significant corrosion of any of the SS or even the PS. In contrast, for the cracked specimens with all the SSs (with the possible exception of some of the type 2205 SS samples) some corrosion was observed at the intersection of bars and the cracks. Initiation was thought to take place early in the test exposure but neither OCP nor current density measurements yielded consistent enough results to assess a precise moment of corrosion initiation. Indeed, the authors concluded that the recommendations of ASTM 876 [29] for interpretation of corrosion potentials of PS bar cannot be applied freely to SS rebar, and more detailed guidelines for that are needed.

The corrosion morphology was uneven, with some indication that corrosion and its products often migrated along the surface of the rebar and away from the intersection of the rebar and a transversal crack. The duplex grades tended to outperform the austenitic grades, which is not surprising for S24100 given its low PREN, but unusual for the type 316 SS which fared low in the corrosion product visual examination. Surface flaws on the latter were mentioned by the authors as a possible cause, which might be eliminated with stricter surface control in production.

The authors concluded that structural cracks in concrete are a major concern in corrosion vulnerability. It was noted however that test exposure conditions (very high chloride concentrations with low cover and at lab temperatures much higher than those normal in deicing salt regimes) were particularly harsh. With the cover thicknesses present in actual field conditions some crack healing or blocking by corrosion products would be expected and provide corresponding mitigation. Some reduction in corrosion rate with time was observed in the tests possibly due to those mitigating effects.

DISCUSSION

Evaluation of evidence

The performance of SS rebar in actual structures in service is the ultimate metric for realistic assessment, as it does not involve artificial test acceleration and includes exposure to all service damage processes, anticipated or not. The downside is very sparse opportunities for evaluation both on number of structures available and, with one exception, length of service. Thus, this review did not uncover any fully direct evidence of SS reinforcement having reached the end of the corrosion propagation stage, in any of the bridge cases examined. The closest situation found was for the Progreso pier. There, a few instances of external concrete cracking examined at 60 years structure age were reported as being attributed to corrosion of the type 304 SS rebar, presumably with associated formation of expansive products. The attribution was based on indirect evidence: the location and orientation of the cracks (present where bars were placed, and aligned with embedded bars) as well as on chloride content of the concrete (exceeding the assumed C_T value for type 304 SS) and electrochemical measurements consistent with ongoing corrosion of the steel. However, direct evidence, in the form of samples actually showing corrosion of the bars at those locations as well as presence of expansive corrosion products, is not yet available. Assuming nevertheless that the observed cracking was due to corrosion of the SS rebar, a rough estimate of the length of the corrosion propagation stage may be made by noting that the chloride penetration profiles in the bridge at age 60+ years were nearly flat. That is, the chloride concentration ~10-20 cm deep into the concrete was nearly equal to the surface concentration, which was >~1 %CcWt and thus in the order of values of C_T expected for type 304 SS. Given the flat ~60 y profile and the functional form ruling diffusional penetration [3], it would be expected that those near-surface chloride concentrations were already present at the rebar cover depth (~10 cm in some locations) already by ~1/2 of the inspections age. In consequence, the propagation stage in those cases might have started by age 30 years. That rough estimate, together with the rarity of observations of cracking that could be attributed to corrosion of the SS rebar (only ~3% of beams affected after 60+ years) suggests that the length of the propagation stage for a cracked-concrete-cover limit state was at least several decades. That value far exceeds the typical value of only several years recognized for PS rebar [4], and if supported by further evidence would represent a substantial added benefit of using SS bars for marine applications.

The remaining evidence of the corrosion propagation stage examined for bridges in service with SS rebar was limited, but nevertheless invariably indicative of minimal or non-existing corrosion distress of SS reinforcement. This performance may be ascribed in some of those cases to the young service age of the bridge (oldest structure evaluation age other than at Progreso pier was only 26 years), and consequently less opportunity for chloride enrichment at the rebar depth. In some cases, however, the chloride content at rebar depth had already exceeded typical C_T values for PS bar, or preexisting cracks in the concrete were present that might have already allowed deep local chloride ingress. While the lack of corrosion under these conditions attests to the excellent corrosion initiation resistance of SS bars in general, it still does not provide sufficient added field evidence to either support or contradict the rough estimate made above for the length of the propagation stage made from the Progreso pier results.

While the swimming pool incidents do not concern SS embedded in concrete, those EAC failures serve a reminder that unexpected modes of failure often accompany the introduction of a new material class to an established application. The initial agent, gas phase chlorine, is not anticipated in the concrete environment, and EAC is less likely in the moderate strength class usually associated with reinforcing steel. However, chloride-induced EAC of SS rebar might still be an issue, especially in warm marine service. Furthermore, EAC could become the final fracture mode of a cross-section that was previously reduced and made irregular by deep pitting, thus elevating the local stress intensity. So far one field instance of corrosion of exposed rebar at the Progreso pier has been tentatively identified as exhibiting SCC [37]. Examinations of future sampling should carefully search for any other similar evidence. Any further observations of that type would be an indication that an EAC limit state alternative to concrete cracking may need to be seriously considered.

Second to actual structural service, the environmental exposures of specimens attached to in-service structures or at outdoors test yards offered the next best opportunity for realistic performance assessment of SS reinforcement. These exposures can benefit from having a larger number of specimens and more frequent and detailed monitoring. Moreover, a judicious degree of test acceleration can be achieved by the use of thin concrete cover, high concrete permeability, and expanding tests to some alloys (such as plain Cr SSs) more likely to reveal otherwise undetected corrosion trends. Those provisions succeeded in producing valuable insight. Of the selections presented, two sets of tests merited special attention: the 10-year BRE Beckton exposure, and the 5- to10-year Florida marine shore ponded tests. Those two investigations were the only found in this review providing full direct evidence that outdoor exposure produced corrosion induced cracking of SS reinforced concrete. In both instances of propagation stage completion, the SSs involved were ferritic straight-Cr alloys with low PREN values (~11 to ~17). Moreover, the SS bars were placed at either very low cover depths (~10 mm in the Beckton tests) or under low deficient cover (25 mm with intersecting simulated wide preexisting cracks in the Florida tests), and experienced high chloride concentrations. For those conditions and materials, corrosion was in the form of severe pitting not unlike that found in accelerated exposure of type ASTM A1035 (MMFX) 9-Cr steel [66]. Strong corrosion localization is expected to mitigate cracking [49], but in these cases it was not sufficient to prevent corrosion induced concrete cracks from forming and propagating to the outer surface. The value of t_p in these cases was short, no more than 5 years in the Florida tests and likely to have been of that order in the Beckton tests as well. This duration is comparable to that expected for PS bar, albeit under normally sound and thicker cover. Thus, it is possible that t_p might have been longer in these low PREN SS tests if the concrete cover would not have been so shallow or without preexisting concrete deficiencies. However, that possible increase for thicker or better cover remains speculative, and would in any event have had to be very substantial to reach a multi-decade improvement on t_p over that for PS, such as that estimated for the higher PREN type 304 SS in Progreso pier.

Although not reaching completion of the propagation state, indication of more promising performance of straight Cr (~12%) ferritic steel was obtained at natural/field environments at the South Africa and Swiss sites. In both cases, instances of the end of the corrosion initiation stage were reported, for exposure times as short as 1.5 years. However, subsequent surface-averaged corrosion rates were much less (by a factor of 5 in one case) than for PS controls. Since no instances of completion of the corrosion propagation stage were reported for the entire test durations (up to 4.5 years) then t_p for these low PREN SS could be lower-bound to ~3 years but with the expectation of a significant improvement over PS. It is cautioned however that notwithstanding the reduced average corrosion rates for SS, pit penetration rates in SS in the Swiss site were comparable to those on PS due to more corrosion localization in the former.

The other environmental test exposures by BRE (continuation test at Beckton/Hurst Castle and at Langstone Harbor, over a period of up to 22 years) highlighted mostly the large improvement in corrosion initiation resistance that can be achieved by increasing the alloy content of components that elevate PREN. Even the basic type 302 SS showed excellent performance over the long term, including when placed in previously cracked concrete. Thus, in most instances the propagation stage had not started and cannot be assessed. In a few cases, minor superficial corrosion as well as one case each of localized corrosion were noted indicating the onset of the corrosion propagation stage at apparently very low rate. Similar outstanding performance on delaying corrosion initiation by Ni-containing austenitic and for duplex SS was found at the Treat Island site and the Swiss highway tunnel location. At Treat Island there was indication of corrosion initiation at Mn-austenitized type XM-28 SS after <2 years in low-cover mortar, with corrosion rates that were extremely small. Types 304, 316, and 2205 SS did not appear to have completed the initiation stage. In contrast, type XM-28 SS showed significant discoloration and some pitting.

Overall, the field/natural exposure experience, albeit limited, suggests that corrosion propagation progression on stainless grades is somewhat slower than for PS for the lesser, ferritic grades or the low PREN Manganese-austenitized SS, and much slower than PS for the higher PREN regular austenitic and duplex SS grades.

The laboratory investigations are at present the main source of corrosion rate and mechanism information, but at the price of using variously unrealistic degrees of test acceleration with consequent risk of uncertainty of the relevance of the findings. The cases reviewed show attempts to quantify the rate of corrosion penetration in the propagation stage with basic-principles interpretation of experimental data as in the pitting model by Hurley and Scully [10] [61] [25], or more empirical approaches as in [62] [63]. Both treatments result in propagation stage forecasts that parallel the observations from service and field exposures, whereby low PREN alloys yield moderate increases over PS or low alloy (akin to MMFX) while high PREN alloys such as high alloy austenitic stainless and duplex steels exhibit order-of-magnitude increases. Comparable observations have been made in a recent review of corrosion-resistant rebar [8]. Those investigations provide potentially powerful approaches to create rational models for propagation stage durability forecasts.

Laboratory investigations where the end of the propagation stage has actually been reached for specimens in concrete are rare, and this survey identified only two, both associated with the Florida study [52] that included as well the field exposure mentioned earlier. Both instances are notable in that they did not involve low PREN straight chromium alloys as the cases noted above for the environmental exposure cases, but rather duplex alloys with PREN~26. One of the two experiments, where both types 2101 and 2304 SS showed cracking, involved chloride penetration acceleration by imposed electric field but without masking mitigation of stray currents. Therefore, it is possible that the cracking on a relatively short time (~6 mo) reflected unrepresentatively high corrosion rates difficult to measure accurately. While the experiment could not yield useful propagation rate information, the results still provided some indication that the value of the critical penetration for through-the-cover cracking was comparable or exceeded that for PS cases. The other laboratory experiment, with less extreme acceleration other than use of very shallow cover and high permeability mortar, resulted in cracking after ~2 years induced by the corrosion of type 2101 duplex SS bars. The bars affected however had vulnerable surface conditions, one with high temperature scale, the other descaled only by abrasive blasting. Given the low cover and permeability of the mortar, a test under similar conditions with PS bar would have been expected to show some form of cracking in about the same time frame. Thus, this experiment served to indicate that deficiently descaled duplex SS rebar can indeed corrode enough to result in concrete cover cracking, and that the resulting rates of corrosion may be similar to those involving PS.

The findings from the investigation concerning performance of SS rebar in previously cracked concrete [65] highlighted an area of application of SS that is often the justification for the use of that material, namely as a primary defense barrier against corrosion in the case of local concrete deficiency. The results complement the findings from the Florida marine shore yard test, whereby a high PREN rating is critical for adequate propagation stage performance, as otherwise the corrosion initiation stage is essentially bypassed and corrosion rates become too high. Further research is required to address in each application area the performance of SS rebar under local concrete deficiencies as an integral - and critical- issue in quantitative durability forecasting of the system.

Summary of findings on SLS mode and duration of the propagation stage

The overall evidence on the most likely SLS mode for SS reinforcement remains scant, but it is generally indicative of corrosion-induced concrete cover cracking. That is supported by the (albeit indirect) identification of that mode at the Progreso pier for an austenitic steel, the various direct observations of cracking for straight Cr or low alloy SSs in outdoor exposures, and direct evidence of concrete cracking for higher performance alloys in accelerated laboratory tests. The corrosion morphology in the concrete cracking cases for the low alloy steels was found to be in the form of pronounced localized pitting of the bars. That strong localization of the corrosion was clearly as able to form through-cover concrete cracks as the often moderately localized corrosion seen on PS rebar. Because of the paucity of data, the corrosion morphology on the higher SS alloys is less known for actual service or outdoor exposures. The overall indications, supported by results from the accelerated laboratory tests, are also of rebar corrosion localization, in the form of perhaps even more isolated pits than in the case of the lower SS alloys. That increased corrosion localization would suggest the possibility of an alternative SLS mode via rebar failure by plastic/partially brittle overload of a locally reduced cross-section, perhaps especially in cases of corrosion at preexisting structural cracks. However, no reported instance of such event was found. Thus, for now it can only be considered theoretically in predictive models, for example analog to strand failure projections for post-tensioned grouted tendons [67]. An EAC-related alternative SLS mode for SS rebar has not been reported either and it remains largely hypothetical. However, because of its potential for high risk events (as witnessed by the non-rebar structural service swimming full failures), and the apparent signs of EAC in one Progreso pier case, this mode merits careful future consideration as well. Notwithstanding those alternatives, pending new evidence to the contrary a concrete-cover cracking SLS mode seems to be for now the most reasonable working assumption for durability estimates.

With that SLS choice, the survey revealed glimpses of the duration of the propagation stage carried to full completion for a few of the more realistic experiences and test conditions. In particular, the survey provided the basis for an educated indirect estimate of t_p in the actual service conditions at the Progreso pier. The result was a t_p value of several decades for a rebar material (austenitic type 304 SS), design (permeable concrete but thick cover, roughly comparable to a thinner cover of less permeable concrete) and service (marine exposure) not too far removed from those where SS rebar would be specified today. That estimate represents an encouraging several-fold improvement over the t_p of only a few years which would be normally expected for PS rebar in similar conditions. The other full completion t_p observations in outdoor/service environment tests, but not in actual structure placement, were limited to straight Cr SSs tests in BRE tests and a Florida test, showing modest improvement over PS. The picture for outdoor/service exposure cases became more complete when considering cases where SLS was not reached, but where active corrosion rate estimates could still be obtained. Those cases (the other BRE tests, Treat Island, Durban Bluff, Swiss Highway Tunnel, Florida) confirmed the natural exposure experience-based expectation of strong t_p increase over that of PS for high PREN austenitic and Duplex SS, and of modest increase for use of low PREN ferritic or no-Ni austenitic SSs. Mechanistic insight from the laboratory tests suggested that the concept of an X_{CRIT} value (averaged on an intermediate space scale) to produce concrete cover cracking can be reasonably extended to the case of SS rebar, with t_p estimated by the ratio of X_{CRIT} to the (properly averaged) corrosion rate. While the information is still scant, the values of X_{CRIT} for SS rebar for a given concrete and spatial geometry do not appear to be radically different from those encountered for PS rebar.

Overall, the information available at present suggests that propagation stage corrosion forecasting methodology already in place for PS rebar may on first approximation be translatable to SS rebar, with nominal corrosion rates during the propagation stage severalfold lower than for PS rebar for the higher PREN SSs. Because of the present paucity of data, this review stops short of recommending particular t_p multiplier factor values relative to PS. It recommended instead that further research be conducted to resolve uncertainty and to guide parameter selection choices in tentative modeling updates [4] [3]. Caveats apply in the conservative direction by noting for example that performance of SS rebar can be seriously degraded by insufficient descaling, and that unexpected failure modes (e.g., EAC) may have not been revealed yet in the limited service experience to date. Excessive conservativeness may take place too, by not taking sufficient credit for the repassivation potential for SSs being higher than for PS, and for the higher cathodic polarizability of SS rebar [68]. Thus, beneficial cathodic prevention of the rest of the rebar assembly by galvanic macrocell coupling with an earlier corroding region [69] [70] could be more important for SS than for PS rebar, contingent on the relative extent of macrocell coupling on both materials. More sophisticated modelling approaches should take into account the aforementioned alternative SLSs, as well as updated X_{CRIT} formulations tailored to the corrosion morphology prevalent in SS rebar. Continuing investigation of these issues as well as careful monitoring of existing structures should assist in achieving the full benefit of increasing use of SS reinforcement bars.

CONCLUSIONS

a. Information on the duration of the corrosion propagation stage (t_p) of stainless steel (SS) rebar in actual reinforced concrete structures in service is scant and indirect. The one long term experience case available (Progreso pier in Mexico) suggests a t_p value in the order of several decades for austenitic Cr-Ni rebar in marine service. That value is severalfold greater than that expected for plain steel (PS) rebar in similar conditions.

b. Outdoor tests not in actual structural service but still retaining some realistic features provided a few cases where the end of the propagation stage was reached, albeit for less resistant straight Cr SS rebar. The t_p values were in those cases modestly longer than expected for PS rebar, an indication supported by limited available outdoor corrosion rate measurements.

c. Laboratory experiments and both physical and empirical modeling tended to support the structural and field test indications that the corrosion rates of the more corrosion-initiation resistant SSs, once in the propagation stage, are markedly lower for the higher pitting resistant stainless steels than for plain steel rebar. That finding appears to apply as well to SS rebar exposed at preexisting concrete cracks.

d. The field and laboratory results support the use of corrosion-induced concrete cover cracking as a practical descriptor of the serviceability limit state (SLS) of SS rebar in concrete. Other SLSs, for example stress overload fracture of pitted rebar, or environmentally assisted cracking are possible but so far not seen in practice.

e. SS rebar corrosion tended to be more in the form of localized pitting than for PS rebar. Nevertheless, the concept of a critical corrosion penetration for cover cracking appears to be useful to forecast the value of t_p when an effective corrosion rate value is known. The critical penetration for SS seems to be comparable to or exceeding that for PS.

f. Overall, SS rebar made with high pitting resistant grades and thoroughly descaled was found to have a positive outlook for t_p values that substantially exceed those of PS rebar. Quantification of that improvement is much in need of further field and laboratory assessment.

ACKNOWLEDGEMENTS

REFERENCES

[1]   K. Tuutti, Corrosion of steel in concrete, Stockholm: Swedish Cement and Concrete Research Institute, 1982.

[2]   R. Weyers, B. Prowell, I. Al-Qadi and M. Sprinkel, "Concrete Bridge Protection, Repair, and Rehabilitation Relative to Reinforcement Corrosion: A Methods Application Manual, SHRP S-360," National Research Council, Washington, DC, 1993.

[3]   A. Sagüés, "Modeling the Effects of Corrosion on the Lifetime of Extended Reinforced Concrete Structures (NACE-03100854)," Corrosion, vol. 59, no. 10, pp. 854-866, 2003.

[4]   M. Ehlen, M. Thomas and E. Bentz, "Life-365 service life prediction model TM version 2.0," Concrete international, vol. 31, no. 5, pp. 41-46, 2009.

[5]   Florida Department of Transportation, "Structure Design Guidelines - Structures Manual Volume 1, January 2018," Florida Department of Transportation, Tallahassee, 2018.

[6]   Virginia Department of Transportation - Structure and bridge division, "Instructional and Information Memorandum No. IIM-S&B-81.8," Virginia Department of Transportation, 2018.

[7]   F. Lollini, M. Carsana, M. Gastaldi and E. Redaelli, "Corrosion Behaviour of Stainless Steel Reinforcement in Concrete.," Corrosion Reviews, vol. 36, no. 6, pp. 1-17, 2018.

[8]   NACE International TG 057 Technical Committee, "State of the Art Report on Corrosion-Resistant Reinforcement," NACE International, Houston, 2019.

[9]   U. Angst, B. Elsener and C. L. a. O. Vennesland, "Critical Chloride Content in Reinforced Concrete – A Review," Cement and Concrete Research, vol. 39, no. 12, pp. 1122-1138, 2009.

[10]   M. F. Hurley and J. R. Scully, "Lateral and radial corrosion propagation behavior of 9-21% Cr and 18% Cr + 2.8% Mo stainless steel reinforcing materials in simulated concrete environments," Materials and Corrosion, vol. 64, no. 9, pp. 752-763, 2013.

[11]   C. K. a. S. W. Mark Mistry, " LCA and LCC of the world's longest pier: a case study on nickel-containing stainless steel rebar," The International Journal of Life Cycle Assessment, vol. 21, no. 11, pp. 1637-1644, 2016.

[12]   Y. Schiegg, C. -H. Voute, H. Peter, S. Hasler and U. Urlau, "Initiation and Corrosion Propagation of Stainless Steel Reinforcements in Concrete Structures," in European Corrosion Conference: Long Term Prediction and Modelling of Corrosion, EUROCORR 2004, September 12, 2004 - September 16, Nice, France, 2004.

[13]   K. W. J. Treadaway, R. N. Cox and B. L. Brown, "Durability of Corrosion Resisting Steels in Concrete.," Proceedings of the Institution of Civil Engineers (London). Part 1 - Design & Construction, vol. 86, pp. 305-331, 1989.

[14]   M. Hren, T. Kosec and A. Legat, "Characterization of stainless steel corrosion processes in mortar using various monitoring techniques," Construction and Building Materials, vol. 221, pp. 604-613, 2019.

[15]   W. H. Hartt, R. G. Powers, D. K. Lysogorski, M. Paredes and Y. P. Virmani, "Job Site Evaluation of Corrosion-Resistant Alloys for Use as Reinforcement in Concrete. Report No. (FHWA-HRT-06-078)," Federal Highway Administration, Virginia, 2006.

[16]   F. Presuel-Moreno, J. Scully and S. Sharp, "Literature Review of Commercially Available Alloys That Have Potential as Low-Cost, Corrosion-Resistant Concrete Reinforcement," Corrosion, vol. 66, no. 8, pp. 086001-1 - 086001-13, 2010.

[17]   D. McDonald, M. Sherman, D. Pfeifer and Y. Virmani, "Stainless Steel Reinforcing as Corrosion Protection," Concrete International, vol. 17, no. 5, pp. 65-70, 1995.

[18]   W. H. Hartt, R. G. Powers, V. Leroux and D. K. Lysogorski, "A Critical Literature Review of High-Performance Corrosion Reinforcements in Concrete Bridge Applications. Report No. (FHWA-HRT-04-093)," Federal Highway Administration, Virginia, 2004.

[19]   W. H. Hartt, R. G. Powers, D. K. Lysogorski, V. Liroux and Y. P. Virmani, "Corrosion Resistant Alloys for Reinforced Concrete. Report No. (FHWA-HRT-07-039)," Florida Atlantic University and Florida Department of Transportation, Florida, July 2007.

[20]   ASTM Designation: A 380 – 06, "Standard Practice for Cleaning, Descaling, and Passivation of Stainless Steel Parts, Equipment, and Systems," ASTM International, West Conshohoken, 2006.

[21]   ASTM Designation: A 967 – 05, "Standard Specification for Chemical Passivation Treatments for Stainless Steel Parts," ASTM International, West Conshohoken, 2005.

[22]   G. G. Clemena, D. N. Kukreja and C. S. Napier, "Trial Use of a Stainless Steel-clad Steel Bar in a New Concrete Bridge Deck in Virginia (VTRC 04-R5)," Federal Highway Administration, Virginia, 2003.

[23]   F. Cui and A. Sagüés, "Exploratory Assessment of Corrosion Behavior of Stainless Steel Clad Rebar - I: Experimental," Corrosion, vol. 62, p. 822, 2006.

[24]   F. Cui and A. Sagüés, "Exploratory Assessment of Corrosion Behavior of Stainless Steel Clad Rebar - II: Modeling of Galvanic Corrosion at Cladding Breaks," Corrosion, vol. 62, p. 918, 2006.

[25]   M. F. Hurley and J. R. Scully, "Threshold Chloride Concentrations of Selected Corrosion-Resistant Rebar Materials Compared to Carbon Steel," Corrosion, vol. 69, no. 10, pp. 892-904, 2006.

[26]   G. Mullins, R. Sen and A. Sagüés, "Design and construction of precast piles with stainless reinforcing steel (BDK84 977-07)," Civil & Environmental Engineering, USF, Tampa, 2014.

[27]   R. Moser, P. Singh, L. Kahn and K. Kurtis, "Durability of Precast Prestressed Concrete Piles in Marine Environment, Part 2. Volume 2: Stainless Steel Prestressing Strand and Wire," Georgia Institute of Technology, Atlanta, 2012.

[28]   A. Fahim, A. E. Dean, M. D. A. Thomas and E. G. Moffatt, "Corrosion Resistance of Chromium-steel and Stainless Steel Reinforcement in Concrete (DOI: 10.1002/maco.201709942)," Materials and Corrosion, vol. 69, no. 2, pp. 1-17, 2018.

[29]   ASTM International, ASTM C876-91; Standard test method for half-cell potentials of uncoated reinforcing steel in concrete., West Conshohocken, PA: American Society for Testing and Materials, 2009.

[30]   S. Mameng, C. Tigerstrand, T. Larsson, G. Gedge and J. McCray, "Experience of duplex stainless steels as construction materials in bridges: Results of seven inspections," in IABSE Symposium Vancouver 2017: Engineering the Future, Sweden,London., 2017.

[31]   Arminox Stainless, "Research and Development, Pier in Progreso, Mexico.," Arminox Stainless, Progreso, Mexico., 1999.

[32]   A. Christensen, "Pier at Progreso," in 50 Years of Civil Engineering, 1904 - 1954, Copenhagen,Denmark, Christiani & Nielsen, 1954, pp. 39-54.

[33]   A. A. Torres-Acosta, "Viaducto de Arcos de Progreso,Yucatan: Primera Obra de Concreto Construida con Acero Inoxidable.," Instituto Mexicano del Transporte, Mexico., 2018.

[34]   P. Castro-Borges, O. Troconis, E. Moreno, A. A. Torres-Acosta, M. Martinez-Madrid and A. Knudsen, "Performance of a 60-year-old concrete pier with stainless steel reinforcement," Materials Performance, vol. 41, no. 10, pp. 50-55, 2002.

[35]   E. I. Moreno, A. Torres-Acosta and P. Castro Borges, "Construccion del Muelle de Progreso," Ingeniería Revista Academica, vol. 8, no. 1, pp. 61- 66, 2004.

[36]   A. Sagüés, E. Moreno, W. Morris and C. Andrade, "Carbonation in Concrete and Effect on Steel Corrosion," University of South Florida, Tampa, FL, 1997.

[37]   A. Torres-Acosta, P. Castro and M. Martinez, "Estudio de la Durabilidad del Antiguo Muelle Fiscal y Pruebas de Carga de Tres Arcos del Viaducto. Primer Informe," Instituto Mexicano del Transporte, Mexico, 2005.

[38]   A. Torres-Acosta, P. Castro and M. Martinez, "Estudio de la Durabilidad del Antiguo Muelle Fiscal y Pruebas de Carga de Tres Arcos del Viaducto. Segundo Informe," Instituto Mexicano de Transporte, Mexico, 2005.

[39]   S. Kahl, "Stainless and Stainless-Clad Reinforcement for Highway Bridge Use. Final Report (RC-1560)," Michigan Department of Transportation, Michigan, 2012.

[40]   A. Ip, F. Pianca and B. Hope, "Application of stainless steel reinforcement for highway bridges in Ontario," in Concrete under severe conditions 2, Proc. 2nd International conference on concrete under severe conditions, Volume 2, London, 1998.

[41]   J. D. Wenzlick, "Evaluation of Stainless Steel Reinforcement In Bridge Decks Report (Report OR08-011)," Missouri Department of Transportation, Missouri, 2007.

[42]   L. Xing, D. Drawin and J. Browning, "Evaluation of Multiple Corrosion Protection Systems and Corrosion Inhibitors for Reinforced Concrete Bridge Decks (Contract No. DTFH61-03-C-00131)," The University of Kansas Center for research, Lawrence, Kansas, 2010.

[43]   J. Oldfield and B. Todd, "Ambient Temperature Stress Corrosion Cracking of Austenitic Stainless Steel in Swimming Pools," Materials Performance, vol. 29, no. 12, pp. 57-58, 1990.

[44]   Heselmans, Jan; Vermeij, Peter., "Fatal Accident in Dutch Swimming Pool caused by Environmentally Cracked Bolts., Paper No. 2331," in Corrosion 2013, NACE International, Houston, 2013.

[45]   M. Fontana, Corrosion Engineering, New York: McGraw-Hill, 1986.

[46]   D. Hirschfeld, H.Busch, I. Stellfeld, N. Arlt, E. Michel, D. Grimme and G. Steinbeck, "Stress corrosion cracking behaviour of stainless steels with respect to their use in architecture, part 1: corrosion in the active state," Steel Research, vol. 64, no. 8/9, pp. 461-465, 1993.

[47]   N. Arlt, E. Michel, D. Hirschfeld, H.Busch, I. Stellfeld, D. Grimme and G. Steinbeck, "Stress corrosion cracking behaviour of stainless steels with respect to their use in architecture, part 2: corrosion in the passive state," Steel Research, vol. 64, no. 10, pp. 526-533, 1993.

[48]   G. N. Flint and R. N. Cox, "The Resistance of Stainless Steel Partly Embedded In Concrete to Corrosion by Seawater," Magazine of Concrete Research, vol. 40, pp. 13-27, 1988.

[49]   A. Torres-Acosta and A. Sagüés, "Concrete Cracking by Localized Steel Corrosion - Geometric Effects," ACI Materials Journal, vol. 101, no. 6, pp. 501-507, 2004.

[50]   R. Cox and J. Oldfield, "The Long-Term Performance of Austenitic Stainless Steel in Chloride Contaminated Concrete.," SPECIAL PUBLICATION-ROYAL SOCIETY OF CHEMISTRY, vol. 183, no. 1, pp. 662-669, 1996.

[51]   B. Callaghan, "Performance of a 12% chromium steel in concrete in severe marine environments," Corrosion Science, vol. 35, no. 5 -8 pt 2, pp. 1535-1541, 1993.

[52]   F. Presuel-Moreno, F. Gutierrez, J. Zielske, V. Casas and Y.-Y. Wu, "Analysis and Estimation of Service Life of Corrosion Prevention Materials Using Diffusion, Resistivity and Accelerated Curing for New Bridge Structures - Volume 1: Corrosion Prevention Materials (Monitoring and Forensic Examination) (No. BDK79-977-02).," Florida Atlantic University, Florida Department of Transportation, Florida, 2013.

[53]   F. Presuel-Moreno and F. Gutierrez, "Corrosion Initiation and Propagation of Two Duplex Stainless Steels Embedded in Concrete. NACE-2014-4359," in CORROSION 2014. NACE International., San Antonio, Texas, USA, 2014.

[54]   U. Nurnberger, "Stainless steel in Concrete : State of the Art Report," Institute of Materials (UK), pp.30, vol. 657, p. 30, 1996.

[55]   U. Nurnberger, "STAINLESS STEEL REINFORCEMENT – A SURVEY," Otto-Graf Journal, vol. 16, pp. 111-138, 2005.

[56]   Y. Tadokoro, M. Kojima and N. Otsuki, "Corrosion Propagation Behavior of Stainless Steel Reinforcing Bars in Concrete.," Corrosion Engineering / Zairyo to Kankyo., vol. 59, no. 5, pp. 179-186, 2010.

[57]   M. Serdar, L. V. Žulj and D. Bjegović, "Long-term corrosion behaviour of stainless reinforcing steel in mortar exposed to chloride environment," Corrosion Science, vol. 69, pp. 149-157, 2013.

[58]   B. Elsener, D. Addari, S. Coray and A. Rossi, "Stainless Steel Reinforcing Bars - Reason for their High Pitting Corrosion Resistance.," Materials and Corrosion, vol. 69, no. 2, pp. 111-119, 2011.

[59]   M. Gastaldi and L. Bertolini, "Effect of Temperature on the Corrosion Behaviour of Low-nickel Duplex Stainless Steel Bars in Concrete," Cement and Concrete Research, vol. 56, p. 52–60, 2014.

[60]   M. Garcia-Alonso, M. L. Escudero, J. M. Miranda, M. I. Vega, F. Capilla, M. J. Correia, M. Salta, A. Bennani and J. A. Gonzalez, "Corrosion behaviour of new stainless steels reinforcing bars embedded in concrete," Cement and Concrete Research, vol. 37, no. 10, pp. 1463-1471, 2007.

[61]   J. Scully and M. Hurley, "Investigation of the corrosion propagation characteristics of new metalics reinforcing bars. Final Contract Report (VTRC 07-CR 09)," Virginia Department of Transportation, Virginia, 2007.

[62]   A. Pachón-Montaño, J. Sánchez-Montero, C. Andrade , J. Fullea , E. Moreno and V. Matres , "Threshold Concentration of Chlorides in Concrete for Stainless Steel Reinforcement: Classic Austenitic and New Duplex Stainless Steel," Construction and Building Materials, vol. 186, p. 495–502, 2018.

[63]   C. Alonso, C. Andrade, M. Castellote and P. Castro, "Chloride Threshold Values to Depassivate Reinforcing Bars Embedded in a Standardized OPC Mortar," Cement and Concrete Research, vol. 30, no. 7, pp. 1047-1055, 2000.

[64]   F. Gutierrez Trellez, Corrosion Initiation and Propagation on Corrosion Resistant Alloys Embedded in Concrete by Accelerated Chloride Transport, Boca Raton: Florida Atlantic University, 2013.

[65]   D. Hansson, C. Van Niejenhuis and S. Walbridge, "The Performance of Austenitic and Duplex Stainless Steels in Cracked Concrete Exposed to Concentrated Chloride Brine," Journal of Materials Science, vol. 51, no. 1, pp. 362-374, 2016.

[66]   A. International, ASTM A1035 / A1035M - 20 Standard Specification for Deformed and Plain, Low-Carbon, Chromium, Steel Bars for Concrete Reinforcement, West Conshohocken, PA: ASTM International, 2020.

[67]   W. Hartt, "Failure Projection of Corroding Bridge Post-Tensioning Tendons Considering Influential Factors and Issues," Corrosion, vol. 75, no. 9, pp. 1146-1151, 2019.

[68]   F. Cui and A. Sagüés, "Cathodic Behavior of Stainless Steel 316LN Reinforcing Bars In Simulated Concrete Pore Solutions. Paper No. 08323," in Corrosion 2008, NACE International, Houston, 2008.

[69]   M. Walsh and A. Sagüés, "Steel Corrosion in Submerged Concrete Structures—Part 2: Modeling of Corrosion Evolution and Control," Corrosion, vol. 72, no. 5, pp. 665-678, 2016.

[70]   A. Sagüés, A. Sánchez, K. Lau and S. Kranc, "Service Life Forecasting for Reinforced Concrete Incorporating Potential-Dependent Chloride Threshold," Corrosion, vol. 70, no. 9, pp. 942-957, 2014.

[71]   G. Gedge, Structural uses of stainless steel — buildings and civil engineering, vol. 64, 2008, pp. 1194-1198.

[72]   E. Jouannais, "Stainless Steel in Bridges and Footbridges," 2004. [Online]. Available: http://www.constructalia.com/repository/Publications/Stainless%20Bridges%20and%20Footbridges/stainlesssteelbridges_EN.pdf.

[73]   F. H. Rasheeduzzafar, F. H. Dakhil, M. A. Bader and M. M. Khan, "Performance of Corrosion Resisting Steels in Chloride-bearing Concrete.," ACI Materials Journal, vol. 89, no. 5, pp. 439-448, 1992.

[74]   L. Bertolini, F. Bolzoni, T. Pastore and P. Pedeferri, "Behaviour of Stainless Steel in Simulated Concrete Pore Solution," British Corrosion Journal, vol. 31, no. 3, pp. 218-222, 1996.

[75]   Arminox Stainless, "American Arminox, Inc," 2016. [Online]. Available: http://americanarminox.com/.

[76]   SASSDA, "South Africa Stainless Steel Development Association," March 2018. [Online]. Available: https://sassda.co.za/millennium-bridge-thriving-after-18-years/.

[77]   Cedinox - Stainless Steel, "Stainless Steel Spanish Association," 2014. [Online]. Available: http://www.cedinox.es/en/acero-inoxidable/application/02.-civil-engineering/.

[78]   D. Cochrane, "Success for Stainless Steel, Concrete in, on and Under Water.," Concrete, pp. 26-28, 2003.

[79]   B. Sørensen, P. B. Jensen and E. Maahn, "The Corrosion Properties of Stainless Steel Reinforcement.," in Corrosion of Reinforcement in Concrete, London, UK, Elsevier Applied Science, 1990, pp. 601-610.

[80]   P. Gu, S. Elliott, J. J. Beaudoin and B. Arsenault, "Corrosion resistance of stainless steel in chloride contaminated concrete," Cement and Concrete Research, vol. 26, no. 8, pp. 1151 - 1156, 1996.

[81]   J. MccGrun, "Stainless Steel Reinforcing Bars in Concrete," in Proceedings of the International Conference of Corrosion and Rehabilitation of Reinforced Concrete Structures, Orlando, FL, FHWA, Orlando, Florida, 1997.

[82]   D. McDonald, D. Pfeifer and P. Virmani, "Corrosion - Resistant Reinforcing Bars Findings of a 5-years FHWA Study," in Proceedings of International Conference on Corrosion and Rehabilitation of Reinforced Concrete Structures, Orlando,Florida, 1999.

[83]   D. McDonald, D. Pfeifer and M. Sherman, "Corrosion Evaluation of Epoxy-Coated, Metallic-Clad and Solid Reinforcing Bars in Concrete. Final Contract Report (FHWA-RD-98-153)," Federal Highway Administration, Virginia, 1998.

[84]   L. Bertolini, M. Gastaldi, M. Pedeferri and P. Pedeferri, "Stainless Steel in Concrete," in European Comission, COST521 Action Corrosion of steel in reinforced concrete structures, Workshop proceedings, Tampere, Finland, 2000.

[85]   F. N. Smith, "Stainless Steel Reinforcement for Concrete Construction," in 12th Middle East, Corrosion conference & Exhibition, Bahrain, 2008.

[86]   M. Rosso, G. Melotti, D. Gyppaz and M. Cornoglio, "Corrosion Behaviour of Duplex Stainless Steels for Concrete Reinforcement Application," in Duplex Stainless Steels 97 - 5th World Conference, Italy, 1997.

[87]   P. Pedeferri, "Behaviour of Stainless Steel in the Rehabilitation of Corrosion Damaged Infrastructures and Effects of Galvanic Coupling Between Carbon Steel and Stainless Steel," Rehabilitation of Corrosion damaged infraestructure. Chapter I: Case and Laboratory Studies, pp. 1-7, 1998.

[88]   Giatec Scientific, "Giatec Scientific Inc," [Online]. Available: https://www.giatecscientific.com/education/a-new-technique-for-rebar-corrosion-rate-measurement-in-concrete/. [Accessed 29 01 2019].

[89]   Nickel Institute, "Stainless Steel Reinforcement," 2015. [Online]. Available: https://www.nickelinstitute.org/~/media/Files/TechnicalLiterature/Ni_StainlessSteel-Rebar-LD.ashx. [Accessed 15 01 2019].

[90]   IMOA, "International Molybdenum Association," 2007. [Online]. Available: https://www.imoa.info/download_files/stainless-steel/StainlessSteelReinforcement.pdf. [Accessed 21 12 2018].

[91]   N. Baddoo and A. Kosmač, "Sustainable Duplex Stainless Steel Bridges," The Steel Construction Institute,Euro Inox, 2010. [Online]. Available: http://www.worldstainless.org/Files/issf/non-image-files/PDF/Sustainable_Duplex_Stainless_Steel_Bridges.pdf. [Accessed 14 01 2019].

[92]   ISSF, "International Stainless Steel," 07 05 2016. [Online]. Available: http://www.worldstainless.org/Files/issf/non-image-files/PDF/ISSF_Stainless_Steel_in_Infrastructure_English.pdf. [Accessed 15 12 2018].

[93]   ISSF, International Stainless Steel Forum, "Stainless Steel Rebar Application," 2018. [Online]. Available: http://www.stainlesssteelrebar.org/applications/. [Accessed 17 11 2018].

[94]   Fib Model Code for Concrete Structures, Lausanne, Switzerland: Ernst & Sohn, a Wiley brand, 2010.

[95]   C. Andrade, C. Alonso and F. J. and Molina, "Cover Cracking as a Function of Rebar Corrosion: Part I—Experimental Test," Materials and Structures, vol. 26, pp. 453-464, 1993.